INTEGRATED MULTIAXIAL EXPERIMENTATION AND CONSTITUTIVE MODELING

Dissertation

Submitted to

The School of Engineering of the

UNIVERSITY OF DAYTON

In Partial Fulfillment of the Requirements for

The Degree of

Doctor of Philosophy in Engineering

By

Peter Louis Phillips

UNIVERSITY OF DAYTON

Dayton, Ohio

May, 2017

INTEGRATED MULTIAXIAL EXPERIMENTATION

AND CONSTITUTIVE MODELING

Name: Phillips, Peter Louis

APPROVED BY:

Robert A. Brockman, Ph.D.
Advisory Committee Chairman
Professor, Civil & Environmental
Engineering and Engineering Mechanics

Steven L. Donaldson, Ph.D.
Committee Member
Associate Professor, Civil &
Environmental Engineering and
Engineering Mechanics

Thomas J. Whitney, Ph.D.
Committee Member
Assistant Professor, Civil &
Environmental Engineering and
Engineering Mechanics

Reji John, Ph.D.
Committee Member
Principal Materials Research Engineer,
AFRL/RXCM

Andrew H. Rosenberger, Ph.D.
Committee Member
Senior Materials Research Engineer,
AFRL/RXCM

Robert J. Wilkens, Ph.D., P.E.
Associate Dean for Research and
Innovation, Professor
School of Engineering

Eddy M. Rojas, Ph.D., M.A., P.E.
Dean
School of Engineering

ABSTRACT

INTEGRATED MULTIAXIAL EXPERIMENTATION

AND CONSTITUTIVE MODELING

Name: Phillips, Peter Louis
University of Dayton

Advisor: Dr. Robert A. Brockman

Modern plasticity models contain numerous parameters that no longer correlate directly to measurements, leading to a lack of uniqueness during parameter identification. This problem is exacerbated when using only uniaxial test data to populate a three-dimensional model. Parameter identification typically is performed after all experiments are completed, and experiments using different loading conditions are seldom conducted for validation. Experimental techniques and computational methods for parameter identification are sufficiently advanced to permit real-time integration of these processes. This work develops a methodology for integrating multiaxial experimentation with constitutive parameter calibration and validation. The integrated strategy provides a closed-loop autonomous experimental approach to parameter identification. A continuous identification process guides the experiment to improve correlation across the entire axial-torsional test domain. Upon completion of the interactive test, constitutive parameters are available immediately for use in finite element simulations of more complex geometries. The autonomous methodology is demonstrated through both analytical and physical experiments on Ti-6Al-4V. The proposed approach defines a framework for parameter identification based on complete coverage of the stress

and strain spaces of interest, thereby providing greater model fidelity for simulations involving multiaxial stress states and cyclic loading.

To my true love, Gretchen

ACKNOWLEDGMENTS

I will be forever grateful to Dr. Robert Brockman for patiently mentoring me throughout my undergraduate and graduate studies and my initial professional career. The countless hours of support provided by Dr. Brockman have undoubtedly shaped my career and enabled me to develop the skills necessary to perform this work. Thank you Bob for all of your help. I want to thank my committee members, Drs. Steven Donaldson, Reji John, Andrew Rosenberger, and Thomas Whitney, for their guidance and encouragement throughout all stages of this work. I am grateful for the opportunity to perform this research at the Materials and Manufacturing Directorate, United States Air Force Research Laboratory (AFRL), Wright-Patterson Air Force Base, Ohio, USA. I would like to acknowledge both AFRL and the Dayton Area Graduate Studies Institute (DAGSI) for funding this work through the AFRL/DAGSI Ohio Student-Faculty Research Fellowship program through topic RX14-12 and through Department of Defense contract FA8650-14-D-5205. Additional thanks go to Dr. Reji John for seeing the merit in this work and sponsoring the fellowship topic. Special thanks are also in order for Dr. Dennis Buchanan for facilitating this work and for the beneficial discussions and guidance provided throughout the years.

Many others have provided fundamental support for this work and require acknowledgment, including: my supervisors at the University of Dayton Research Institute, Drs. William Braisted, Steven Olson, and Mr. Michael Bouchard, for allowing me the flexibility to complete this work; Mr. Philip Blosser for educating me on experimental methods; Messrs. Mark Ruddell, Dan Knapke, and Dale Osborne for their support and guidance pertaining to experimental techniques; Mrs. Molly

Walters for helping obtain specimens and fixturing necessary for this work; Mr. William Porter for aiding me with metallurgy and microscopy work; Dr. Martin DeSimio for educating me on digital filtering; and the countless others who have assisted through the years. I am also thankful to my parents, extended family, and friends for always providing encouragement in all aspects of life.

Finally, I could not have completed this work without the motivation, support, and patience of my wife, Gretchen, my son, Thomas, and my daughter, Molly.

TABLE OF CONTENTS

LIST OF FIGURES

LIST OF TABLES

CHAPTER I

INTRODUCTION

1.1 Problem Statement

Modern plasticity models contain numerous parameters that no longer correlate directly to laboratory experiments, leading to a uniqueness problem during parameter identification. Computational methods, like the finite element method, that use modern material models are commonly replacing experimental tests to avoid the high costs associated with designing and manufacturing complex subcomponents for the aerospace industry, building test fixtures, and conducting subcomponent experiments. In addition, certain stress states commonly of interest are difficult, if not impossible, to physically reproduce in some experiments. Accurate material models that are calibrated over a wide range of stress and temperature conditions are critical to ensuring the accuracy and reliability of computational results for complicated geometries, like turbine engine disks, subjected to realistic loading conditions.

Continuing advancements in test methods for uniaxial and multiaxial stress conditions, crack growth, and progressive damage have contributed to a wealth of information regarding the behavior of materials. Computation power continues to increase allowing analytical models of these phenomena to become more sophisticated and complex. The success of a finite element analysis of complicated geometries relies on accurate plasticity models. However, modern plasticity models have numerous parameters that can be difficult to fit. The physical significance of certain parameters can be indistinguishable, and identifying them turns into a time consuming trial and error fitting procedure using any experimental data available. Further delays are encountered during the transfer of experimental data to the analyst performing the fitting, because the analyst first has to manipulate the experimental data into a suitable form for the fitting process. Economic considerations limit the number of different experiments used in the fitting process. As such analytical methods play an increasingly important role in guiding experimental investigations, allowing researchers to determine which experiments are most important to the fitting process. However, the resulting experiments used for fitting have commonly targeted relatively simple stress conditions like tension and compression tests, cyclic stress- or strain-controlled tests, or plastic shakedown tests. Furthermore, additional experiments used to validate models for stress conditions different from the fitting process are limited in the open literature.

Experimental methodology has evolved over the past century to provide measurements and validation of analytical models and theories. The definition of yield criteria is of paramount importance to plasticity models. Laboratories began to use digital computers to assist in the determination of yield surfaces as early as the 1970's [1, 2], and efforts are still ongoing to map both initial and subsequent yield surfaces [3, 4, 5, 6, 7, 8, 9]. Digital image correlation (DIC), which is a recent experimental technique that provides full-field measurements, continues to garner the attention of researchers throughout many fields of material science [10, 11, 12]. Axial-torsional experiments [13, 14, 15, 16, 17, 18, 19] are now being performed, as an alternative to uniaxial loading, to impart complex, history dependent loading on materials.

Methods of reducing modern experimental test data have been established. However certain data sets, like full-field measurements from DIC, require lengthy post-processing to obtain desired results, such as strain or displacement fields. Often, the experimentalist and the analyst performing the parameter identification are different individuals, and exchanging of the data is required, which leads to delays. The process of parameter identification has been researched extensively in past decades as well, with the advent of the virtual fields method (VFM) [20, 21] and continued use of finite element model updating (FEMU) [22, 23, 24, 25, 26, 27]. Manual fitting is aided through use of optimization methods, such as Powell's method [28], Genetic Algorithms [29], and Particle Swarm Optimization [30], that have been well researched and applied to a variety of different problems. However, parameter identification occurs after experiments are performed, and the time lapse is often too great to allow for collection of additional data to improve parameter correlation.

Despite many advances in both experimentation and property identification, the two processes still are performed separately, limiting the quality of the end result. The norm is for the experimentalist to pass measured data to the analyst to perform the fitting and then implement the model. The separation between experiments and model fitting likely contributes to the limited appearance of additional experiments in the open literature conducted to validate the model for experimental conditions outside those used in the fitting. Constitutive parameter identification and validation procedures need to be directly integrated with experimental testing to eliminate the flaws inherent in current practices. Integration will increase the capability and validity of constitutive models over broader ranges of stress trajectories and decrease the time and cost required for model parameter identification.

1.2 Objective

The objective of this research is to develop an integrated test methodology and create the necessary software to reconcile the division between experimentation and analytical modeling. In the developed approach, a closed-loop autonomous identification process guides an axial-torsional experiment to improve correlation of the constitutive parameters across a multiaxial test domain, which differs from traditional uniaxial conditions. Experimentation continues until sufficient data is collected to populate the constitutive model reliably. The integrated methodology also performs parameter validation as an integral part of the experiment. Upon test completion, a set of constitutive parameters are immediately available for use in finite element simulations of more complex geometry and loading.

1.3 Significance of Research

The developed test methodology and software will allow modern laboratories to integrate experimental testing and constitutive modeling. The effort is significant in that it:

- Creates a flexible, integrated experimental and analytical testing platform for the investigation of materials under complex multiaxial loading.
- Integrates experimentation, material model fitting, and experimental validation in a single piece of software that works in real time.
- Yields a material model upon test completion that has been calibrated and validated over a broad range of multiaxial stress conditions.
- Eliminates time delays and provides a seamless transition for the use of the calibrated material model in finite element simulations of more complicated geometries under realistic loading.
- Potentially reduces both the time and cost associated with the model fitting and validation process.
- Allows for any user-written material model to be utilized directly in the parameter identification process.
- Reconciles experimental and analytical modeling efforts for the mutual benefit of both efforts.

The work not only narrows the divide between modern experimentation and analytical modeling, but also sets the stage for further integration of new and emerging experimental techniques for the purpose of optimizing material models in real time.

CHAPTER II

BACKGROUND

2.1 Experimental Mechanics

Researchers have been conducting experimental investigations of materials for centuries to further material science and engineering. In Timoshenko's historical review [31] da Vinci, Galileo, and Hooke are cited as some of the first to have conducted tension tests to determine the response of materials. The eighteenth and nineteenth century saw advancements through investigations of torsion by Coulomb, fatigue by Wohler [31], and material yielding by Tresca, Saint-Venant, Bauschinger, Mohr, von Mises [32] and many others. Much of this work was done in support of the expanding infrastructure of roadways and railway lines. Notable experimental investigations carried out by J. Guest [33] in 1900, Lode [32, 34] in 1926, and Taylor and Quinney [35] in 1932 all sought to examine the yield surface of materials under multiaxial states of stress. The yield surface defines the boundary between reversible (elastic) deformation and the onset of permanent (plastic) deformation that cannot be recovered even through unloading.

The experimental determination of the yield surface for multiaxial stress states has been studied extensively by many researchers throughout the 1900's. Michino and Findley [36] provide a detailed summary of many yield surface experiments conducted up to the 1970's. Mention is given to laboratories beginning to use digital computers to assist in the determination of yield surfaces, such as efforts of Phillips and coworkers in the 1970's [1, 2]. Others [3, 4, 5, 6, 7, 8, 9] have continued to perform experiments to determine both initial and subsequent yield surfaces. Related multiaxial investigations have been conducted by Hu et al., [37] Liu and Greenstreet [38], and Kalluri and Bonacuse [39] to name a few. Much of this work was done in support of emerging, and increasingly complex, theories of plasticity.

Another relevant modern experimental technique, which has seen a large volume of research in the past two decades [10, 11, 12], is the method of digital image correlation (DIC). Both two- and three-dimensional digital image correlation techniques have been applied to engineering applications and have shown improving degrees of accuracy throughout the years. DIC has been utilized in experiments for fracture mechanics [40, 41, 42], plasticity of metals [43, 44, 45], residual stress prediction [46, 47], and high temperature testing [48, 49, 50]. DIC is appealing because the full-field displacement information obtained from DIC can provide more detailed information than single strain gages or extensometers.

The use of combined axial and torsional loading is also prevalent in the past decades [13, 14, 15, 18, 19, 16, 17]. Cailletaud et al. [18] performed a series of axial torsional experiments on 316 stainless steel to study the influence of cross-hardening. Benallal et al. [19] conducted experiments on both 316 stainless steel and a 2024 aluminum alloy to also study the influence of cross-hardening due to changes in loading type from proportional to non-proportional in both tension and torsion. Shamsaei et al. [51] have more recently found that certain titanium alloys do not exhibit significant cross-hardening when subjected to proportional and non-proportional loading. However, Batane et al. [52] as well as Bees et al. [53] have shown through axial-torsional experiments that nickel-based alloys do have significant cross-hardening.

2.2 Constitutive Modeling

Throughout the 1900's, theories were derived in attempt to explain the complex behavior of plastic deformation. Two different categories of analytical models emerged: physical and mathematical (or phenomenological) models. Physical models try to explain behavior on a crystalline structure level, and parameter for these models are populated from test conducted on single crystal specimens, like those performed by Taylor and Elam, Schmid, and Goler and Sachs [32]. The plastic deformation of crystals of metal was found to be tied to a critically resolved shear stress occurring on planes dependent on the crystal structure. Advances in physical models, also known as crystal plasticity models, have evolved due to work by Cailletaud [54], Dunne [55], McDowell [56, 57], Acharya [58], and many others with applications to Air Force systems by many researchers including Choi [59], Turner [60], and Brockman [61].

In looking at a continuum scale rather than the microscopic scale, advances in mathematical plasticity models have been made in the past century by Prager, Armstrong and Frederick, Hill [62], Chaboche [63], Ohno and Wang [64], and others [65, 66]. These phenomenological plasticity models are routinely incorporated in finite element (FE) software commonly used today to analyze test specimens, engine disks, ribs, spars, skins of aircraft, and more. The plasticity models are formulated as incremental theories consisting of three parts: (1) a yield surface that defines the boundary between elastic and plastic behavior; (2) a flow rule that describes the deformation behavior in the plastic range; and (3) hardening laws that define the evolution of the yield surface and flow rule.

A number of the continuum scale models developed over the last 30 years are reviewed in a recent paper by Chaboche [66]. Many of the modern plasticity material models require a large number of material dependent parameters that must be calibrated based on experimental tests. The number of constitutive parameters has grown so large and diverse that manual fitting is inefficient and often does not yield the best correlation [65]. For example, the Abaqus [67] FE software has a rate-dependent Johnson-Cook plasticity model that requires 8 parameters. Abaqus also has a rate-independent nonlinear isotropic-kinematic cyclic plasticity model that requires 12 parameters when 3 backstresses are used. Each additional backstress term used to define the kinematic behavior requires 2 additional parameters. The multimechanism cyclic plasticity model used by Taleb and Cailletaud [68] uses 17 parameters. The modified Chaboche model used by Krishna [65] requires over 45 parameters.

2.3 Parameter Identification

Substantial literature exists on using numerical methods and optimization techniques for the identification of material model parameters [69, 70, 71, 72, 73, 65, 74]; however, the methods are all applied at the completion of experimental testing. As a result the fidelity of model correlation only becomes known after experimental testing is complete and can only be assessed for the specific conditions of the experiments performed. If better correlation is required, additional time and money must be spent to manufacture specimens, set up and execute testing, and repeat model correlation. Often the constitutive parameters are defined using data from only uniaxial tests, which are insufficient to define the material constants uniquely and accurately. Unique parameter identification based on only uniaxial tests is an impossible task, and the application of the resulting models to multiaxial plasticity problems can yield poor results despite the mathematical sophistication of the models.

Two methodologies for parameter identification that have grown in popularity in recent decades are the virtual fields method (VFM) and finite element model updating (FEMU). Both seek to identify parameters through the combination of experimental testing and analytical modeling. However, both methods are currently utilized upon completion of the experimental tests. Each method does have merit; therefore, further details on the methods are provided in the following sections.

2.3.1 Virtual Fields Method

The virtual fields method (VFM) is an emerging experimental and numerical technique for identifying constitutive parameters from full-field measurements. In 2006, Grediac et al. [20] summarized previous decades of progress and highlighted the numerous advancements of the VFM. A more recent technical review [21] by the same authors, Grediac and Pierron, provides a thorough explanation of the theory and illustrates many applications of the method.

The VFM has been applied successfully to linear elastic behavior for isotropic and anisotropic materials. Grediac et al. [75] demonstrated the use of the VFM to identify in-plane linear elastic stiffnesses of glass fabric composite panels. The accuracy of the VFM was proven through numerical simulations by Grediac et al. for in-plane anisotropic stiffnesses [76] and bending stiffnesses of thin plates [77]. Experimental efforts by Moulart et al. [78] showed consistent results for the determination of in-plane anisotropic stiffnesses using thick glass epoxy laminated tubes. The VFM has also been applied to high strain rate testing of composites for the determination of in-plane stiffnesses [79] with order-of-magnitude accuracy when compared to reference data.

Recently, efforts have focused on extending the VFM to plasticity. Grediac and Pierron [80] were some of the first to apply VFM to elasto-plastic problems in 1996 using a Prandlt-Reuss model. Around the same time Pannier et al. [81] applied a similar technique for a Voce hardening model. Pierron et al. [82] fit both a Voce and a nonlinear kinematic hardening model for austenitic stainless steel. Palmieri et al. [83] used the VFM on rubber for both an Ogden and Mooney-Rivlin model. More recently Rossi and Pierron [84] performed parameter identification using 3D full-field measurements, thus eliminating simplifying assumptions like plane strain or stress. Kim et al. [85] characterized post-necking behavior for uniaxial testing for Swift and Voce models. Spranghers et al. [86] used the VFM with both a Cowper-Symonds and Johnson-Cook model for aluminum panels subjected to blast loading.

Kim et al. [87] recently used the VFM to determine the parameters for an orthotropic Hill yield criterion with isotropic hardening. However, the determination of the plasticity parameters required the use of a predictor-corrector algorithm similar to that used in certain plasticity routines in FE codes. Notta-Cuvier et al. [88] applied the VFM to identify non-linear Johnson-Cook rate dependent plasticity parameters for Ti-6Al-4V by using a notched flat tension specimen. Furthermore, Notta-Cuvier et al. [89] used numerical simulations of the VFM to identify parameter for an elasto-plastic damage model. However, in both cases the application of VFM to non-linear constitutive models leads to iterative solutions [89], unlike the direct solutions used for elastic parameters. The VFM is using the principle of virtual work directly with the full-field measurements, while FEMU uses a particular mesh and a set of FE equations based on the principle of virtual work. Similar optimization methods like the genetic algorithm are used in both FEMU and the VFM for parameter identification of non-linear material models [89].

Leading researchers in the field of VFM have noted [21] that a current limitation of the method is the inability to obtain compressive data due to the 2D nature of testing. Also, much of the research in VFM applied to non-linear constitutive models has been focused on monotonic loading and not the cyclic plasticity response of interest to much of the metals community. The use of VFM for identification of plasticity parameters requires iterative solutions coupled with optimization procedures similar to FEMU, with the main difference being the analytical solution used in the optimization. Another limitation of VFM is the requirement of full-field measurements and complex specimen design to introduce heterogeneous strain fields. Research on the full-field measurement technique, DIC, is prevalent but two fundamental issues are the inherent noise in the setup and the complicated data reduction.

2.3.2 Finite Element Model Updating

Another solution to the inverse problem involves the use of an optimization scheme where the cost function is computed by comparing results from experiments and those from finite element simulations. This methodology is commonly referred to as finite element model updating (FEMU). The efforts in the field of digital image correlation over the past decades, coupled with increased computation power have allowed FEMU to be applied to a variety of interesting problems.

There have been many efforts in FEMU using specialized uniaxial test specimens to introduce heterogeneous strain fields [22, 23, 24, 25, 26, 27]. Robert et al. [25] evaluated the specimen geometries from Meuwissen et al. [22] and Haddadi et al. [23, 27] for aluminum 2024-T3. A Nedler-Mead simplex method was used for optimization of the cost function, similar to other FEMU work [24].

Kavanagh and Clough [90] proposed the use of a biaxial specimen for property identification. The FEMU method has been used on biaxial cruciform specimens for determining anisotropic parameters in both composites [91] and metallic specimens [92, 93].

An area that has received little attention is the application of the inverse problem to cylindrical specimens subjected to both axial and torsional loading. This type of testing is ideal because it generates both axial and shear components of stress and strain. Furthermore, the gage section of the specimen undergoes almost uniform conditions allowing for simplification of measurement techniques and data reduction. One of the few studies that used FEMU with axial-torsional loading was done by Fedle et al. [94]. They assessed a ferritic-pearlitic steel, used for railroad wheels, under combined axial and torsional loading and fit parameters for a Chaboche nonlinear hardening model. The analysis was performed using the commercial software Abaqus and an axisymmetric model of the specimen gage section using a mesh of CGAX4 elements that allow for twist. Three layers of elements were used to simulate the gage section. The inverse problems was solved using both a global optimization method (genetic algorithm) and a local optimization method (Needler and Mead simplex method).

Avril et al. [95] provided a review of parameter identification methods using full-field experimental data, highlighting both VFM and FEMU. They conclude that FEMU is flexible as it can use either full-field data or point strain data; however, the computation cost associated with the numerical models can be high. The VFM requiring full-field data is not as computationally expensive because the constitutive response is evaluated implicitly, not numerically, but only for linear parameters. However, this direct solution of the VFM is replaced by an iterative solution when dealing with non-linear constitutive model, increasing the computational expense to levels likely similar to FEMU.

The major limitation in FEMU work thus far is the limiting states of strain and the minor role that history-dependent plasticity plays in the role of parameter identification. The use of complex test specimens for the introduction of heterogeneous strain fields requires an analysis with many elements. History-dependent cycling can quickly become computationally expensive for such models. A viable alternative is to apply a procedure similar to Fedle et al. [94] where a cylindrical specimen is subjected to axial and torsional loads, thus allowing for different stress trajectories. One limitation of [94] is the use of the commercial FE code Abaqus. Development of a compact, parallel execution finite element code for axial-torsional problems can drastically reduce the computational expense making FEMU a much more appealing option. In addition, full-field data is not required as reliable strain measurements techniques like strain gages or extensometers can be used to obtain the axial and torsional strains that are uniform throughout the gage section.

2.4 Optimization

Optimization methods are used extensively in engineering to find the extreme points for cost or fitness functions. The FEMU, discussed in the previous section, can use a variety of optimization techniques to identify parameters for constitutive models. Different methods have been used with success in the past; among them are: gradient-based methods like the Nedler-Mead method [24], Powell's derivative-free method [74], and evolutionary algorithms such as the genetic algorithm [94] and particle swarm optimization. Parameter identification seeks to minimize the difference between experimental and analytical results. When analytical results are obtained numerically, through a technique like the finite element method, solutions are pointwise and derivative information can only be calculated numerically. Therefore, the optimization methods used and the discussion that follows are limited to derivative-free methods. While the background below is not exhaustive, it provides pertinent information to support the discussion of the developed computer code presented in Appendix D.

Powell's method [28] is a derivative-free method that uses conjugate gradients to search for a local minimum. Initially, the procedure uses line searches for each variable in the optimization. Then based on Powell's algorithm [28] a new search direction and starting point is chosen. The process is continued until the change in the fitness falls below a specified tolerance. The original method is unconstrained, but for material parameter identification, bounds are required to prevent infeasible parameters. A simple penalty method can be added to Powell's method such that if a parameter is outside the desired bounds, the objective function (fitness) is set artificially high for minimization problems (low for maximization problems). One limitation of Powell's method is the tendency to favor local convergence rather than seeking a global minimum. Therefore, the solution can become highly dependent on the starting point.

A class of derivative-free optimization methods that seek to find a global minimum are evolutionary algorithms (EA). Evolutionary algorithms are mathematical formulations that attempt to mimic the behavior of natural systems like genetic evolution or an animal group's search patterns.

Goldberg and Holland [29] developed optimization methods called genetic algorithms (GA). A GA has three main parts: selection, crossover, and mutation. Optimization variables are coded as bits, or chromosomes, using binary representation of integers. The algorithm starts with an initial population set that is randomly generated. The selection process mates two parents based on their desirable fitness. Crossover then occurs in which the selected parents give portions of their chromosomes to a child for the next generation. Lastly, mutation of the child's chromosomes can then occur. The population of children are used in the next generation and the process is repeated.

In the GA, the selection method dictates which individuals' traits will be passed to the next generation. Selection methods have received considerable attention [96], yet many variants still remain in use based on user preference. Many crossover strategies exist such as single points, multi-point, or random. The GA can be bounded by simple checks during the initial seeding of the first generation. All other operations restrict scaled values based on the number of chromosomes. One downside to the GA is the limitation of variables to the instantiations of the current gene pool. Mutation does help; however, simple GA can converge on potential non-global extrema points.

A second type of evolutionary algorithm that has been gaining popularity, due in part to Kennedy et al. [30], is particle swarm optimization (PSO). PSO attempts to find a global extremum through methods similar to animal population search patterns. An initial sample size of particles are randomly assigned positions (variable values) and velocities (step sizes). Fitnesses are evaluated for each particle location. Particle positions are updated by computing a new velocity from inertial, cognitive, and social factors. The inertial factor allows a particle to continue along its current trajectory. The cognitive factor adds memory capability so a particle is attracted to its best position. Lastly, the social factor allows all particles to be attracted to the current global best. Additional attractive factors, called pheromones, can be added to the velocity computation to allow for attraction to localized minima [97, 98]. The factors can also evolve over each iteration to improve performance [99] so particles are initially more cognitive but become more social as iterations increase.

2.5 Summary

The experimental investigation of material behavior allows researchers to understand the strengths and physical limitations of materials. To expand upon the experimental understanding, analytical material models continue to be developed to explain the behavior observed during experimental testing. Historically, the testing and modeling were simple, but as computation power and experimental equipment has advanced, the modeling has grown complex.

As more complex test conditions are used, like multiaxial non-proportional loading, researchers turn to numerical methods to perform parameter identification since physical meaning of certain model parameters becomes difficult or impossible to ascertain. In addition, the fidelity of the material models only becomes known after testing, and additional, separate, rigorous validation experiments are rarely performed.

Both the VFM and FEMU continue to receive considerable attention as researchers seek to identify the best tools for constitutive model parameter identification. The use of full-field measurement techniques, such as DIC, allows researchers to leverage more complex specimen designs that develop heterogeneous strain fields to lessen the number of tests required for parameter identification. When dealing with non-linear constitutive models, such as modern plasticity models, both VFM and FEMU require iterative solution procedures coupled with an optimization method. The computational benefit of the VFM when applied to linear elastic material parameters diminishes as non-linear models are utilized. The often overlooked axial-torsional testing of cylindrical specimens provides multiaxial strain fields, has a uniform distribution of strain in the gage section, and leads to much simpler data reduction when compared to full-field measurement techniques. Furthermore, this test geometry allows for fully reversed loading which is lacking in the current specimens used in the VFM. As discussed earlier, both the VFM and FEMU are still applied at the conclusion of experimental testing which limits the opportunity for validation on test conditions outside those used in the fitting procedure.

2.6 Thesis Effort

This thesis aims to develop a new test methodology that seamlessly and efficiently integrates experimental testing and constitutive parameter identification. The integrated approach performs calibration and validation for non-linear constitutive model parameters in real time and deviates from the traditional approach of separate experimental and analytical endeavors. Experiments performed with the integrated methodology yield calibrated non-linear material models that are validated over a broad range of multiaxial stress conditions, thereby reducing the time and cost to develop the models for use in finite element simulations of more complicated geometries under realistic loading conditions. The application of FEMU to axial-torsional loading of cylindrical specimens provides the necessary strain complexity, but also greatly simplifies the data reduction, which is essential to enabling real-time parameter identification. The integrated methodology and corresponding software required are developed and successfully demonstrated in this thesis.

Chapter III outlines the proposed, integrated test methodology and provides contrast to the conventional approach to parameter identification. The physical demonstration of the integrated methodology relies on the careful execution of specific algorithms and techniques applied within an efficient software tool. Chapter IV provides specific details on the methodology and the associated software required for successful implementation. Chapter V demonstrates the success of the methodology using simulated experiments which remove any constitutive model error. Chapter VI details the revolutionary application of the methodology to integrated multiaxial experimentation on Ti-6Al-4V to calibrate and validate viscoplasticity parameters in real time using a single specimen. Chapter VII compares results from additional, separate experiments (both uniaxial and multiaxial) performed on Ti-6Al-4V to assess the accuracy of the parameters identified with the new methodology. Finally, conclusions and extensions for the current work are given in Chapter VIII.

CHAPTER III

TEST METHODOLOGY FOR INTEGRATED EXPERIMENTATION AND CONSTITUTIVE PARAMETER IDENTIFICATION

3.1 Overview of Integrated Testing Approach

The seamless and efficient integration of experimental testing and analytical modeling for the purpose of fitting and validating non-linear constitutive model parameters in real time requires a new, novel testing methodology. The aim of this methodology is to provide a modular, general framework that can easily be adapted or expanded by researchers depending on their equipment, materials of interest, and requirements for calibration and validation. Figure 3.1 shows the framework of the integrated methodology with the test steps shown in gray boxes. Specific examples of items and techniques used for each modular step are shown in the white boxes. The lists of techniques are not all encompassing, and will continue to expand and evolve as researchers apply the methodology to their fields of interest. The scope of the new methodology is broad in that new and emerging experimental and analytical techniques can be incorporated. The methodology is also broad in terms of definitions of the methods for calibration, the algorithms used for determining the testing process, and also by the diversity of the equipment used for conducting the test. The deviation from current test methods is the use of a single specimen for both calibration and validation of the constitutive parameters, thereby letting the identification process guide the experiment rather

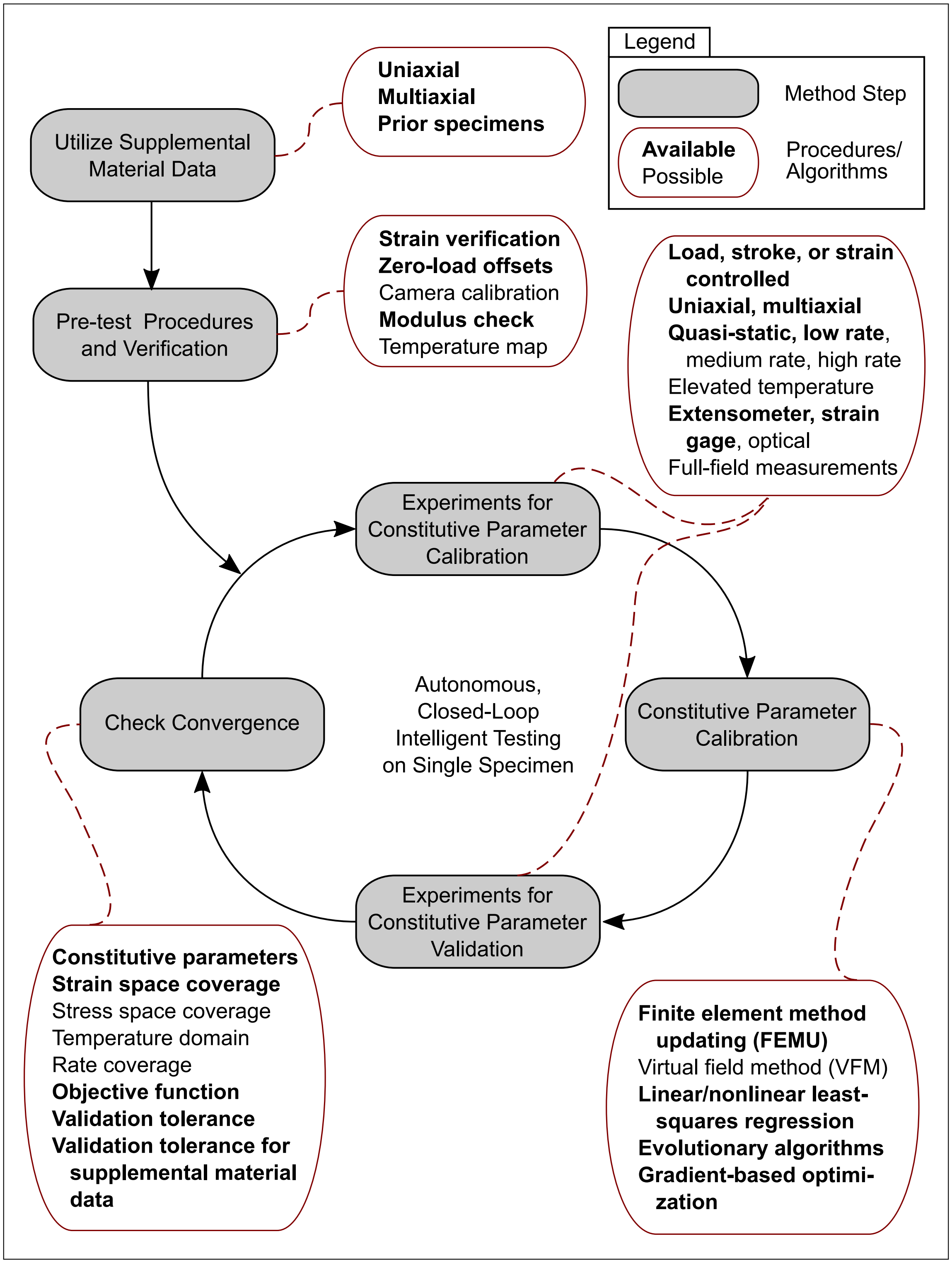

Figure 3.1: Overview of the integrated methodology. Test flow is shown in gray, while items in the whites boxes are some examples of the techniques that may be used for each step of the methodology. Items in bold are currently incorporated into the newly developed software.

than waiting until test completion to perform the calibration. The experiment is therefore directly influenced by the evolving status of the parameter identification process.

Several steps occur prior to the start of the closed loop, intelligent testing process, as shown in Figure 3.1. One important step is the incorporation of relevant, supplemental material test data into the database used for property identification. These data come from tests such as tension, compression, cyclic, uniaxial, multiaxial, high rate, elevated temperature, or even previous tests conducted using the new methodology. The supplemental data can be used throughout the test with possible applications in the calibration and validation steps. The second initialization step consists of performing any necessary pre-test verification or calibration procedures. Such procedures may include load and strain channel verification, elastic modulus checks, camera calibration, or temperature mapping. These procedures are required for verification of the experimental setup and to ensure data fed to the autonomous methodology are accurate, and that experimental errors have been minimized or eliminated.

The loop shown in the center of Figure 3.1 represents the iterative cyclic process of specimen loading, constitutive parameter calibration, and model validation, under autonomous control of the test software. The first step is a set of load excursions conducted during a physical experiment that will be used in the parameter calibration. The number of excursions, the magnitude, and direction in stress or strain space are all dictated by the user's input, their choice of algorithms, tolerances, and convergence criteria. The type of physical experiment and the measurement equipment utilized can vary, but the fundamental requirement is that enough information is obtained during the load excursions to perform a constitutive parameter calibration. The experiments may be uniaxial or multiaxial; they may employ various rates of testing, different temperatures, or several control methods; and they may utilize a variety of measurement techniques such as strain gages, extensometer, load cells, or optical techniques such as digital image correlation or the grid method.

Following each set of loading events, constitutive parameter identification is performed, which may use one of a variety of techniques. Two common techniques addressed in the literature review are finite element model updating (FEMU) and the virtual fields method (VFM); however, other methods can certainly be applied. Both methods have their merits, and have different requirements for experimental hardware needed to collect the appropriate data. Considerations for choosing a parameter identification method are efficiency, hardware requirements, and duration of computations. Because parameter identification occurs many times during the iterative process, laboratory computing resources are likely to increase from current experimental test methods; however, these resources would already be utilized by those individuals performing the calibration procedures outside the experimental laboratory. It is therefore a reallocation of resources, not a requirement for new resources. Most parameter identification techniques rely heavily on an objective function that evaluates the difference between the physical experiment and the analytical results using the constitutive parameters identified. The effectiveness of the objective function (or cost function) depends heavily on the sensitivity to the parameters being identified; therefore, care should be taken to develop or verify the effectiveness prior to the autonomous testing. Regardless of the method or objective function chosen, the output of this step is a current best estimate of the constitutive parameters being identified.

The next phase of the iterative test sequence is the in-test validation of the constitutive parameters. The purpose of this step is to perform load excursions, in addition to those used in the parameter calibration, which can be used for validation of the best constitutive parameter estimates obtained from the previous step. The specifics of how the parameters are validated depends on the identification method chosen. For example, with the FEMU, the finite element model can be used to simulate the load excursions already carried out on the specimen and deviations from the validation data can then be measured. For the VFM, the error within the load points of the validation excursions can be computed using the best estimate parameters, rather than using an optimization to minimize the errors. Further validation can occur using supplemental data to augment the objective function. This allows data other than the current test to influence the accuracy of the constitutive parameters identified.

The final step of the closed loop process is the checking of applicable convergence metrics. Suitable metrics for the integrated test may include checks for stress or strain space coverage to ensure the experiment has sampled the region of interest defined by the user. Examples of coverage criteria may be the amount of accumulated plastic strain at a particular ratio of stress, or computed slip on a given crystallographic orientation. Convergence checks can also be used for the constitutive parameters being identified to ensure they have stabilized on a particular set of values. Comparisons between the experimental and analytical solutions can be completed for the ongoing experiment as well as any supplemental material data. There may even be checks for sufficient variation in the strain rate or temperature fields. Because many of the non-linear models of interest are history dependent, the calibration and validation experiments conducted for the first cycle are added to additional calibration experiments for cycle two. All the experimental data are then used for the parameter calibration during subsequent cycles. Regardless of the number or type of convergence checks, the iterative steps are repeated until all the convergence metrics are satisfied, the user stops the experiment, or the specimen fails.

3.2 Comparison to Conventional Approach

The new methodology outlined in the previous section is fundamentally different from conventional procedures because the calibration and validation steps dictate the course of experimental testing rather than relying on a predetermined experimentation plan. This dictation provides an opportunity to ensure the constitutive parameters are calibrated and validated over a desired range of multiaxial conditions prior to stopping the experiment. The proposed methodology does borrow heavily from conventional procedures. Many of the basic techniques such as the finite element method updating or the virtual field method are the same as conventional methodology; however, in the integrated methodology, they are being applied automatically during testing without human intervention. It is important to compare and contrast the conventional and the proposed methodology to illustrate the advantages of the proposed methodology. Figure 3.2 indicates the different steps of both the conventional and proposed methodologies.

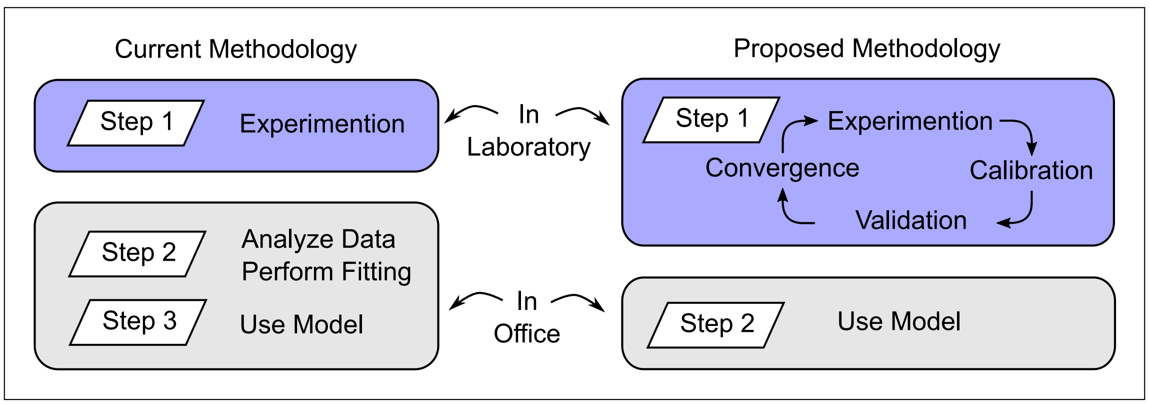

Figure 3.2: Comparison of the conventional and proposed methodology for experimentation and constitutive model calibration.

The current method for parameter identification of non-linear constitutive models is sequential in nature and the experimentation and calibration are carried out as separate endeavors. The current methodology does however have its advantages. The experiments used have been in place for decades and follow standard testing procedures such as those outlined in the numerous ASTM test standards. The experiments lead to relatively simple data reduction, unless they use digital image correlation or other advanced measurement techniques. Also, the methods have been in place and worked well for years. However, experiments are typically uniaxial which limits the correlation of parameters to simple stress states. Each test on a specimen is also commonly limited to single set of conditions, e.g. temperature, strain rate, deviatoric stress, etc. These limitations may necessitate the use of many specimens to acquire enough data to successfully calibrate the constitutive parameters.

A big drawback to the current methodology is that parameter calibration occurs post test; therefore, if additional data is needed the whole experimental process has to be repeated, leading to increase in cost and time delays. Regardless of the need for additional experiments, there are already time delays between the experiments and model calibration because the endeavors are commonly carried out by different individuals. Lastly, due to time and budget constraints experimental data is often all used in the calibration procedure and separate, carefully planned validation experiments are limited in practice.

As illustrated in early discussions, the proposed methodology is iterative in nature allowing the calibration and validation procedures to dictate the course of testing. The proposed method is advantageous because it can be applied to uniaxial experiments as well as more complex experiments such as multiaxial, proportional, or nonproportional loading. Because the experiments break away from the traditional approach of requiring simple, physically based data reduction, the tests can become more elaborate as long as algorithms can be written to process the experimental data. This allows for multiple test conditions to be carried out on a single specimen, e.g. temperature and strain rate fluctuations, various relative proportions of stress components, etc. One of the biggest advantages is that parameter fitting is a real-time, iterative process that leads to fewer delays and a better fitting procedure. Also, information about model validity is obtained as part of the test sequence. The final outcome of a test conducted with the integrated methodology is a set of calibrated and validated constitutive parameters that can be used directly after test completion, rather than the large piles of data common to the current methodology.

There are currently no widely accepted standards for complex test sequences or interactive strategy that would cover the new approach; however, any applicable test standard for laboratory practices are followed, such as equipment calibration requirements, data reporting, etc. Also the experiments lead to complex history and more complicated data reduction which necessitates greater computing resources for experimental equipment. With the ongoing advances in computing resources, the additional burden for experimental equipment will continue to lessen as resources become more powerful and less expensive. The complexity of the test history can also be an improvement over the common uniaxial test procedures in the current methodology.

3.3 Summary

Advances in experimental testing procedures allow for a broad scope of possible experimental tests. The volume and type of data that can be acquired during a single experiment also continues to increase. Constitutive models used in modern numerical techniques such as the finite element method continue to increase in complexity. Calibration and validation of the many constitutive parameters becomes a numerically intensive procedure that requires more data than can be obtained from simple uniaxial experiments, and requires advanced knowledge of the constitutive models themselves. Fortunately, recent years have brought continued advancements to parameter identification methods such as finite element method updating and the virtual fields method. However, to date the experimentation and parameter identification procedures have been separate tasks, leading to inefficiencies and delays. The combination of multiaxial experimentation and constitutive model calibration and validation in real time is feasible due to previous advances in both the experimental and modeling communities. Real-time constitutive parameter calibration and validation over multiaxial states of stress is now possible using the proposed methodology. The following chapters document the successful real-time calibration and validation of a non-linear plasticity model for Ti-6Al-4V using the integrated approach with an autonomous axial-torsional experiment.

CHAPTER IV

SOFTWARE FOR INTEGRATED EXPERIMENTATION AND CONSTITUTIVE PARAMETER IDENTIFICATION

4.1 Introduction

Currently, calibration and validation of parameters for modern constitutive models requires numerous experiments and significant post-processing of test data by individuals with in-depth knowledge. The previous chapter outlines a new methodology for the integration of multiaxial experimentation and material model calibration and validation. The proposed approach allows real-time identification of constitutive model parameters for multiaxial stress states, uses fewer specimens, and provides immediate feedback based on the accuracy of the parameter calibration process. Standalone software written with FORTRAN has been developed to implement the new methodology discussed in the previous chapter and is called the Intelligent Integrated Material Analysis and Testing Environment, or I^{2}MATE in abbreviated form. Rather than producing sets of raw data, laboratory experiments conducted using the integrated methodology produce calibrated constitutive models validated over multiaxial conditions that can be immediately used in finite element models of larger structures.

The integrated testing approach requires some software components, including test control algorithms and the constitutive model fitting process, to be embedded within I^{2}MATE (Figure 4.1).

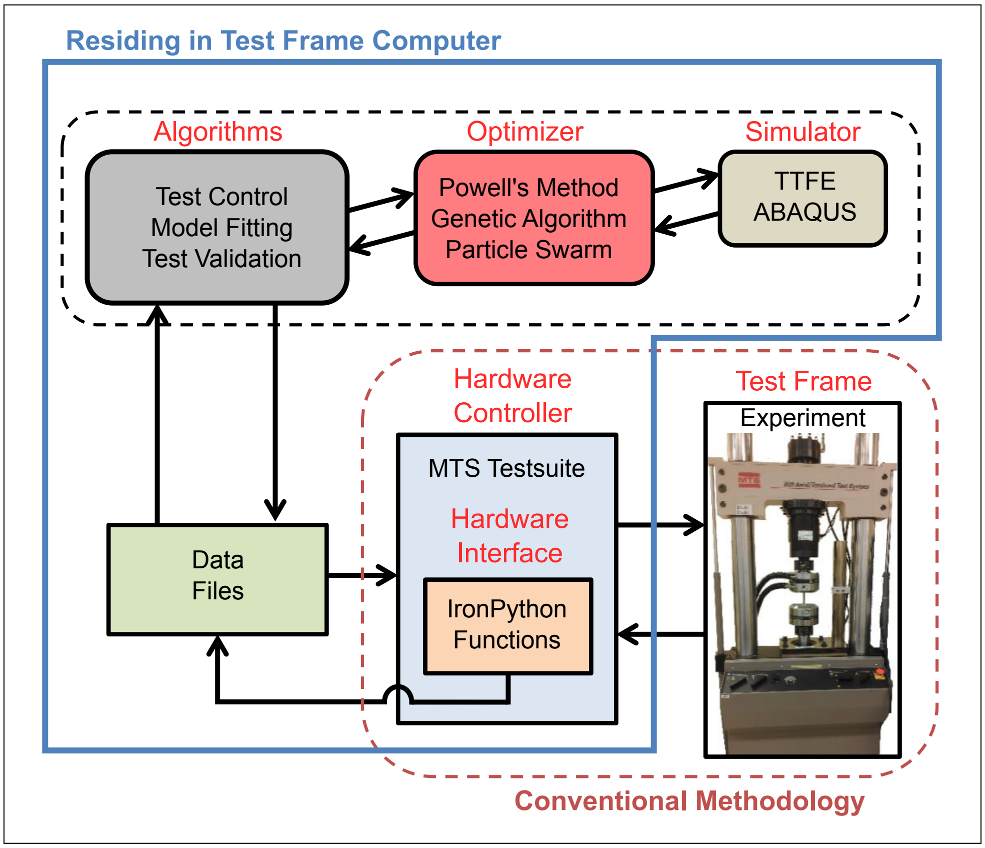

Figure 4.1: Overview of the test methodology and software required for integrating multiaxial experimentation and constitutive model fitting.

The methodology has been described as a flexible, adaptable process; however, the key components from Figure 4.1 need to be developed and demonstrated prior to expanding the functionality. These components form the basis of the methodology and serve as the platform upon which more complex algorithms and test methods can be added in the future. This chapter describes the critical software and discusses the current procedures employed to demonstrate the methodology through the autonomous calibration of a viscoplasticity model for Ti-6Al-4V.

4.2 Experimental Hardware Interface

The multiaxial experiments are conducted on a MTS 809 axial/torsional hydraulic test machine with force and torque capabilities of 100 kN and 1,100 N-m, respectively. The test machine is controlled by an MTS Flextest Controller which has the necessary hardware to drive the hydraulic actuators, communicate with the MTS test software running on the personal computer, and acquire analog or digital inputs from devices such as load cells, extensometers, and strain gages.

Currently, axial and shear strain measurements can be obtained using a MTS 632.68 High-Temperature Axial/Torsional Extensometer and/or strain gages. The extensometer has a gage length of 25.0 mm, an axial travel of $\pm$ 2.5 mm, a torsional rotation of $\pm$ 5 degrees, and a maximum usage temperature of 1200 degrees Celsius. If resistance strain gages are used, they are connected to Vishay 2310 Signal Conditioning Amplifiers which provide the Wheatstone bridge circuit (quarter, half, or full) and signal amplification. The amplified signals can then be fed to the analog-to-digital converters within the MTS Flextest Controller. Various other strain measurement techniques could be incorporated in the future, such as digital image correlation; however, only the extensometer and strain gages are used in this effort.

Generally, experiments are conducted by using either 1) a test procedure written in the test machine vendor's control software, or 2) through custom user software (and possibly custom hardware) that directly interfaces with the test hardware. Custom test software is potentially more versatile; however, it would require continual maintenance. Therefore, this work leverages the commercial MTS test software, Multipurpose Elite (MPE) Testsuite .

Traditionally, test procedures are completely defined and only require specification of load limits, number of cycles, or other pertinent information. A different approach has been implemented in this work which allows I^{2}MATE to define, or redefine the testing procedure in real time based

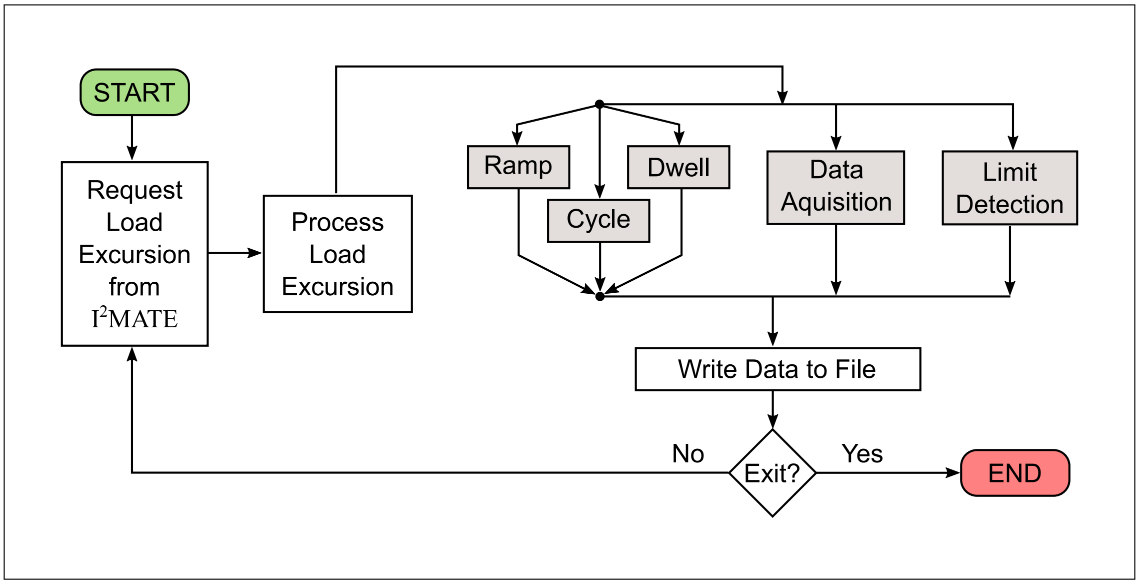

Figure 4.2: Outline of MPE test program that communicates with I^{2}MATE to allow real-time control of the experiment.

on knowledge acquired throughout the test. To allow for real-time test control, a communication interface has been created between I^{2}MATE and MPE which allows both pieces of software to pass information bidirectionally. Message exchange is accomplished through the IronPython programming language available inside MPE. Figure 4.2 shows the outline of the MPE test program that has been written to communicate with I^{2}MATE.

4.3 Basic Features of Autonomous Experimentation

With a protocol for hardware control in place, the basic functionality of the autonomous testing can be developed. The software follows the closed-loop approach outlined in the previous chapter in Fig. 3.1. Pretest procedures can be conducted. Then supplemental data can be utilized either for initial fitting or for extra validation of the constitutive parameters. Next, a closed-loop process is employed in which a set of calibration load excursions are conducted to gather experimental data. After that, the constitutive parameter calibration can be performed. This is followed by additional validation excursions on the specimen, then convergence checks are made. The process is repeated until all the convergence metrics have been satisfied.

The cyclic process is currently defined based on the concept of test blocks. A test block consists of a specified number of cycles in which calibration excursions are performed, calibration occurs, validation excursions are performed, and lastly convergence metrics are checked. An illustration of a test block is given in Fig. 4.3. The testing domain is defined for each test block. Currently the testing domain is given in the axial-shear strain space as a series of angular bins in which the load excursions will be conducted. Along with the testing domain, the maximum and minimum magnitude of multiaxial strain are provided. In addition, the strain rate is also chosen. A series of test rounds can then be defined that limit the load excursions to some fraction of the test block maximum and minimum strain values. Figure 4.4 provides an example of a test block with a test domain of $\pm$ 90 degrees in the axial-shear strain space, and four rounds of increasing strain amplitude. The minimum and maximum magnitudes of strain for the example test block are 0 and 0.015 m/m, respectively.

Details on some basic functionality of the I^{2}MATE software are provided in the next section. Then Section 4.3.2 describes the current load excursions available during both the calibration and validation excursions.

4.3.1 Basic Test Procedures

Three loading sequences are essential in any mechanical experiment and are therefore integral to I^{2}MATE. They are: 1) a ramp from the current load level to a new prescribed level; 2) a dwell which holds at the current load for a prescribed time; and 3) a series of cycles between prescribed load levels. While the term *load* is used, all these procedures can use either load, stress, pseudo-strain, or stroke control. Stress control is just load control with the convenience of specifying loads in terms of

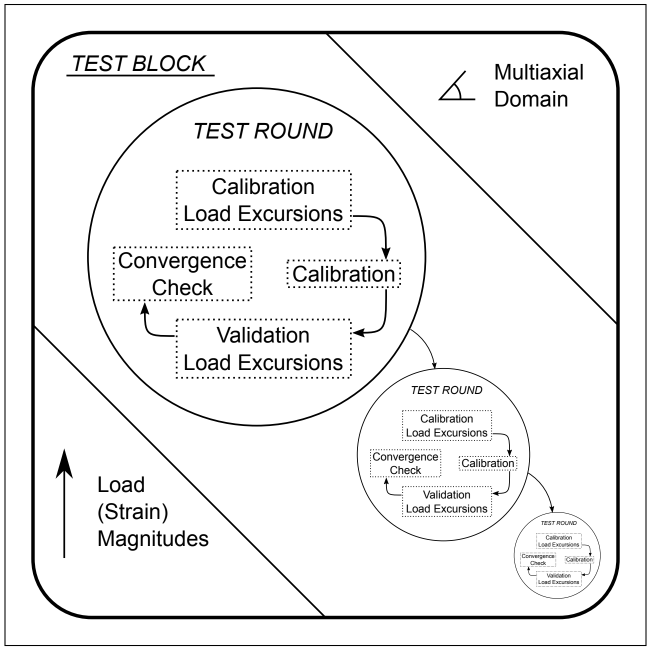

Figure 4.3: Illustration of test block defined by the test domain, load or strain magnitudes, and number of test rounds.

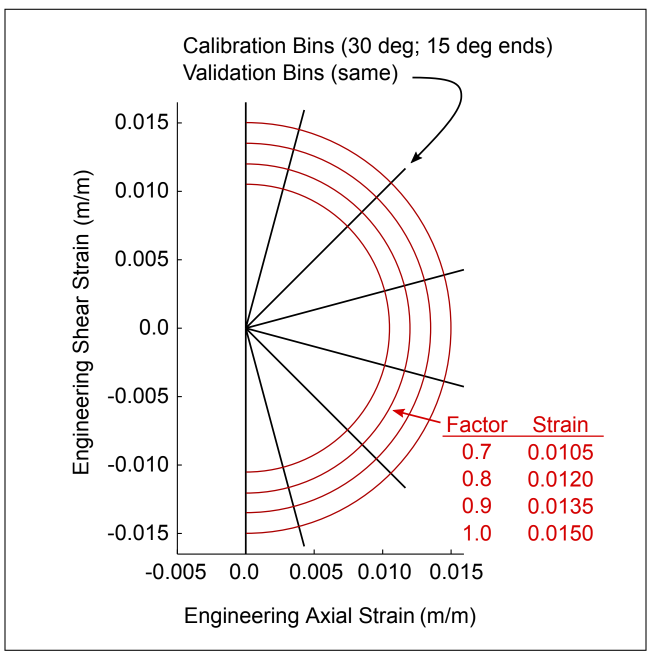

Figure 4.4: Example of test block with tension-torsion strains. Black lines indicate angular bins while the red lines show the increasing levels of strain for four rounds of testing.

desired stresses. Information from the specimen is used to convert the stresses to the required load levels. Pseudo-strain control is implemented indirectly through stroke control. Pseudo-strain control avoids the potential problems and instabilities of direct strain control methods. The correlation between stroke and strain can be computed during preliminary elastic load excursions. Pseudo-strain control is then utilized but with additional limits imposed using strain values from either an extensometer or strain gages. Stroke control is achievable through actuator displacement and rotation. These three procedures form the basis of any load excursion utilized within the autonomous testing process. They also allow for convenient control of any other non-autonomous axial-torsional test.

4.3.2 Load Excursions

Currently, a series of proportional multiaxial load excursion can be conducted for calibration and validation. Other types of loading events are potentially desirable, but proportional loading has been chosen as a starting point for the demonstration of the integrated methodology. A load excursion is subject to the current limits and boundaries for a round of a test block. The load refers to the magnitude of the axial and shear strain (or stress) while the trajectory is defined as the angle in the axial-shear space. Figure 4.5 a depicts the definition of these terms. For strain control, the trajectory is defined as $\theta = tan^{-1}(d\gamma/d\varepsilon)$ and the load magnitude is defined as $\delta = \sqrt{d\gamma^2 + d\varepsilon^2}$. For a given trajectory, the user has the option of randomly varying the load up to the current load limit or always reaching the current load limit. Similarly, the user can decide (through the settings) to randomly select the trajectory or use a predefined series of trajectories created for the imposed bounds.

Figure 4.5b shows an example of the load excursions for random load values at a series of trajectories. The trajectory is linear in all the load excursions 1-8, with the exception of excursion 6. The trajectory for excursion 6 is the same as excursion 5; however, the rate of shear strain is greater

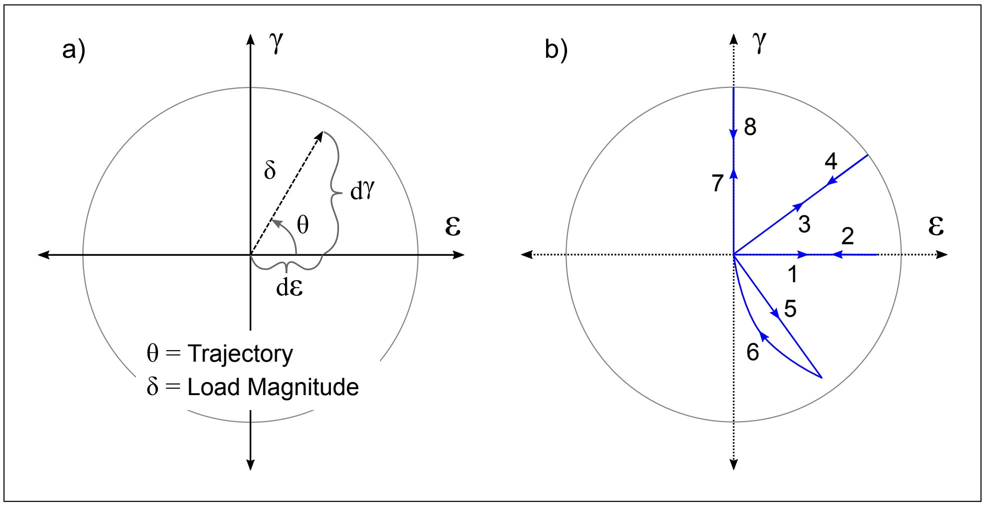

Figure 4.5: Illustration of the a) trajectory and the load magnitude definitions and b) an example of load excursions with random load magnitudes and random trajectories. Both are shown for strain, but concepts apply for stress control.

than the axial strain rate causing the curved path. The ratio of the rates can be varied randomly or the can be held linear depending on the user's preferences. Allowing for varied ratios introduces some nonproportional loading and may be desirable depending on the in-service loading for the more complex subcomponents that will ultimately be modeled using the fitted and validated constitutive model.

Extensions of this work could develop a series of different loading types to be implemented within a test block. These additional loading types could be nonproportional loading with various phase shifts, more drastic changes to the proportions as seen when traveling along a rectangle in axial-shear strain space, or even load events that are free to explore the test domain using a random walk. All of these may perform better than the proportional load excursions that are currently available; however, the identification of ideal loading events is beyond the scope of the current work.

4.4 Pretest Procedures and Verification

Prior to conducting the autonomous experimental test, certain pretest procedures may be required. For example, analog or digital data coming from the load cell, extensometer, and strain gages need to be verified. Certain measurement techniques like DIC require other pretest procedures like camera calibration. If testing is to occur at elevated temperatures, checks are needed for the temperature field on the specimen and the command and feedback signals. The software currently has pretest procedures available, and others can easily be added to accommodate varied experimental setups in the future.

4.4.1 Modulus, Pseudo-Strain, and Additional Calculations

A common method for verification of data channels for extensometers, strain gages, load cells, etc. is the computation of a modulus (axial and/or shear) from elastic load excursions. The resulting modulus can be compared to known reference standards to ensure all channels are properly gained and being acquired and combined correctly. The modulus check feature of I^{2}MATE can be used for the in-situ calculation of both the Young's modulus from axial cycling and the shear modulus from torsional cycling. During the calculation of the moduli, the zero-load offsets for each strain channel are computed. The offsets are used for subsequent strain calculations, ensuring that any initial strain imbalance under zero load is negated.

During multiaxial measurements, both extensometers and strain gages are known to exhibit cross-talk [6, 100]. Strain crosstalk occurs when an applied shear strain causes a change in measured axial strain or an applied axial strain causes a change in the shear strain reading. For an isotropic material in the elastic regime, a cylindrical specimen subjected to only a torque should have no axial strain; thus any axial reading is erroneous and wholly a function of the measuring device and not the material. This error can affect the accuracy of results when applying both forces and torques.

Crosstalk can optionally be identified during the modulus checks and removed for subsequent strain calculations. The correction factor, k_{11}, is the slope determined by linear, least-squares regression for ε_{11} versus γ_{12} during the torsional cycling and represents the torsion-into-axial crosstalk. The correction factor, k_{12}, is similarly found for γ_{12} versus ε_{11} during axial cycling and indicates the axial-into-torsional crosstalk. Finally, the adjusted strain, ${\varepsilon'}_{11}$ and ${\gamma'}_{12}$, can be computed from Eq. (4.1).

$$\begin{aligned} {\varepsilon'}_{11} &= \varepsilon_{11} - k_{11}{\gamma'}_{12} \\ {\gamma'}_{12} &= \gamma_{12} - k_{12}{\varepsilon'}_{11} \end{aligned} \tag{4.1}$$

Solving Eq. (4.1) in terms of the uncorrected strains yields the more useful form

$$\begin{aligned} {\varepsilon'}_{11} &= \frac{\varepsilon_{11} - k_{11}\gamma_{12}}{1 - k_{11}k_{12}} \\ {\gamma'}_{12} &= \frac{\gamma_{12} - k_{12}\varepsilon_{11}}{1 - k_{11}k_{12}} \end{aligned}. \tag{4.2}$$

Lastly, the modulus checks can be used to configure pseudo-strain control, where users provide desired strain values, but the test machine is controlled through stroke and rotation commands for the actuator rather than strain commands. This is accomplished through limit detection for the strain channels from which the user wishes to control. The strain limits prevent the stroke from exceeding the desired strain values. Cyclic data from the modulus checks are used to determine the linear relationship between stroke (rotation) and strain in the elastic regime. The slopes of stroke (rotation) versus strain can be computed for the extensometer or appropriate strain gage pairs. Pseudo-strain control also allows for future development of algorithms to continuously monitor strain signal integrity and switch strain control mechanisms mid-test if integrity diminishes (due to debonding of strain gages, or slipping of the extensometer rods).

4.4.2 Predefined Initial Loading and Yield Surface Probing

An experimentalist may wish to conduct a particular set of load conditions prior to initiating the autonomous process for calibration and validation of the constitutive parameters. Currently, user-defined load excursions and yield surfacing probing are available in the software.

The predefined load excursions (if desired) are given in terms of the basic testing procedures outlined in Section 4.3 which allow for ramping, cycling, and dwelling under a variety of test control modes. All of the data are condensed and used during any constitutive parameter calibration procedure. The user can therefore impose known history dependent loading on the specimen prior to turning control over to the autonomous algorithm.

A critical component of a continuum plasticity model is the yield surface which separates the elastic region (where the deformation is recoverable) and the plastic region (in which the material experiences non-recoverable permanent deformation). Previously determining a yield surface has required dozens of experiments [33, 35, 37], as indicated by each test point in Figure 4.6a, or time consuming manual intervention [36]. However, as mentioned in Section 2.1, many researchers [1, 2, 3, 4, 5, 6, 7, 8, 9] have developed custom preprogrammed software routines to assist in the determination of yield surfaces. Figure 4.6b illustrates the concept of using a single specimen to probe multiple points on the yield surface with one specimen, which is prevalent in the literature.

Options within I^{2}MATE provide a method to probe the yield surface in multiple places using one specimen. The loads are gradually increased until the in-situ data analysis indicates the onset of plasticity, which is based on the level of Mises equivalent plastic strain, $\bar{\varepsilon}^{pl}$, defined as

$$\bar{\varepsilon}^{pl} = \sqrt{\frac{2}{3}\varepsilon^p_{ij} : \varepsilon^p_{ij}}. \tag{4.3}$$

For the case of axial-torsional loading on a solid or tubular cylindrical specimen, $\bar{\varepsilon}^{pl}$ reduces to

$$\bar{\varepsilon}^{pl} = \sqrt{(\varepsilon^p)^2 + \frac{1}{3}(\gamma^p)^2}. \tag{4.4}$$

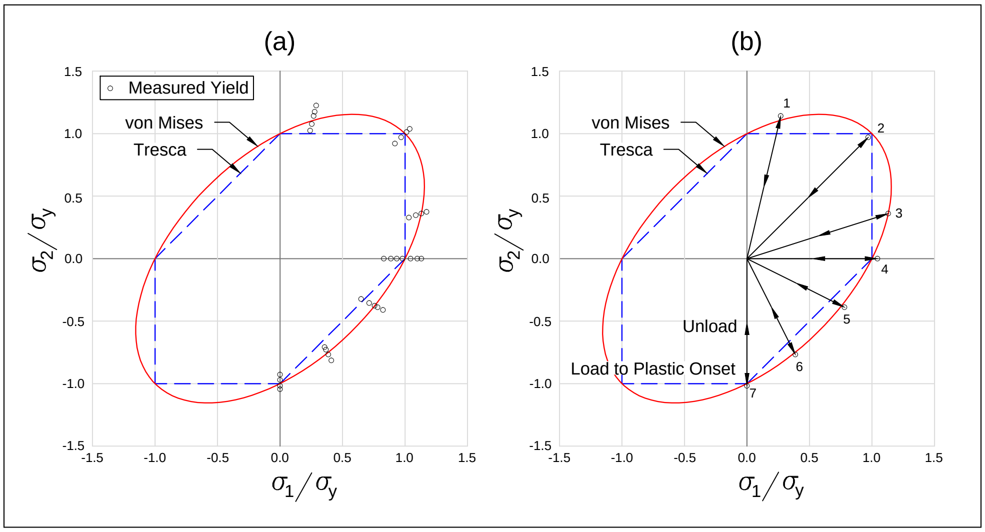

Figure 4.6: Identification of the yield surface using a) traditional methods and b) modern methods. In a) each data point on the yield surface is generated using a new specimen or manual intervention. In b) multiple data points can be acquired with a single specimen.

Once the increment in $\bar{\varepsilon}^{pl}$ for an excursions exceeds the user specified tolerance, the specimen is unloaded back to the preload position and another portion of the yield surface is probed. A common tolerance used in the literature is $10\mu\varepsilon$.

The yield surface probing procedure can be called at the start of an experiment to map the virgin yield surface. It can also be used to map subsequent yield surfaces after the specimen undergoes history dependent, irreversible loading. While the approach used is similar to that used by previous researchers, the present algorithm can correct for cross-talk, so the axial and shear moduli are used rather than a new modulus for each probe angle as is common in the literature [1, 2, 3, 4, 5, 6, 7, 8, 9].

4.5 Utilizing Supplemental Material Data

Data from experiments conducted on the same material can be used as supplemental data during both the calibration and validation procedures. Initial estimates of the constitutive parameters can be defined based on the supplemental data. Certain experiments, such as the tension test, may have closed form solutions for the stress-strain relationship and may led to more computationally efficient approaches for parameter identification. Other experiments like combined axial-torsional loading will have to rely on methods like FEMU. Regardless of the experiment or identification method used, the supplemental data can provide initial solutions for the constitutive parameters being identified, which can be used through the calibration procedure. The supplemental data also can be used during the validation procedure to assess the accuracy of the current best parameter estimates. The remainder of this section provides details for algorithms currently available that make use of supplemental data. Some methods are specific to the chosen viscoplasticity model; however, others are general and can work for any desired constitutive model.

4.5.1 Supplemental Tension Test Data

Tension test data can be used to develop initial estimates of the constitutive parameters for the desired material model prior to the autonomous calibration and validation procedures. Parameter identification using only tension test data may be unable to uniquely identify constitutive parameters for certain models, e.g. plasticity models with combined isotropic and nonlinear kinematic hardening. However, the tension data still may be useful to the overall autonomous process by providing initial parameter estimates for the identification procedures. Additionally, the tension data can be used during each calibration procedure such that parameters are calibrated using both the tension test and the autonomous experiment.

For a generic material model, the tension test data can be used with the FEMU software outlined in Appendix D. If the material model of interest has a closed form solution for the tension test, additional steps can be leveraged to lessen the computation cost of the initial fitting. The viscoplasticity model presented in Section 5.1 and Appendix C has a closed form solution for the monotonic tension test. Therefore, nonlinear least square regression can be used for initial parameter identification, since it is more computationally efficient than the FEMU.

Regression requires the experimental tension data (both stress and strain), the closed form solution for the tension tests, an initial parameter set, and lower and upper bounds for the parameters to be identified. The Intel$^{(R)}$ Math Kernel Library 11.1 Update 2 for Windows* (MKL) procedure *dtrnlspbc* is used to perform nonlinear least square regression. The *dtrnlspbc* procedure minimizes the error measure

$$\min_{x \in R^n} \|F(v)\|_2^2 = \min_{x \in R^n} \|y - f(v)\|_2^2, y \in R^m, v \in R^n, f : R^n \rightarrow R^m, m \geq n \tag{4.5}$$

within the design space

$$l_i \leq v_i \leq u_i, i = \{1, ..., n\}, l \in R^n, u \in R^n. \tag{4.6}$$

Regression is performed for a series of initial parameter sets. The series is generated using a Latin hypercube sampling procedure to ensure the feasible design space given by Eq. (4.6) is adequately sampled. A series of parameter sets is preferred over a single set because there are likely multiple local minima. The unique converged solutions can be used to generate an initial population for evolutionary algorithms, or the converged solution with the lowest error can be used as a single starting point.

Equation (4.5) is specialized for the closed form solution of the monotonic tension test for the viscoplasticity model. The vector y represents stress, while x represents the equivalent plastic strain. The vector f is defined as

$$f(v, x) = \alpha\left(\sigma_y + D\dot{\varepsilon}^{1/n}\right) + \sum_{i=1}^{P} Q_i\left(1 - \exp\left(-b_i x\right)\right) + \sum_{i=1}^{W} \frac{A_i}{B_i}\left(1 - \exp\left(-B_i x\right)\right) + A_L x \tag{4.7}$$

$$v = \{Q_1, b_1, \ldots, Q_P, b_P, A_1/B_1, B_1, ..., A_W/B_W, B_W, A_L\}, x \in R^m. \tag{4.8}$$

The viscoplasticity parameters, σ_y, D, and n, are assumed constant and defined prior to the regression procedure. The term $\alpha = 0$ for $x_j = 0$ and $\alpha = 1$ for $x_j > 0$ for $j = \{1, 2, ..., m\}$. The notation $\|a\|_2^2$ represents the square of the Euclidean norm of vector a, such that $\|a\|_2^2 = a_1^2 + ... + a_m^2$

where m is the length of the vector. In Eq. (4.5), $\|y - f(x)\|_2^2$ represents the sum of the squares of the residual error for all pairs of measured stress and equivalent plastic strain $\left(\sigma_j, \bar{\varepsilon}_j^{pl}\right) = (y_j, x_j)$ for $j = \{1, 2, ..., m\}$.

4.5.2 Supplemental Uniaxial Cyclic Data

For plasticity models with both isotropic and kinematic hardening, contributions from the different hardening mechanism are indistinguishable from monotonic tension tests. In the closed form solution, both hardening terms take an identical form; therefore, additional tests are necessary to isolate their effects. The different contributions are visible in the Bauschinger effect where a specimen re-yields at a lower yield stress than predicted from isotropic hardening alone when loading is reversed. Usually fully reversed, strain-controlled tests are conducted for a range of strain levels to determine the evolution of the hardening parameters.

Strain-controlled experiments with negative strain ratios, R, (minimum over maximum strain) are ideal for isolating the influence of different hardening mechanisms. Certain constitutive models have a closed form solution for the uniaxial cyclic experiment. However, the FEMU procedure can be used with any model and with data that may have slight deviations from a standard cyclic test. As with the tension test, the parameters identified from the strain-controlled, fully-reversed, axial only test can be used as initial estimates during the calibration procedures or as additional validation experiments. However, unlike the tension test, the isotropic and kinematic hardening parameters are easier to decipher from the fully-reversed test as the effects of both hardening mechanisms can be isolated.

4.5.3 General Supplemental Experiments

The tension test and the axial cyclic test are only two types of experiments that one may want to use as supplemental data. Any other type of experiment, both axial or multiaxial in nature, can be used to perform initial parameter fitting or as supplemental validation experiments during the validation process. To avoid having to develop and implement closed-form solutions (which may not exist), the FEMU procedure can be used for general experiments.

4.6 Calibration Load Excursions

As described in Section 4.3.2, the current software is capable of performing a series of proportional load excursions at various trajectories in strain space. For a given round of a test block, a set of calibration load excursions are performed to gather additional experimental data for the constitutive parameter calibration. First, a single excursion into each of the angular bins is performed. Figure 4.4 provides an example of angular bounds and testing rounds. Then, the coverage criterion, which is discussed in Section 4.9.1, is checked to see if a significant event has occurred within each angular bin. Currently, significance is dictated by the amount of plastic work occurring inside each angular bin, for the current test round. Future efforts can focus on improving the determination of significance. Regardless of the metric, the point is to ensure that each portion of the test domain has useful information to contribute to the constitutive parameter calibration. The maximum number of excursions within a given angular region is defined for a test block to prevent unnecessary testing for conditions that may be primarily elastic, and which might not meet the convergence criterion. Once all the excursions are completed, the constitutive parameter calibration can occur. Details of this process are given in the next section.

4.7 Constitutive Parameter Calibration

Once the specified series of load excursions is performed and the test data is obtained, the constitutive parameter calibration can occur. The literature review discussed two predominant methods for performing the parameter fittings: the virtual fields method (VFM), and finite element method updating (FEMU). The FEMU is implemented within the I^{2}MATE software.

The constitutive models are implemented within a finite element framework similar to the commercial finite element code, Abaqus. Both existing and new constitutive models, written in the user material routine format of Abaqus, can be used during the calibration process. The current work utilizes a viscoplasticity model with rate-dependence and nonlinear isotropic and kinematic hardening. Details of the formulation of this viscoplasticity model can be found in Section 5.1 and Appendix C.

The user is responsible for defining a preferred constitutive model for the calibration and validation process. They also prescribe the parameters to be identified, and the minimum and maximum bounds in which the FEMU will search. Currently, only a single constitutive model can be used for each experiment; however, the organization of the software and the testing procedure allow for the use and calibration of multiple constitutive models in future applications. Regardless of the chosen constitutive model, the experimental data must first be analyzed and reduced prior to performing the parameter calibration through FEMU. The next section discusses the data analysis and reduction methods. Then the FEMU is discussed in the following section.

4.7.1 Experimental Data Analysis and Reduction

The experimental data must be reduced prior to use in the FEMU procedure. I^{2}MATE imports the data from either a binary or ASCII file and computes stress and strain from the raw load cell and extensometer signals, strain voltages, specimen information, and extensometer and strain gage calibration information. The stress and strain data is filtered using a low-pass digital filter that can be either an Infinite Impulse Response (IIR) filter like the Butterworth filter, or a Finite Impulse Response filter. Once the data is filtered, it is condensed to decrease the total number of load increments to be utilized in the finite element method. For a complete description of the filtering and data condensing capabilities within I^{2}MATE, see Appendix A. The output from the data analysis process is the condensed experimental strain and corresponding stress (both axial and shear) that will drive the finite element analysis that utilizes the chosen constitutive relationship. The following section details the FEMU process that is used to calibrate the parameters of the chosen constitutive model.

4.7.2 Finite Element Method Updating (FEMU)

The FEMU process seeks to minimize the residual error between experimental stress and a corresponding finite element analysis by updating the parameters used with a constitutive model. The minimization process can be handled by a number of different optimization procedures. Regardless of the method, an objective function is computed for each set of parameters requested by the optimization procedure. For each objective function, a finite element analysis must be completed using the given constitutive parameters.

The expense of the FEMU process has been greatly reduced through the development of a compact axial-torsional finite element code. This code and the required optimization methods are integrated directly into I^2MATE to eliminate any overhead associated with file input and output. The developed finite element code also prevents having to use commercial general purpose finite element software that is expensive and carries a significant amount of computation overhead. The software for FEMU has also been developed to use parallel processing and has been shown to have an almost linear speedup when additional cores are utilized. A complete description of the finite element software and the optimization methods that can be used for FEMU is provided in Appendix D.

The outcome of the FEMU process is a set of constitutive parameters that lead to minimum error for the current set of experimental data. With the best estimate of the parameters identified, the next phase of the autonomous testing is to perform additional load excursions to evaluate the accuracy of the current best parameter set.

4.8 Validation Load Excursions

The result of the FEMU procedure is a set of constitutive parameters, v_{best}, that best correlate with all of the available experimental results. However, the best parameters should be validated using additional loading conditions not used for the parameter fitting. Validation is crucial to verifying that the parameters are well suited over the entire test domain being considered. I^{2}MATE therefore has a validation procedure that occurs after each FEMU to examine the behavior of v_{best}.

To begin, a set of validation load excursions are identified that sufficiently cover the test domain. Next, the best parameters, v_{best}, are used with the finite element model and the preliminary validation excursions to generate numerical results of stress and strain. These predicted results are checked to determine if any significant loading is likely to occur. The current criterion for significant loading is dependent on plastic strain and defined in Section 4.9.1. Additional validation excursions are analyzed numerically until the criteria for significance is met based on the FE analysis using v_{best}.

Once the criterion for significant loading is met, the validation excursions are physically carried out on the specimen. The experimental data for the validation excursions is collected, analyzed, and reduced. A finite element analysis is then conducted using the current best estimate of parameters and all the experimental data for the specimen, including the recently completed validation data. The objective function (which compares experimental and analytical stress) is computed for the validation data and errors are compared to the convergence criteria. Further descriptions of the convergence criteria are discussed in the following section.

4.9 Convergence Criteria

Convergence criteria are checked after the validation load excursions are performed. Criteria focus on exploration of the testing domain, error between experimental and analytical results, and convergence of the constitutive parameters. Details of the current implementation of convergence criteria are given in the following sections.

4.9.1 Test Domain Coverage

Coverage of the multiaxial test domain is checked to ensure thorough sampling before moving to the next test block or finalizing the entire procedure. The criterion is a based on the increment in equivalent plastic strain, $\Delta\bar{\varepsilon}^{p(k)}$, measured at each reduced data point, k, given as

$$\Delta\bar{\varepsilon}^{p(k)} = \sqrt{\frac{2}{3}\Delta\varepsilon_{ij}^{p\ (k)}\Delta\varepsilon_{ij}^{p\ (k)}}. \tag{4.9}$$

Plastic strain is computed based on engineering stress for the cylindrical specimens. While neither the stress nor $\Delta\bar{\varepsilon}^{p(k)}$ will agree with those computed using the constitutive model, the accuracy should be sufficient to determine if the test domain is adequately sampled. Trajectories for each point, $\theta^{(k)}$, are measured from the origin; thus each point, k, has a data pair $\left(\Delta\bar{\varepsilon}^{p(k)}, \theta^{(k)}\right)$.

The trajectory angles are used to sort each point into one of the angular bins defined for the current test block. The total increment in equivalent plastic strain for all points in a single bin is computed, in addition to the overall total. Each bin sum can be normalized by the total sum so criteria can be defined using the total increment and the normalized values or alternately the unnormalized bin sums. Figure 4.7 shows an example of a) the individual bins and the reduced experimental points mapped on the axial-shear strain space and b) the normalized bin values and the total sum for each bin.

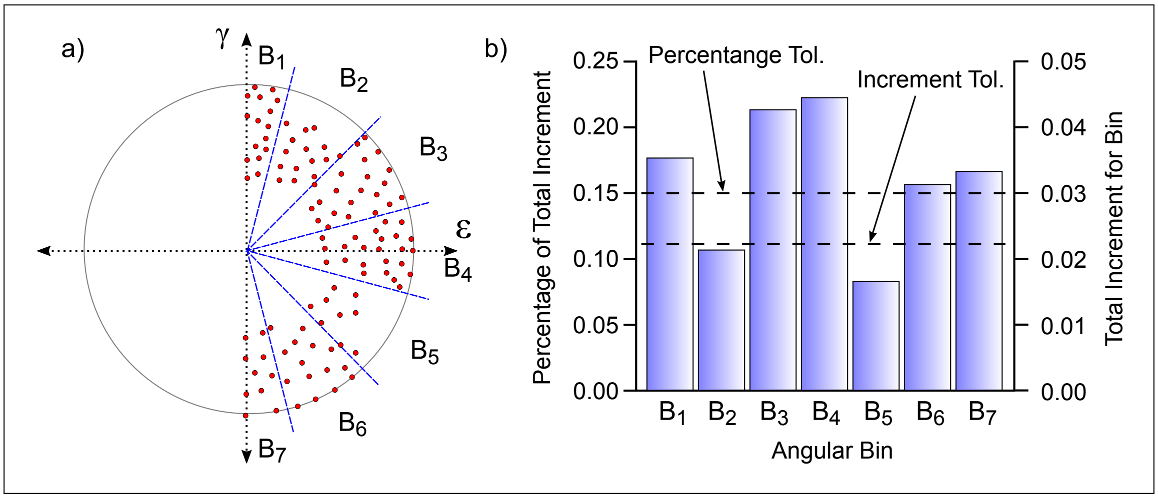

Figure 4.7: Example of a) the individual bins and the reduced experimental points mapped on the axial/shear strain space and b) the percentages of the total increment in equivalent plastic strain and the increment for each bin.

4.9.2 Analysis Error

During the calibration of the constitutive parameters, the errors between the experiment and the analyses are computed. The errors obtained with the best estimate of the constitutive parameters are compared to both a maximum and a mean criterion. The error function, given as

$$err = \sum_{k=1}^{N} R_k = \sum_{k=1}^{N} \sqrt{w_F \left(F_{\text{exp}}^{(k)} - F_{FE}^{(k)}\right)^2 + w_T \left(T_{\text{exp}}^{(k)} - T_{FE}^{(k)}\right)^2} \tag{4.10}$$

is the summation of the weighted residual error of force, F, and torque, T. The error function is similar to the objective function used during FEMU, where N is the number of condensed data points used in the FE solution, and k denotes an individual data point. The weight factors are $w_F = A^{-2}$ where A is the initial cross-section area and $w_T = r^2 J^{-2}$ where r is the outer radius of the specimen and J is the polar moment of inertia. The weights are chosen such that the error function has units of engineering stress. Both the maximum and the mean error function value for all data points are computed and compared to the criteria.

4.9.3 Constitutive Parameter Convergence

Prior to finalizing the entire test methodology, the constitutive parameters need to be checked to ensure they have stabilized. For this check, the approximate relative error, ε_a, given as

$$\varepsilon_a^{(j)} = \left| \frac{x_v^{(j)} - x_{v-1}^{(j)}}{x_v^{(j)}} \right| \tag{4.11}$$

is computed, where the subscript v is the current set of parameters and $v-1$ is the previous set. The error is computed for each parameter, j, used in the calibration procedure. The maximum error must be less than the criterion prior to finalizing the test.

4.10 Summary

The integration of multiaxial experimental testing and material model calibration can provide a research platform potentially capable of providing higher fidelity material models in less time and using fewer specimens than conventional test procedures. The required test methodology, and associated software called Intelligent Integrated Material Analysis and Testing Environment (I^2MATE), have been created to achieve this new, novel integration. Rather than producing sets of raw data, experiments conducted using I^2MATE produce calibrated constitutive models that can be directly used in tools like the finite element method. An additional benefit is that the constitutive model parameters are not only fit over a multiaxial test domain, but are also validated over additional conditions not used in the fitting. The test iterates autonomously until the residual error between the experiment and the analysis (using the best constitutive parameters) is below a user-defined tolerance. All the necessary software and interfaces with the experimental hardware have been developed and allow a user to effortlessly compute coefficients validated over complex multiaxial loading.

The simulated behavior of the integrated methodology is discussed in Chapter V, where the physical experiments are replaced with FE analyses using a set of ”exact” constitutive parameters. After verification of the methods through the simulation results, Chapter VI discusses the results of an autonomous, integrated experiment performed on Ti-6Al-4V to identify viscoplasticity parameters.

CHAPTER V

EVALUATION OF METHODOLOGY USING SIMULATED EXPERIMENTS ON Ti-6Al-4V

The methodology discussed in Chapters III and IV has been evaluated using simulated experimental data to assess the capabilities of the method and the accompanying software prior to running physical experiments. The material of interest is Ti-6Al-4V [103]. Details on the material processing can be found in Appendix B.3. During the evaluation, the physical experiments are replaced with finite element simulations using a set of ”exact” constitutive parameters. If the methodology is successful, the parameters identified with the integrated approach should be very close to the ”exact” set of parameters. Using simulated experimental results eliminates any errors due to constitutive model deficiencies (model not able to capture physical phenomena); therefore, all errors in the evaluations are solely attributed to the methodology. The simulated behavior also provides a useful platform for incorporating additional features and fine-tuning the behavior of the current methodology. Three different evaluations of the methodology and software have been performed to target three different axial-torsional test procedures. The three evaluations are:

1. An experiment with tension-torsion strains (R = 0);
2. A fully reversed experiment (R = -1); and
3. A combination of test blocks with tension-torsion strains (R = 0) and fully reversed strains (R = -1).

The exact constitutive parameters have been chosen to closely resemble the behavior of Ti-6Al-4V. Section 5.1 defines the exact parameters and compares simulated tensions test using the parameters to experimental strain-controlled tension tests for Ti-6Al-4V at various rates. Section 5.2 describes the supplemental material data that is used throughout the methodology. Section 5.3 identifies the remaining setup and required settings for the methodology. Section 5.4 steps through results for the three different evaluations of the integrated methodology. The success of the developed methodology when applied to the simulated experiments is discussed in Section 5.5.

5.1 Exact Constitutive Parameters

The physical experiments have been replaced with numerical simulations that require a choice of both the type of constitutive model and the material parameters for the chosen model. A rate-dependent viscoplasticity model with combined isotropic and kinematic hardening has been selected throughout this work to represent the behavior of Ti-6Al-4V and has been used to generate the simulated results. A rigorous explanation of the constitutive model and the influence of each of the constitutive parameters can be found in Appendix C. A brief description of the governing equations is presented below for context.

The yield function, f, is $f = q - \sigma_y$ where σ_y is the current radius of the yield surface, $\sigma_y = \rho_0 + \sum\limits_w \rho^{(w)}$, and q is the von Mises stress.

$$q = \sqrt{{}^3\!/_2 \left(S_{ij} - X_{ij}\right)\left(S_{ij} - X_{ij}\right)} \tag{5.1}$$

$$S_{ij} = \sigma_{ij} - {}^1\!/_3 \sigma_{uu}\delta_{ij} \tag{5.2}$$

$$X_{ij} = \sum_w \left(\chi_{ij}^{(w)} - {}^1\!/_3 \chi_{uu}^{(w)}\delta_{ij}\right). \tag{5.3}$$

The initial yield surface size is ρ_0 and the terms S_{ij} and X_{ij} are the deviatoric stresses and backstresses, respectively. The relevant rate equations for plastic strain, stress, and hardening are given in Eq. (5.4) through (5.8).

$$\dot{\varepsilon}_{kl}^{p} = \dot{\gamma}\frac{\partial f}{\partial \sigma_{kl}} = \Omega_{\gamma}\frac{\partial f}{\partial \sigma_{kl}} \tag{5.4}$$

$$\dot{\gamma} \;=\; \Omega_{\gamma}(\sigma, \rho, \chi) \;=\; \left\langle \frac{f}{D} \right\rangle^{n} \tag{5.5}$$

$$\dot{\sigma}_{ij} = \Omega_{\sigma ij}\left(\sigma, \rho, \chi\right) = D_{ijkl}\left(\dot{\varepsilon}_{kl} - \dot{\varepsilon}_{kl}^{p}\right) \tag{5.6}$$

$$\dot{\rho}^{(w)} = \Omega_{\rho}^{(w)}\left(\sigma, \rho, \chi\right) = b^{(w)}\left(Q^{(w)} - \rho^{(w)}\right)\Omega_{\gamma} \tag{5.7}$$

$$\dot{\chi}_{ij}^{(w)} = \Omega_{\chi ij}^{(w)} = \Omega_{\gamma}\left(\frac{2}{3}A^{(w)}\frac{\partial f}{\partial \sigma_{ij}} - B^{(w)}\chi_{ij}{}^{(w)}\right). \tag{5.8}$$

The term $\rho^{(w)}$ is the w^{th} isotropic hardening parameter, and $\chi_{ij}^{(w)}$ is the w^{th} set of kinematic hardening parameters (or backstresses).

The elastic parameters for this model (Young's modulus, E, and Poisson's ratio, ν) are present in the elastic stiffness matrix, D_{ijkl}. The remainder of the constitutive parameters for this model are: D, n, ρ_0, $Q^{(y)}$, $b^{(y)}$, $A^{(w)}$, and $B^{(w)}$. Each hardening model term introduces two parameters, ($Q^{(y)}$, $b^{(y)}$) for isotropic hardening and ($A^{(w)}$, $B^{(w)}$) for kinematic hardening. Table 5.1 provides a summary of the coefficients and the corresponding role in defining the behavior of the material. Table 5.2 defines alternate parameters for some hardening variables that are actually used throughout the parameter identification process. The alternate parameters provide more intuitive relationships for the parameters and address the interdependences of the two parameters for each hardening term. A more thorough discussion of the constitutive model and the derivation of the alternate hardening parameters can be found in Appendix C.

The exact constitutive parameters have been fit to experimental results from strain-controlled tension tests on Ti-6Al-4V conducted at various strain rates. Figure 5.1 compares the stress-strain curves for the exact constitutive model and the Ti-6Al-4V tension tests. The exact constitutive parameters have been selected to smooth out the initial yield region rather than trying to reproduce the upper and lower yield points as seen in the experimental data. Capturing the upper and lower

Table 5.1: Constitutive parameters for viscoplasticity model.

Parameter	**Units**	**Type**
E	MPa	Elastic
ν	-	
D	MPa	Rate-Dependent
n	-	
ρ_0	MPa	Yield
$Q^{(y)}$	MPa	Isotropic Hardening
$b^{(y)}$	-	
$A^{(w)}$	MPa	Kinematic Hardening
$B^{(w)}$	-	

Table 5.2: Alternate hardening parameters used in parameter identification.

Original	**Alternate**	**Hardening**	**Type**
$b^{(y)}$	$5/b^{(y)}$	isotropic	rapidity
$A^{(w)}$	$A^{(w)}/B^{(w)}$	kinematic	saturation
$B^{(w)}$	$5/B^{(w)}$		rapidity

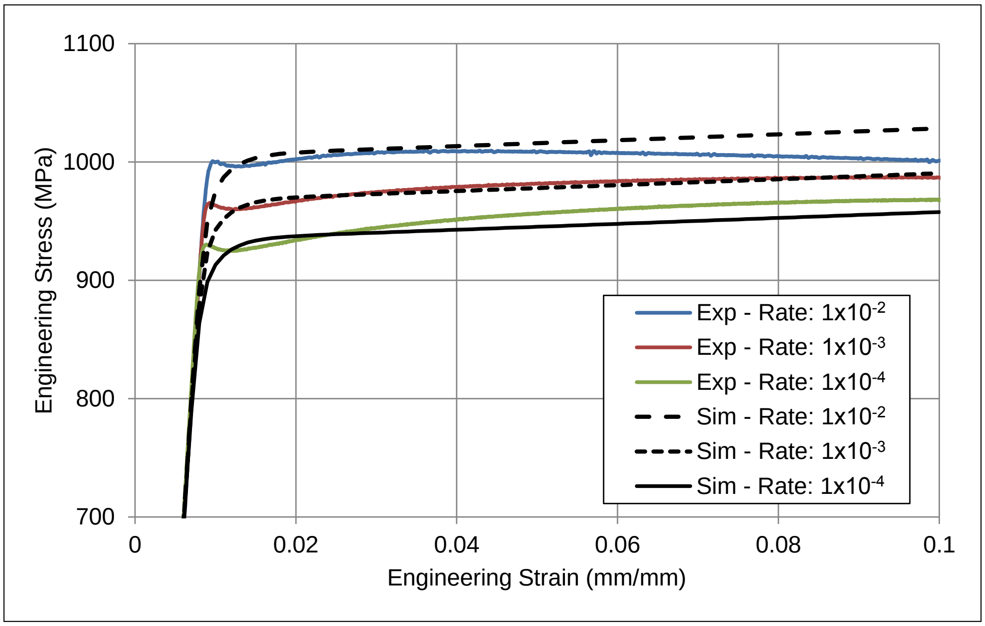

Figure 5.1: Experimental results for tension tests conducted at various strain rates for Ti-6Al-4V and corresponding finite element results using the developed ”exact” set of constitutive parameters.

yield would require many additional constitutive parameters that only affect the initial yielding of virgin material; therefore, the behavior has been ignored to reduce model complexity at the expense of small errors during initial yielding. Table 5.3 provides a complete list of the exact parameters used in this study along with the bounds for the hardening parameters involved in the optimization. One isotropic and three kinematic hardening terms (one linear, two nonlinear) are used in the exact parameter set.

5.2 Supplemental Material Test Data

Section 4.5.1 discussed the significant advantages of using tension experiments as supplemental material data for the intelligent integrated autonomous test methodology. Therefore, a simulated set of tension test data has been generated for a strain rate of 1×10^{-4} m/m/s using the finite element code within I^{2}MATE and the exact constitutive parameters as defined in Table 5.3. The data from

Table 5.3: Complete list of exact parameters used to generated the simulated experimental results. The optimization bounds are also given for the hardening parameters. All other parameters are predefined to the exact values.

		Parameter Bounds		
Parameter	Exact Value	Min	Max	Units
Elastic				
E	116,000	-	-	MPa
G	44,275	-	-	MPa
ν	0.31	-	-	-
Rate Dependent				
D	371	-	-	MPa
n	15.5	-	-	-
Yield				
ρ_0	430	-	-	MPa
Isotropic Hardening				
Q_1	50	5	750	MPa
$5/b_1$	1.00E-02	1.00E-04	1.00E-01	-
Kinematic Hardening				
A_1/B_1	200	5	750	MPa
$5/B_1$	5.00E-04	1.00E-04	1.00E-01	-
A_2/B_2	50	5	750	MPa
$5/B_2$	1.00E-03	1.00E-04	1.00E-01	-
A_3	250	0	2000	MPa

the finite element analysis corresponds to the solid black line in Figure 5.1. The tension test data has been used to generate initial parameter seeds for FEMU procedure. It is also used during the FEMU as a second load case for which the objective function is computed (the first being the autonomous test). Additional supplemental material data can be fed into I^2MATE; however, a limited set of data was chosen intentionally to assess the capability of the methodology with only prior knowledge of a single tension test.

5.3 Evaluation Configuration

The methodology has been evaluated using three different types of strain-controlled tests. The testing bounds are defined in Section 5.3.1. Convergence criteria for the methodology is discussed in Section 5.3.2. Details on the specimen used for each test are presented in Section 5.3.3. Lastly, Section 5.3.4 presents the details of the finite element method updating (FEMU) used for parameter calibration.

5.3.1 Test Bounds

The three evaluations represent a wide variety of test conditions. The first evaluation has tension-torsion strains (R = 0, where R is the ratio of minimum to maximum strain), while the second evaluation is fully reversed (R = -1). The third evaluation utilizes a combination of R = 0 and R = -1 test blocks to assess the evolution of the constitutive parameters as reversed loading data are introduced.

As shown in Figure 5.2, the first evaluation (Eval. 1) has angular bounds of $\pm$ 90 degrees with no compressive strain allowed. A single test block is used with a maximum strain magnitude of 0.015 m/m. Four rounds of increasing strain at factors of 0.7, 0.8, 0.9, and 1.0 times the maximum strain magnitude are used. Figure 5.2 shows the bounds of Eval. 1 with the black lines representing

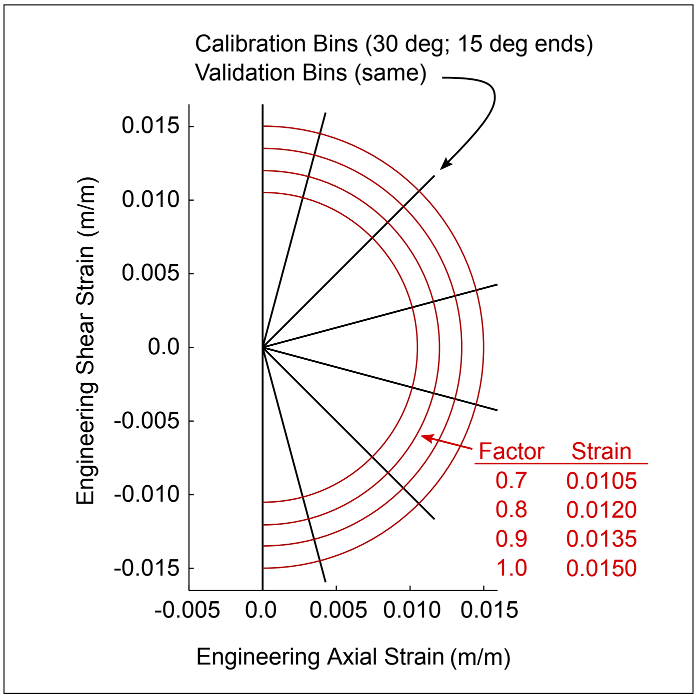

Figure 5.2: Test bounds used for Eval. 1 in which compressive strain is not allowed. Black lines indicate angular bins while the red lines show the increasing levels of strain.

the angular bins for calibration and validation and the red arcs designating the increasing levels of strain. Bins for calibration span 30 degrees with 15-degree bins at the ends.

The second evaluation (Eval. 2) again uses only a single test block, but covers the full circle in axial-shear strain space. The maximum strain magnitude is 0.015 m/m, and the same four rounds are used with increasing strain factors of 0.7, 0.8, 0.9, and 1.0. Figure 5.3 shows the bounds of Eval. 2 with black lines representing the angular bins of 30 degrees used for both calibration and validation. The red arcs designate the four increasing strain levels.

The third evaluation (Eval. 3) uses four different test blocks as defined in Table 5.4. The test blocks alternate between R = 0 and R = -1 conditions, starting with R = 0. Figure 5.2 and Fig. 5.3 encompass the angular definitions and the increasing rounds used within Eval. 3.

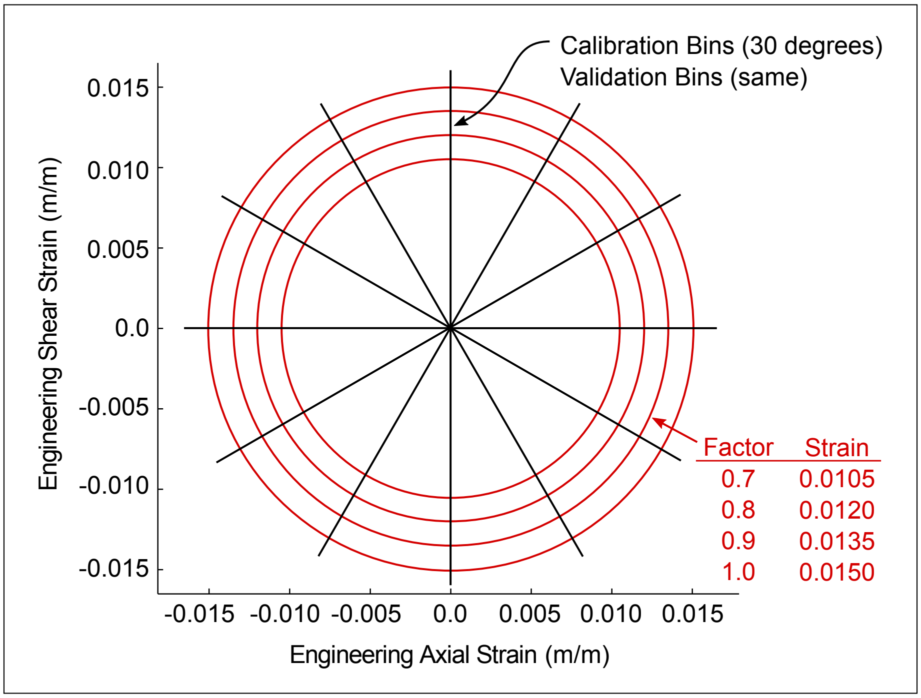

Figure 5.3: Test bounds for Eval. 2 which is fully reversed. Black lines indicate angular bins while the red lines show the increasing levels of strain.

Table 5.4: Test blocks used for Eval. 3

Block	Angular Bounds	Strain Min. (m/m)	Strain Max. (m/m)	Rounds	Fact 1	Fact 2
1	Fig. 5.2	0	0.015	2	0.7	0.8
2	Fig. 5.3	-0.015	0.015	1	0.8	
3	Fig. 5.2	0	0.015	2	0.9	1.0
4	Fig. 5.3	-0.015	0.015	1	1.0	

5.3.2 Convergence Criteria

Convergence criteria are needed for the both the objective function and the approximate relative error for successive best estimates of the constitutive parameters from FEMU. All the evaluations use the same set of convergence criteria. The objective function used during FEMU is again used to compute the maximum and the mean error at each condensed simulated experimental data point. All evaluations are limited to a maximum error of 50 MPa and a mean error less than 25 MPa. The approximate relative error for the constitutive parameters must converge to below 10 percent.

Load trajectories are randomly determined within each angular bin. Each angular bin must obtain a minimum total increment of equivalent plastic strain of 0.0005 m/m during the calibration process. The requirement for validation has also been set to 0.0005 m/m. Exceptions to the angular coverage can be made. If the maximum sum of any angular bin is below some fraction of the tolerance (these evaluations use 30 percent), then the excursions for the given calibration or validation process are stopped. Continuing with excursions will likely not produce the desired increment of equivalent plastic strain. This stoppage is not equivalent to meeting the original criteria, but it does prevent unnecessary excursions that are primarily elastic. Another exception compares the total increment in equivalent plastic strain for current excursions to the first load excursion into each angular bin. If the sum for the current iteration is less than a portion of the very first iteration, (these evaluations use 15 percent) then the coverage for both the calibration and validation are assumed to have converged. The motivation is that if the total for all the bins is significantly decreased, it is likely that no additional significant amount of equivalent plastic strain will be developed. Lastly, a maximum number of load excursions per angular bin is set for each round to ensure the process does not continue indefinitely if the current limits restrict the creation of plastic strain.

5.3.3 Specimen Design

Evaluation 1 uses a specimen designed to utilize the MTS axial/torsional high-temperature extensometer. This specimen has a solid cylindrical gage section with a gage diameter of 9.5 mm and a gage length of 44.5 mm. The element mesh size for both the simulated experiments and the FEMU procedure is set at 0.50 mm, which leads to 10 total elements. Details on the design of the specimen used for Eval. 1 can be found in Appendix B.

Evaluations 2 and 3 both use a specimen that is designed to achieve fully reversed loading without buckling. The specimen has a solid cylindrical gage section with a gage diameter of 6.35 mm and a gage length of 19 mm. The element mesh size is set at 0.25 mm, which leads to 13 elements. Details on the design of this specimen can also be found in Appendix B.

5.3.4 FEMU Settings

The stress-strain data from the experiments (in this case, the simulated experiments) are filtered and condensed to decrease the total number of load steps used in the FEMU process. The filtering and condensing procedures are identical to those employed with actual simulated experimental data. A complete description of the filter and the data condensing procedures are given in Appendix A. The experimental data is processed using a finite impulse response 100th order low-pass filter and then condensed. The data is condensed using a nonlinear strain increment of 1×10^{-3}, an end tolerance of 1×10^{-6}, an increment tolerance of 5×10^{-5}, an averaging increment of 1×10^{-4}, and a nonlinear stress tolerance of 10 MPa.

The same optimization settings have been used for all the FEMU procedures. As mentioned earlier, only the hardening terms have been optimized, with all other terms required for the viscoplasticity model set equal to their exact value. This leads to seven total optimization variables as one of the kinematic terms is assumed linear with the recovery term set to zero. Particle swarm optimization (PSO) is used with 10 particles, and 10 rounds. A detailed description of the settings available for PSO is given in Section D.2. The cognitive, social, and pheromone coefficients are assumed constant through the rounds and are 0.25, 1.25, and 0.0, respectively. An inertia weight of 0.25 is used, and velocity clamping is used with a maximum velocity of 0.20 for any particle.

5.4 Intelligent Integrated Testing Results

5.4.1 Evaluation 1 - No Compressive Strain

Evaluation 1 has been designed to replicate a strain-controlled test similar to R = 0, where R is the ratio of the minimum to maximum strain. Strain limits of 0.0 and 0.015 m/m are used which prevents any compressive strain, but does not explicitly exclude compressive stress. The test bounds range from -90 to 90 degrees with angular bins for determining strain-space coverage set at 30 degrees with end bins of 15 degrees. Four test rounds are used with strain limits that are a specified fraction of the maximum strain magnitude (0.015 m/m). The four rounds have factors of 0.7, 0.8, 0.9, and 1.0, which leads to strains of 0.0105, 0.012, 0.0135, and 0.015 m/m.

Figure 5.4 shows the axial vs. shear strain points for the condensed data set. The black lines represent the angular bins and the red arcs are the four load limits of 0.7, 0.8, 0.9, and 1.0 times the strain magnitude. The circles represent data generated during the calibration load excursions while the diamonds represent validation load excursions. In figures with the color bar present, the data point colors correspond to the time at which the data point is taken (ranging from 0 to 100 percent of the test). Figure 5.5 show the engineering axial vs. shear stress points using the same color bar and marker types as those in the strain plot. These two figures illustrate the evolution of the autonomous test in both stress and strain space for the strain-controlled experiments.

Table 5.5 show the five sets of parameters from non-linear least-square regression performed on the supplemental tension test data. The first set in the table is the best in terms of minimizing the objective function, and the remaining four are randomly selected from the top 25 percent of remaining sets. These five sets have been used as initial seeds for the FEMU conducted in the first round of test block 1, with five additional sets generated using Latin hypercube sampling.

Table 5.5: Results for Eval. 1 from non-linear least-squares regression using supplemental tension test data.

Parameter	Q_1	$5/b_1$	A_1/B_1	$5/C_1$	A_2/B_2	$5/B_2$	A_3
Min	5.00	1.00E-04	5.00	1.00E-04	5.00	1.00E-04	212.50
Max	750.00	1.00E-01	750.00	1.00E-01	750.00	1.00E-01	287.50
Exact	50.00	1.00E-02	200.00	5.00E-4	50.00	1.00E-3	250.00
Best	202.62	8.00E-04	45.27	1.20E-02	51.98	8.00E-04	229.47
Set 2	229.47	8.00E-04	43.78	1.15E-02	25.14	8.00E-04	286.60
Set 3	34.08	8.00E-04	64.66	8.00E-03	198.89	7.00E-04	287.50
Set 4	9.47	9.26E-02	254.08	8.00E-04	40.05	9.70E-03	212.50
Set 5	11.71	1.41E-02	22.15	1.40E-02	264.52	9.00E-04	282.09
Best/Exact	4.05	0.08	0.23	24.00	1.04	0.80	0.92

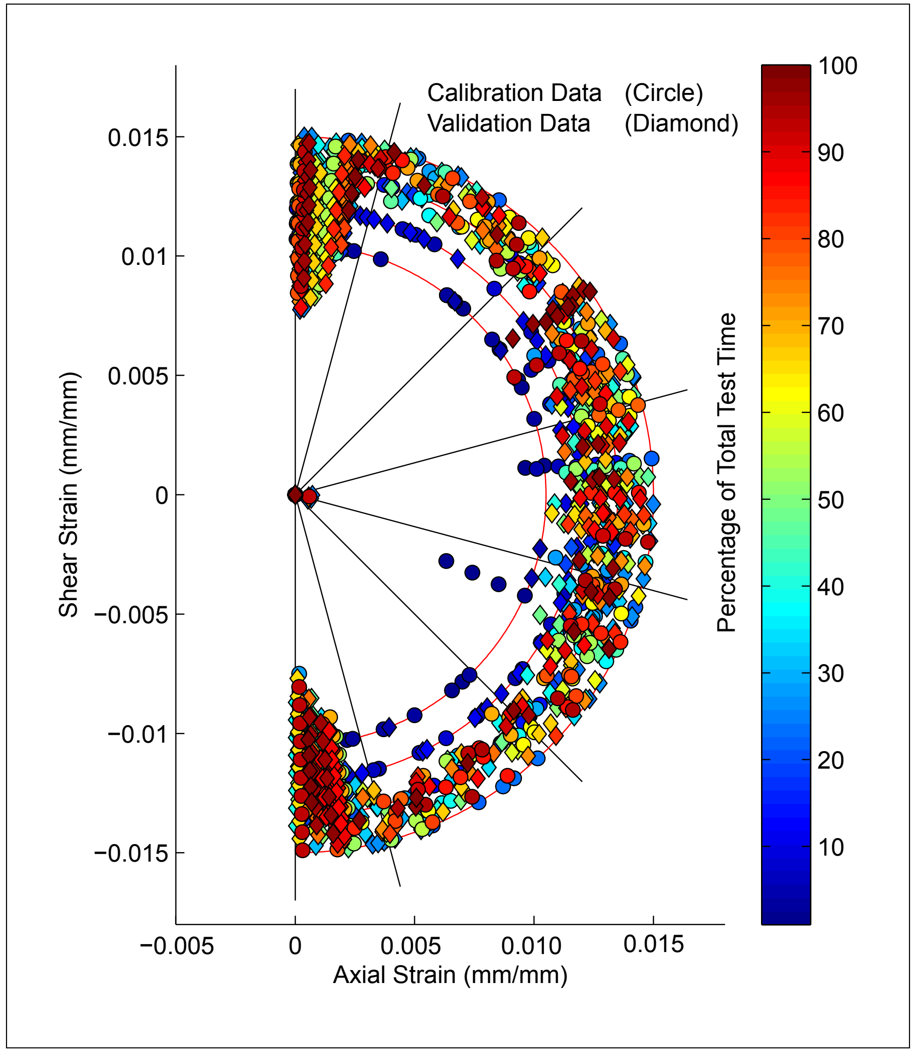

Figure 5.4: Engineering axial and shear strain points for Eval. 1. The color bar indicates the sequential order of the data points.

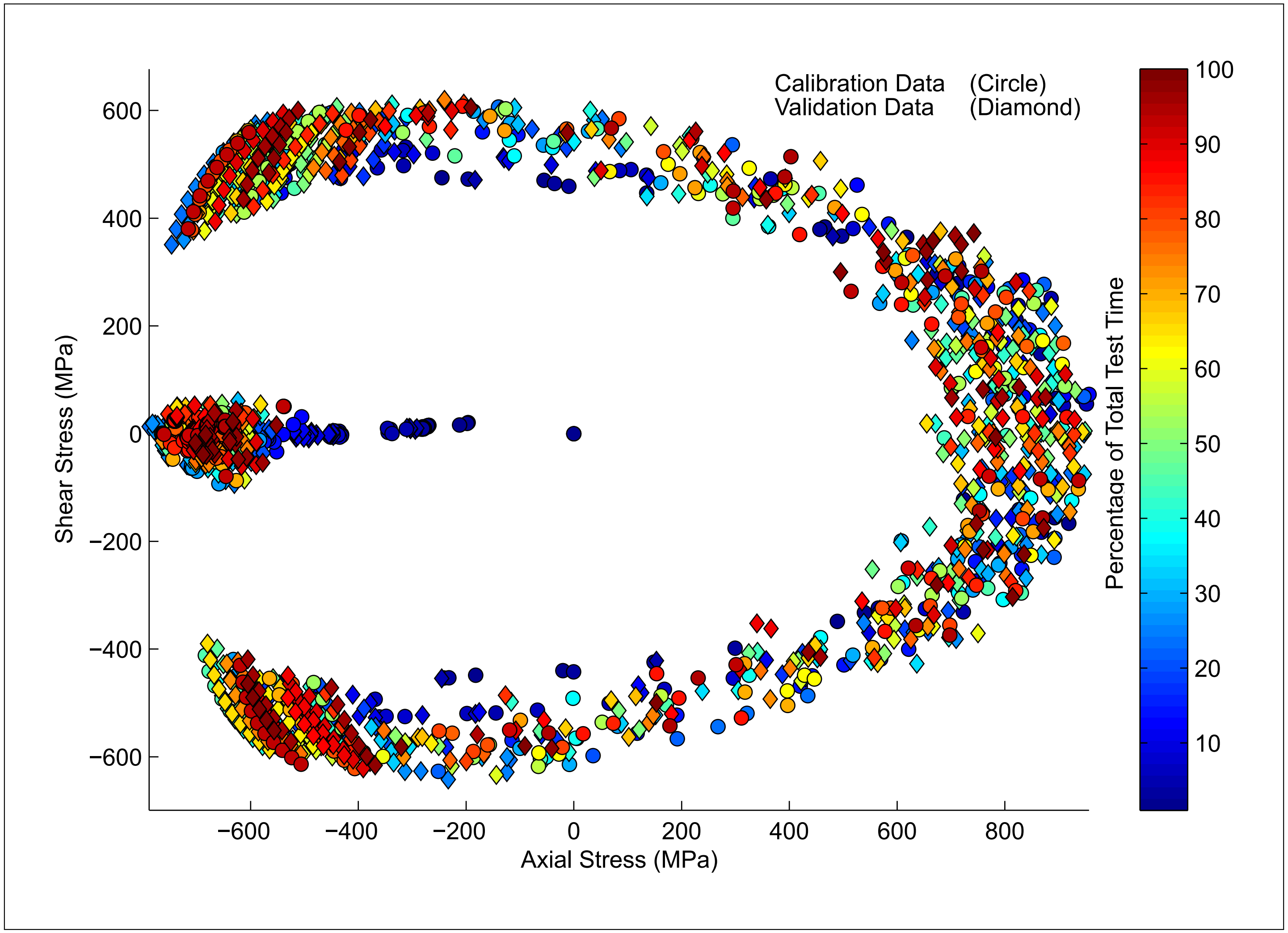

Figure 5.5: Engineering axial and shear stress points for Eval. 1. The color bar indicates the sequential order of the data points.

Figure 5.6 shows the engineering axial stress vs. strain, and Figure 5.7 shows the engineering shear stress vs. strain. The axial stress strain plot shows that after reaching 0.015 m/m, the amount of plastic strain achieved during each load segment is minimal (as indicated by the almost straight lines). The method did not fully converge due to a lack of plastic strain near the end of the test; rather, the method stopped after ten iterations at the maximum strain limit. Table 5.6 shows the convergence status for the overall method for each round, indicating strain-space coverage and the max and mean objective function values. Table 5.7 shows the evolution of the best-estimate optimization parameters after each fitting round completed during FEMU. The constitutive parameters stabilized after Round 4, Iteration 2, but the process continues because the strain coverage criteria is never met.

Figure 5.8 shows the simulated experimental versus analytical stress that have been computed for the final set of constitutive parameters from Round 4, Iteration 10. Error lines are included for 5 and 10 percent. The analysis results match closely with the experiment as the data points are grouped close to the 1:1 line. Figure 5.9 provides a closer view of the analysis error for both axial and shear stress. Again, the color bar is added to distinguish the time during the test at which the errors occur. The axial and shear stress are represented by circles and diamonds, respectively. Figure 5.9 provides a concise view of how well the methodology performs and allows for the identification of times during the test at which errors are highest. The errors for Eval. 1 are all very minimal in comparison to the levels of stress at which the errors occur. The majority of stress points greater than 400 MPa are all below 5 percent error; however, there are points at the beginning of the experiment (blue points) that have high errors due to poor fitting of the initial yield behavior of the material. Subsequent errors at low stress levels are due to differences experienced during unloading.

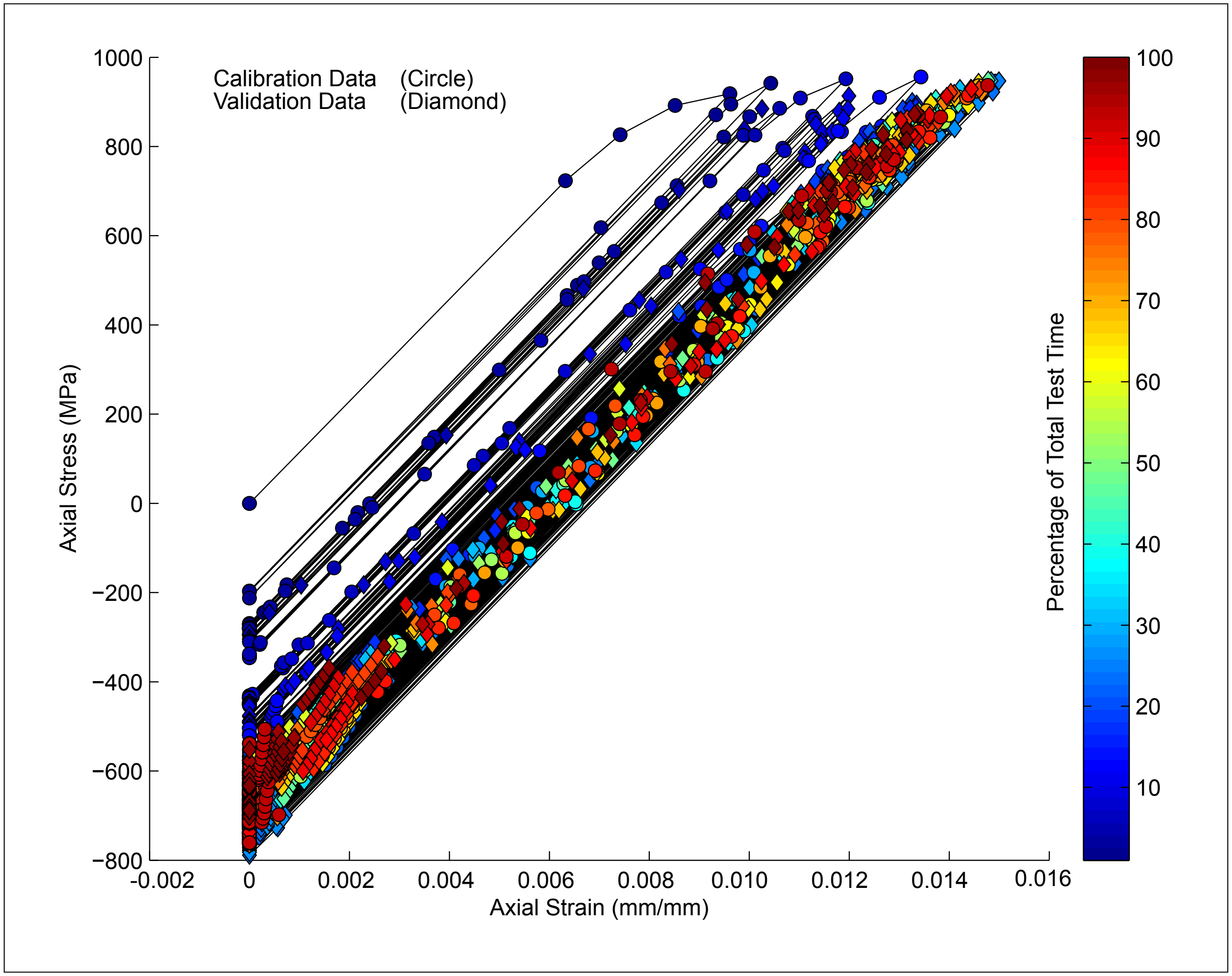

Figure 5.6: Engineering axial stress vs. strain for Eval. 1. The color bar indicates the sequential order of the data points.

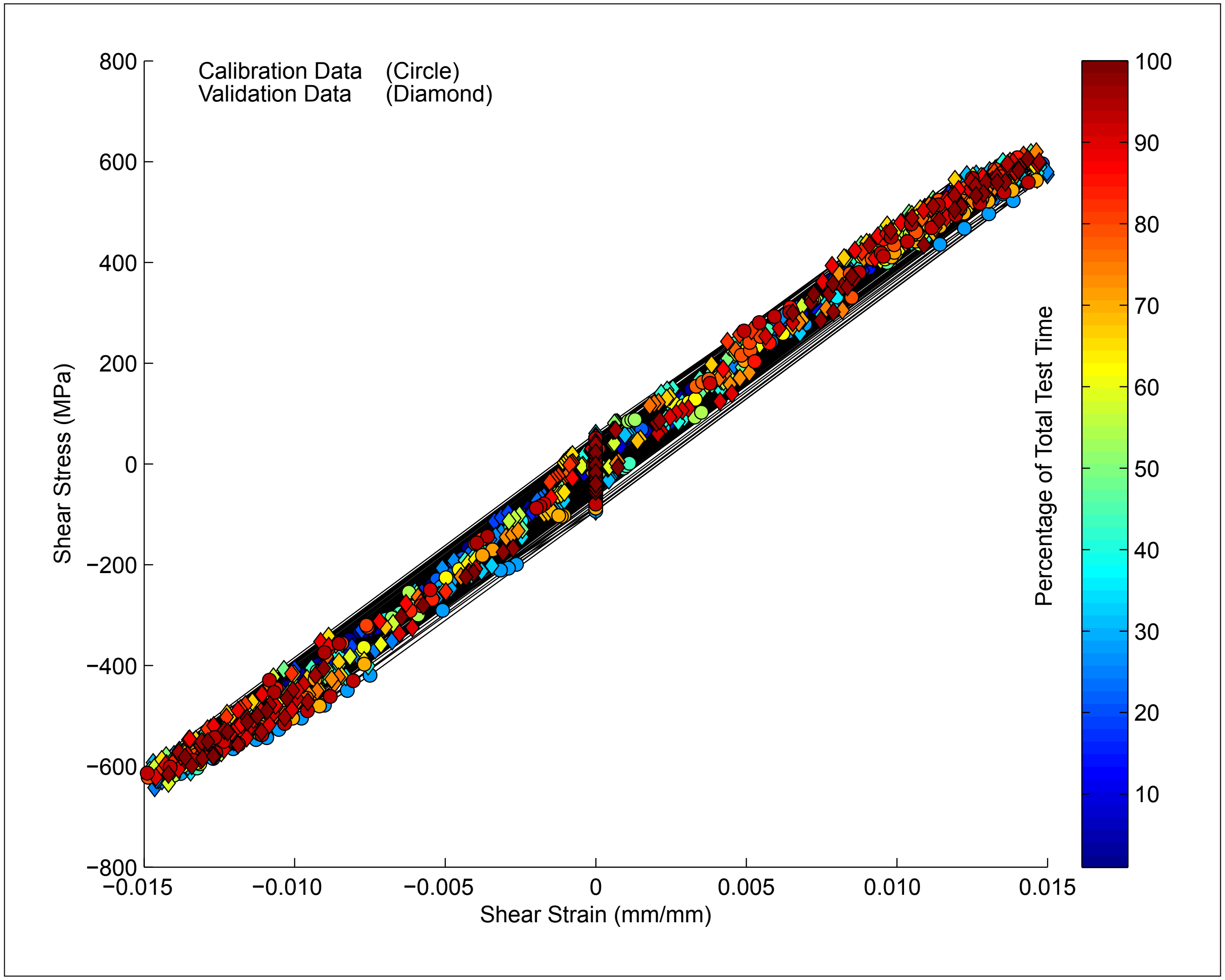

Figure 5.7: Engineering shear stress vs. strain for Eval. 1. The color bar indicates the sequential order of the data points.

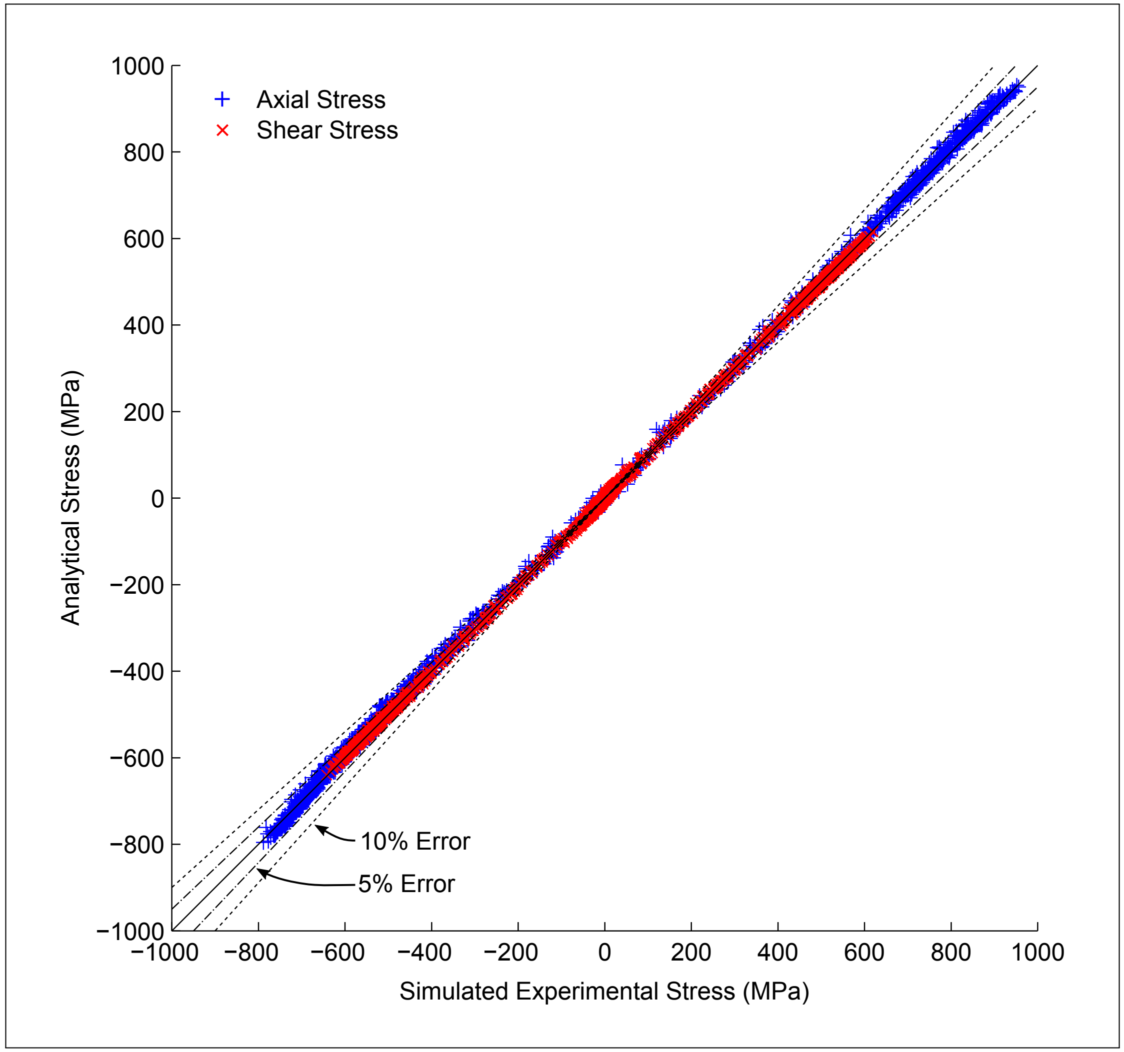

Figure 5.8: Simulated experimental stress for Eval. 1 and the corresponding analytical stress derived using the final set of constitutive parameters.

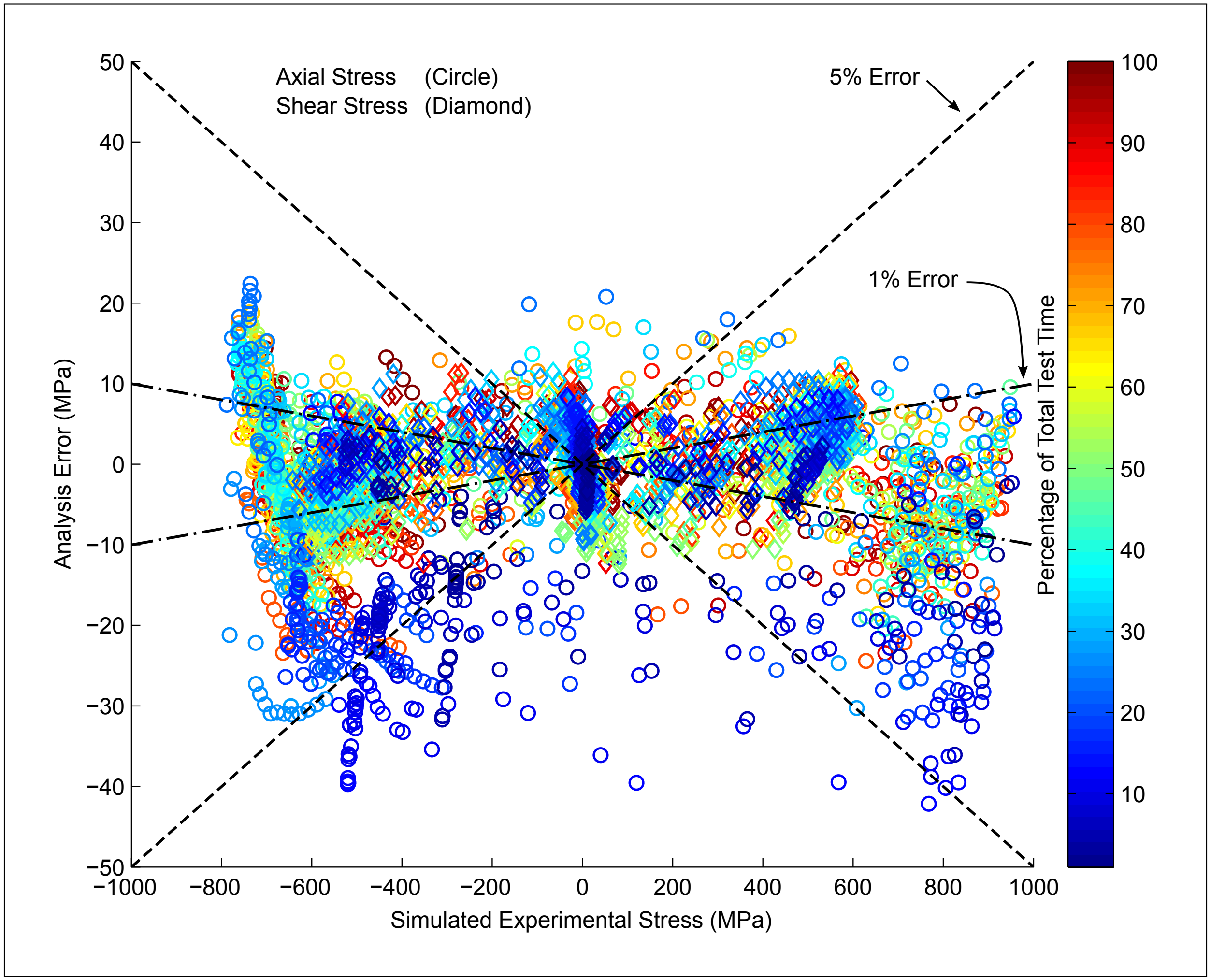

Figure 5.9: Analytical error using the final set of constitutive parameters for Eval. 1. Axial and shear stress are represented by circles and diamonds, respectively. The color bar indicates the sequential order of the data points.

Figure 5.10 shows that the computation time required for the FEMU procedures is approximately linear with respect to the number of analysis points. The analysis has been conducted on a personal computer running Windows 64-bit, with an Intel$^{(R)}$ Core$^{(TM)}$ i7-4790K CPU @4.00 GHz, with 32.0 GB of memory. Each FEMU procedure requires a total of 100 separate finite element analyses; therefore, it has been run using four cores using OpenMP. Scalability studies of the FEMU procedure have shown a speedup factor of 0.92 where 1.00 is perfect scalability. Therefore, if eight cores are used, the total time would be approximately half. The total computation time required for all the FEMU procedures when using four cores is 4741 seconds (79 minutes).

The strain limits in Eval. 1 preclude re-yielding upon unloading, which is necessary for determining the appropriate ratio of isotropic and kinematic hardening. Without re-yielding, the isotropic and kinematic hardening terms cause similar material responses, thus decreasing the sensitivity of the optimization. Therefore, there are many combinations of hardening that produces very low errors just like the final set of parameters from Eval. 1. Because reversed loading is not permitted, the incremental plastic strain diminishes as the test progresses. As a result, the hardening parameters identified by the autonomous test do not match well with the exact parameters used to generate the simulated results. However, the method does converge for all the criteria except for the strain space coverage requirement. Repeating Eval. 1 may lead to better results as the optimization algorithm that is used in FEMU has some randomness to the seeding. Ultimately a better test approach should be developed or additional fully reversed supplemental data should be included so the methodology can converge on the correct parameters regardless of the random initial seeding of the optimization algorithm. Evaluation 2 and 3 have test bounds that allow for re-yielding and as such produce better correlation with the exact set of constitutive parameters.

Table 5.6: Convergence summary for Eval. 1.

		Objective Function (MPa)						Opt. Par.	Cal. Bin	Val. Bin
		Calibration			Validation			Max. Error	Min.	Min.
Rnd	Iter	Pts	Max	Mean	Pts	Max	Mean	(%)	$\Delta\bar{\varepsilon}^p$	$\Delta\bar{\varepsilon}^p$
4	1	454	36.1	13.7	83	40.6	19.6	30.0	1.77E-04	1.96E-04
4	2	589	35.9	14.5	121	22.7	12.0	183.3	2.55E-04	4.74E-04
4	3	766	35.1	13.7	109	34.3	17.8	20.0	2.39E-04	5.03E-04
4	4	921	35.7	14.1	128	29.2	15.6	25.0	1.24E-04	2.05E-04
4	5	1114	38.3	14.0	99	21.0	11.3	300.0	3.31E-04	9.42E-04
4	6	1264	39.0	13.7	124	26.6	12.2	1.1	2.46E-04	4.62E-04
4	7	1447	39.0	13.5	114	18.2	10.0	0.0	4.30E-04	2.55E-04
4	8	1625	39.0	13.2	58	32.1	17.4	0.0	4.45E-04	2.88E-05
4	9	1731	41.3	12.7	116	22.5	12.4	21.3	1.96E-04	2.63E-04
4	10	1912	42.0	12.6	100	14.0	8.2	66.7	9.81E-05	4.41E-04

Table 5.7: Best constitutive parameters identified during each test block for Eval. 1.

Parameter		Q_1	$5/b_1$	A_1/B_1	$5/C_1$	A_2/B_2	$5/B_2$	A_3
Min		5	1.00E-04	5	1.00E-04	5	1.00E-04	212.5
Max		750	1.00E-01	750	1.00E-01	750	1.00E-01	287.5
Exact		50	1.00E-02	200	5.00E-04	50	1.00E-03	250
Round	Iter	Q_1	$5/b_1$	A_1/B_1	$5/C_1$	A_2/B_2	$5/B_2$	A_3
1	1	202.62	7.00E-04	45.27	1.20E-02	51.98	8.00E-04	229.32
2	1	202.62	4.00E-04	45.27	1.21E-02	51.98	8.00E-04	229.32
3	1	164.59	2.00E-03	55.71	9.60E-03	80.32	1.30E-03	254.62
4	1	177.27	1.70E-03	51.24	1.16E-02	70.63	1.00E-03	263.10
4	2	179.51	6.00E-04	46.02	1.11E-02	74.35	8.00E-04	261.52
4	3	178.76	5.00E-04	45.27	1.10E-02	75.10	8.00E-04	261.82
4	4	181.74	4.00E-04	44.52	1.09E-02	73.61	8.00E-04	261.15
4	5	191.44	1.00E-04	40.80	1.09E-02	66.15	3.00E-04	260.17
4	6	191.44	1.00E-04	40.80	1.08E-02	66.90	3.00E-04	260.40
4	7	191.44	1.00E-04	40.80	1.08E-02	66.90	3.00E-04	260.40
4	8	191.44	1.00E-04	40.80	1.08E-02	66.90	3.00E-04	260.40
4	9	189.20	1.00E-04	37.81	8.90E-03	72.86	3.00E-04	259.35
4	10	189.20	3.00E-04	36.32	8.70E-03	74.35	3.00E-04	259.57
Final/Exact		3.78	0.03	0.18	17.4	1.49	0.30	1.04

Rnd.	Iter.	Pts.	Time (sec)
1	1	65	48.0
2	1	152	68.0
3	1	293	119.5
4	1	454	163.9
4	2	589	225.9
4	3	766	301.8
4	4	921	334.6
4	5	1114	452.8
4	6	1264	496.5
4	7	1447	537.8
4	8	1625	607.1
4	9	1731	622.0
4	10	1912	763.3

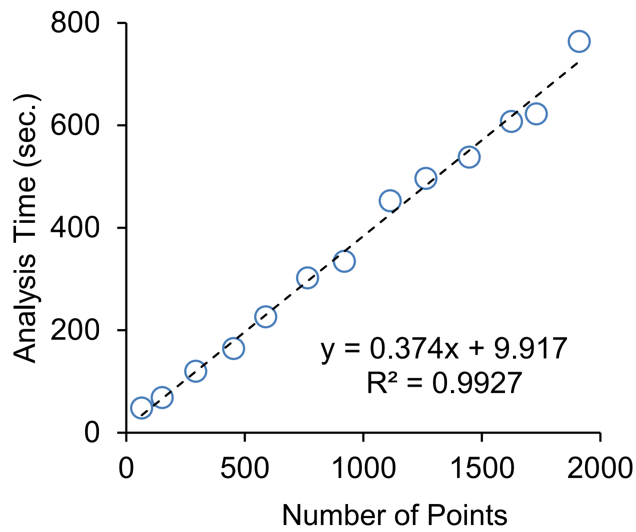

Figure 5.10: Number of points and time required to complete each FEMU procedure in Eval. 1.

5.4.2 Evaluation 2 - Fully Reversed Loading

Evaluation 2 has strain limits of ±0.015 m/m with angular bounds of 0 to 360 degrees and uniform angular bin sizes of 30 degrees. Figure 5.11 shows the axial vs. shear strain points for the condensed data set. The black lines represent the angular bins and the red circles are the four load limits of 0.7, 0.8, 0.9, and 1.0 times the strain magnitude. The circles represent data generated during the calibration load excursions while the diamonds represent validation load excursions. In figures with the color bar present the data point color corresponds to the percentage of the test time complete. Figure 5.12 show the axial vs. shear stress points using the same color bar and marker types. These two plots provide a large amount of data regarding the autonomous test procedure. They also indicate complete coverage of the strain space.

Table 5.8 show the five sets of parameters that have been obtained from using non-linear least-square regression on the supplemental tension test data. The first set in the table is the best in terms of minimizing the objective function, and the remaining four are randomly selected from the top 25 percent of remaining sets. As is done for Eval. 1, the five sets of parameters from the non-linear regression procedure have been used as initial seeds for the FEMU conducted in round 1. Five additional sets have been generated using Latin hypercube sampling to make up the ten sets used during PSO.

Figure 5.13 shows the engineering axial stress vs. strain, while Figure 5.14 shows the engineering shear stress vs. strain. Table 5.9 shows the evolution of the best-estimate optimization parameters after each fitting round completed during FEMU. Table 5.10 shows the convergence status during each round of the overall method, indicating strain-space coverage and the maximum and mean objective function values.

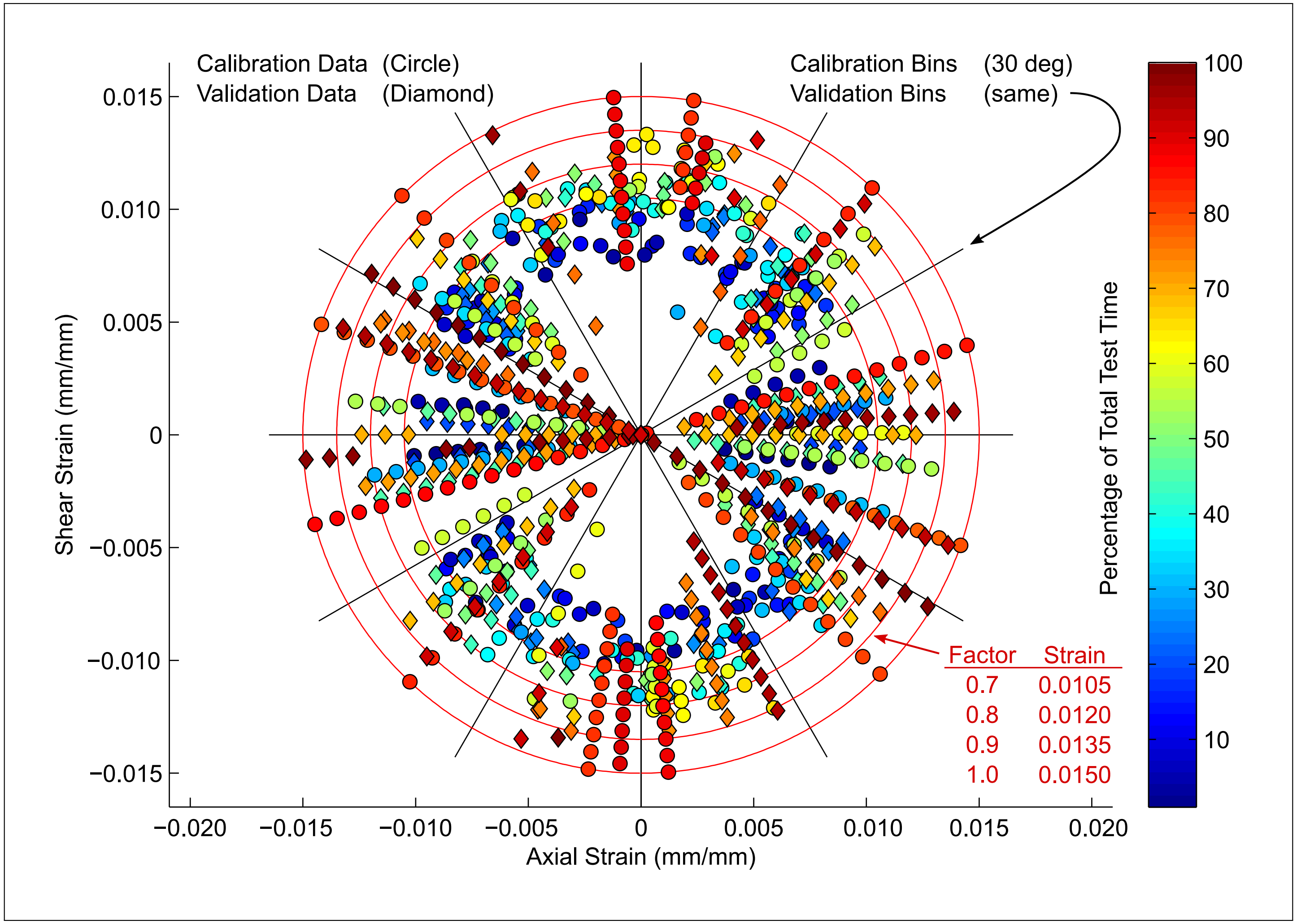

Figure 5.11: Engineering axial and shear strain points for Eval. 2. The color bar indicates the sequential order of the data points.

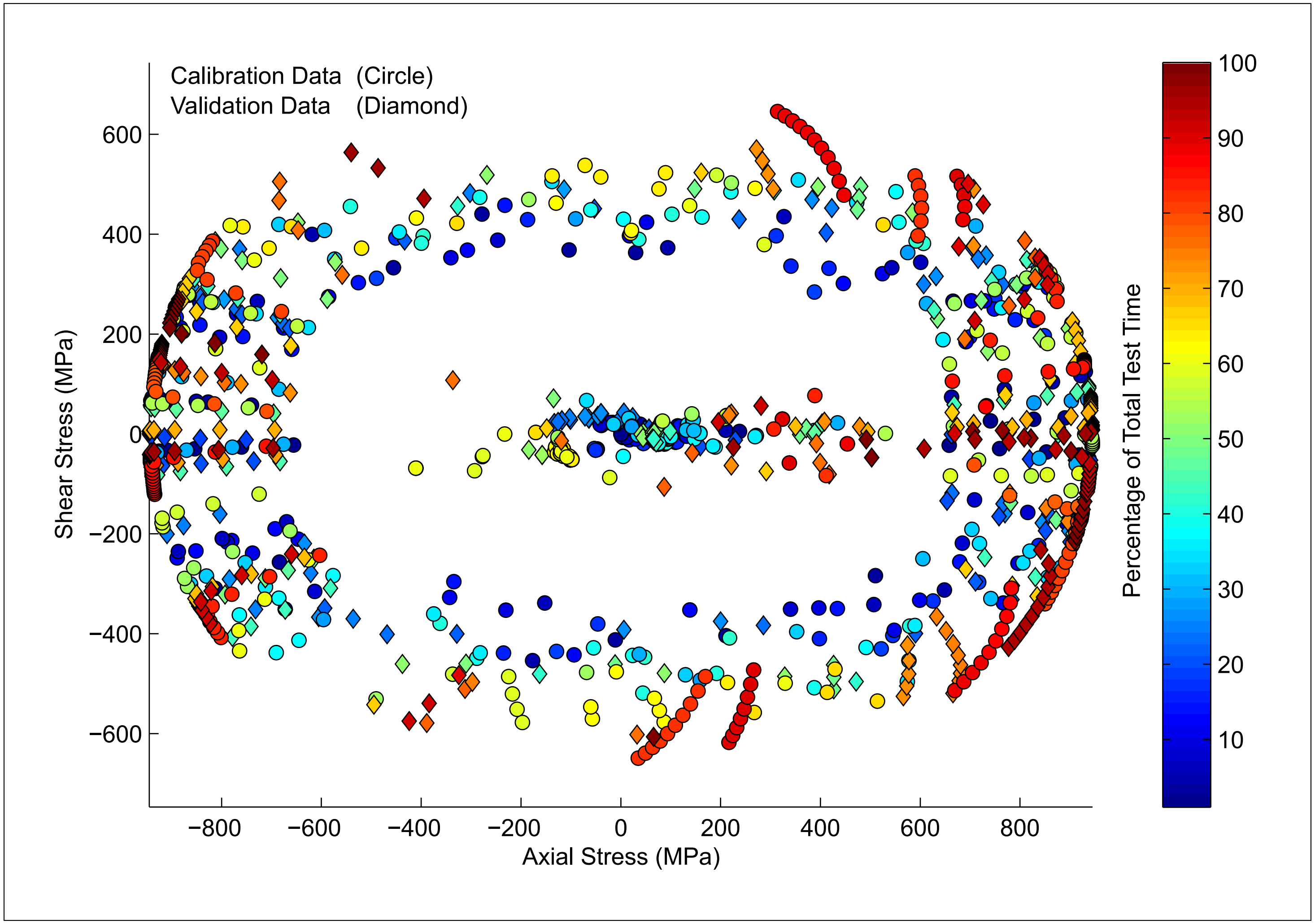

Figure 5.12: Engineering axial and shear stress points for Eval. 2. The color bar indicates the sequential order of the data points.

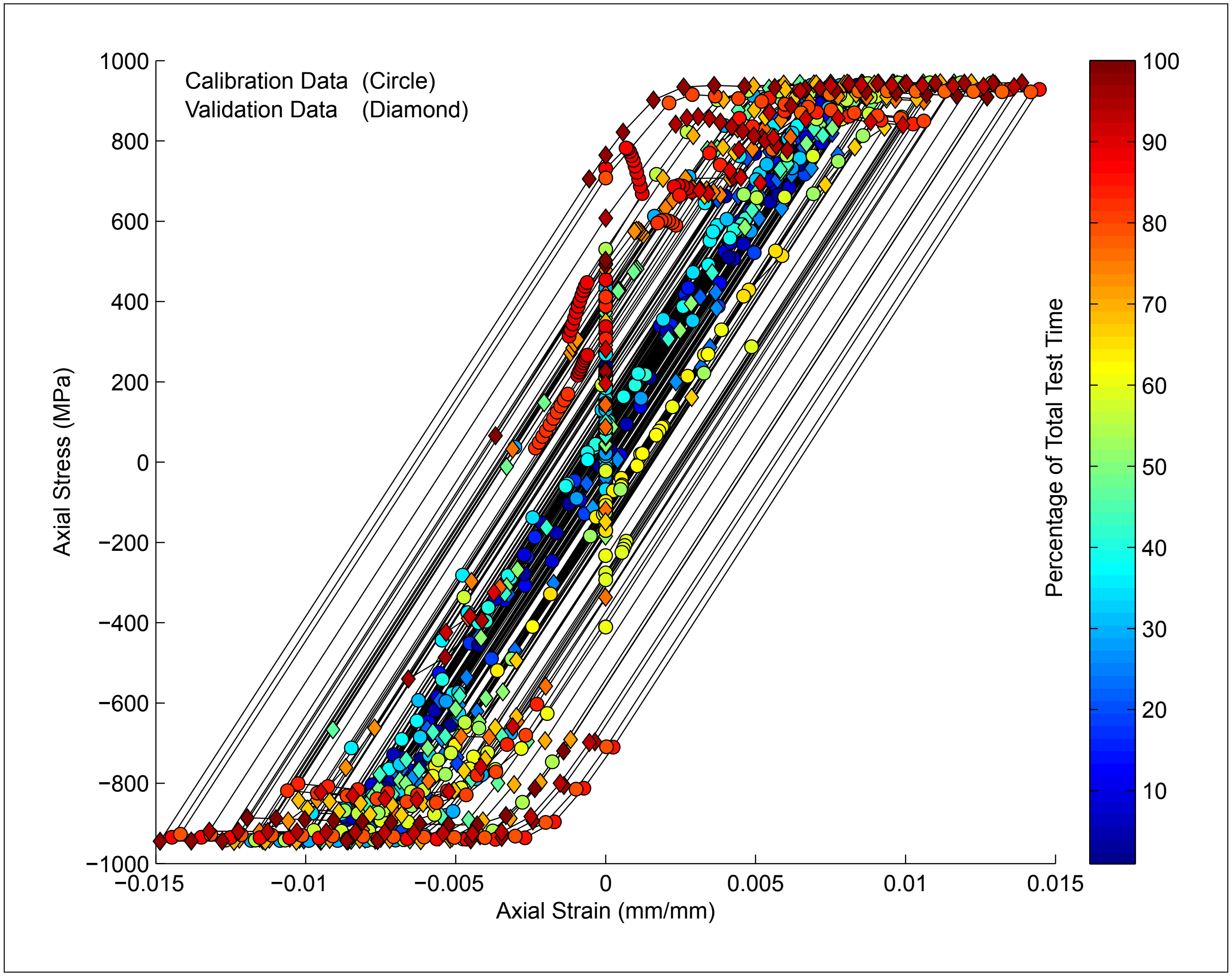

Figure 5.13: Engineering axial stress vs. strain for Eval. 2. The color bar indicates the sequential order of the data points.

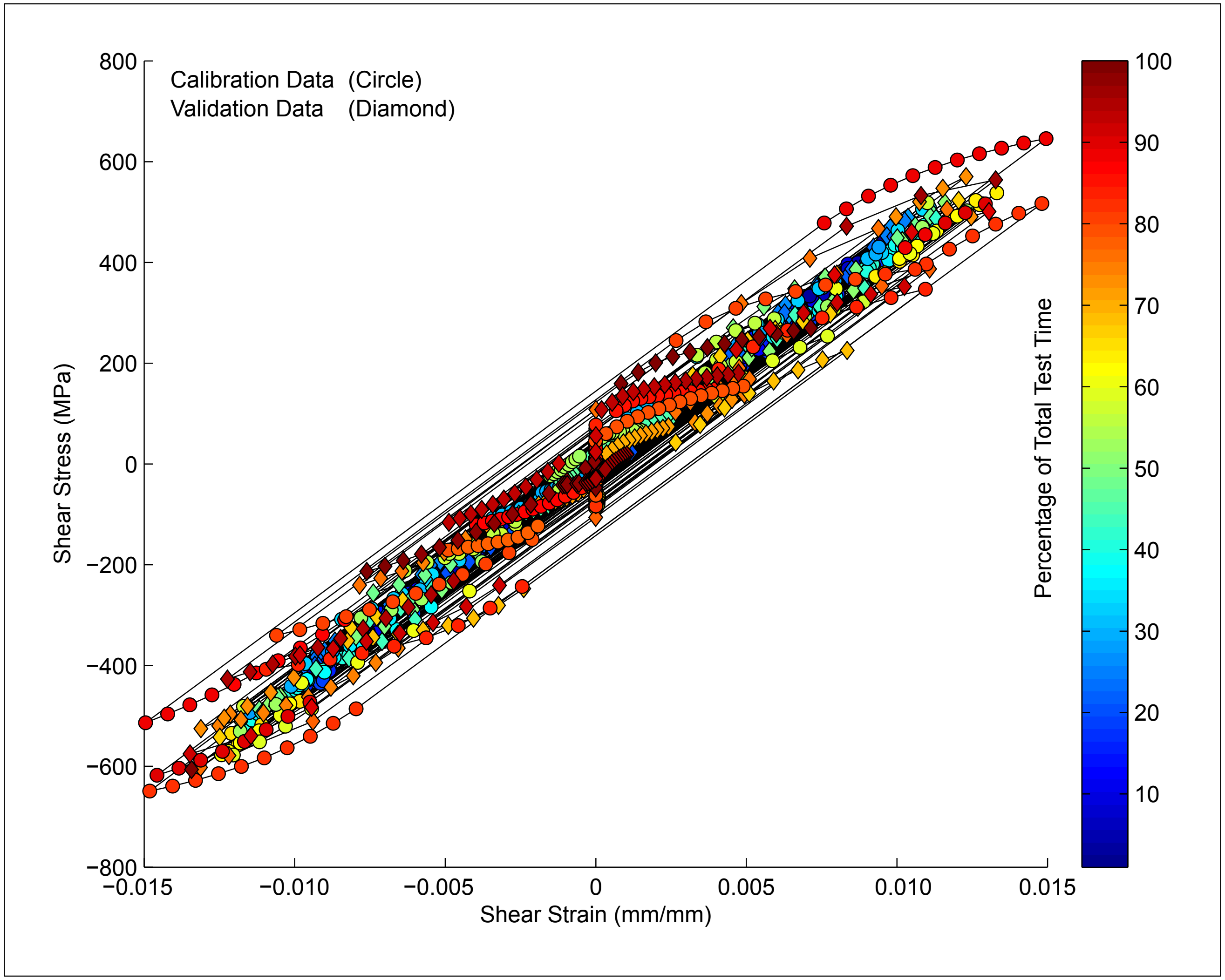

Figure 5.14: Engineering shear stress vs. strain for Eval. 2. The color bar indicates the sequential order of the data points.

Table 5.8: Results from non-linear least-squares regression using supplemental tension test data.

Parameter	Q_1	$5/b_1$	A_1/B_1	$5/C_1$	A_2/B_2	$5/B_2$	A_3
Min	5.00	1.00E-04	5.00	1.00E-04	5.00	1.00E-04	212.50
Max	750.00	1.00E-01	750.00	1.00E-01	750.00	1.00E-01	287.50
Exact	50.00	1.00E-02	200.00	5.00E-4	50.00	1.00E-3	250.00
Best	22.54	8.72E-04	46.44	1.20E-02	231.73	8.63E-04	216.24
Set 2	34.19	1.16E-02	12.11	1.16E-02	253.85	8.62E-04	246.17
Set 3	48.27	9.41E-03	239.55	8.30E-04	9.94	1.30E-03	287.50
Set 4	5.00	1.59E-02	25.53	1.59E-02	268.92	9.42E-04	281.41
Set 5	276.60	9.88E-04	16.40	1.97E-02	6.29	1.97E-02	281.66
Best/Exact	0.45	0.09	0.23	24	4.63	0.86	0.86

Table 5.9: Best constitutive parameters identified during each round of Eval. 2.

Parameter		Q_1	$5/b_1$	A_1/B_1	$5/C_1$	A_2/B_2	$5/B_2$	A_3
Min		5.00	1.00E-04	5.00	1.00E-04	5.00	1.00E-04	212.50
Max		750.00	1.00E-01	750.00	1.00E-01	750.00	1.00E-01	287.50
Exact		50.00	1.00E-02	200.00	5.00E-4	50.00	1.00E-3	250.00
Round	Iter	Q_1	$5/b_1$	A_1/B_1	$5/C_1$	A_2/B_2	$5/B_2$	A_3
1	1	48.25	9.90E-03	236.93	3.00E-04	16.93	1.00E-03	287.28
2	1	48.25	1.01E-02	198.89	4.00E-04	53.47	9.00E-04	277.52
3	1	48.25	1.01E-02	198.89	4.00E-04	51.98	7.00E-04	277.59
4	1	48.25	1.01E-02	198.89	4.00E-04	52.73	7.00E-04	277.67
Final/Exact		0.97	1.01	0.99	0.80	1.05	0.70	1.11

Figure 5.15 shows the simulated experimental stress versus the analytical stress computed for the final set of constitutive parameters from round 4. Error lines are included for 5 and 10 percent. The analysis results once again match closely with the experiments as the data points are all tightly grouped around the 1:1 line. Figure 5.16 provides a closer view of the analysis error for both axial and shear stress. The color bar is added to distinguish the time during the test at which the errors

occur. The axial and shear stress are represented by circles and diamonds, respectively. Figure 5.16 provides a concise view of how well the methodology performs and allows for the identification of points during the test at which errors are highest. The errors for Eval. 2 are all minimal in comparison to the levels of stress at which the errors occur. If points near 0 MPa are excluded, almost all the data points fall below 1 percent error.

Table 5.11 gives the number of points and the total computation time (in seconds) for the FEMU procedure for each round. The evaluations have all been conducted on the same personal computer running Windows 64-bit, with an Intel$^{(R)}$ Core$^{(TM)}$ i7-4790K CPU @4.00 GHz, with 32.0 GB of memory. Each FEMU procedure has been run using four cores, and again 100 finite element analyses with separate constitutive parameters are required for each FEMU procedure. All four of the FEMU procedures have been completed in only 1520 seconds (25.3 minutes) using four cores.

The results from Eval. 2 clearly demonstrate the success of the methodology if constitutive model uncertainly is removed by using a simulated set of experiments. The fully reversed, multiaxial strain conditions provide enough data to distinguish between the two different hardening mechanisms of the plasticity model. The ratio of isotropic and kinematic hardening is easier to distinguish when the load excursions exhibit re-yielding upon reversal of loading. The optimized parameters are also very close to the exact parameters after just one round of testing, and all convergence criteria are met after only four rounds.

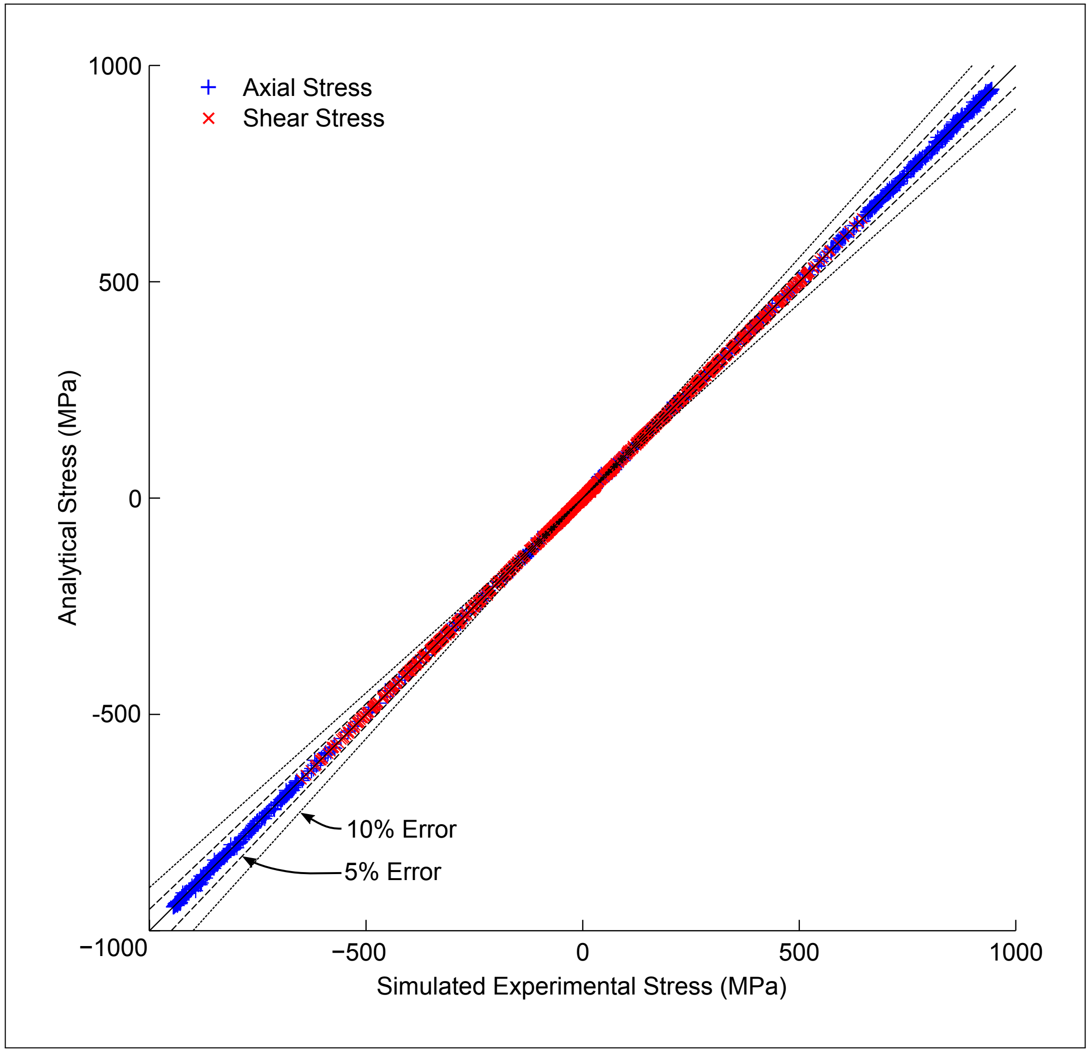

Figure 5.15: Simulated experimental stress for Eval. 2 and analytical stress using the final set of constitutive parameters.

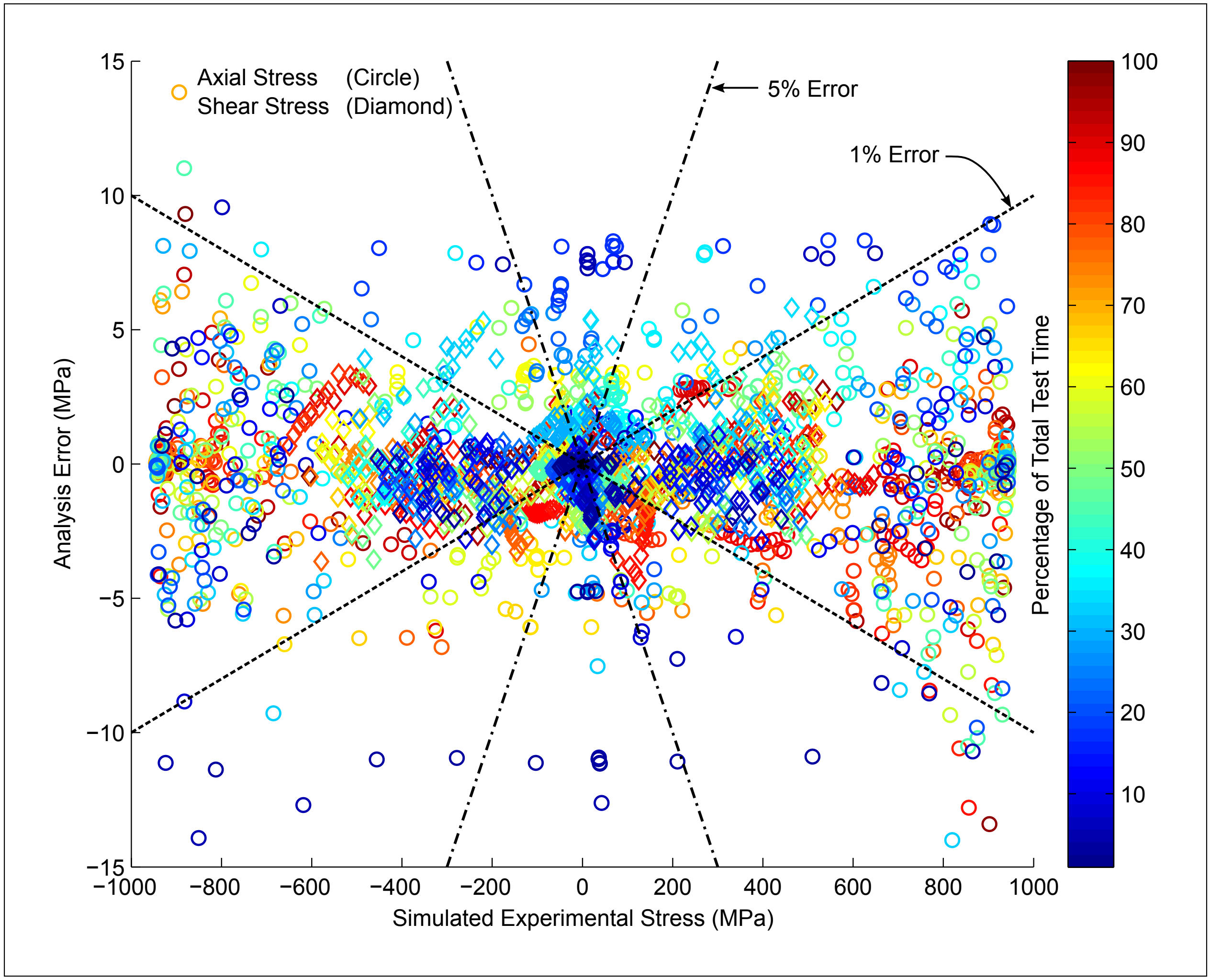

Figure 5.16: Analytical error using the final set of constitutive parameters for Eval. 2. Axial and shear stress are represented by circles and diamonds, respectively. The color bar indicates the sequential order of the data points.

Table 5.10: Convergence summary for Eval. 2.

	Objective Function (MPa)						Opt. Par.	Cal. Bin	Val. Bin
	Calibration			Validation			Max. Error	Min.	Min.
Round	Pts	Max	Mean	Pts	Max	Mean	(%)	$\Delta\bar{\varepsilon}^p$	$\Delta\bar{\varepsilon}^p$
1	212	11.9	5.7	106	11.3	4.3	-	1.15E-04	1.47E-04
2	488	16.1	4.8	117	7.1	3.8	68.3	1.91E-04	1.02E-04
3	767	15.8	4.4	137	11.3	3.9	28.6	5.67E-04	1.92E-03
4	1055	15.6	4.1	114	13.8	3.2	1.4	2.15E-03	2.05E-03

Table 5.11: Number of points and CPU time required to complete each FEMU procedure in Eval. 2.

Round	Pts	Time (sec)
1	212	141.3
2	488	296.8
3	767	448.9
4	1055	633.3

5.4.3 Evaluation 3 - Multiple Test Blocks

Evaluation 3 utilizes multiple test blocks with independent test bounds and strain limits. A test block is defined as a series of testing rounds for which each round has a different strain limit. During each round, multiple load excursions are conducted within the testing domain. The definition of test blocks allows for more versatility in defining the autonomous test. Evaluation 3 uses two types of angular bounds. Type 1 bounds are from -90 to 90 degrees with bin sizes of 30 degrees and end bins of 15 degrees (similar to Eval. 1 bounds). For Type 1, the strain magnitudes range from 0.0 to 0.015 m/m. Type 2 bounds are from 0 to 360 degrees with bin sizes of 30 degrees (similar to Eval. 2 bounds). The strain magnitudes for Type 2 range from -0.015 to 0.015 m/m. Table 5.12 shows the test bounds for the four test blocks used during Eval. 3.

Table 5.12: Test blocks used for Eval. 3

Block	Angular Bounds	Strain Min. (mm/mm)	Strain Max. (mm/mm)	Rounds	Fact 1	Fact 2
1	Type 1	0	0.015	2	0.7	0.8
2	Type 2	-0.015	0.015	1	0.8	
3	Type 1	0	0.015	2	0.9	1.0
4	Type 2	-0.015	0.015	1	1.0	

Figure 5.17 shows the axial vs. shear strain points for the condensed data set with the color corresponding to the percentage of total test time. The dashed blue lines are the Type 1 bounds, while the black lines represent Type 2 bounds. The red circles are the four round factors (0.7, 0.8, 0.9, and 1.0) that are used throughout the various test blocks to modify the strain magnitudes. The circular data points represent calibration load excursion data while the diamonds represent validation load excursions. Figure 5.18 show the axial vs. shear stress points using the same color bar and marker types. These two plots provide an overview of the test domain employed during the autonomous test. They show that Eval. 3 also has comprehensive coverage of the test domain.

Again, the FEMU procedure for round 1 of Test Block 1 has been seeded using initial fits that are generated using non-linear least-squares regression and the supplemental tension test data. Table 5.13 show the five sets of parameters from the supplement data fitting. Five additional sets have been generated using Latin hypercube sampling to make up the ten sets used during PSO.

Figure 5.19 shows the engineering axial stress vs. strain, while Figure 5.20 shows the engineering shear stress vs. strain. Table 5.14 shows the evolution of the best-estimate optimization parameters after each fitting round completed during FEMU. Table 5.15 shows the convergence status during each round of the overall method, indicating strain-space coverage and the maximum and mean objective function values.

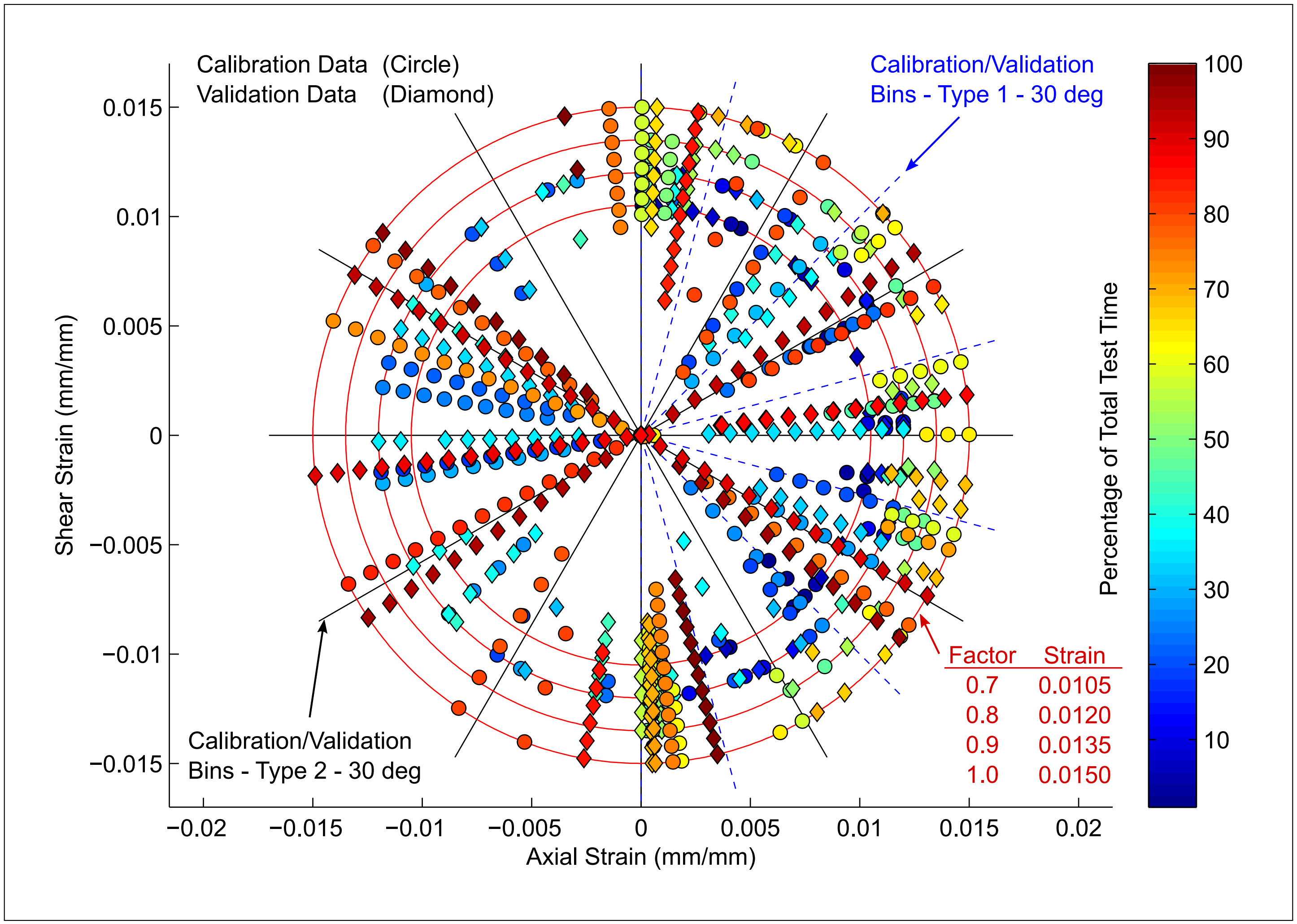

Figure 5.17: Engineering axial and shear strain points for Eval. 3. The color bar indicates the sequential order of the data points.

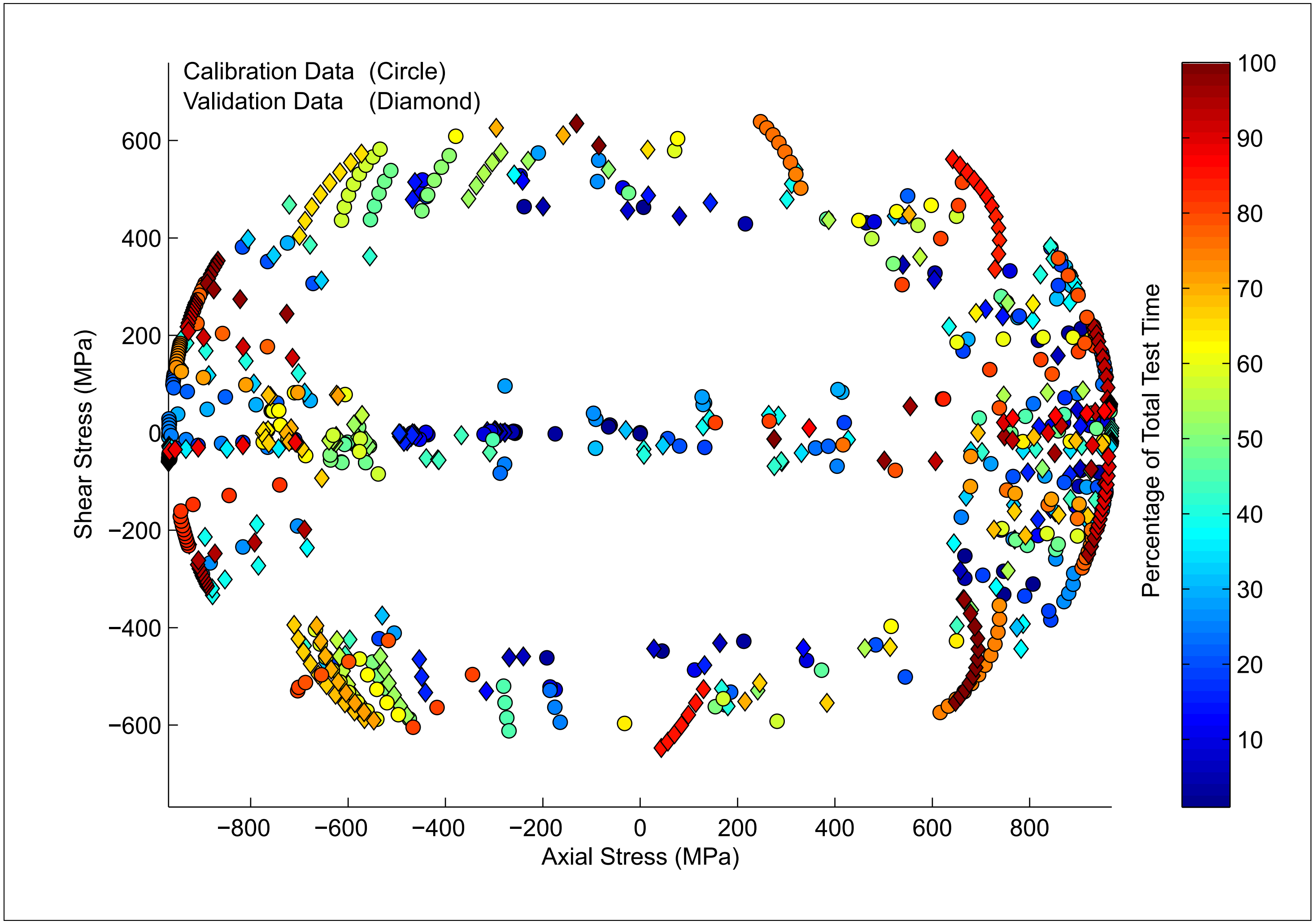

Figure 5.18: Engineering axial and shear stress points for Eval. 3. The color bar indicates the sequential order of the data points.

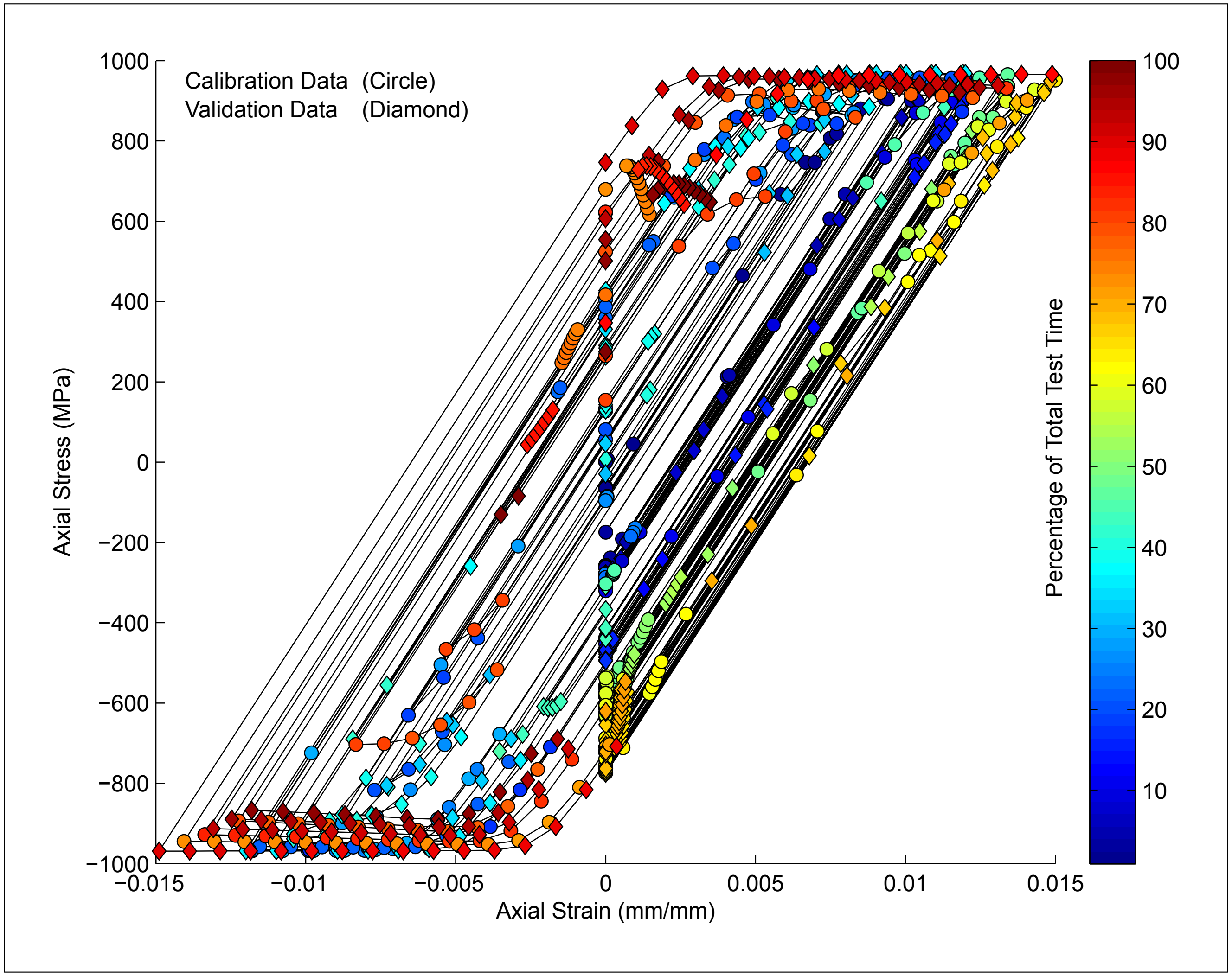

Figure 5.19: Engineering axial stress vs. strain for Eval. 3. The color bar indicates the sequential order of the data points.

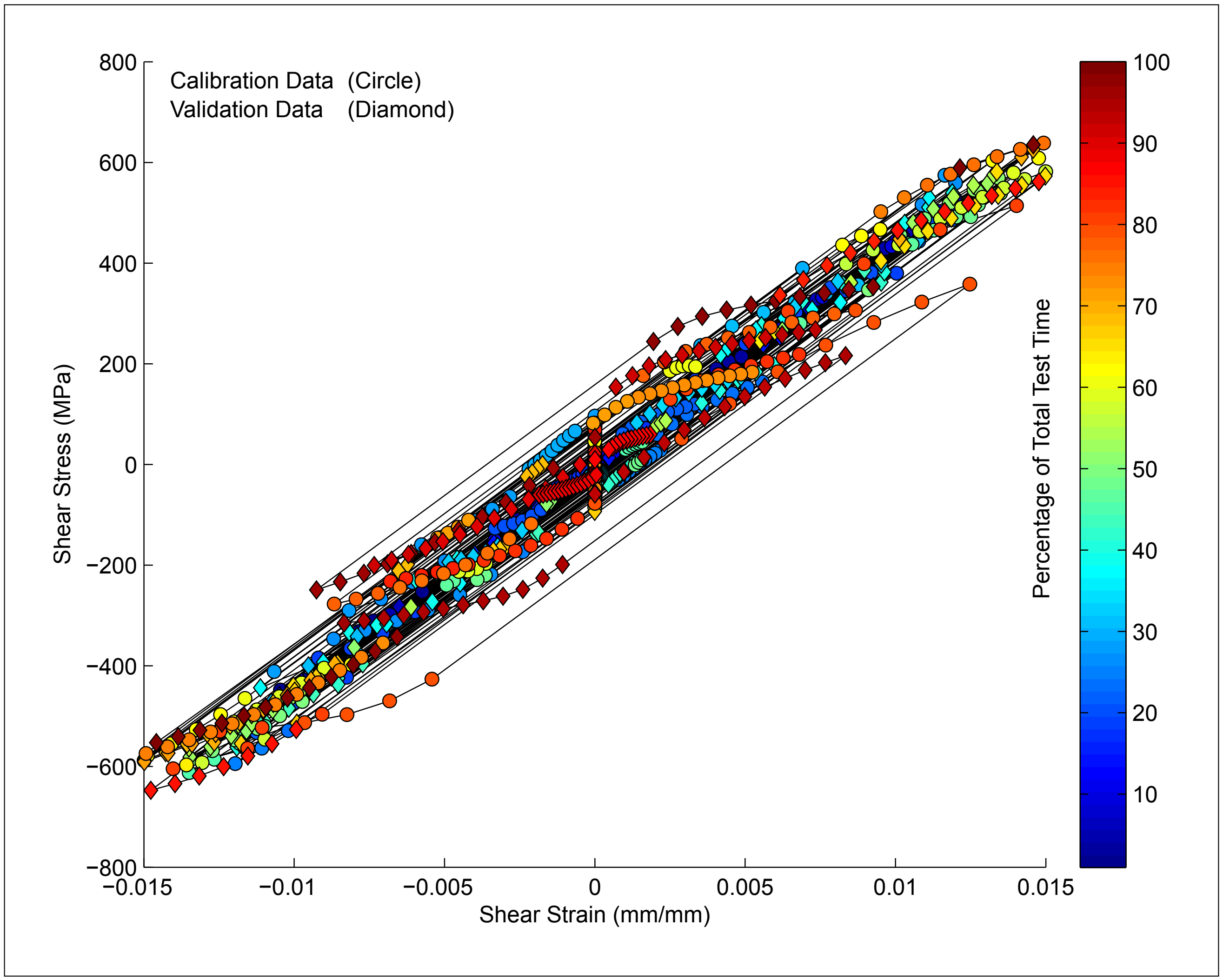

Figure 5.20: Engineering shear stress vs. strain for Eval. 3. The color bar indicates the sequential order of the data points.

Table 5.13: Results for Eval. 3 from non-linear least-squares regression using supplemental tension test data.

Parameter	Q_1	$5/b_1$	A_1/B_1	$5/C_1$	A_2/B_2	$5/B_2$	A_3
Min	5.00	1.00E-04	5.00	1.00E-04	5.00	1.00E-04	212.50
Max	750.00	1.00E-01	750.00	1.00E-01	750.00	1.00E-01	287.50
Exact	50.00	1.00E-02	200.00	5.00E-4	50.00	1.00E-3	250.00
Best	255.57	8.00E-04	34.08	1.22E-02	9.47	1.22E-02	240.05
Set 2	6.49	1.90E-02	16.19	1.90E-02	275.71	9.00E-04	285.40
Set 3	75.10	7.00E-04	61.68	8.30E-03	161.61	7.00E-04	284.50
Set 4	61.68	8.20E-03	230.96	7.00E-04	5.75	1.00E-03	287.50
Set 5	56.46	8.40E-03	15.44	3.00E-03	226.49	7.00E-04	279.39
Best/Exact	5.11	0.08	0.17	24.4	0.19	12.2	0.96

Figure 5.21 shows the simulated experimental stress verses the analytical stress using the final set of constitutive parameters from Test Block 4. Error lines are included for 5 and 10 percent relative error. The analysis results once again match closely with the experiments and the data points are all near the 1:1 line. Figure 5.22 provides a closer view of the analysis error for both axial and shear stress. Again, the color bar is added to distinguish the time during the test when the errors occur. The axial and shear stress are represented by circles and diamonds, respectively. Figure 5.22 provides a concise view of how well the methodology performs. The highest errors occur at the beginning of the experiment due to error in the kinematic hardening term A_1/B_1 which dominates the initial yielding of the material. If points near 0 MPa are excluded (because relative error is used), almost all the data points fall below 1 percent relative error. The errors for Eval. 3 are all minimal (less than 20 MPa) in comparison to the levels of stress at which the errors occur.

Table 5.16 gives the number of points and the total computation time (in seconds) for the FEMU procedure for each round. The evaluations have once again been conducted on the same personal computer running Windows 64-bit, with an Intel$^{(R)}$ Core$^{(TM)}$ i7-4790K CPU @4.00 GHz, with

Table 5.14: Best constitutive parameters identified during each test block for Eval. 3.

Parameter			Q_1	$5/b_1$	A_1/B_1	$5/C_1$	A_2/B_2	$5/B_2$	A_3
Min			5	1.00E-04	5	1.00E-04	5	1.00E-04	212.5
Max			750	1.00E-01	750	1.00E-01	750	1.00E-01	287.5
Exact			50	1.00E-02	200	5.00E-04	50	1.00E-03	250
Block	Iter	Round	Q_1	$5/b_1$	A_1/B_1	$5/C_1$	A_2/B_2	$5/B_2$	A_3
1	1	1	256.32	8.00E-04	36.32	1.24E-02	7.98	1.22E-02	239.98
1	1	2	255.57	8.00E-04	34.08	1.22E-02	9.47	1.22E-02	240.05
2	1	1	51.24	1.00E-02	185.47	3.00E-04	63.17	2.00E-04	287.28
3	1	1	51.24	1.00E-02	185.47	3.00E-04	63.17	2.00E-04	287.28
3	1	2	50.49	1.02E-02	183.23	5.00E-04	66.15	1.00E-04	287.43
4	1	1	50.49	1.02E-02	183.23	5.00E-04	66.15	1.00E-04	287.43
Final/Exact			1.01	1.02	0.92	1.00	1.32	0.10	1.15

32.0 GB of memory. Each FEMU procedure has been run using four cores, and each FEMU procedure contains 100 finite element analyses with separate constitutive parameters. All the FEMU procedures have been completed in only 720 seconds (12 minutes) when using four cores.

The results from Eval. 3 further demonstrate the success of the methodology if constitutive model uncertainly is removed by using a simulated set of experiments. The use of multiple test blocks on the same specimen allows the constitutive parameters to evolve after being subjected to different types of loading conditions. Optimization parameters identified after the initial excursions with limits of 0.0 and 0.015 m/m (R = 0) incorrectly identify the ratio of isotropic to kinematic hardening. The addition of fully reversed strain conditions provides enough data to distinguish between the two different hardening mechanisms of the plasticity model. The ratio of isotropic and kinematic hardening is easier to distinguish when the load excursions exhibit re-yielding upon reversal of loading. Overall, the optimized parameters are very close to the exact parameters after Test Block 2 is completed (fully reversed loading). In addition, all the convergence criteria for the method are met after a single iteration of the final test block.

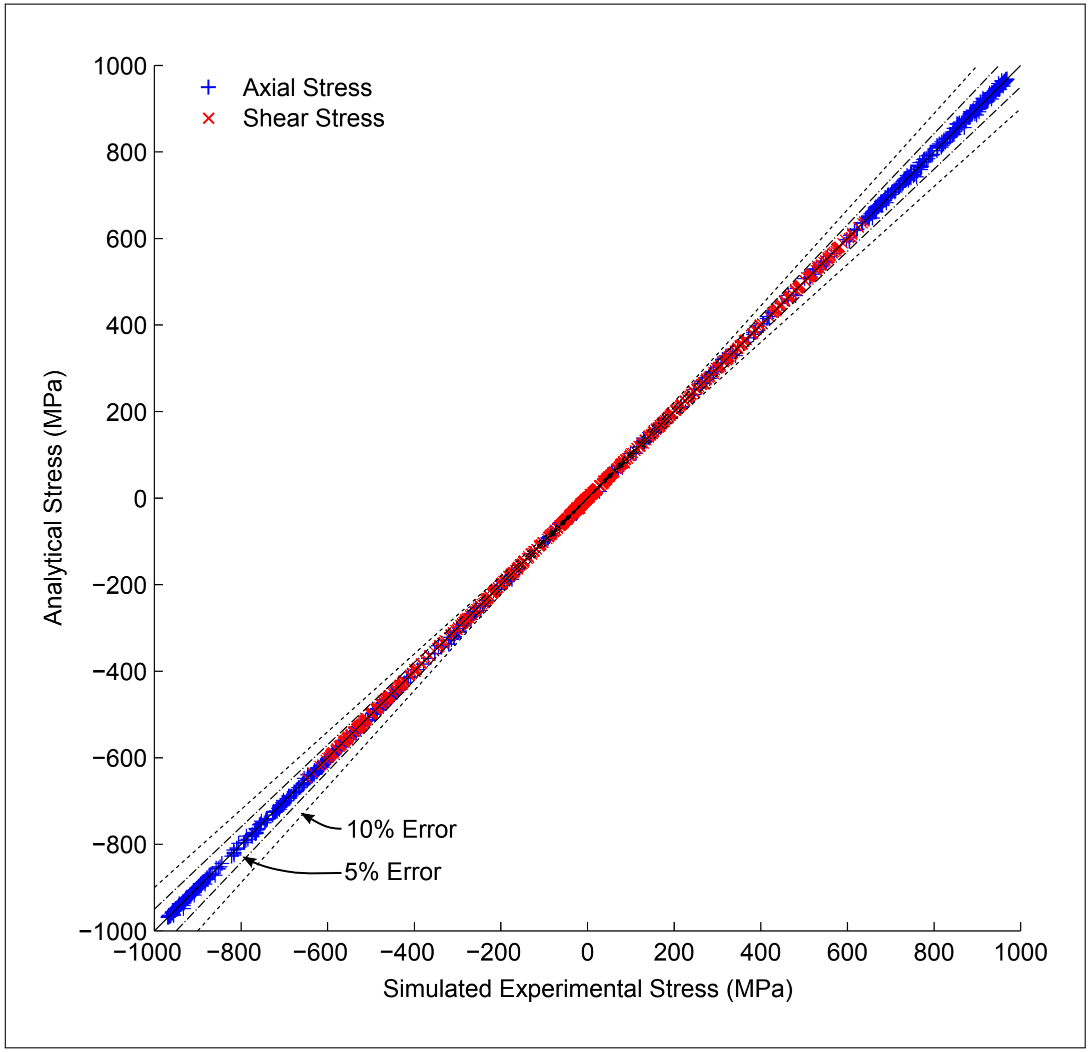

Figure 5.21: Simulated experimental stress and analytical stress using the final set of constitutive parameters for Eval. 3.

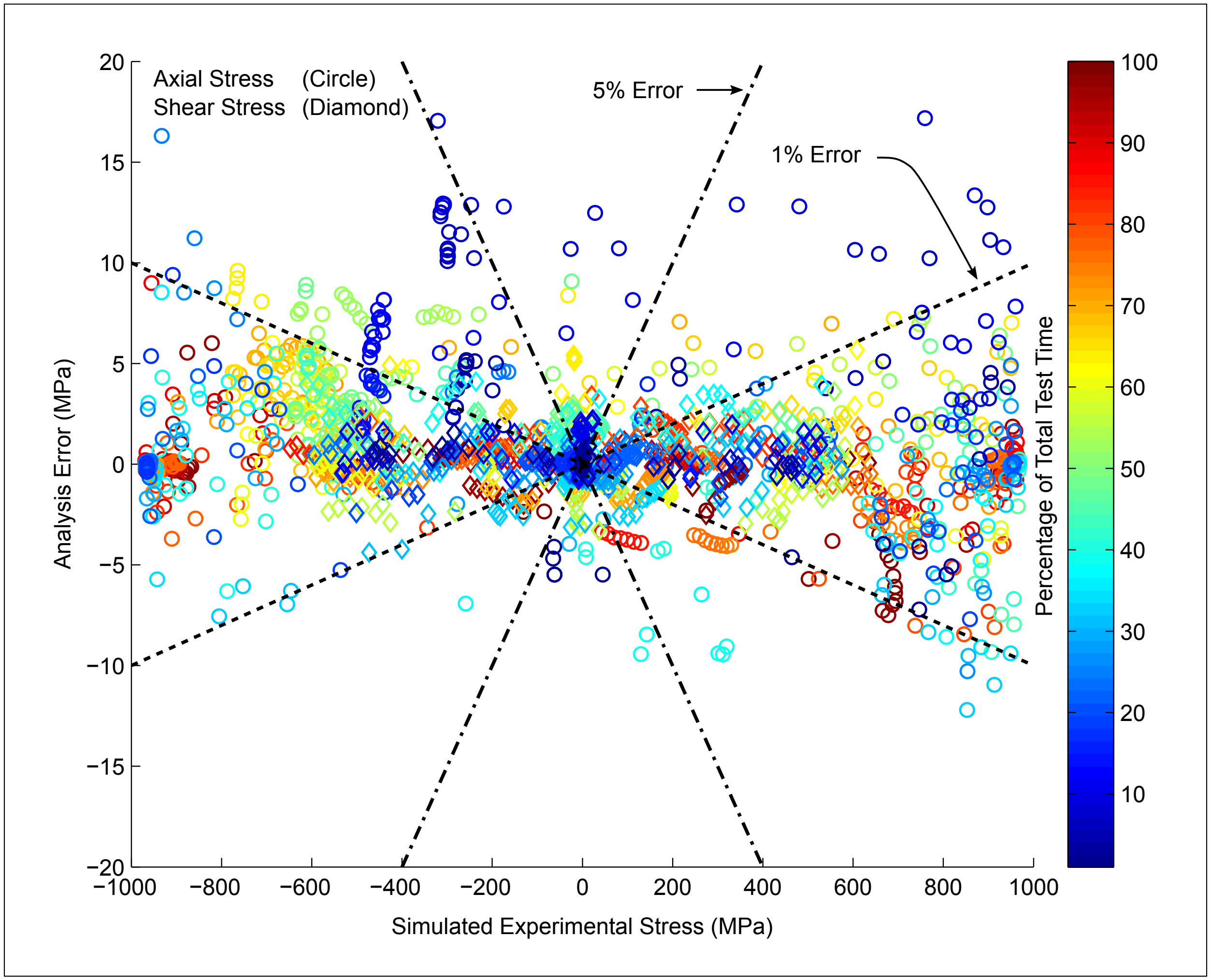

Figure 5.22: Analytical error using the final set of constitutive parameters for Eval. 3. Axial and shear stress are represented by circles and diamonds, respectively. The color bar indicates the sequential order of the data points.

Table 5.15: Convergence summary for Eval. 3.

		Objective Function (MPa)						Opt. Par.	Cal. Bin	Val. Bin
		Calibration			Validation			Max. Error	Min.	Min.
Block	Rnd	Pts	Max	Mean	Pts	Max	Mean	(%)	$\Delta\bar{\varepsilon}^p$	$\Delta\bar{\varepsilon}^p$
1	2	101	17.4	7.9	34	27	21	15.7	4.68E-06	1.29E-05
2	1	261	18	6.4	116	15.8	5.8	6000	1.67E-04	2.37E-04
3	2	544	15	5.2	62	15	6.9	100	7.45E-04	3.78E-04
4	1	715	15	5.2	139	10.8	2.6	0	9.48E-04	1.35E-03

Table 5.16: Number of points and CPU time required to complete each FEMU procedure in Eval. 3.

Block	Iter	Round	Points	Time (sec)
1	1	1	37	28
1	1	2	101	38
2	1	1	261	93
3	1	1	432	146
3	1	2	544	180
4	1	1	715	235

5.5 Conclusions

The integrated methodology and the associated software has been evaluated using simulated experimental data. This approach eliminates any model uncertainty and allows for the direct calculation of errors attributed solely to the methodology. The simulated experiments have been generated using the finite element code within the developed software. The viscoplasticity model with nonlinear combined kinematic and isotropic hardening has been used with "exact" constitutive parameters that are determined based on correlation to strain-controlled tension test data for Ti-6Al-4V. Three different evaluations have been performed. The first is a strain-controlled axial-torsional test with tension-torsion strains (R = 0). The second is a strain-controlled fully reversed axial-torsional test (equivalent to R = -1). Finally, the third evaluation utilizes alternating test blocks of R = 0 and R = -1.

The evaluations with negative R (Eval. 2 and 3) show the integrated approach can accurately and quickly calibrate and validate constitutive parameters for a modern plasticity model over multiaxial states of stress and strain. Evaluation 1 does not have compressive strain and fails to converge on the correct hardening parameters due to minimal re-yielding upon load reversal. Evaluation 1 also fails to meet all the method convergence criteria due to a lack of significant increase in plastic strain as the test progresses. A possible approach to improve the identification of isotropic and kinematic hardening is through the use of supplemental test data that exhibit significant re-yielding (negative R tests).

The fully reversed strain-controlled evaluations show excellent convergence for all metrics, including strain-space coverage. All convergence criteria are met quickly using the iterative methodology. The use of both R = 0 and R = -1 test blocks in Eval. 3 allows for accurate calibration over the two drastically different test conditions. However, the constitutive parameters do not converge on the correct values until after fully reversed loading is introduced into the specimen. Evaluation 3 provides a comprehensive demonstration of the success of the developed methodology and the associated software.

The new, novel test methodology has been proven successful in representative, simulated experiments and can now be applied to actual experiments. The following chapter documents the application of the integrated methodology to the real-time, autonomous identification of constitutive parameters for Ti-6Al-4V using a single test specimen for calibration and validation. Then Chapter VII documents validation of the autonomously identified constitutive parameters for additional multiaxial tests performed on Ti-6Al-4V.

CHAPTER VI

APPLICATION OF INTEGRATED MULTIAXIAL EXPERIMENTATION AND CONSTITUTIVE MODELING TO Ti-6Al-4V

The evaluation of the developed methodology using simulated experimental data (discussed in Chapter V) shows that calibration and validation of a modern plasticity model over multiaxial states of stress can be accomplished through the autonomous integration of experimentation and constitutive model fitting. Further demonstration of the integrated methodology using actual experiments would show both the feasibility and success of the new, novel methodology. However, many components must function properly and communicate seamlessly across different software and hardware platforms to obtain a calibrated and validated set of parameters. These issues do not appear in the simulated experiments during which the entire process is carried out in software. Furthermore, challenges can arise when the experimental behavior of a material deviates from the ideal depiction in the constitutive model, which is also not present in the simulated response from the previous chapter. As such, physical experiments have been conducted on Ti-6Al-4V to calibrate and validate a viscoplasticity model under multiaxial loading in real time to illustrate the success of the developed methodology and software.

Details pertaining to the specimen design and material pedigree are given in Section 6.1. Ti-6Al-4V is particularly challenging for a plasticity model as it exhibits softening under repeated strain-controlled cycling (room temperature creep). Issues with hardware limitations, strain non-uniformity, and plastic buckling are also addressed. Section 6.2 provides details on the viscoplasticity model used throughout the autonomous calibration and validation procedures. Section 6.3 describes the initial fitting that has been performed using supplemental test data from previous experiments on Ti-6Al-4V. The initial parameter fittings based on supplemental data are used throughout the optimization procedures during the autonomous multiaxial test process.

The configuration of the integrated experiment is outlined in Section 6.4, including details on the bounds of the test and the convergence criteria for the overall methodology. Results of the experiment are presented in Section 6.5. The overall success of the methodology is discussed in the summary in Section 6.6.

6.1 Specimen Design and Hardware Constraints

A solid cylindrical specimen made from Ti-6Al-4V was used for the autonomous, multiaxial, experiment. The material was forged to simulate fan blade and disk material for the compressor stage of gas turbine engines for commercial or military applications [103]. A description of the processing and resulting microstructure is provided in Appendix B.3. The specimen has been evaluated for both strain uniformity in the gage section and plastic buckling. A thorough description of the analysis can be found in Appendix B. Figure 6.1 shows the dimensions of the specimen. It has a gage diameter of 9.53 mm and a gage length of 44.0 mm.

The diameter of the specimen was chosen based on the limits of the axial/torsional load frame and the desired maximum stress. The load frame is rated for 100 kN of force and 1,110 N-m of torque. Table 6.1 shows the maximum attainable diameter for various ultimate stresses when the load and torque are limited to 90 kN and 990 N-m. It is common to only use 80 - 90 percent of the full capability of the load frame for stability and safety reasons. The diameter of 9.5 mm

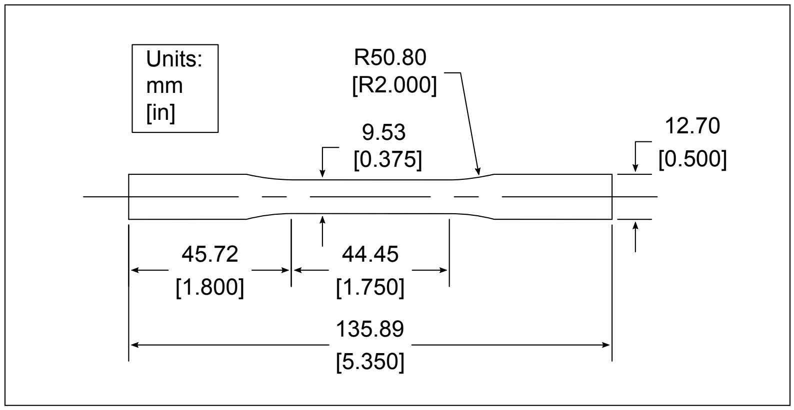

Figure 6.1: Specimen dimensions in mm [in.] for the solid cylindrical specimen used for tension-torsion strain conditions.

was chosen to allow for 1200 MPa of axial stress. While Ti-6Al-4V only has an ultimate stress of approximately 1000 MPa, other engine disk materials like nickel-based super alloys have higher strengths. A common specimen design is desired. The smaller diameter decreases the load required which in turn also lowers the required hydraulic grip pressure needed to prevent slippage under force and torque. Thick- or thin-walled tubular specimens could be utilized to allow for higher ultimate stresses; however, axial and torsional buckling become a concern. The cost to machine tubular specimens is also much higher than that of solid cylindrical specimens.

The specimen gage length is dictated by the strain measurement instrumentation, strain non-uniformity, and plastic buckling. A MTS high-temperature axial-torsional extensometer is used for measuring axial and shear strain. The extensometer has a nominal gage length of 25.0 mm; therefore the gage length of the specimen must be long enough to ensure uniform strain over the extensometer gage length. The error in strain over a length of 27 mm compared to the strain at the center of the gage length is 1 percent or less for this specimen. Details on the strain error analysis are given in Appendix B.2.

Table 6.1: Maximum specimen diameter based on load/torque and desired ultimate axial/shear stress.

Axial 90 kN		Shear 990 N-m	
Stress (MPa)	Max Dia. (mm)	Stress (MPa)	Max Dia. (mm)
1000	10.70	1000	17.15
1100	10.21	1100	16.61
1200	9.77	1200	16.14
1300	9.39	1300	15.71
1400	9.05	1400	15.33

The length to diameter ratio for the specimen is L/D = 44/9.5 = 4.63 which is quite high for compressive loading. The plastic buckling analysis discussed in detail in Appendix B.1 shows buckling may occur at the onset of plasticity under compressive load. The combination of plasticity, geometric imperfections in the specimen, and minor load frame misalignment require limitations on the testing domain due to risk of plastic buckling. Compressive stress should be limited, and the compressive tangent modulus should remain very close to the elastic modulus to prevent reduction in stiffness which accelerates buckling.

The specimen design is not ideal because it does not allow for fully reversed loading which highlights the ratio of isotropic and kinematic hardening as seen in Bauschinger's effect. Shorter gage length specimens have been evaluated using strain gages for strain measurement; however, the strain gages are not rated for repeated cycles at strain levels at or above 0.01 m/m. Fully reversed loading could be obtained for larger diameter specimens; however, this requires a larger load frame which is not available at the time of this work. Shorter gage lengths would require the use of alternate strain measurement techniques like digital image correlation (DIC). However, there are non-trivial issues with DIC that would need to be overcome - namely real-time output of axial and shear strain, and measurement of strains on highly curved surfaces that rotate approximately 10 - 15 degrees. Thus, the selected specimen is a compromise that allows for demonstration of the autonomous methodology under multiaxial loading, but restricts the feasible test domain.

6.2 Constitutive Model

The rate-dependent viscoplasticity model presented in Section 5.1 has been selected to represent the behavior of Ti-6Al-4V. The governing equations for the constitutive model were given in Eq. (5.1) through (5.8). Appendix C provides a thorough discussion of the chosen model and addresses the influence of each constitutive parameter. The parameters were given in Table 5.1 with the alternate parameters provided in Table 5.2.

The elastic behavior is dictated by Young's modulus, E, and Poisson's ratio, ν. Rate-dependence is captured through parameters D and n, while the initial yield surface size is ρ_0. Each hardening term adds two parameters, ($Q^{(y)}$,$b^{(y)}$) for isotropic hardening and ($A^{(w)}$, $B^{(w)}$) for kinematic hardening. Multiple hardening terms can be used for both isotropic hardening and kinematic hardening to refine the material behavior. Two isotropic and three kinematic terms are used to define the hardening for this work, thus requiring a total of 15 parameters for the constitutive model. The simulated experiments from the previous chapter only used one isotropic term; however, a second isotropic term has been added to allow for a possible decrease in the yield surface size with increasing plastic strain.

The elastic parameters, E and ν, are identified during the modulus check that is performed on the test specimen prior to the start of the autonomous testing process. The axial modulus, E, comes from axial cycling while the shear modulus, G, comes from torsional cycling. Poisson's ratio, ν, is derived from the moduli as $\nu = E/\left(2G\right) - 1$.

For the current work, the rate-dependent parameters (D, n) and the yield parameter (ρ_0) are defined prior to the start of the autonomous process using supplemental material data from previous uniaxial tests. Further discussion and specification of the rate and yield parameters for Ti-6Al-4V follow in the next section. In future work, these parameters could be fit and validated within I^{2}MATE. However, they have been predefined to reduce the complexity of the parameter identification process.

The hardening parameters for both isotropic and kinematic hardening are fit and validated during the autonomous, multiaxial testing. These parameters define the evolution of plasticity in the material and account for hardening (or softening) with increasing plastic strain. The hardening terms define the bulk of the nonlinear region on the stress-strain curves. In their current form, most of the hardening parameters are hard to relate to typical testing or to stress-strain relationships. They also cause difficulty for convergence during optimization due to their interactions. To overcome these issues, alternate relationships for the hardening parameters have been defined and are used through the parameter identification procedure.

Table 5.2 provided a summary of the alternate forms of certain hardening parameters. The Q and A/B terms are saturation values which represent the maximum hardening (or softening) of the stress for isotropic and kinematic hardening, respectively. The $5/b$ and $5/B$ terms are rapidity coefficients which dictate how fast the hardening occurs in terms of accumulated equivalent plastic strain. In their alternate relationships, the values of the rapidity coefficients are approximately equal to the equivalent plastic strain at which the hardening is saturated to 99 percent of the maximum. In relation to a stress-strain curve for a tension tests, the rapidity indicates the plastic strain at which the hardening is done acting. For further details, and derivation of the alternate parameters, see Appendix C.

6.3 Supplemental Material Test Data

Data from previous tests performed on the same material can be used to improve the optimization methods that are critical to parameter identification for non-linear material models. Optimization methods utilize either one or more initial starting points, or seed points, which consist of initial values for the variables used in the optimization. As starting points get closer to local minima, the efficiency of the optimization method typically increases, which decreases the computation time. Also, supplemental material data can be used to predefine certain parameters in the constitutive model to decrease the number of variables involved in the optimization.

For this work, four axial tests performed on Ti-6Al-4V specimens are used as supplement data to predefine parameters and provide initial starting points for the optimization method employed by the FEMU process. Figure 6.2 shows three tension tests conducted at different strain rates that are used to predefine the rate-dependent parameters of the model (D, n) and the yield parameter (ρ_0). Figure 6.3 illustrates a uniaxial strain-controlled (rate of 1×10^{-3} m/m/s) fully reversed cyclic test with strain loops of various magnitudes. Initial seeds for the optimization procedure have been identified using the tension data and the uniaxial cyclic test. The incorporation of the cyclic data should improve the identification of the isotropic and kinematic hardening terms that are difficult to determine when fully reversed loading cannot be completed, like in this experiment. Complete details of the process for calculating the predefined parameters and generating the initial seeds for the hardening parameters are provided in Appendix C.2.

Table 6.2 lists the predefined values and gives the minimum and maximum bounds for the hardening parameters used throughout the parameter identification process. The elastic coefficients in Table 6.2 are the initial estimates used during the identification of seed points for the hardening parameters. The actual elastic constants are found using pre-test modulus checks, which are addressed in Section 6.5.1. The steps taken to predefine parameters and identify seeds for the optimization

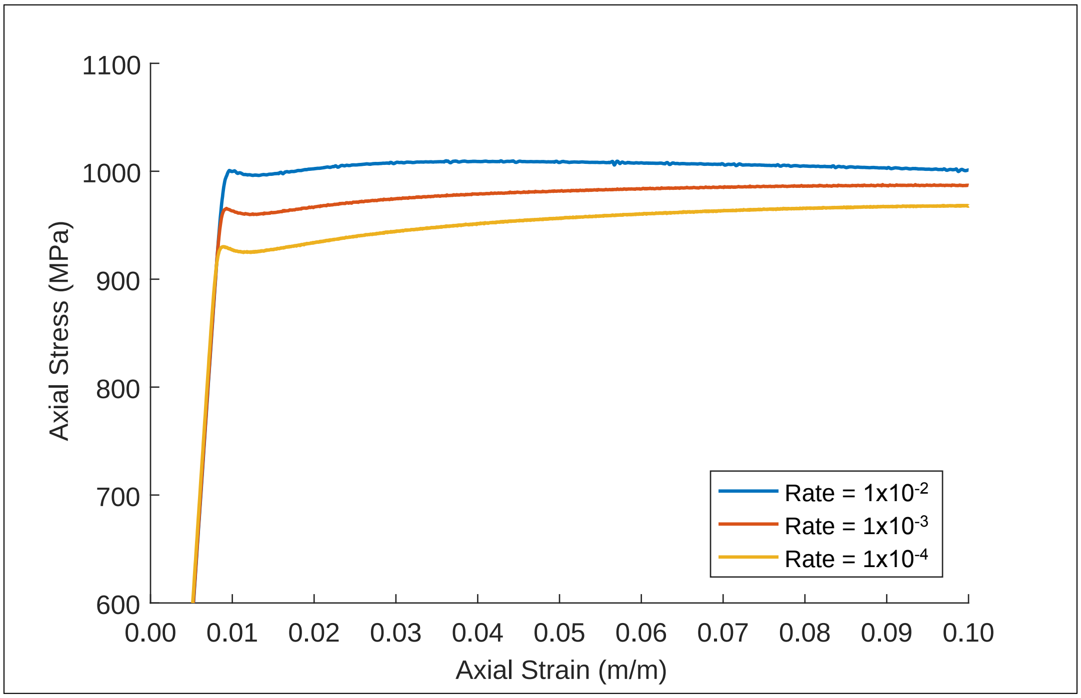

Figure 6.2: Strain-controlled tension tests for Ti-6Al-4V at rates of 1×10^{-2}, 1×10^{-3}, and 1×10^{-4} m/m/s.

method are not requirements of the developed methodology, but they will typically decrease the time required and improve the accuracy of the integrated parameter identification experiment. Table 6.3 lists the five sets of parameters that are used as starting points in the parameter identification process during the autonomous experiment.

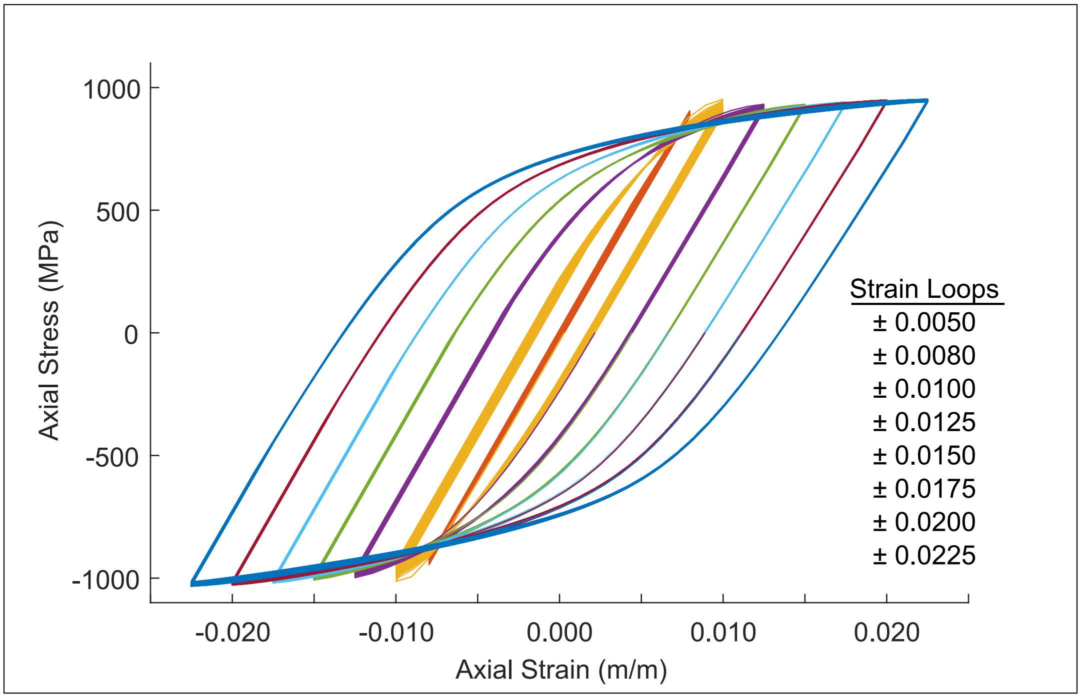

Figure 6.3: Experimental results for Ti-6Al-4V strain-controlled (rate of 1×10^{-3} m/m/s), fully-reversed loading with increasing magnitude strain loops. Condensed data is shown at intervals of 1×10^{-3} m/m.

Table 6.2: Predefined parameter values, optimization parameters, and minimum and maximum allowable values used for initial fitting based on supplemental data.

Parameter	Value	Min	Max	Units
Elastic				
E	116,000	-	-	MPa
G	44,275	-	-	MPa
ν	0.31	-	-	-
Rate Dependent				
D	371	-	-	MPa
n	15.5	-	-	-
Yield				
ρ_0	430	-	-	MPa
Isotropic Hardening				
Q_1	-	5	750	MPa
$5/b_1$	-	1.00E-04	1.00E-01	-
Q_2	-	-500	0	MPa
$5/b_2$	-	1.00E-01	1.00E+01	-
Kinematic Hardening				
A_1/B_1	-	5	750	MPa
$5/B_1$	-	1.00E-04	1.00E-01	-
A_2/B_2	-	5	750	MPa
$5/B_2$	-	1.00E-04	1.00E-01	-
A_3	-	0	2000	MPa
B_3	0	-	-	-

Table 6.3: Parameter sets and objective function values for the five selected, representative cases. The objective function is computed for the tension test at 1×10^{-4} m/m/s and the cyclic strain-controlled loops of 0.0150 m/m and below.

		Q_1	$5/b_1$	Q_2	$5/b_2$	A_1/B_1	$5/B_1$	A_2/B_2	$5/B_2$	A_3	
MIN		5.0	1.00E-04	-500.0	1.00E-01	5.0	1.00E-04	5.0	1.00E-04	0.0	
MAX		750.0	1.00E-01	0.0	1.00E+00	750.0	1.00E-01	750.0	1.00E-01	2000.0	
RANK	ID	Q_1	$5/b_1$	Q_2	$5/b_2$	A_1/B_1	$5/B_1$	A_2/B_2	$5/B_2$	A_3	FIT
1	99	5.0	2.85E-04	-55.7	1.00E+00	65.2	2.11E-03	281.3	1.40E-02	0.0	3741
2	63	6.8	1.00E-01	-64.7	1.00E+00	308.8	1.25E-02	34.0	6.91E-03	0.0	3815
9	38	8.1	1.00E-01	-68.4	1.00E+00	67.2	9.90E-05	291.7	1.37E-02	0.0	4174
13	81	5.0	9.71E-02	-84.0	7.75E-01	107.2	9.90E-05	218.1	9.17E-03	401.1	5248
14	41	5.0	3.25E-02	-41.0	4.64E-01	71.2	4.32E-02	272.7	4.68E-03	106.0	5281

6.4 Configuration of Experiment

The experiment has been designed within the limits of hardware and instrumentation available at the time of this work. Considerations discussed in Section 6.1 limit the choice of specimen design and test domain. These are solely due to the equipment available; however, larger machines and bigger forgings could be procured that would allow for different ranges of testing. These limitations arise from temporary issues and not from a presence of inherent flaws in the methodology.

The methodology has been evaluated using a single multiaxial, strain-controlled test. Bounds of the test are described in Section 5.3.1. The convergence criteria for the methodology are discussed in Section 5.3.2. Lastly, Section 5.3.4 presents the setup of the FEMU, including settings used for the required optimization procedure.

6.4.1 Test Bounds

Details regarding the configurable options for a test have been described earlier in Section 4.3. The two fundamental aspects defining the test bounds are the strain magnitude and the angular position in the axial-shear strain space. Strain magnitude, ε_{mag}, and the angular position, θ, are

$$\varepsilon_{mag} = \sqrt{\varepsilon^2 + \gamma^2} \tag{6.1}$$

$$\theta = \tan^{-1}\left(\frac{\gamma}{\varepsilon}\right) \tag{6.2}$$

where ε is engineering axial strain and γ is engineering shear strain.

The current experiment on Ti-6Al-4V is conducted within the tensile side of the axial-shear strain space to eliminate the occurrence of plastic buckling. Therefore, the angular position is limited to $\pm$ 90 degrees. Figure 6.4 shows the bounds with black lines representing the angular bins that are used for both the calibration and validation load excursions. Angular bins are 30 degrees

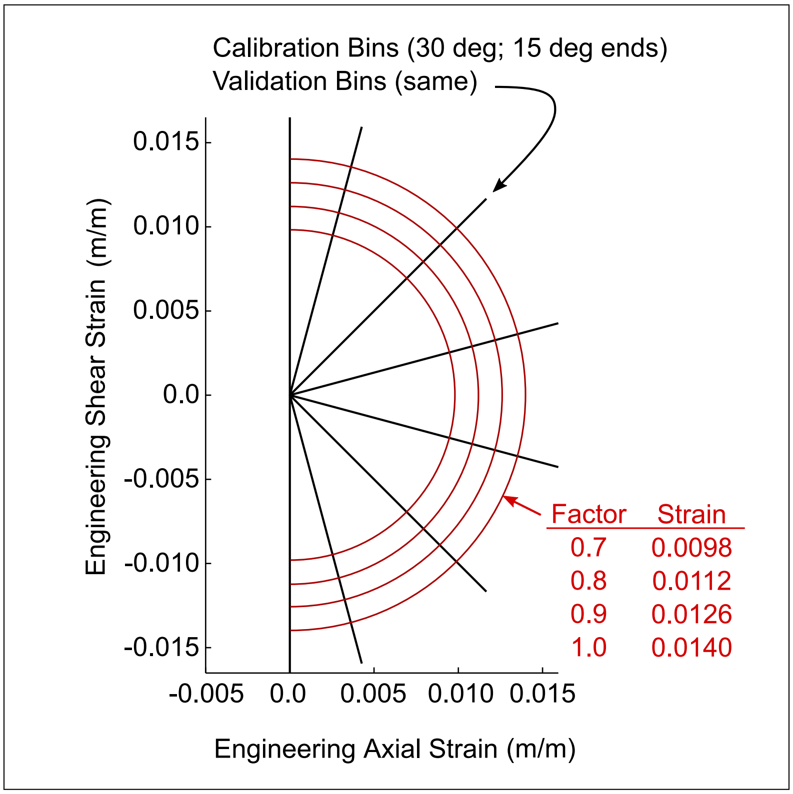

Figure 6.4: Test bounds used for autonomous multiaxial experiment on Ti-6Al-4V. Black lines indicate angular bins while the red lines show the increasing levels of strain.

wide with 15 degree bins at the ends. The red arcs in Fig. 6.4 identify the different levels of strain using during the test blocks.

Two separate test blocks are utilized. Both have a maximum strain magnitude of 0.014 m/m. Test Block 1 has three rounds of increasing strain magnitudes of 0.7, 0.8, and 0.9 times the maximum strain magnitude, or 0.0098, 0.0112, and 0.0126 m/m. During each round (different strain magnitude) calibration excursions are conducted in each angular bin only once prior to the FEMU procedure. Subsequent validation excursions are also only performed once within each angular bin. Very little insight is expected from performing repeated excursions into each bin, unless the overall strain level is increased first as is done in subsequent rounds. Test Block 1 is only conducted a single time, because repetition would lead to primarily elastic behavior until the strain magnitude is increased. Test Block 2 has a single round at the maximum strain magnitude, 0.014 m/m, and up to two excursions can be performed within each angular bin during both the calibration and validation excursions. Test Block 2 can be repeated up to ten times if necessary to satisfy the methodology convergence criteria. For this work, the limit of ten iterations is chosen to prevent the autonomous test from running indefinitely if convergence of all criteria does not happen. Possible causes of non-convergence are inadequate constitutive model choices, limiting test bounds, etc. and further repetition with the current setting likely will not produce better results. Future efforts could include checks for non-convergence and alter the test plan accordingly.

The multiaxial experiment was conducted using pseudo-strain control with axial and shear strain obtained from the extensometer. The target strain rate for the strain magnitude given by Eq. (6.1) was 5×10^{-4} m/m/s.

6.4.2 Convergence Criteria

The current convergence criteria focus on the objective function, the approximate relative error for successive best estimates of the constitutive parameters from FEMU, and coverage of the multiaxial domain. The objective function used during FEMU is again used to compute the maximum and the mean error at each condensed experimental data point. Error limits for Test Block 2 are 75 MPa maximum error and a mean error less than 25 MPa. The approximate relative error for the constitutive parameters must converge to below 10 percent.

Load trajectories are randomly determined within each angular bin. For Test Block 2, each angular bin must obtain a minimum total increment of equivalent plastic strain of 0.0002 m/m during the calibration process. The requirement for validation has also been set to 0.0002 m/m. A maximum of 2 load excursions per angular bin can be conducted during an iteration to ensure the process does not repeat indefinitely for test conditions that will not induce enough plastic strain. The requirements for equivalent plastic strain are quite low; however, they are large enough to ensure that some plasticity occurs because elastic loading excursions are not as useful during the plasticity model fitting process.

6.4.3 FEMU Settings

The axial and shear stress-strain data from the experiment is filtered and condensed to decrease the total number of load steps that are used in the FEMU process. A complete description of the filter and the data condensing procedures are given in Appendix A. The experimental data are processed using a finite impulse response 100th order 5 Hz low-pass filter and then condensed. The data is condensed using a nonlinear strain increment of 1×10^{-3}, an end tolerance of 1×10^{-6}, an increment tolerance of 5×10^{-5}, an averaging increment of 1×10^{-4}, and a nonlinear stress tolerance of 10 MPa. These settings produce points at the ends of the elastic region and points every 1×10^{-3} m/m in nonlinear stress-strain regions.

The same optimization settings have been used for all of the FEMU procedures. As mentioned earlier, only the hardening terms have been optimized. Elastic parameters are identified during the initial modulus checks for the specimen, and all other parameters of the viscoplasticity model are predefined based on supplemental data. The values of these predefined parameters can be found in Table 6.2. Two isotropic pairs and three kinematic hardening pairs are used leading to nine total optimization variables as one of the kinematic pairs is assumed linear with the recovery term set to zero. Particle swarm optimization (PSO) is used with 10 particles, and 10 rounds. A detailed description of the settings available for PSO is given in Appendix D.2. Parameter values are scaled between 0 and 1 based on the given minimum and maximum values. The cognitive, social, and pheromone coefficients are assumed constant through the rounds and are 0.25, 1.25, and 0.0, respectively. An inertia weight of 0.25 is used, and velocity clamping is used with a maximum velocity of 0.20 for any particle.

Five of the ten initial particles (parameter sets) for each FEMU procedure come from the initial fitting that has been performed on the supplemental data. The remaining five are initially randomized using Latin hypercube sampling. The best set of parameters from one FEMU is carried over to the subsequent FEMU procedure as an initial seed, thus making six of the ten predetermined. While this does provide some limitation as only four particles are randomized, the restricted nature allows for the incorporation of information from the supplemental data without having to perform finite element analyses for the supplemental data.

6.5 Experimental Results

This section discusses the experimental and analytical results from the autonomous integrated multiaxial test procedure defined in the preceding sections. Section 6.5.1 shows the results for the autonomous portion of the test. Upon completion of the autonomous experiment, the specimen was subjected to additional excursions prior to removal. These excursions are used for validation outside the range of test conditions used in the autonomous test. Section 6.5.2 compares the final validation excursions and analytical predictions made using the best set of hardening parameters identified in the autonomous test.

6.5.1 Autonomous Test

Initial autonomous modulus checks were performed prior to the start of the autonomous test. Four separate checks were conducted at 0.1 Hz for five cycles in both the axial-only and shear-only directions. The checks were performed under load control for von Mises equivalent stresses of 75 MPa. Axial cycles were performed between 0 and 75 MPa, while shear cycles were between $\pm$ 75/$\sqrt{3}$ $=$ 43.3 MPa. Table 6.4 shows the modulus predictions for both the extensometer and the strain gages. Zero-load offsets for the extensometer and the strain gages were also computed during the modulus check, along with the extensometer strain vs. stroke (rotation) slopes required for the pseudo-strain control method. The modulus values from the extensometer for the final check (E=116,726 MPa, G=44,818 MPa) are used throughout the constitutive model fitting process.

The initial seeding of the FEMU procedures was discussed in Section 6.3. Details on the viscoplasticity model and the required constitutive parameters were discussed in Section 6.2. Table 6.5 provides a summary of the constitutive parameters that are held fixed throughout the FEMU procedures and those that are part of the identification process. Again, only the hardening parameters are calibrated and validated through the autonomous testing process.

Table 6.4: Modulus values for checks performed prior to the start of autonomous testing.

Iteration	Device	E (MPa)	G (MPa)	ν
1	Ext.	116,696	44,815	0.302
1	Gage	117,954	44,107	0.337
2	Ext.	116,709	44,826	0.302
2	Gage	118,041	44,140	0.337
3	Ext.	116,688	44,822	0.302
3	Gage	118,039	44,134	0.337
**4*	*Ext.*	*116,726*	*44,818*	*0.302*
4	Gage	118,094	44,127	0.338

* - Modulus values used in subsequent test

The condensed strain history for the entire autonomous test is shown in Fig. 6.5 on an axial versus shear strain plot. All strain measurements shown in this results section are from the extensometer and have been condensed. Figure 6.6 shows only those points from Test Block 1. Figure 6.7 displays the condensed data for axial versus shear stress for the entire history while Fig. 6.8 shows just Test Block 1. Figure 6.9 and 6.11 show the engineering stress vs. strain for the axial and shear components, respectively. Figure 6.10 and 6.12 show the same information but only for Test Block 1.

The sparsity of condensed points on the strain vs. strain plots between -75 to -45 degrees and 45 to 75 degrees indicate the behavior in these regions is mostly linear and not of interest during the fitting process. The engineering stress vs. stress plots show symmetry in the shear stress limits ($\pm$600 MPa) while the axial stresses range between approximately -600 and 1,000 MPa. The stress vs. strain plots indicate that the axial contribution to the plastic strain is substantially larger than the shear component. All these results are consistent with the outcomes from the simulated evaluation from Section 5.4.1 where no compressive strain is allowed.

The evolution of the hardening parameters identified during FEMU is shown in Table 6.6. The final set of constitutive parameters identified using the integrated methodology is given in Table 6.7. The autonomous process stopped after the tenth iterations of Test Block 2 because the mean and maximum values for the objective function were still above the convergence criteria. The objective function computes the difference between experimental stresses and stresses predicted using the identified constitutive parameters. Further iterations for Test Block 2 likely would not likely decrease the objective function values below the convergence criteria until the constitutive model or test parameters are changed. As mentioned earlier, future work can focus on test redirection when non-convergence occurs. Figure 6.13 shows the analytical stress (using the best parameters in Table 6.7) compared with the corresponding experimental stresses. Figure 6.14 shows the same results but plots the error vs. experimental stress, where error is defined as experimental stress minus analytical stress.

Table 6.5: Predefined model parameters, optimization parameters, and minimum and maximum allowable values used during the autonomous process.

Parameter	Value	Min	Max	Units
Elastic				
E	116,726	-	-	MPa
G	44,818	-	-	MPa
ν	0.302	-	-	-
Rate Dependent				
D	371	-	-	MPa
n	15.5	-	-	-
Yield				
ρ_0	430	-	-	MPa
Isotropic Hardening				
Q_1	-	0	750	MPa
$5/b_1$	-	9.50E-05	1.00E-01	-
Q_2	-	-500	0	MPa
$5/b_2$	-	1.00E-01	1.00E+01	-
Kinematic Hardening				
A_1/B_1	-	0	750	MPa
$5/B_1$	-	9.50E-05	1.00E-01	-
A_2/B_2	-	0	750	MPa
$5/B_2$	-	9.50E-05	1.00E-01	-
A_3	-	0	2000	MPa
B_3	0	-	-	-

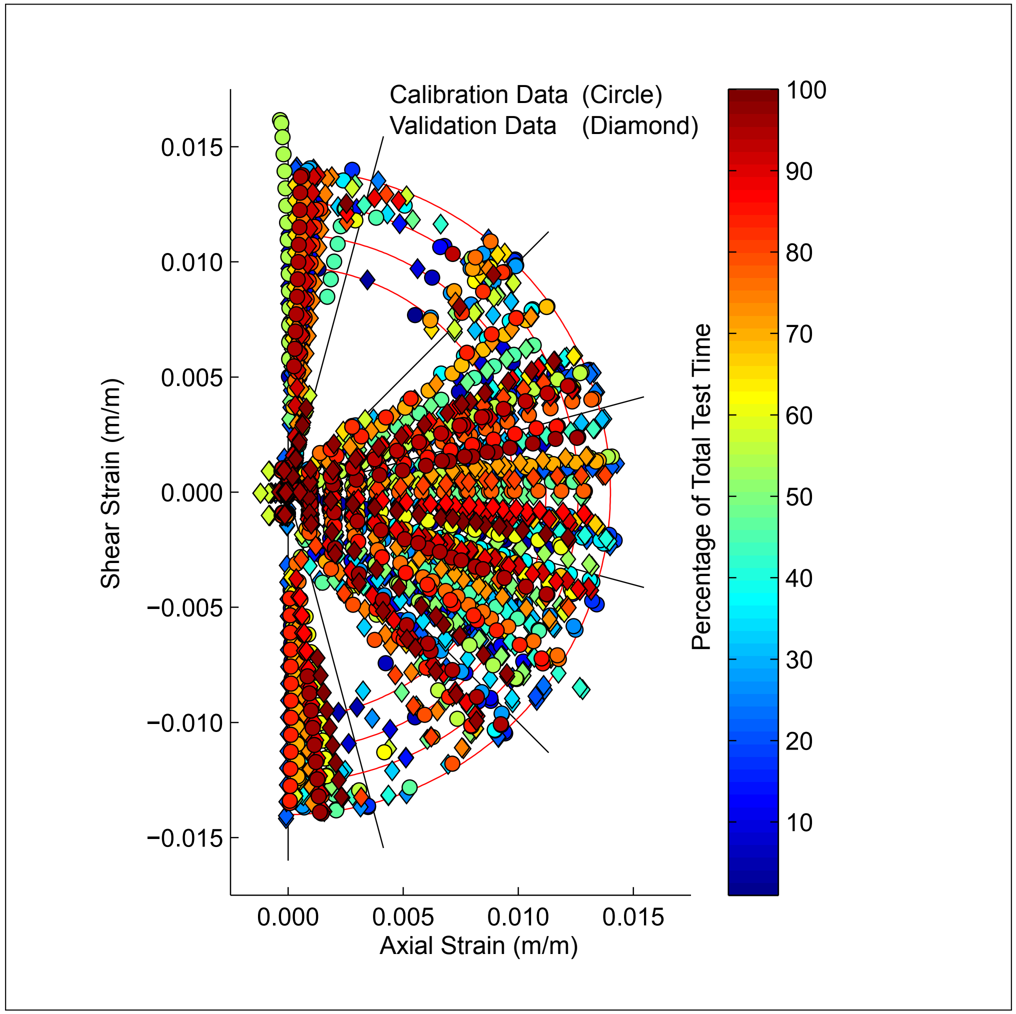

Figure 6.5: Condensed data points for shear strain vs. axial strain for the entire autonomous test. The data from calibration and validation load excursions are shown as circles and diamonds, respectively.

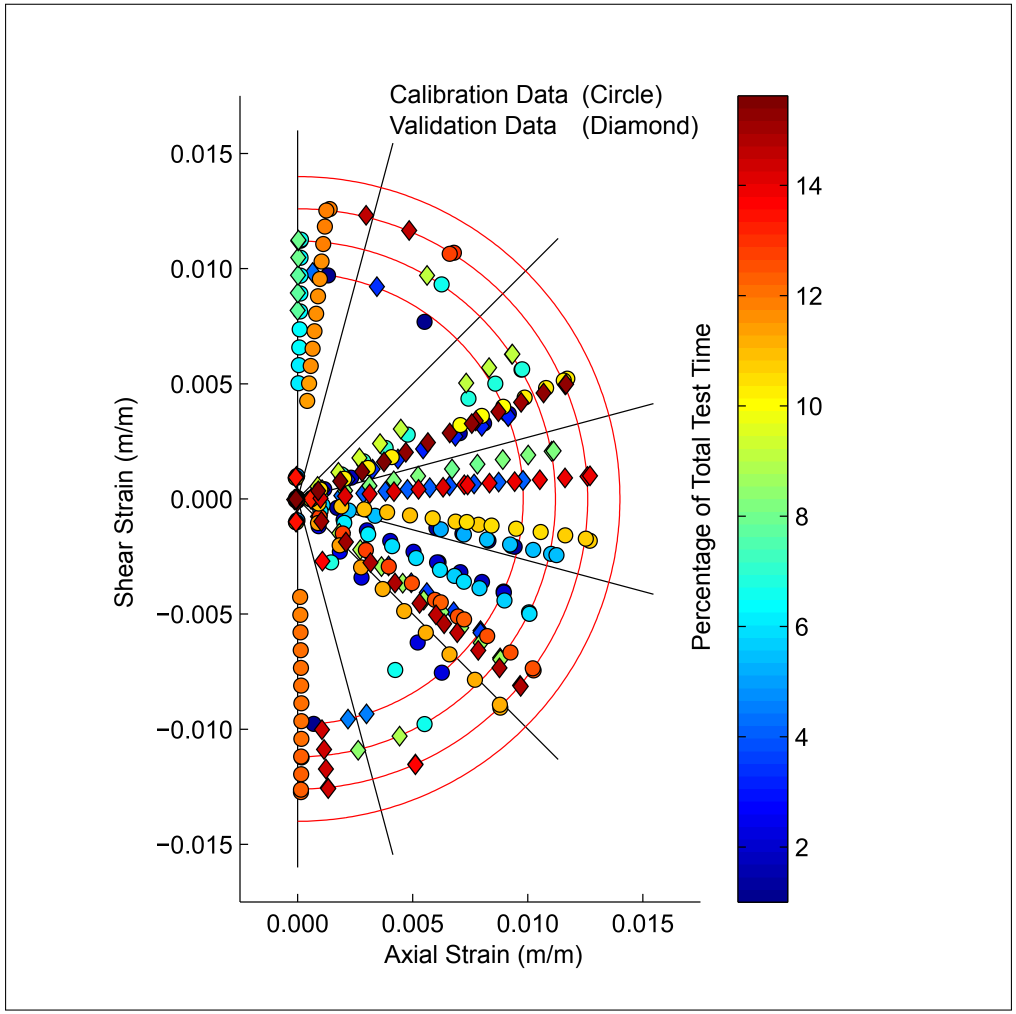

Figure 6.6: Condensed data points for shear strain vs. axial strain for only Test Block 1. The data from calibration and validation load excursions are shown as circles and diamonds, respectively.

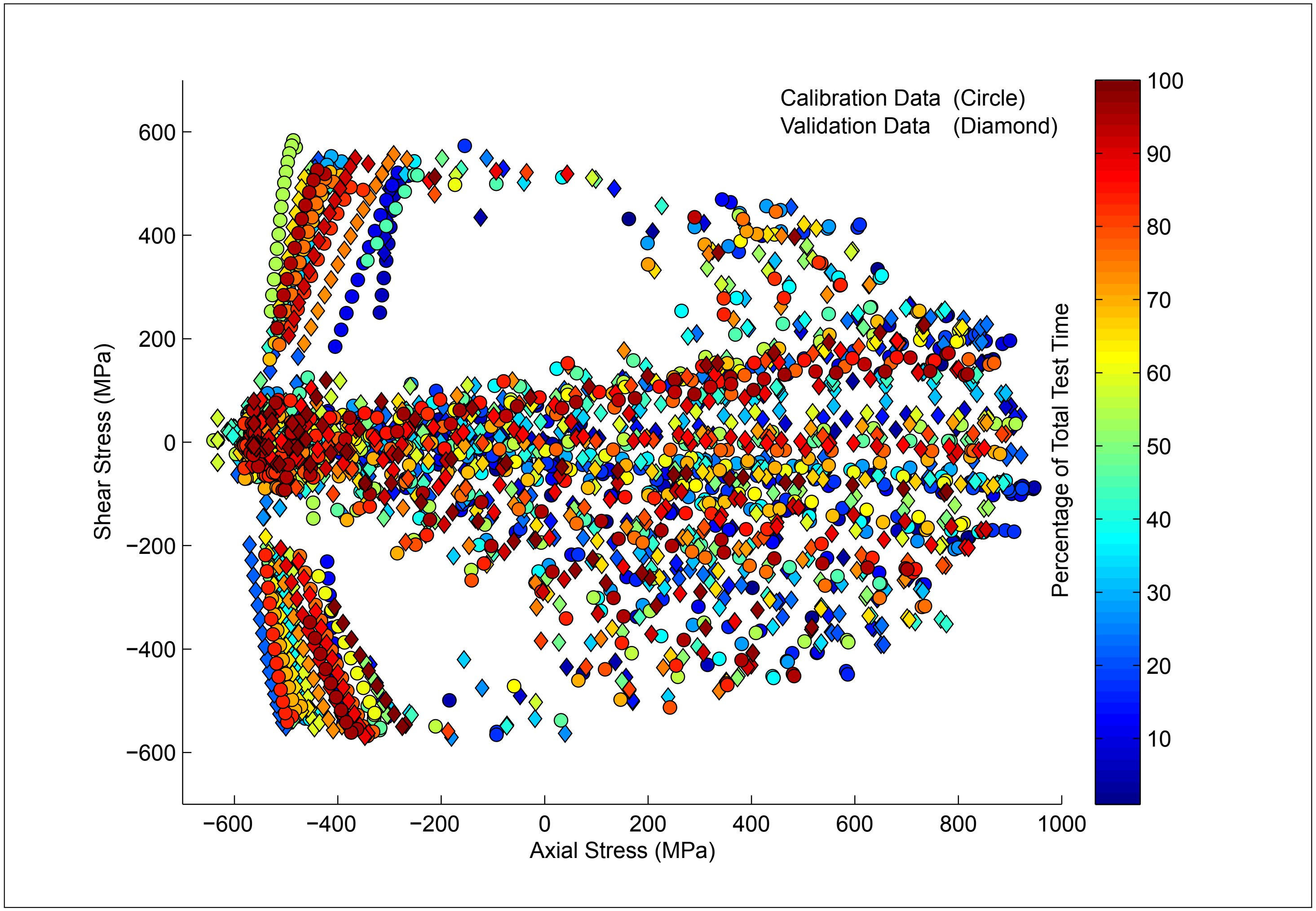

Figure 6.7: Condensed data points for shear stress vs. axial stress for the entire autonomous test. The data from calibration and validation load excursions are shown as circles and diamonds, respectively.

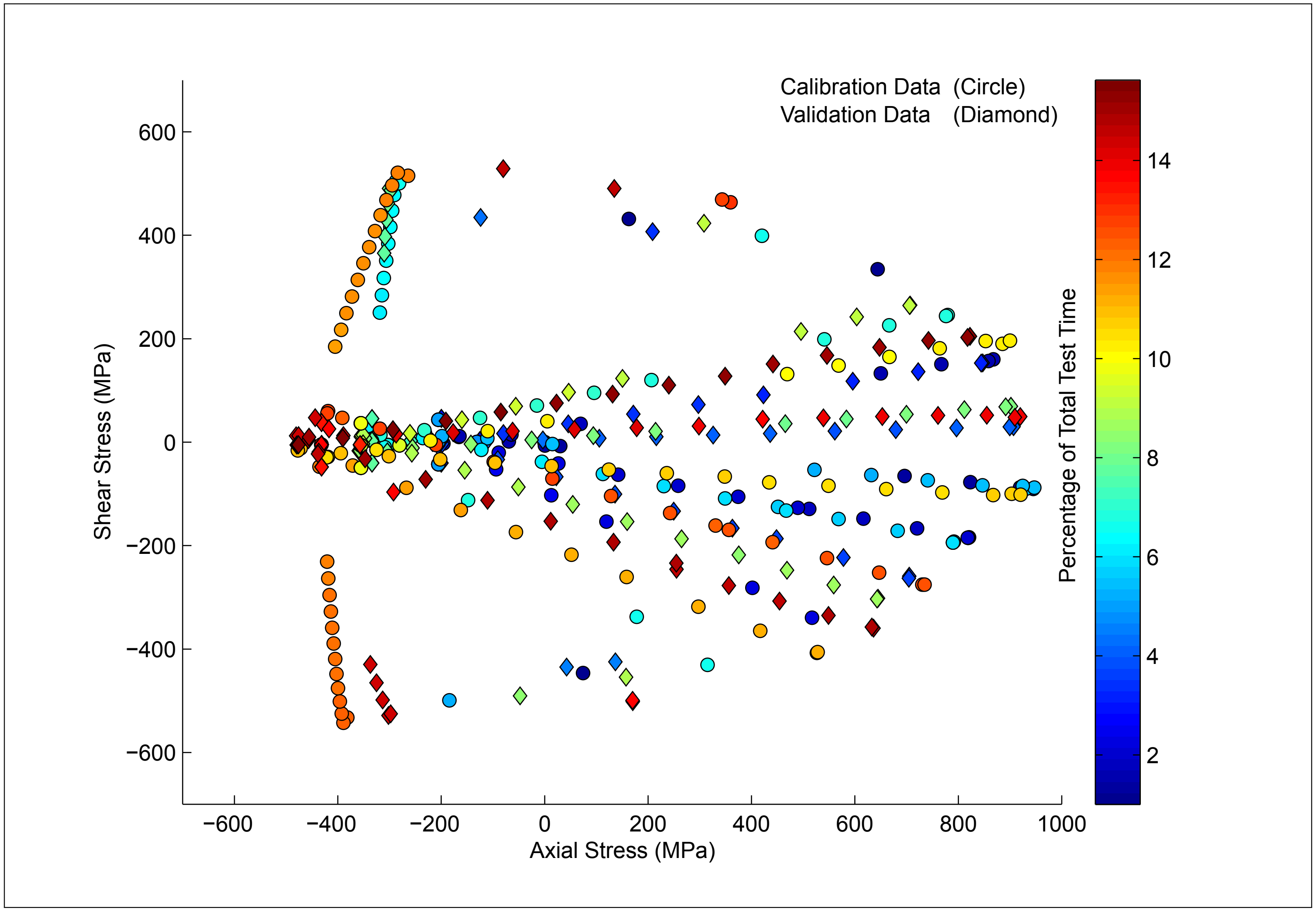

Figure 6.8: Condensed data points for shear stress vs. axial stress for only Test Block 1. The data from calibration and validation load excursions are shown as circles and diamonds, respectively.

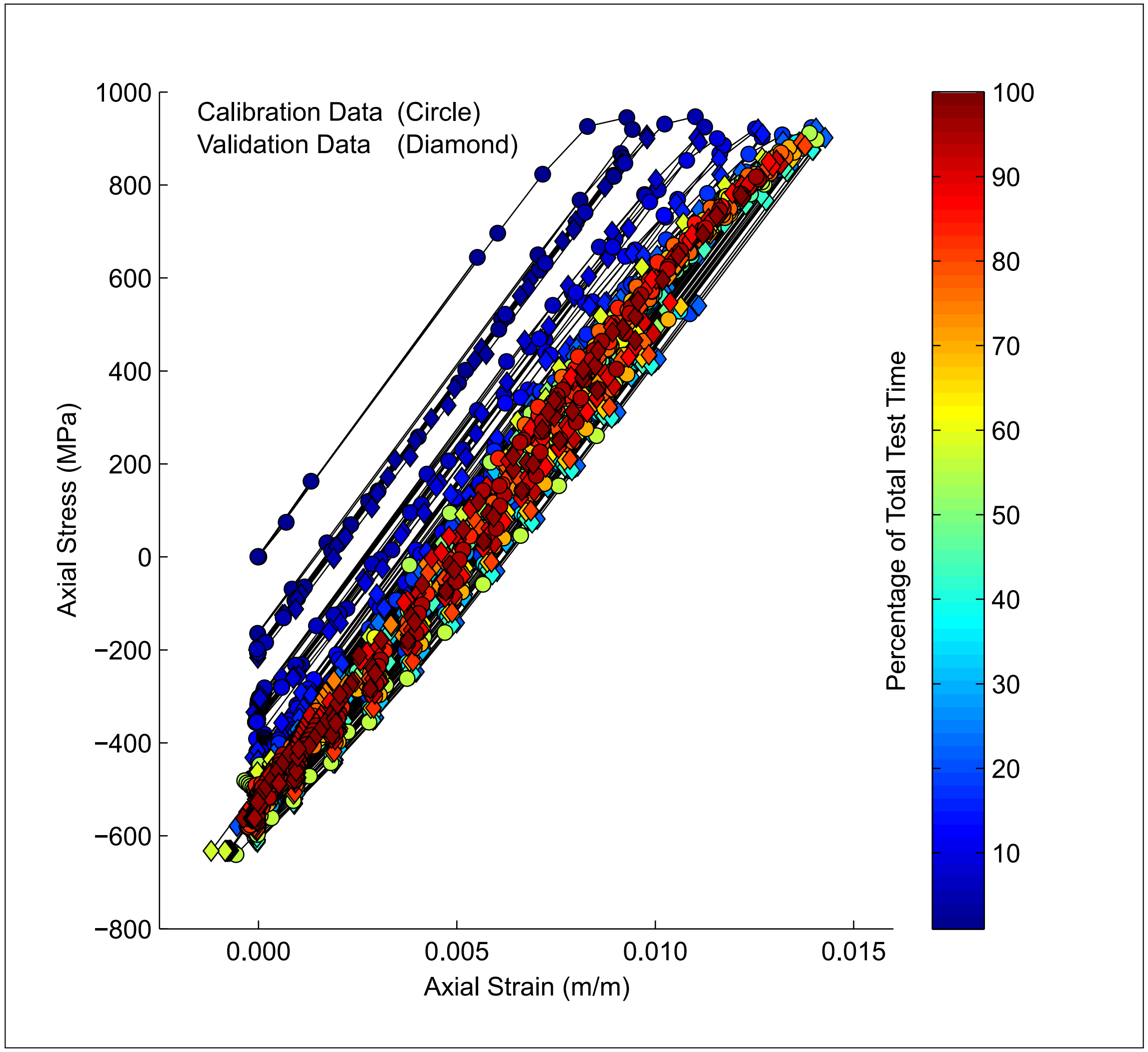

Figure 6.9: Axial stress vs. strain for the entire autonomous test.

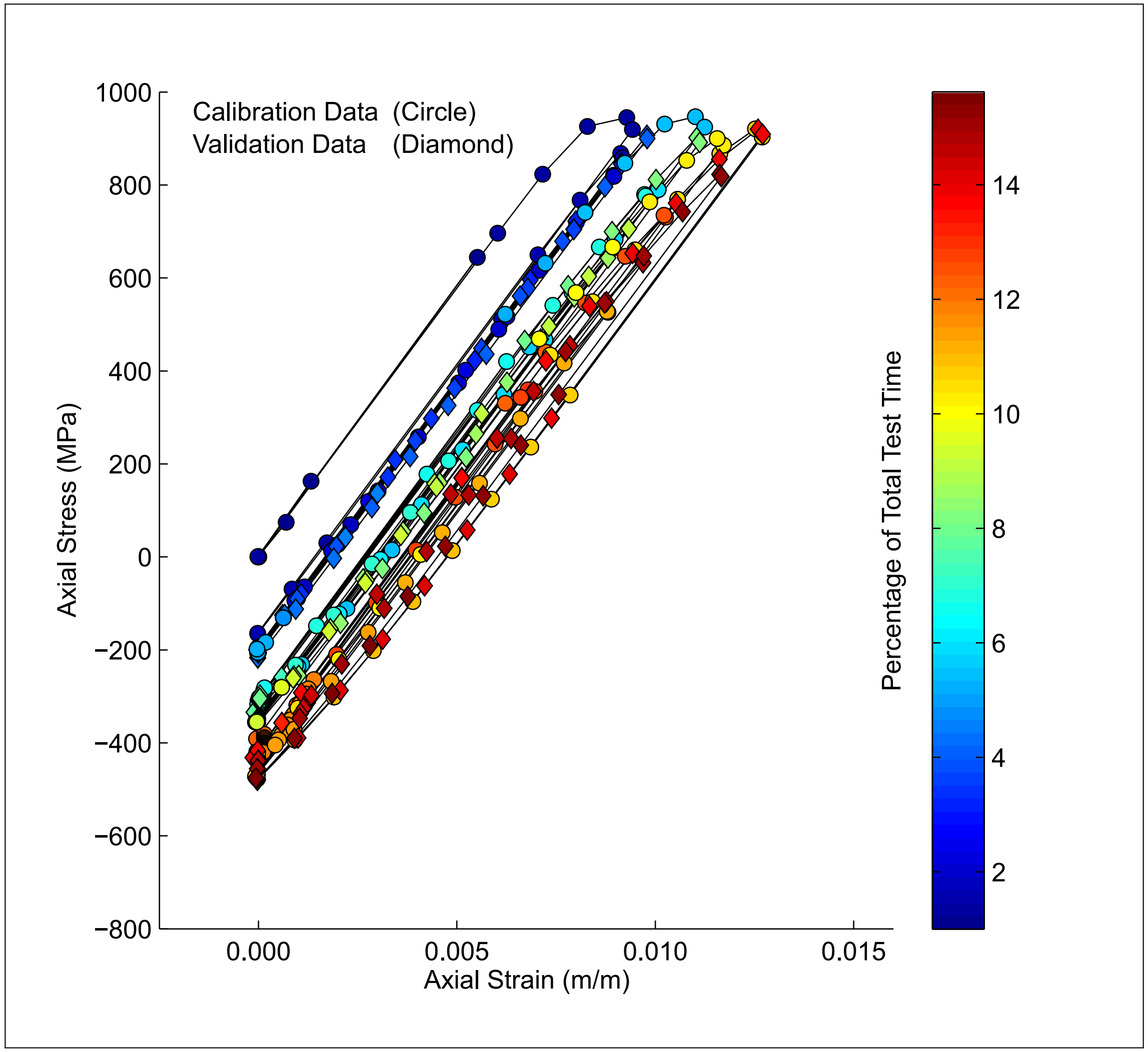

Figure 6.10: Axial stress vs. strain for only Test Block 1.

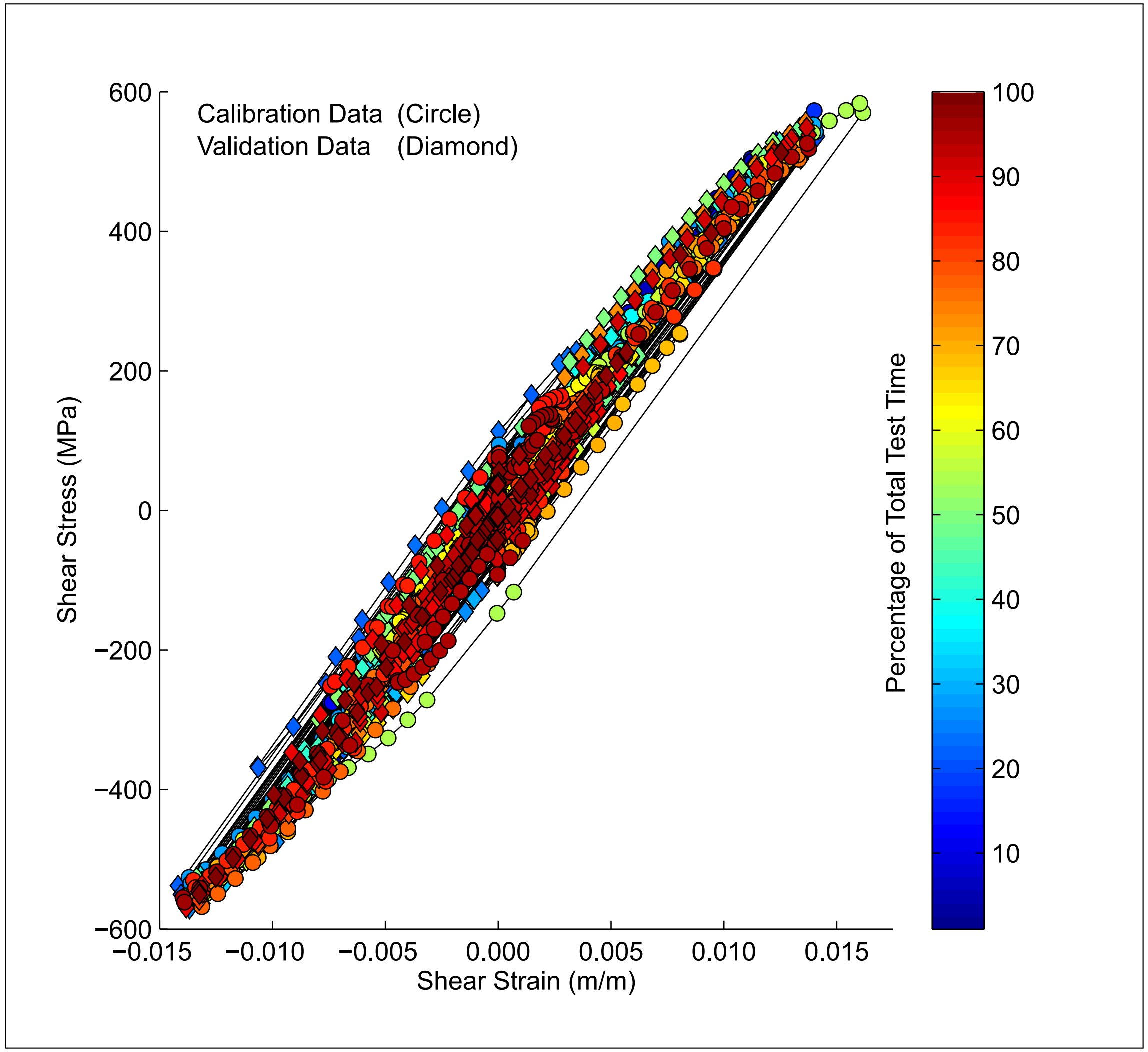

Figure 6.11: Shear stress vs. strain for the entire test.

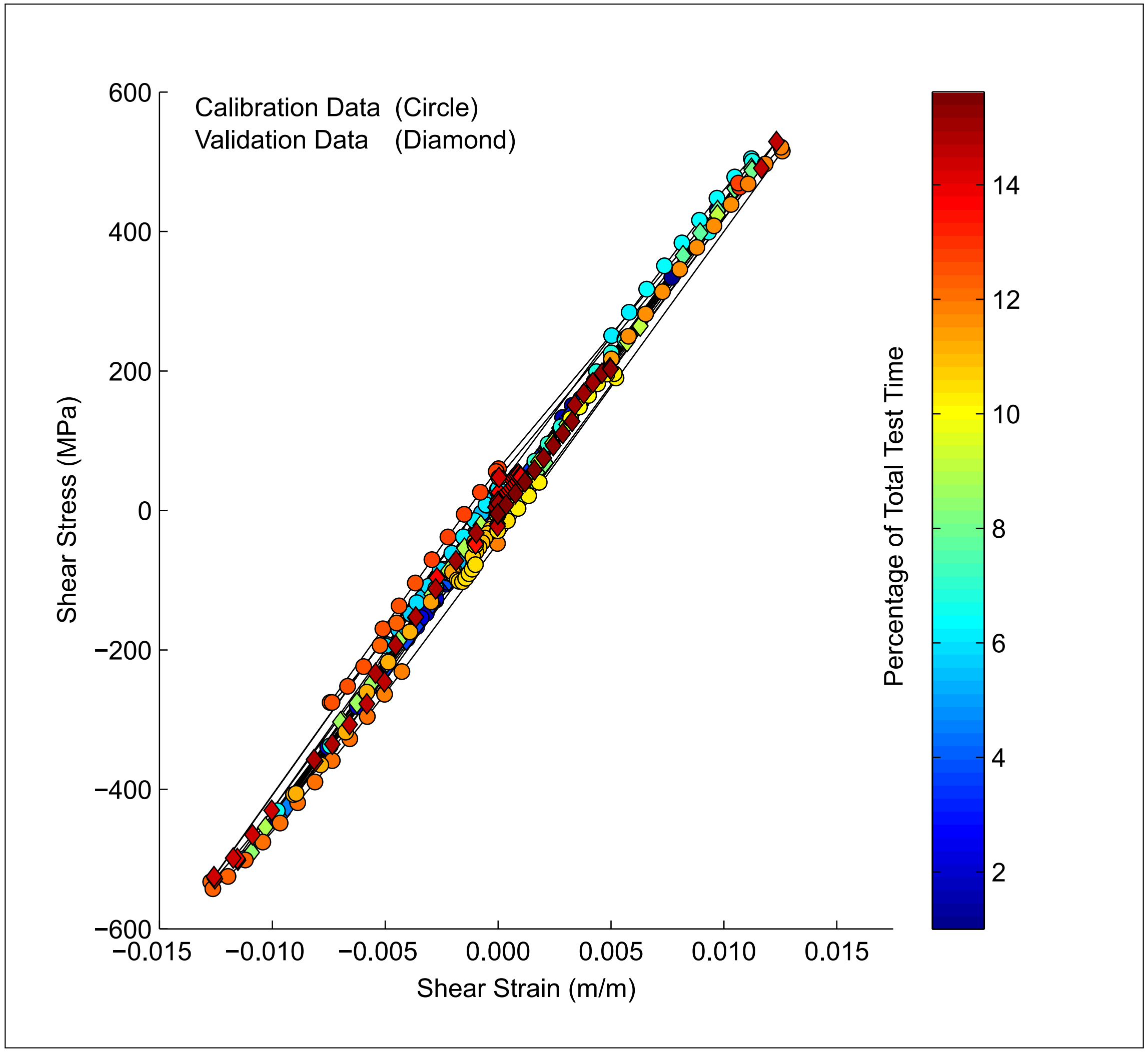

Figure 6.12: Shear stress vs. strain for only Test Block 1.

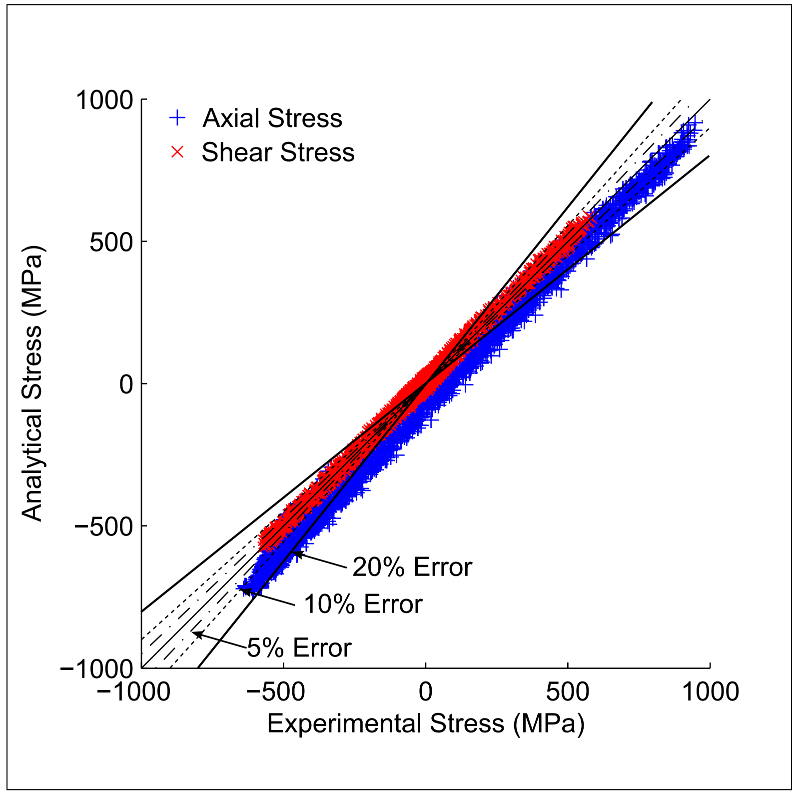

Figure 6.13: Analytical stress vs. experimental stress for the entire test. Axial stresses are shown as blue +'s, while shear stresses are shown as red x's.

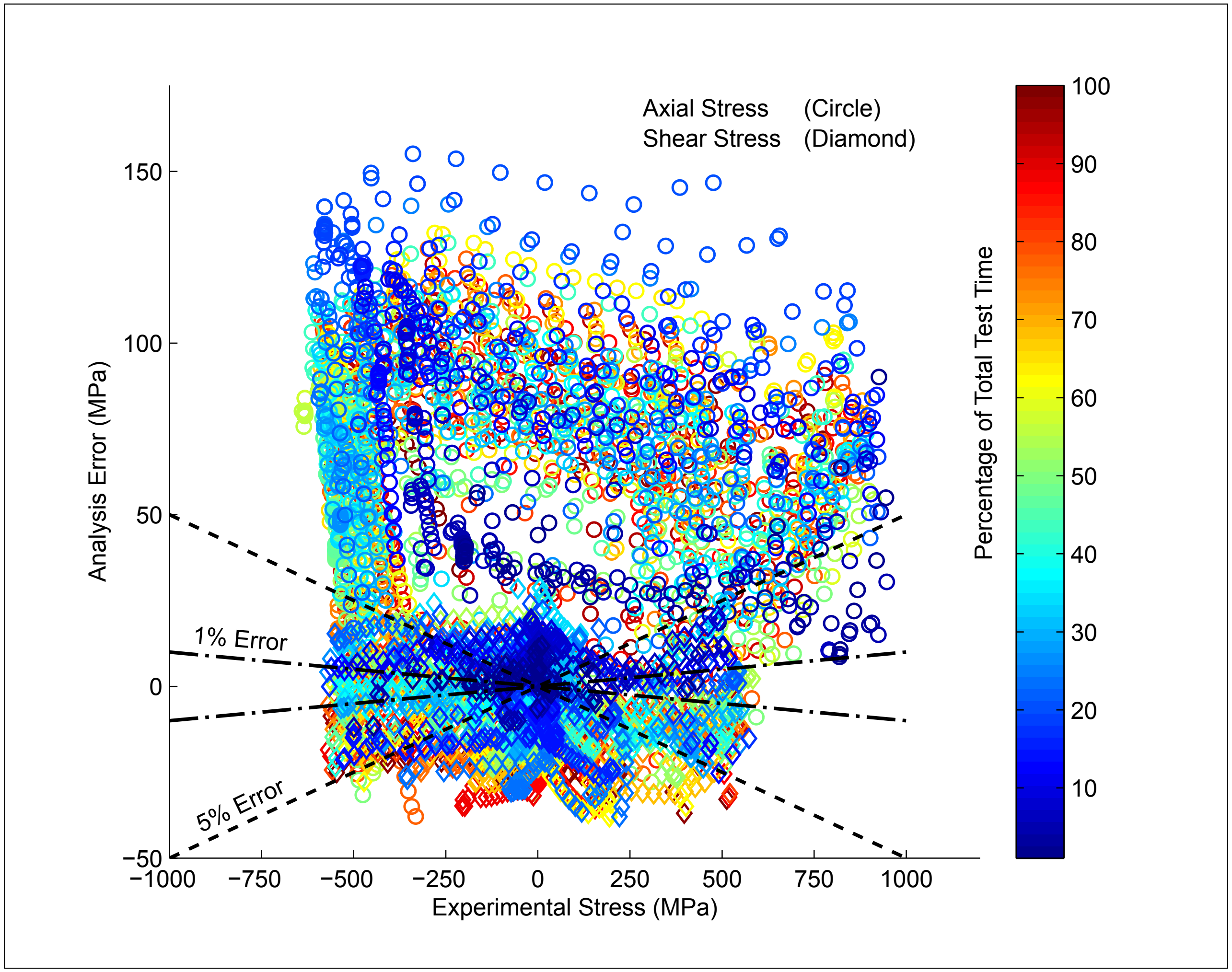

Figure 6.14: Analytical error vs. experimental stress for the entire test. Axial and shear data are shown as circles and diamonds, respectively with colors indicating the point during the test at which the data occurs.

Table 6.6: Evolution of the hardening parameters throughout the autonomous testing process.

		Parameter	Q_1	$5/b_1$	Q_2	$5/b_2$	A_1/B_1	$5/B_1$	A_2/B_2	$5/B_2$	A_3
		Min	0	9.50E-05	-500	1.00E-01	0	9.50E-05	0	9.50E-05	0
		Max	750	1.00E-01	0	1.00E+00	750	1.00E-01	750	1.00E-01	2000
Block	Iter	Round	Q_1	$5/b_1$	Q_2	$5/b_2$	A_1/B_1	$5/B_1$	A_2/B_2	$5/B_2$	A_3
1	1	1	27.0	9.71E-02	-86.6	8.86E-01	241.7	1.95E-04	67.6	7.50E-03	232.2
1	1	2	21.8	9.80E-02	-89.1	8.87E-01	242.5	9.50E-05	75.8	6.50E-03	240.2
1	1	3	21.0	9.80E-02	-89.6	8.69E-01	258.3	9.50E-05	68.3	6.50E-03	240.2
2	1	1	12.0	9.87E-02	-87.6	8.78E-01	279.3	9.50E-05	58.6	5.20E-03	178.2
2	2	1	7.5	9.93E-02	-86.6	8.86E-01	285.3	9.50E-05	61.6	5.80E-03	124.1
2	3	1	5.3	9.95E-02	-86.6	8.82E-01	286.8	9.50E-05	60.1	5.60E-03	112.1
2	4	1	4.5	9.97E-02	-91.1	8.81E-01	288.3	9.95E-04	60.1	4.70E-03	108.1
2	5	1	0.0	3.23E-02	-66.1	4.44E-01	75.1	4.23E-02	286.8	3.30E-03	86.1
2	6	1	0.0	3.15E-02	-66.1	4.48E-01	74.3	4.22E-02	283.8	3.40E-03	84.1
2	7	1	0.0	3.15E-02	-66.1	4.48E-01	74.3	4.22E-02	283.8	3.40E-03	84.1
2	8	1	0.0	3.21E-02	-65.6	4.32E-01	73.6	4.23E-02	283.0	3.40E-03	86.1
2	9	1	0.0	3.22E-02	-65.6	4.32E-01	72.8	4.30E-02	283.0	3.40E-03	92.1
2	10	1	0.0	3.01E-02	-72.6	3.95E-01	72.8	4.90E-02	289.8	4.30E-03	150.2

Table 6.7: Final set of constitutive parameters identified through the new integrated, autonomous methodology. Optimization parameter bounds are given for reference.

Parameter	Value	Min	Max	Units
Elastic				
E	116,726	-	-	MPa
G	44,818	-	-	MPa
ν	0.302	-	-	-
Rate Dependent				
D	371	-	-	MPa
n	15.5	-	-	-
Yield				
ρ_0	430	-	-	MPa
Isotropic Hardening				
Q_1	0.0	0	750	MPa
$5/b_1$	3.01E-02	9.50E-05	1.00E-01	-
Q_2	-72.6	-500	0	MPa
$5/b_2$	3.95E-01	1.00E-01	1.00E+01	-
Kinematic Hardening				
A_1/B_1	72.8	0	750	MPa
$5/B_1$	4.90E-02	9.50E-05	1.00E-01	-
A_2/B_2	289.8	0	750	MPa
$5/B_2$	4.30E-03	9.50E-05	1.00E-01	-
A_3	150.2	0	2000	MPa
B_3	0	-	-	-

The final set of constitutive parameters derived from the experiment lead to errors considerably higher than shown in the simulated results from the previous chapter. The increase in error is almost certainly due to constitutive model deficiencies where the constitutive model cannot accurately represent the entire physical behavior of Ti-6Al-4V, and to a lesser extent the variability and history effects in the test itself. This is evident in the initial fits performed using data from both a tension test and an axial-only strain controlled cyclic test. The initial fits are not able to accurately capture both the initial behavior of the virgin material and the cyclic response after significant plastic strain is developed. This is a known problem of plasticity models and other researches have attempted to address these shortcomings by increasing the complexity of the plasticity model [65]. However, the final set of constitutive parameters show improvement over the starting seeds that use axial-only data. Figure 6.15 shows the cumulative squared residual error for both the top initial seed and the final constitutive parameters for the autonomous test. In both cases, the error for shear stress is relatively low with axial stress error dominating. The parameter set identified through the integrated experiment leads to less error than the set initially generated with only uniaxial test data.

A comparison is shown in Fig. 6.16 for the axial stress vs. strain of the experimental data and the analytical solution using the final set of constitutive parameters derived from the experiment. For clarity, the comparison data is limited to Test Block 1 and iteration 1 from Test Block 2. Figure 6.17 shows the same comparison for shear stress vs. strain. The shear stresses correspond very well. The axial stress from the analytical solution is significantly lower than the experiment (approximately 75-125 MPa). This is likely an influence from the initial parameter seeds that conform to the cyclic supplemental test data. Ti-6Al-4V has a sharp yield region (tangent stiffness drops rapidly) that is not accurately captured by the final set of constitutive parameters. Furthermore, since the test is equivalent to R = 0 to prohibit buckling, no re-yielding can occur and the stresses are likely to continue to be off by the initial amount. This error propagation is visible in the error plot in Fig. 6.16.

The errors in the initial load excursions could likely be lessened through the inclusion of additional hardening terms. The rapidity terms (b and B for isotopic and kinematic hardening, respectively) control when the hardening is applied with regard to increasing plastic strain. The stress errors (particularly those shown in Fig. 6.16) indicate more hardening is necessary prior to reaching approximately 0.001 m/m plastic strain. The rapidity ($5/B$) for the kinematic terms, which occur much sooner than the isotropic terms, are 0.0043 m/m and 0.049 m/m. Adding one or more additional hardening terms with rapidity values of $5/b$ or $5/B$ near 0.001 m/m would address the initial stress errors. However, the influence of the additional terms would also need to be assessed for varied load conditions, such as fully reversed excursions.

Table 6.8 shows the statistics for the error magnitude, e_{mag}, when using the final set of constitutive parameters. The error magnitude, e_{mag}, is

$$e_{mag} = \sqrt{\left(\sigma^{exp} - \sigma^{fe}\right)^2 + \left(\tau^{exp} - \tau^{fe}\right)^2} \tag{6.3}$$

where σ and τ are the axial and shear stress, respectively. The superscript indicates stress from either the experiment (exp) or the analysis (fe). Metrics are shown for each set of excursions (both calibration and validation) for the different stages of the autonomous experiment. The statistics are only taken over the data points for the identified test block, round, and iteration. As mentioned, many of the excursion sets start with a moderate discrepancy between the experiment and the analysis. Therefore, Table 6.9 shows the statistics with the initial error magnitude removed so each excursion starts with zero error. Also, the offset values in the table give an indication of error over the duration of the experiment. Mean, maximum, and standard deviation values for the final validation excursion are actually quite low with the offset removed. The original values for the mean, maximum, and standard deviation are 75.9, 114.3, and 18.0 MPa, and the offset-compensated values are 13.4, 43.3, 12.0 MPa. The cumulative error statistics in Table 6.8 are computed for all data points through the validation excursions for the indicated test block, round, and iteration. The average and maximum errors both increase steadily through Test Block 1 and the first iteration of Test Block 2. The increase is also likely due to inadequate fitting of the constitutive parameters to the initial sharp yielding exhibited by Ti-6Al-4V.

The total time required for the autonomous testing, including the calibration of the constitutive parameters was 993 minutes of which 207.2 minutes were from the experiment and the remaining 786.2 minutes were from the FEMU. Table 6.10 provides a breakdown of time for testing and for all the FEMU. The table also indicates the total number of time steps included in each FEMU process and the computation time. The current computer (Intel$^{(R)}$ Core$^{(TM)}$2 Duo E8400, 3.00 GHz processor, with only 4.0 GB of memory) that is utilized with the axial-torsional test frame is older and slated for replacement. The FEMU code has been implemented to enable parallel processing and experiences an almost linear speedup when additional cores are utilized. For comparison, the same FEMU procedures from the autonomous test have been repeated on a faster computer (4-core, Intel$^{(R)}$ Core$^{(TM)}$ i7-4790K @ 4.00 GHz, 32 GB memory) with the additional advantage of parallel computing using 4 CPU cores. Table 6.10 shows the total time for the FEMU is drastically reduced from 786.2 minutes to just under 100 minutes. The total speedup is approximately a factor of 8. A factor of 2 is likely attributed to the faster CPU, while the remaining factor of 4 is consistent with the gains attained when using parallel computing with the optimization methods. With the use of modern computing resources and parallel computing, the computations that are required for the constitutive model fitting can be done in near real-time, when compared to the duration of the experiment.

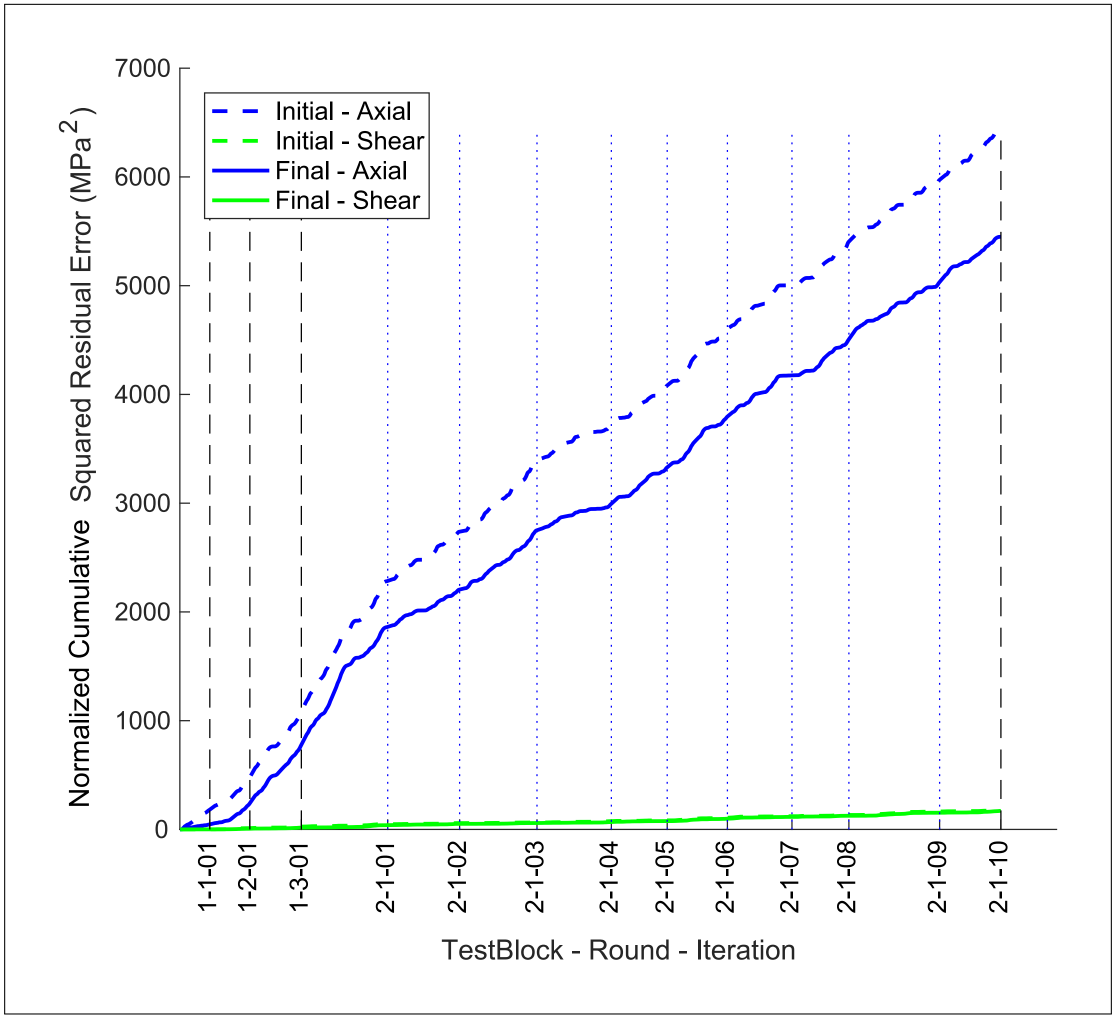

Figure 6.15: Normalized cumulative sum of the squares of the residual error for the top initial seed (Table 6.3) and the final set of constitutive parameters (Table 6.7).

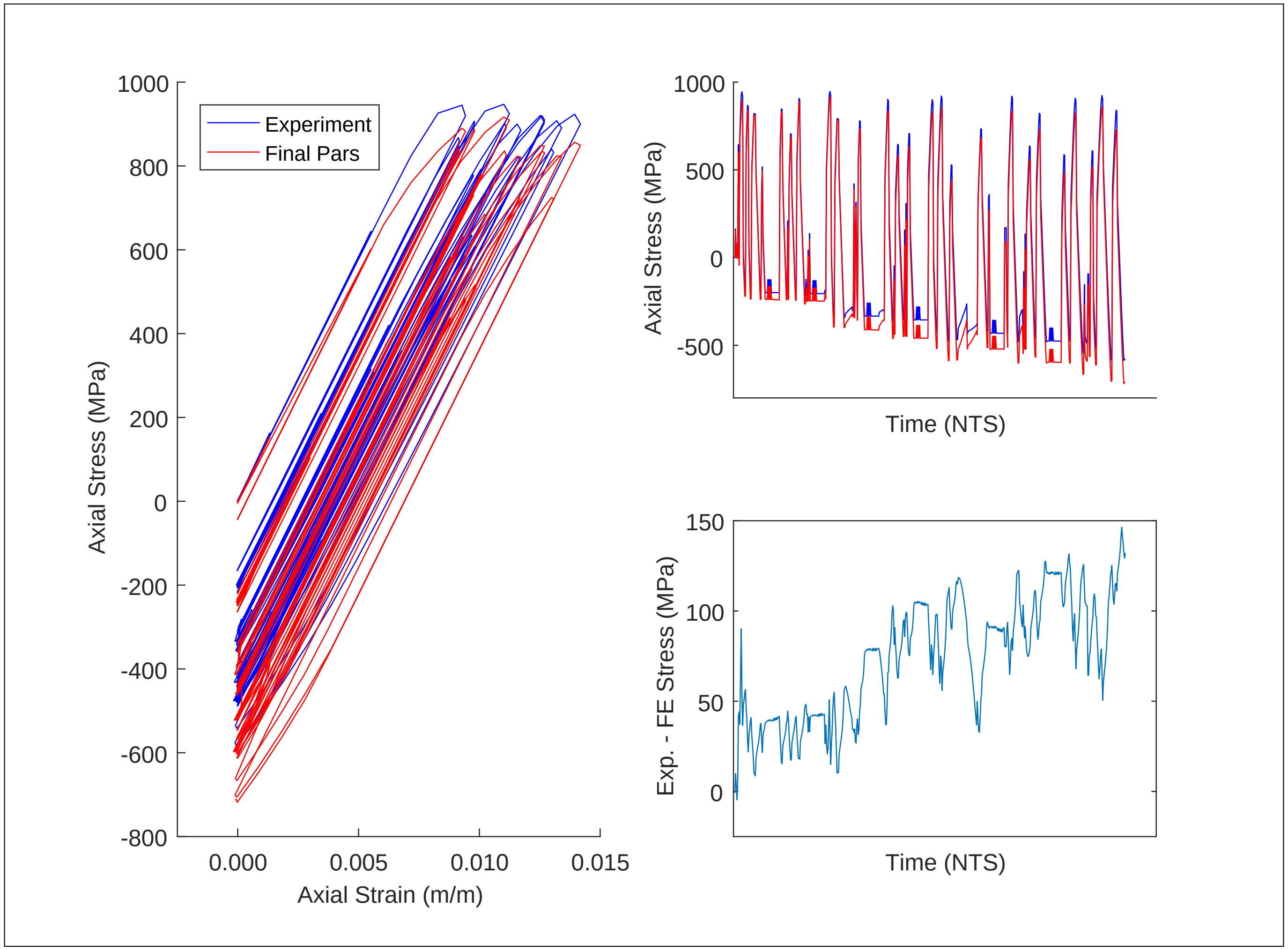

Figure 6.16: Experimental axial stress vs. strain and analytical results using the final set of parameters. Results shown for Test Block 1 and the first iteration of Test Block 2.

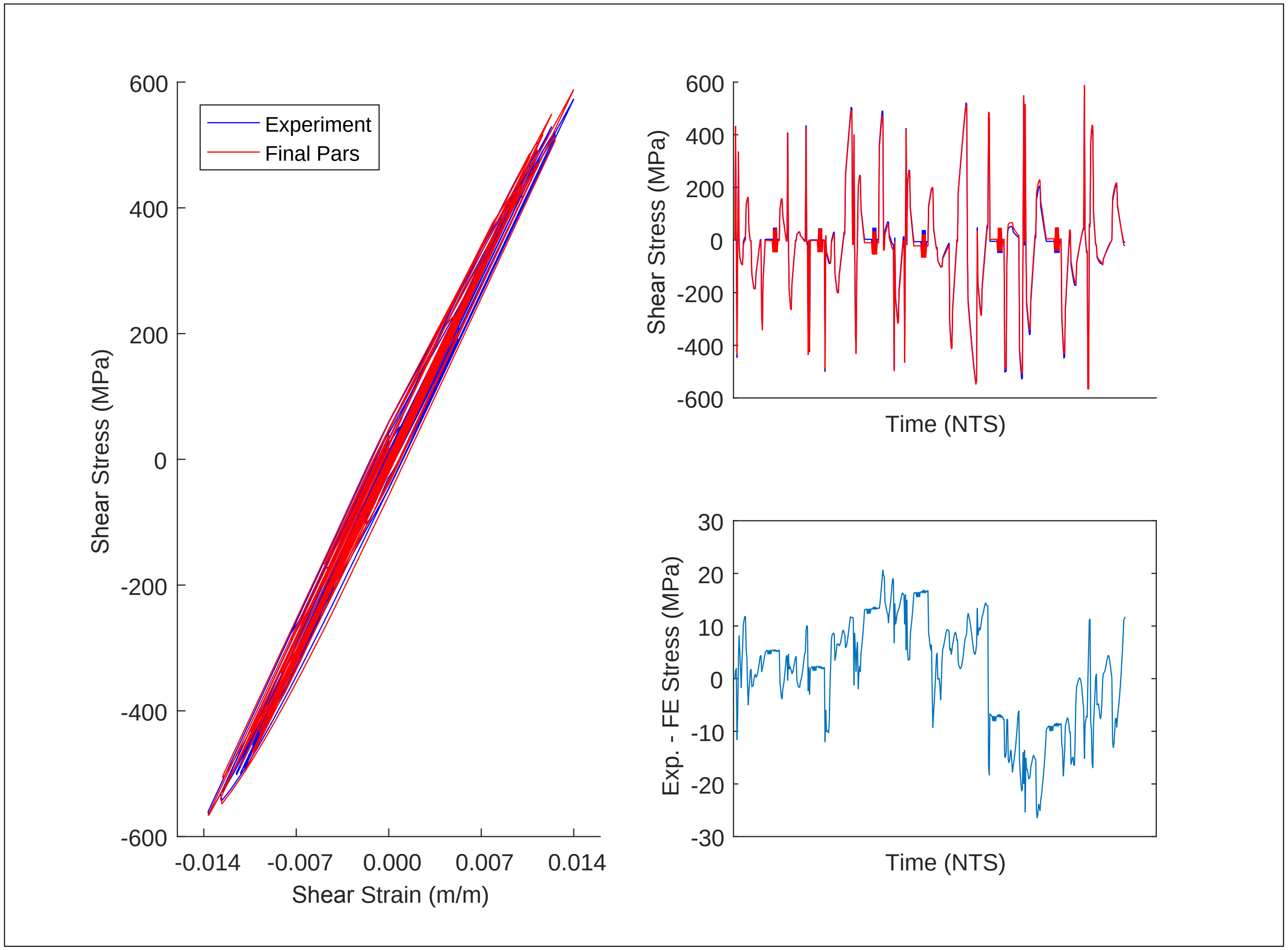

Figure 6.17: Experimental shear stress vs. strain and analytical results using the final set of parameters. Results shown for Test Block 1 and the first iteration of Test Block 2.

Table 6.8: Basic statistics for error magnitude during the calibration and validation excursions using the final set of constitutive parameters.

			Calibration				Validation				Cumulative Through Validation			
TB	Rnd	Iter	Points	Mean	Max	Std	Points	Mean	Max	Std	Points	Mean	Max	Std
1	1	1	46	31.8	90.1	17.8	65	34.9	49.1	8.4	110	33.5	90.1	13.2
1	2	1	78	41.4	78.9	13.4	71	79.6	106.2	13.9	257	48.4	106.2	23.6
1	3	1	109	87.7	118.6	21.9	82	96.4	128.3	13.9	446	66.6	128.3	30.5
2	1	1	111	106.0	146.4	21.4	208	94.0	155.8	33.7	763	79.7	155.8	34.2
2	1	2	116	60.6	103.5	20.2	150	57.1	105.4	27.2	1027	74.3	155.8	33.2
2	1	3	110	63.7	114.3	27.6	176	77.3	129.3	23.1	1311	73.8	155.8	31.7
2	1	4	96	60.8	101.3	15.7	179	40.9	98.9	22.4	1584	69.4	155.8	31.9
2	1	5	108	65.9	114.5	28.5	99	64.7	115.0	28.1	1789	68.9	155.8	31.5
2	1	6	99	81.0	135.1	29.1	124	72.1	132.1	30.1	2010	69.7	155.8	31.4
2	1	7	117	72.6	119.2	25.3	122	54.4	119.8	35.2	2247	69.0	155.8	31.6
2	1	8	120	53.8	127.5	35.4	91	73.9	118.9	22.4	2456	68.4	155.8	31.6
2	1	9	117	69.8	108.0	27.7	218	61.9	121.7	29.7	2789	68.0	155.8	31.4
2	1	10	120	69.3	123.2	28.4	107	75.9	114.3	18.0	3014	68.3	155.8	30.9

Table 6.9: Basic statistics for error magnitude during the calibration and validation excursions when the initial error offset is removed and the final set of constitutive parameters are used.

			Calibration					Validation				
TB	Rnd	Iter	Offset	Points	Mean	Max	Std	Offset	Points	Mean	Max	Std
1	1	1	0.0	46	31.8	90.1	17.8	0.0	65	34.9	49.1	8.4
1	2	1	41.8	78	9.7	37.1	9.2	78.9	71	9.4	39.6	10.1
1	3	1	106.2	109	20.7	72.1	19.8	91.8	82	10.5	36.5	10.2
2	1	1	121.8	111	19.0	71.3	18.6	132.7	208	40.9	117.0	30.9
2	1	2	51.2	116	17.4	52.3	13.9	9.0	150	48.1	96.4	27.2
2	1	3	42.9	110	26.9	71.4	21.7	79.1	176	17.8	62.9	14.7
2	1	4	52.7	96	12.9	48.6	12.0	41.3	179	17.6	57.7	13.8
2	1	5	85.6	108	24.4	82.0	24.5	80.8	99	22.6	76.6	23.1
2	1	6	79.7	99	22.7	56.4	18.2	93.6	124	27.1	91.1	25.1
2	1	7	84.4	117	20.5	68.2	19.0	42.3	122	29.8	77.6	22.1
2	1	8	22.0	120	37.4	105.5	29.5	84.8	91	19.1	54.0	15.9
2	1	9	105.1	117	35.4	100.1	27.6	65.7	218	24.5	63.8	17.2
2	1	10	96.2	120	29.3	85.0	25.9	75.5	107	13.4	43.3	12.0

Table 6.10: Time requirements for FEMU from autonomous testing on existing computer (Computer 1) and faster computer system (Computer 2) that uses parallel processing.

Experiment Time (min)				207.2		
Test Block	Round	Iteration	Num. Points	Computer 1 Time (min)	Computer 2 Time (min)	Ratio 1:2
1	1	1	46	6.1	0.8	7.6
1	2	1	187	10.5	1.4	7.7
1	3	1	365	16.7	2.2	7.5
2	1	1	556	23.0	3.1	7.5
2	1	2	878	36.0	5.0	7.3
2	1	3	1136	47.4	6.2	7.6
2	1	4	1406	59.5	8.1	7.3
2	1	5	1691	72.8	9.5	7.7
2	1	6	1887	83.5	11.6	7.2
2	1	7	2126	88.1	10.7	8.2
2	1	8	2366	101.8	12.5	8.2
2	1	9	2572	114.1	13.8	8.3
2	1	10	2908	126.7	15.2	8.3
			Total	786.2	99.9	7.9

Computer 1:	2 cores (1 used); 64-bit Operating System; Intel$^{(R)}$ Core$^{(TM)}$2 Duo E8400 @ 3.00 GHz, 4 GB RAM
Computer 2:	4 cores (4 used); 64-bit Operating System; Intel$^{(R)}$ Core$^{(TM)}$ i7-4790K CPU @ 4.00 GHz; 32 GB RAM

6.5.2 Final Validation Excursions

A series of experimental excursions were performed on the test specimen after the conclusion of the autonomous test and prior to removal from the test machine. The excursions during the autonomous tests were performed at various angles (proportions) in the axial/shear strain space. A set of validation excursions were performed within the confines of Test Block 2 to mimic the behavior seen during the autonomous test. Further validation excursions were designed and conducted to deviate from the proportional behavior and also to increase the axial strain to induce further plasticity. Table 6.11 provides a summary of the additional load excursion types and strain ranges.

Table 6.11: Validation excursions performed after the autonomous test.

		Strain Range (m/m)			
		Axial		Shear	
Test Type	Cycles	Low	High	Low	High
Half Circles	-	0	0.014	0	0.014
Triangles	-	0	0.014	0	0.014
Boxes	-	0	0.014	0	0.014
R = 0.75 (axial)	100	0.015	0.02	0	0
R = 0.75 (axial)	25	0.019	0.025	0	0
Axial Only	-	-	0.045	0	0
R = -1 (shear)		0.045	0.045	-0.014	0.014
Unload	-				

Test Block 2, Iteration 10, Validation

The final validation excursions conducted during the autonomous testing (Test Block 2, Iteration 10) have similar characteristics to the preceding autonomous test. Figure 6.18 and 6.19 show the summary of stress versus strain for the axial and shear components, respectively. The error plots show significant error at the beginning of the validation excursions. During the final validation excursion, the maximum error magnitude, defined by Eq. (6.3), is 114.3 MPa, and the mean of 107 points is 75.88 MPa. If the initial error magnitude (75.5 MPa) is removed, the maximum error drops to 43.3 MPa, and the mean drops to 13.4 MPa. A complete list of the error statistics for the various portions of the autonomous test were given in Table 6.8 and 6.9. The general trend of the plasticity model is correct, but correlation with the experiment is already offset at the beginning of the validation experiments.

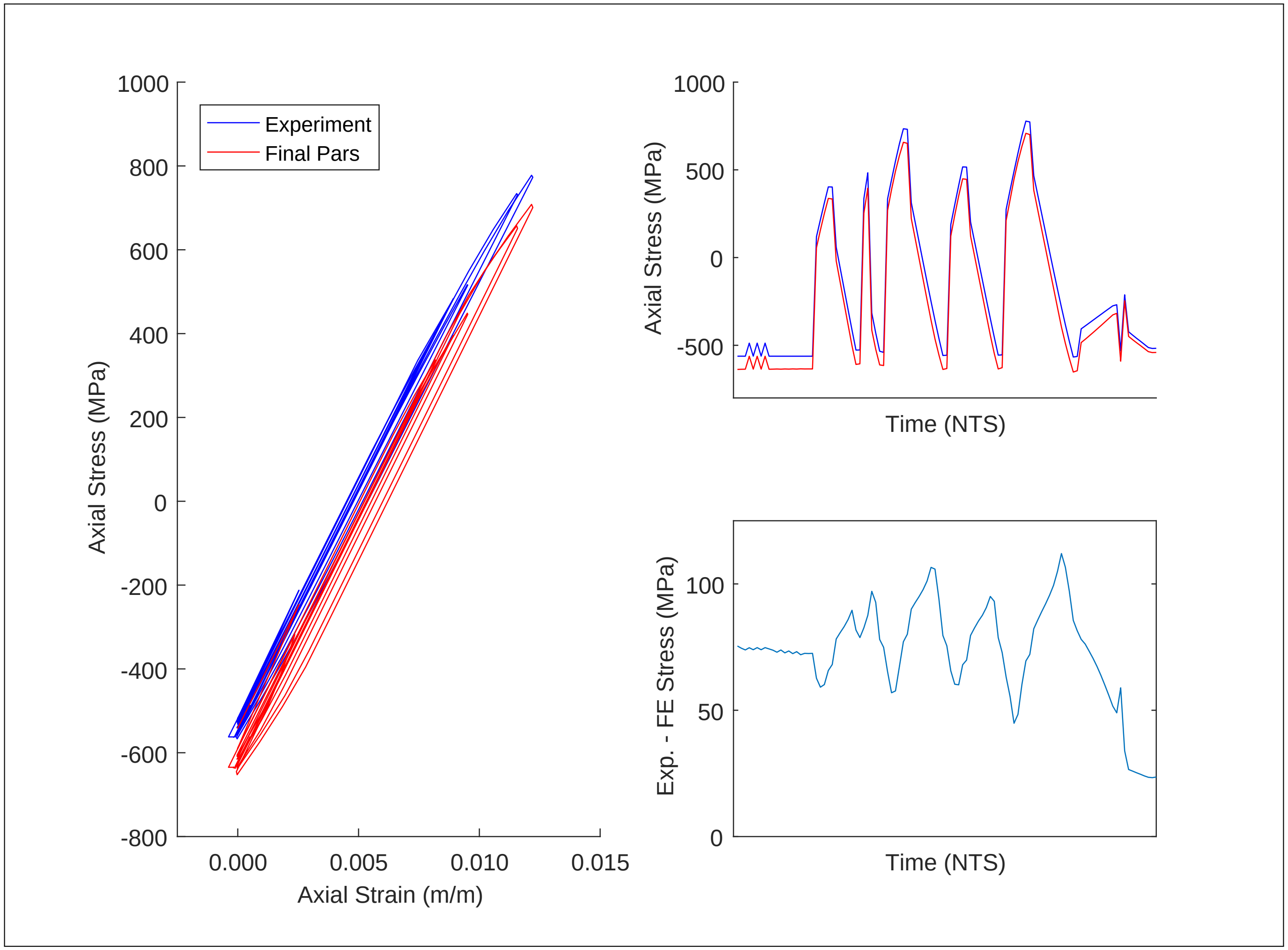

Figure 6.18: Experimental axial stress vs. strain and analytical results using the final set of parameters. Results are shown for the final validation excursions from Test Block 2, round 1, iteration 10.

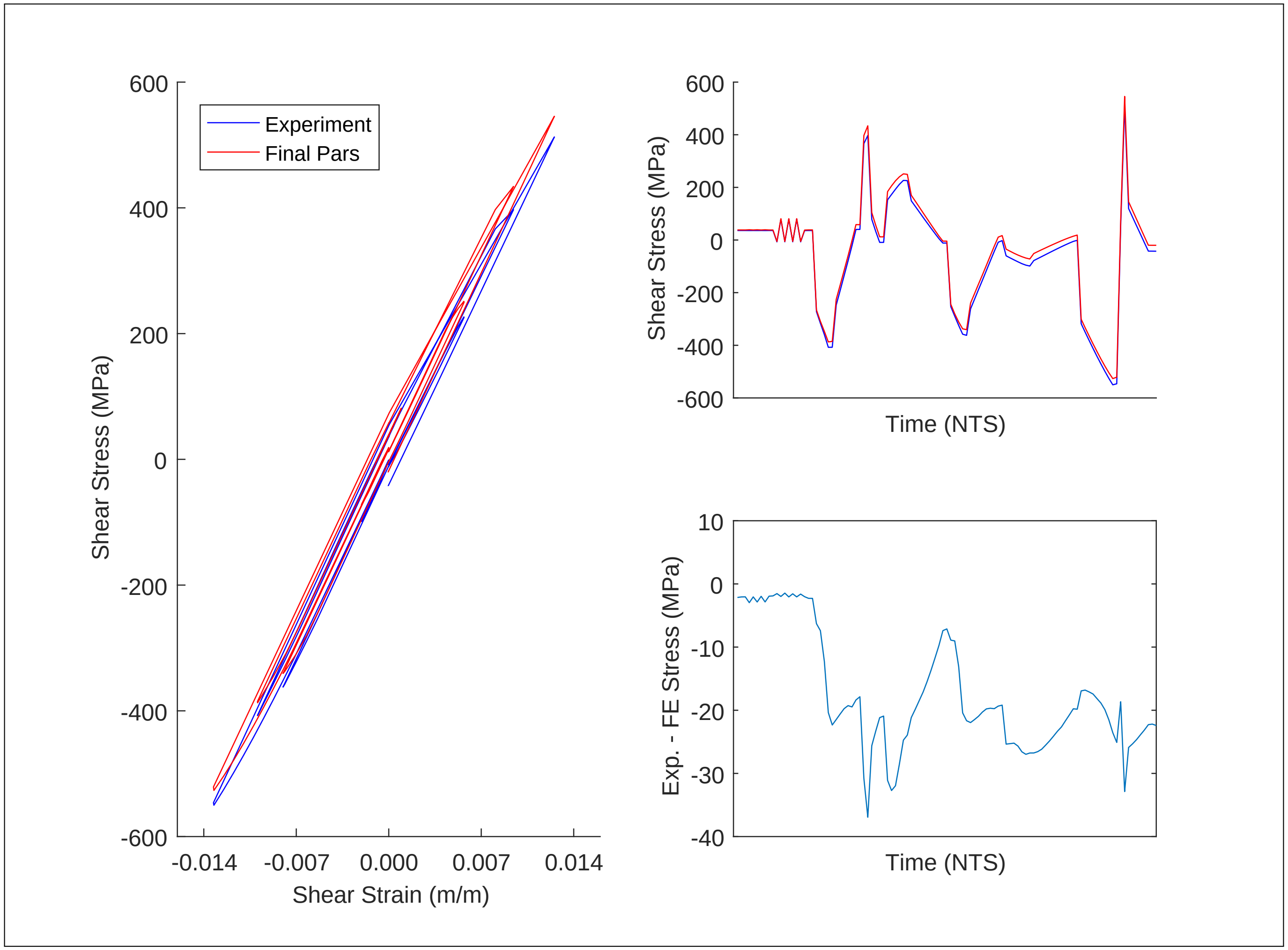

Figure 6.19: Experimental shear stress vs. strain and analytical results using the final set of parameters. Results are shown for the final validation excursions from Test Block 2, round 1, iteration 10.

Remaining Excursions

The remaining validation excursions conducted on the autonomous test specimen prior to removal varied the test conditions and increased the strain magnitude. Figure 6.20 depicts axial vs. shear strain plots for selected multiaxial load excursions conducted at the strain magnitude used in the autonomous experiments. The axial stress vs. strain and shear stress vs. strain for the same interesting excursions are shown in Fig. 6.21 and Fig. 6.22, respectively. Figure 6.23 shows the axial stress vs. strain for all the validation excursions listed in Table 6.11, while Fig. 6.24 shows the shear stress vs. strain.

Figure 6.25 shows the normalized cumulative squared residual error for both the autonomous test and all the validation excursions. Each validation excursion type is separated by dashed vertical lines. The parameters resulting from the autonomous test perform better than the top initial fit using only axial test data. The cumulative residual error grows at approximately the same rate for the final validation excursion from Text Block 2, the half-circles, the triangles, and the boxes. There is very little increase during the R=0.75 cycles. However, there is a significant increase in the cumulative error during the shear cycles. This increase is likely due to the parameters being calibrated for strain magnitudes of only 0.015 m/m. The combination of large axial strain and cyclic shear strain proves to be significantly different than the conditions for which the parameters have been calibrated.

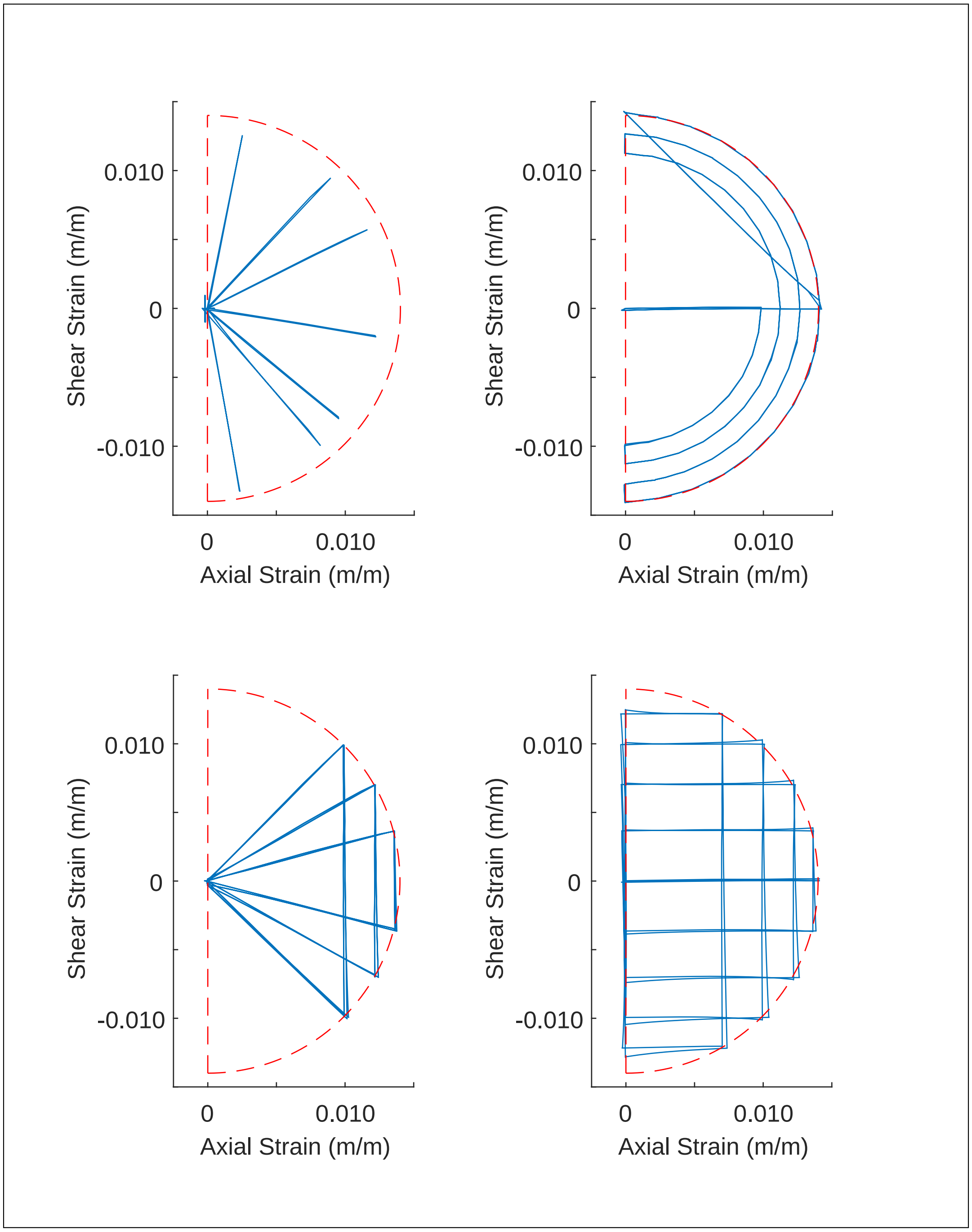

Figure 6.20: Shear strain vs. axial strain for selected multiaxial validation excursions conducted prior to removal of the specimen. Excursions were conducted in following order: TL - final validation excursions; TR - half circles; BL - triangles; and BR - boxes.

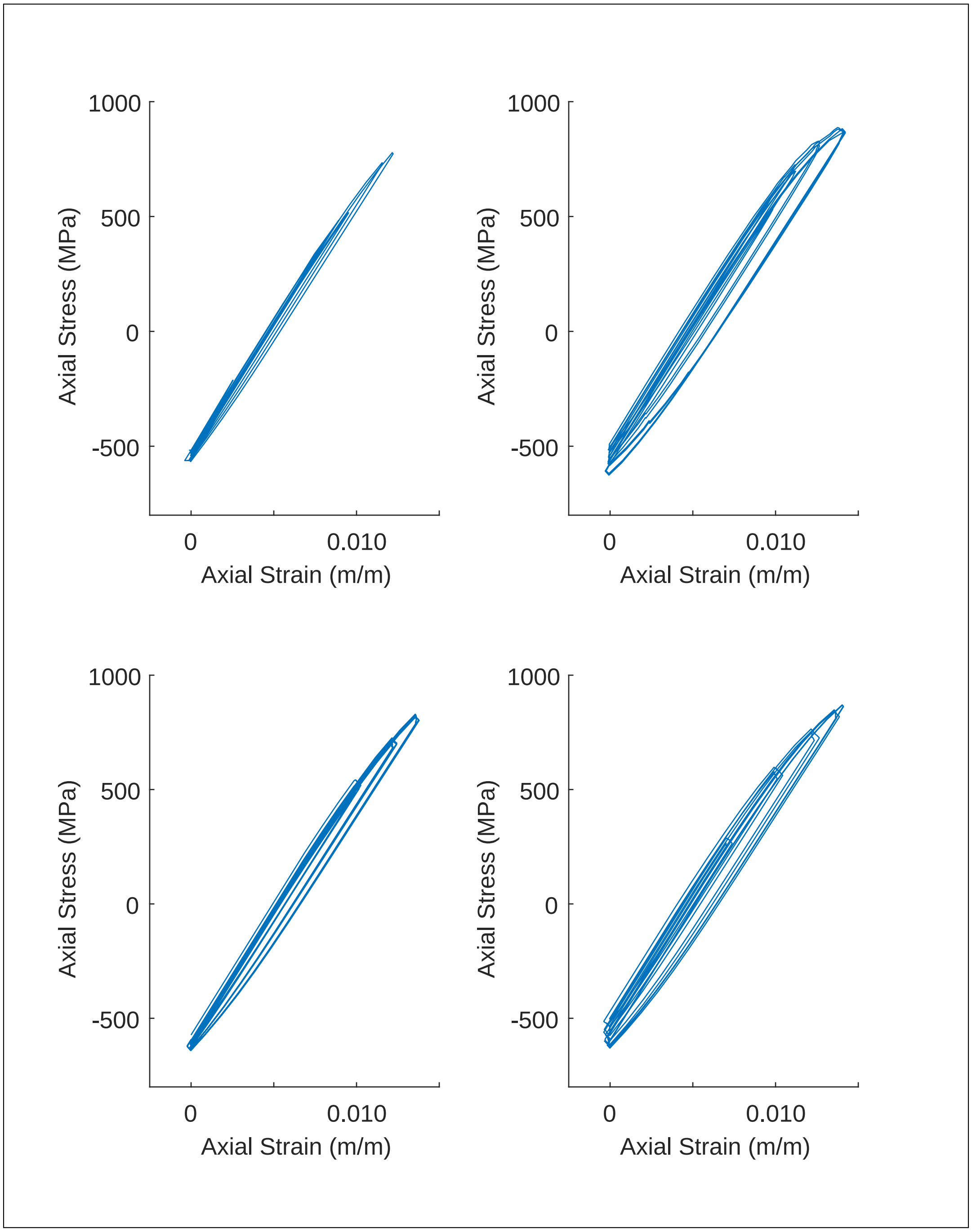

Figure 6.21: Axial stress vs. strain for selected multiaxial validation excursions conducted prior to removal of the specimen. Excursions were conducted in following order: TL - final validation excursions; TR - half circles; BL - triangles; and BR - boxes.

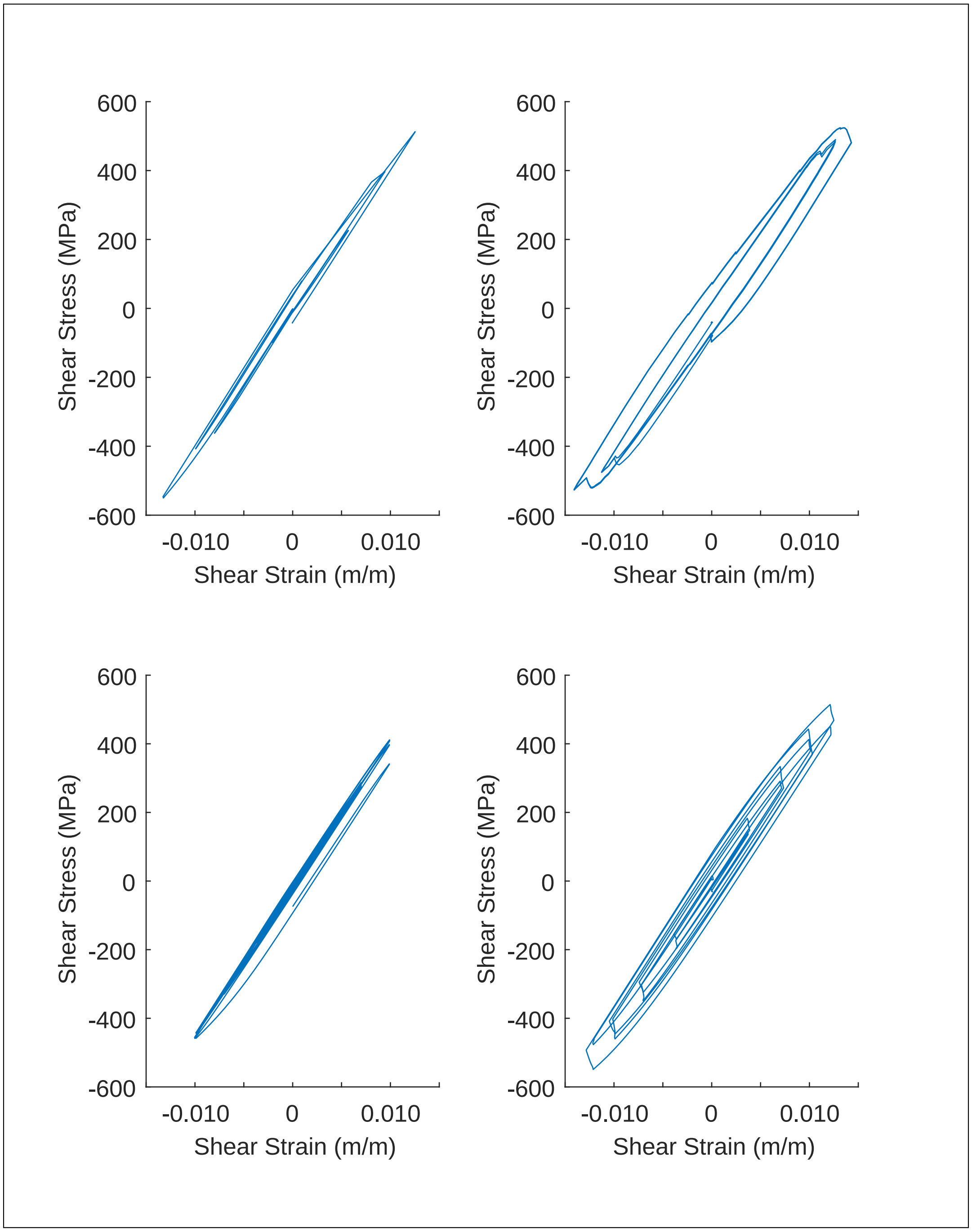

Figure 6.22: Shear stress vs. strain for selected multiaxial validation excursions conducted prior to removal of the specimen. Excursions were conducted in following order: TL - final validation excursions; TR - half circles; BL - triangles; and BR - boxes.

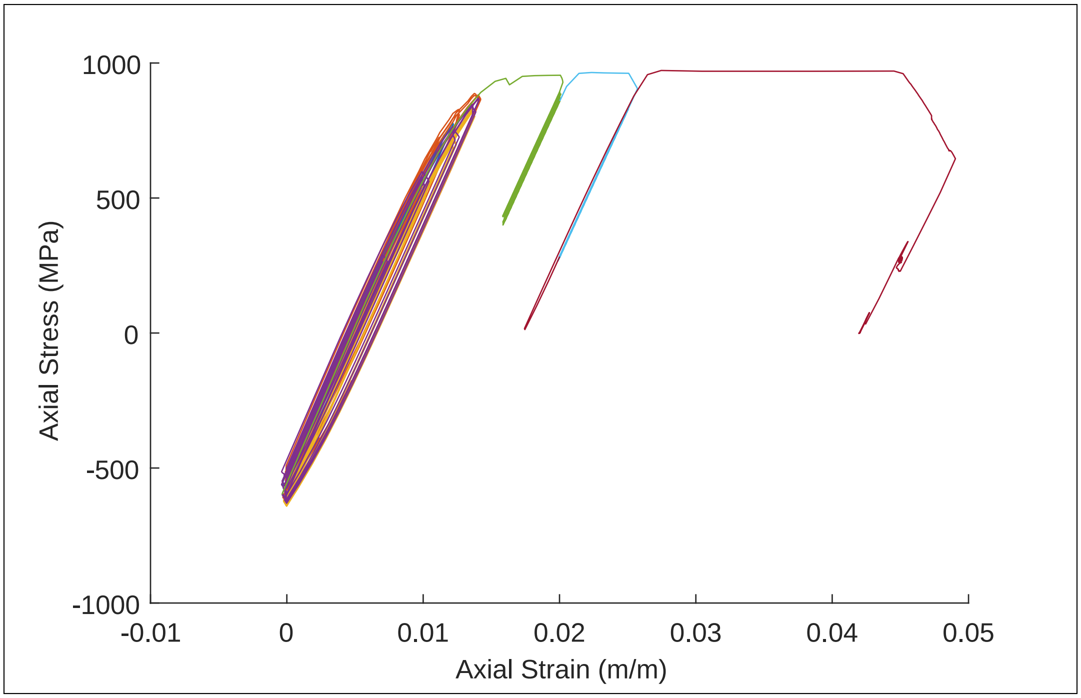

Figure 6.23: Axial stress vs. strain for all validation excursions conducted prior to removal of the specimen.

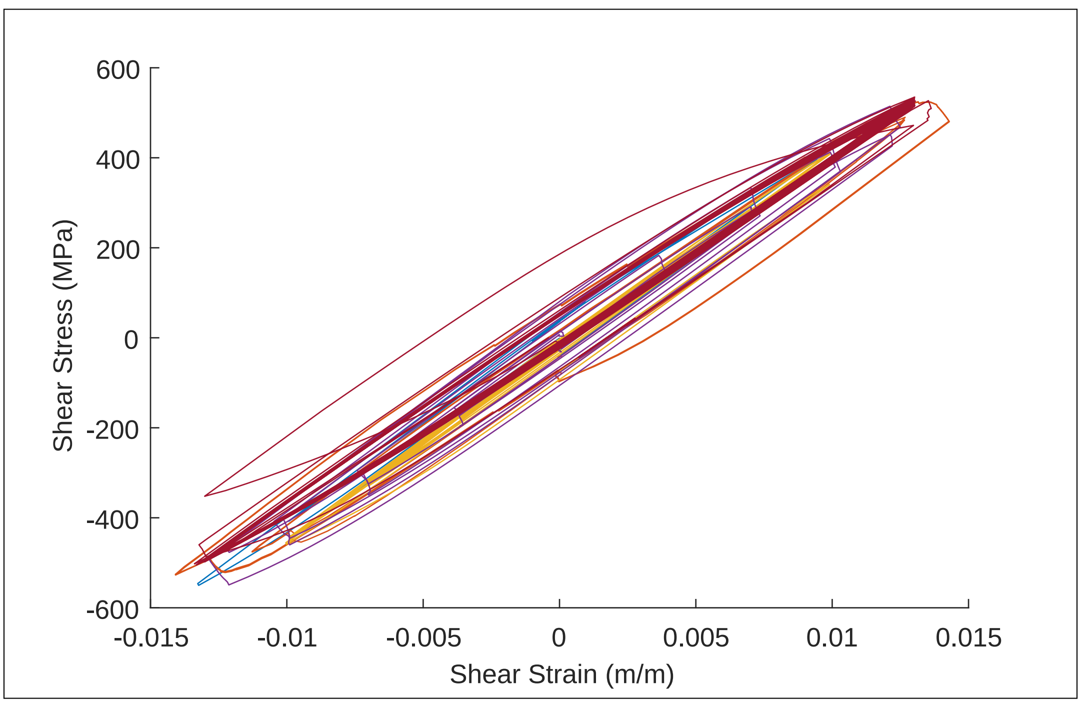

Figure 6.24: Shear stress vs. strain for all validation excursions conducted prior to removal of the specimen.

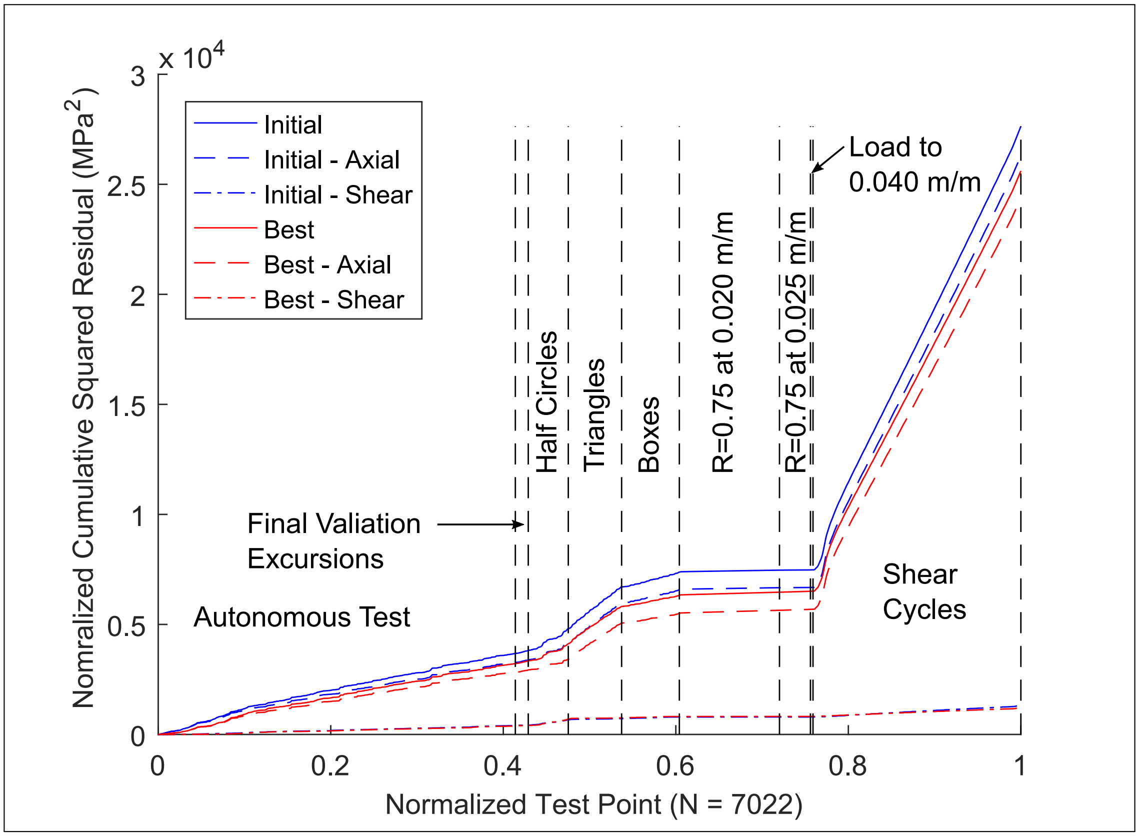

Figure 6.25: Normalized cumulative squared residual error for axial, shear, and total errors for the entire test, including all validation excursions conducted prior to removal of the specimen. Dashed vertical lines indicate transition from one loading type to the next.

6.6 Autonomous Testing Summary

The integration of multiaxial experimentation and constitutive model parameter calibration and validation has been successfully demonstrated. The hardening parameters of a viscoplasticity model for Ti-6Al-4V have been autonomously identified through the use of the developed methodology and associated software. The identified hardening parameters improved correlation for multiaxial experiments compared to the starting parameter set identified using only uniaxial data, and were available immediately upon completion of the integrated experiment. The immediate availability is in stark contrast to the conventional norm of passing large piles of raw, experimental test data to an analyst upon test completion at which point the parameter identification process would begin.

The time required to identify the parameters with the test machine's current computer is quite high in comparison to testing time, but it is still minimal compared to the time required for traditional methods. Furthermore, the same analyses have been shown to take much less time on a more modern computer running the developed software in parallel. Other methods require, first and foremost, the transfer of large amounts of data from the laboratory equipment to the person tasked with performing the parameter identification. The analyst then decides on how to best reduce the multiaxial data, performs the parameter identification, and then assess the validity of the parameters through additional testing. The time required for the traditional approach would easily surpass the computation time necessary for the integrated test completed in this work.

While this current effort focuses only on a viscoplasticity model for Ti-6Al-4V, the methodology could be applied to a broad range of materials. In addition, the methodology is not specific to a material model and incorporating alternate constitutive relationships has been planned for and is easy to implement with the developed methodology. The following chapter discusses additional multiaxial experiments conducted to assess the suitability of the chosen viscoplasticity model and the identified parameters for representing the multiaxial behavior of Ti-6Al-4V. The validation discussed within this chapter and the following chapter show that errors persist between the experiments and the simulated response using the final constitutive parameters. The analytical errors are primarily due to limitations in the constitutive model; furthermore, it is possible to revisit the data from the autonomous test sequence with a more elaborate analytical model to arrive at a more accurate predictive model. The constitutive model used to control the autonomous experiment need not be perfect as long as it forces the experiment to visit a broad enough sample of the material behavior.

CHAPTER VII

VALIDATION OF CONSTITUTIVE PARAMETERS

A series of validation experiments has been performed to assess the capability of both the chosen constitutive model and the final parameters identified with the integrated methodology. For each test, a corresponding finite element analysis has been performed using the final set of constitutive parameters as well as the top initial seed generated from the supplemental uniaxial data. For reference, Table 7.1 provides these parameter sets. The validation cases and the sections in which they are addressed are as follows:

- Section 7.1 - Supplemental test data which includes tension tests and axial-only strain controlled fully reversed cyclic loading at various strain magnitudes;
- Section 7.2 - Two separate multiaxial experiments without compressive strain (similar to the autonomous test);
- Section 7.3 - A multiaxial experiment with fully reversed loading;
- Section 7.4 - Torsion cycling at large shear strain; and
- Section 7.5 - Complex multiaxial loading with increasing axial strain.

Details of the test setup, strain measuring devices, and results are presented in each section. The multiaxial tests have been performed using two specimen designs shown in Figure 7.1 and are referred to throughout this chapter as Type I and Type II. Type II is capable of fully reversed loading, while Type I (which was used in the autonomous test) cannot undergo compressive strain due to the risk of plastic buckling.

Section 7.5 discusses the results when performing a constitutive model fitting with a large portion of the data mentioned throughout this work. Finally, the chapter concludes with comments on the appropriateness of the constitutive model and the identified parameters.

Table 7.1: Parameters for the top initial seed from the supplemental axial-only test data (Case 99) and the final set from the autonomous integrated experiment.

Parameter	Min	Max	Initial (Case 99)	Final
Q_1	0	750	5	0
$5/b_1$	9.50E-05	1.00E-01	2.85E-04	3.01E-02
q_2	-500	0	-55.7	-72.6
$5/b_2$	1.00E-01	1.00E+00	1.00E+00	3.95E-01
A_1/B_1	0	750	65.2	72.8
$5/B_1$	9.50E-05	1.00E-01	2.11E-03	4.90E-02
A_2/B_2	0	750	281.3	289.8
$5/B_2$	9.50E-05	1.00E-01	1.40E-02	4.30E-03
A_3	0	2000	0	150.2

7.1 Supplemental Data

During the autonomous test, data from the ongoing experiment and the supplemental tension test were used during the parameter identification with FEMU. Therefore, the optimization sought to minimize the stress error for both of these tests. In contrast, the cyclic axial-only test data was not included and information from that test had to be conveyed through the initial parameter seeds used in conjunction with FEMU. This approach eliminates the need to analyze the large number of time steps from the cyclic test (8,271 steps) during each function evaluation in the FEMU. However, it is useful to look at how well the identified constitutive parameters fit the cyclic data. Furthermore,

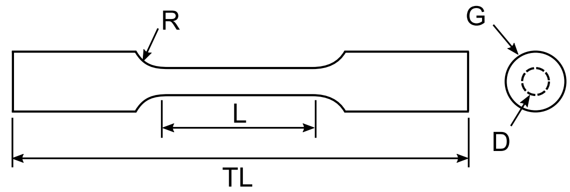

	Type I		Type II	
	mm	in	mm	in
D	9.53	0.375	6.35	0.250
L	44.50	1.752	19.00	0.748
R	50.80	2.000	25.40	1.000
G	12.70	0.500	12.70	0.500
TL	136.00	5.354	136.00	5.354

Figure 7.1: Specimen designs used for the multiaxial tests. Type II is capable of fully reversed loading, while Type I is not.

it is informative to analyze the final parameters for other tension tests conducted at different strain rates.

7.1.1 Tension

Three separate tension tests have been used to identify the rate-dependent parameters of the constitutive model, as previously discussed in Section 6.3. Only one of these tests (rate of 1×10^{-4} m/m/s) has been used during the optimization in the autonomous test FEMU. Figure 7.2 shows the experimental stress-strain curves and the corresponding FE results for best initial and final parameters. Both sets of FE results are notably in error for the sharp yield exhibited by Ti-6Al-4V. The higher rate tests also show more softening as the strain increases, which is not captured in the constitutive model. Table 7.2 shows the mean and maximum absolute errors for the two sets of constitutive parameters for the three rates. The maximum errors are large; however, the initial seeds for the optimization have been determined using both the 1×10^{-4} m/m/s tension test and the strain-controlled fully reversed cyclic loops. Table 7.3 shows the normalized sum of the squares of the residual error for the initial and best parameters for each of the rates. Errors could be reduced by only fitting to the tensile data; however, this would adversely affect the error for all other types of tests.

Table 7.2: Absolute error (MPa) for three tension tests at various rates for the initial and best set of constitutive parameters.

	Error (MPa)			
	Initial		Best	
Rate	Mean	Max	Mean	Max
1.00E-02	39.1	118.0	33.4	85.7
1.00E-03	27.6	124.8	21.8	92.9
1.00E-04	20.1	114.6	16.0	85.5

Table 7.3: Normalized sum of the squares of the residual error for the initial and best parameters for tension tests conducted at three different rates.

		Cumulative Normalized Error (MPa^2)	
Rate	Points	Initial	Best
1.00E-02	96	1,706	1,201.3
1.00E-03	96	1,060	649
1.00E-04	96	801	461

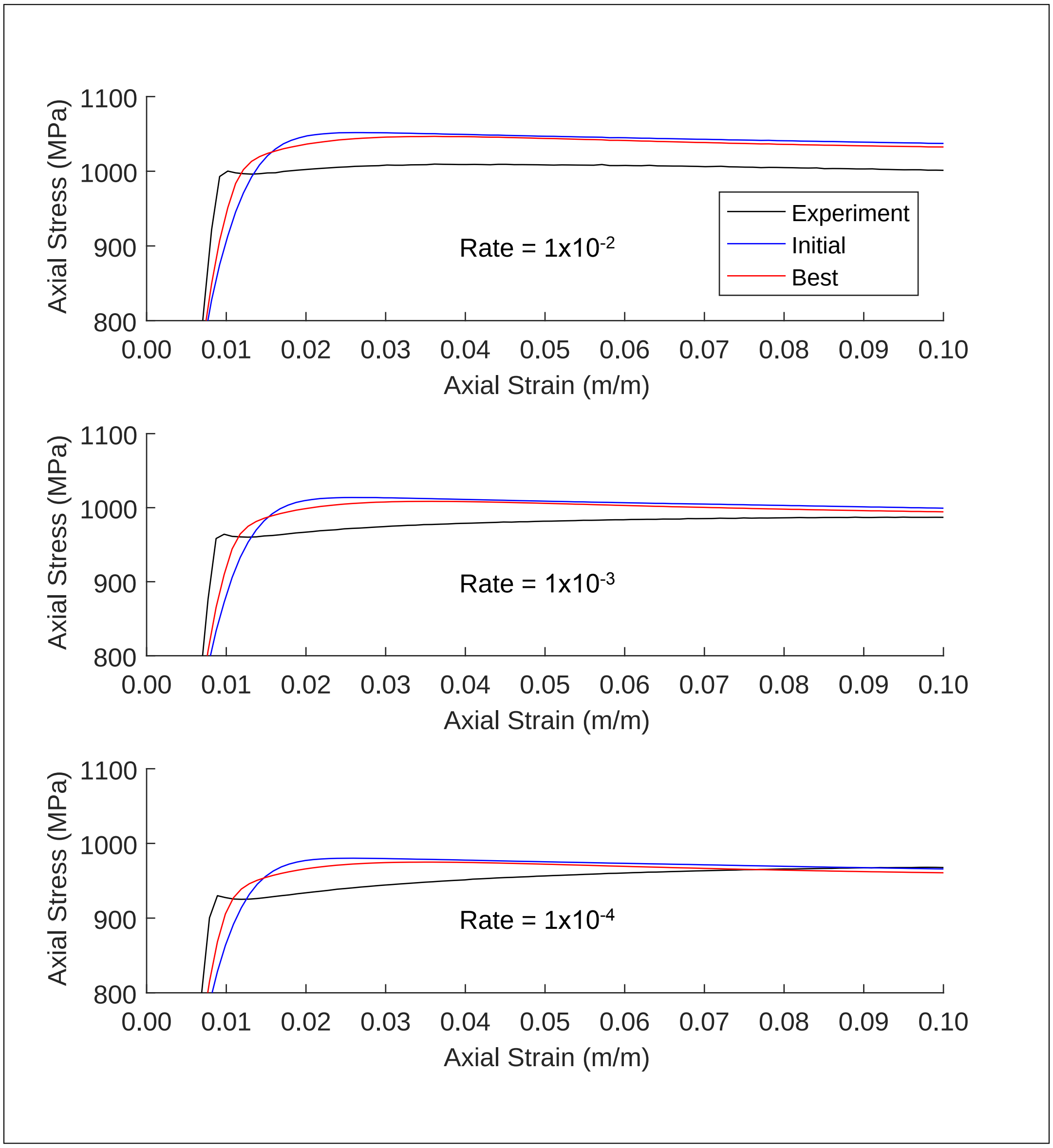

Figure 7.2: Axial stress vs. strain for the various tension tests and the corresponding FE results using the best set of constitutive parameters.

7.1.2 Axial Cycles

A subset of data from the axial-only strain-controlled cyclic test has been used during the initial parameter fitting prior to the autonomous experiment. Only the strain loops for 0.015 m/m and below have been used. Strain loops of 0.0175, 0.0200, and 0.0225 m/m were also performed. The strain controlled test was conducted at a rate of 1×10^{-3} m/m/s. Figure 7.3 shows the experimental stress vs. strain and the FE results using the two parameter sets for the entire cyclic test. Figure 7.4 shows the normalized cumulative squared residual error over the entire duration of the cyclic tests. For comparison, the five parameter sets identified during the initial fitting (Table 6.3) are also shown on the plot as dashed lines.

The stress-strain data and the cumulative error indicate the best set of parameters from the autonomous experiment deviate from the axial-only cyclic test and more closely resemble the initial response of the material which leads to increased error at higher strain loops. However, all the parameter sets show large increases in cumulative error for loops greater than 0.0150 which were not included in the parameter fitting. All the sets compromise on the accuracy for the initial loops and the end loops, with some better correlated to the initial (Best, Case 81, Case 41) and others to the higher strain loops (Initial, Case 63, Case 38). The compromise indicates a deficiency of the constitutive model which requires the parameters to favor either the initial behavior or the behavior after significant plastic strain seen in the large strain range loops. It cannot capture both of these effects.

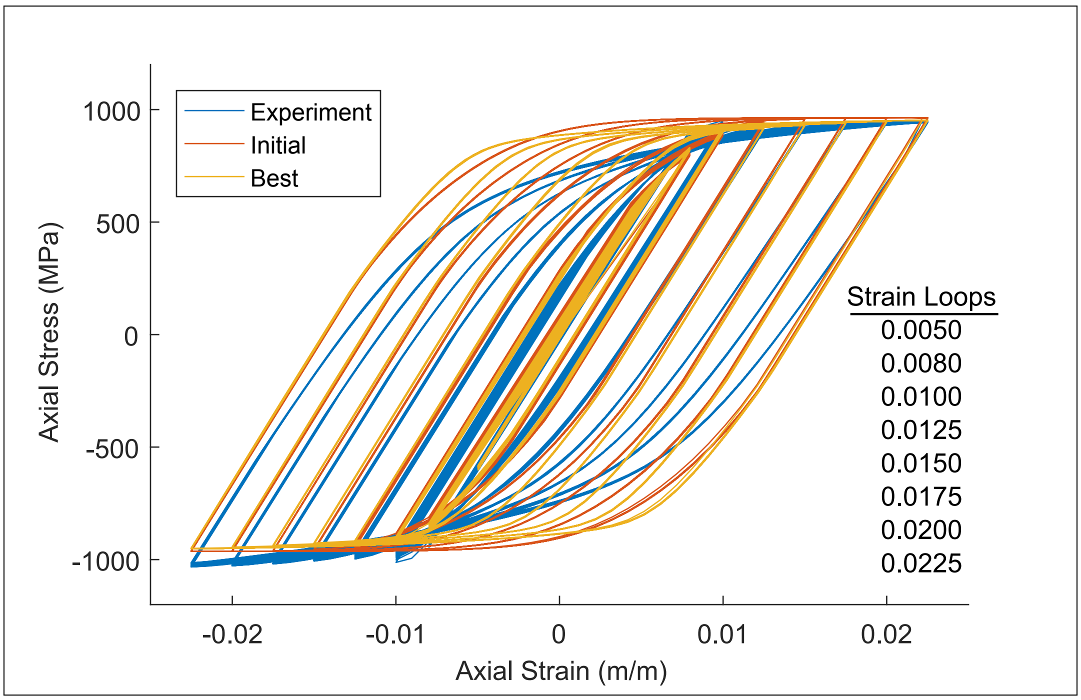

Figure 7.3: Axial stress vs. strain for the loops of the axial-only strain-controlled cyclic test (rate of 1×10^{-3} m/m/s), and the corresponding FE results for the top initial and the best constitutive parameters.

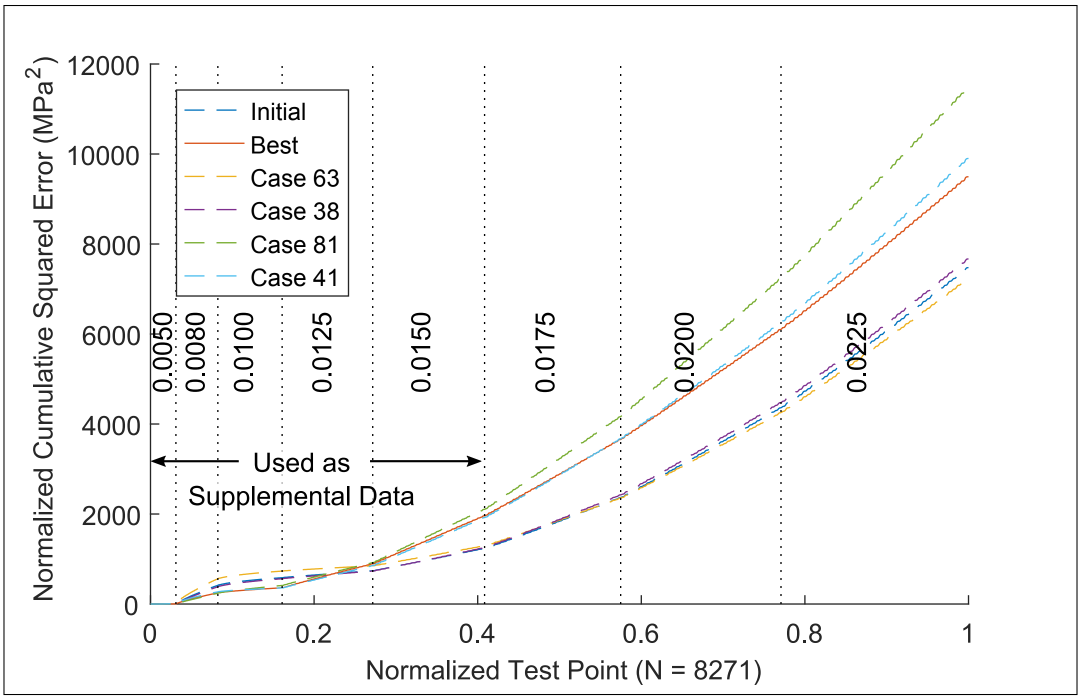

Figure 7.4: Normalized cumulative squared residual error for the axial-only cyclic test for the best set of parameters (solid line) and the five initial parameter seeds identified with the supplemental data (dashed lines). Strain loop magnitudes are divided by the vertical dashed lines with the magnitude given in (m/m) as the vertical text.

7.2 Multiaxial Loading - No Compressive Strain

The simulated experiment (Evaluation 3) outlined in Section 5.4.3 was attempted using the integrated methodology. However, the Type II specimen design (which is configured for fully reversed loading) prevents the use of the extensometer. As such, axial and shear strain gages were used, but were found to have a very short fatigue life at strain levels on the order of 0.010 m/m. Conversations with the gage manufacturer confirmed the very limited fatigue life of any type of strain gage under such large, repeated strains. Some experimental data is still useful, as modulus checks were performed intermittently to enable assessment of the strain signals. Therefore, the valid data from two of these attempted experiments can still be used as validation data for the identified parameters. The valid data includes only load excursions with no compressive strain. The strain gages failed prior to starting the fully reversed portion of the test. The test was controlled using pseudo-strain control at a target total strain rate of 5×10^{-4} m/m/s.

Figure 7.5 and 7.6 depict the experimental axial stress-strain curves and the FE results using the best parameters and the initial parameters for both of these attempted tests. Figure 7.7 and 7.8 are the corresponding shear stress-strain curves. Figure 7.9 and 7.10 show the condensed shear vs. axial strain points for each of the tests with the round limits and angular bins shown as dashed red lines. Figure 7.11 and 7.12 show the normalized cumulative squared residual error for both of the tests when using the best parameters and the initial parameters. Both of the test have calibration and validation excursions at maximum magnitudes of 0.0102 m/m and calibration excursions at a maximum magnitude of 0.0120 m/m.

The final parameter set performs better in both of the experiments. Both of the parameters have higher normalized errors for the second experiment compared to the first.

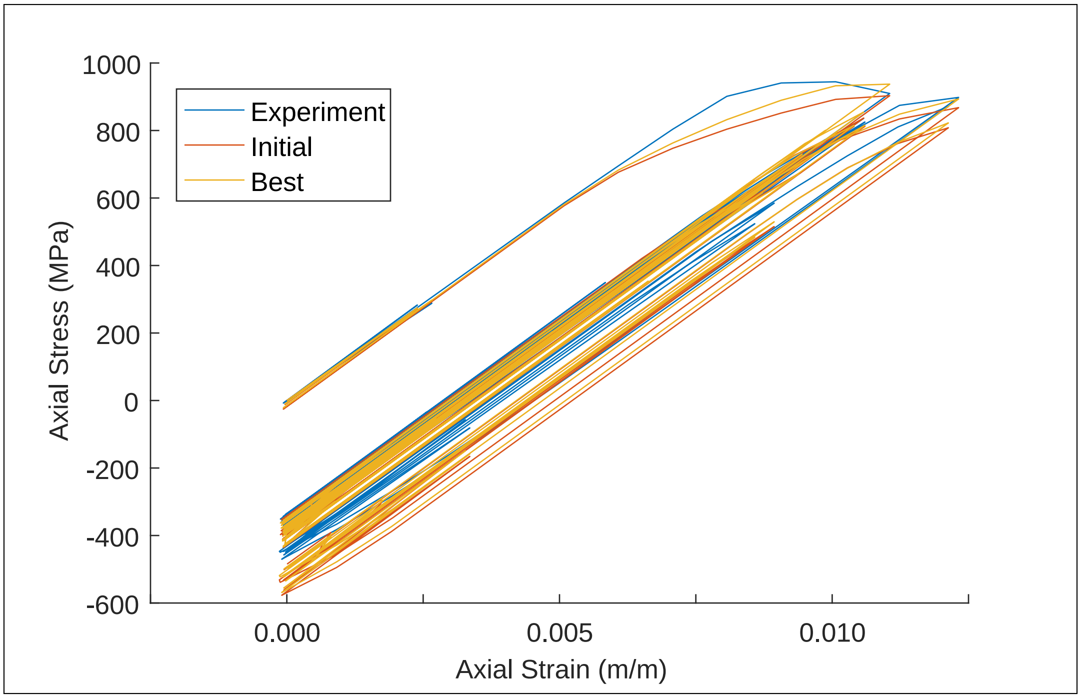

Figure 7.5: Axial stress vs. strain for the first multiaxial test and the corresponding FE results for the initial and best parameters.

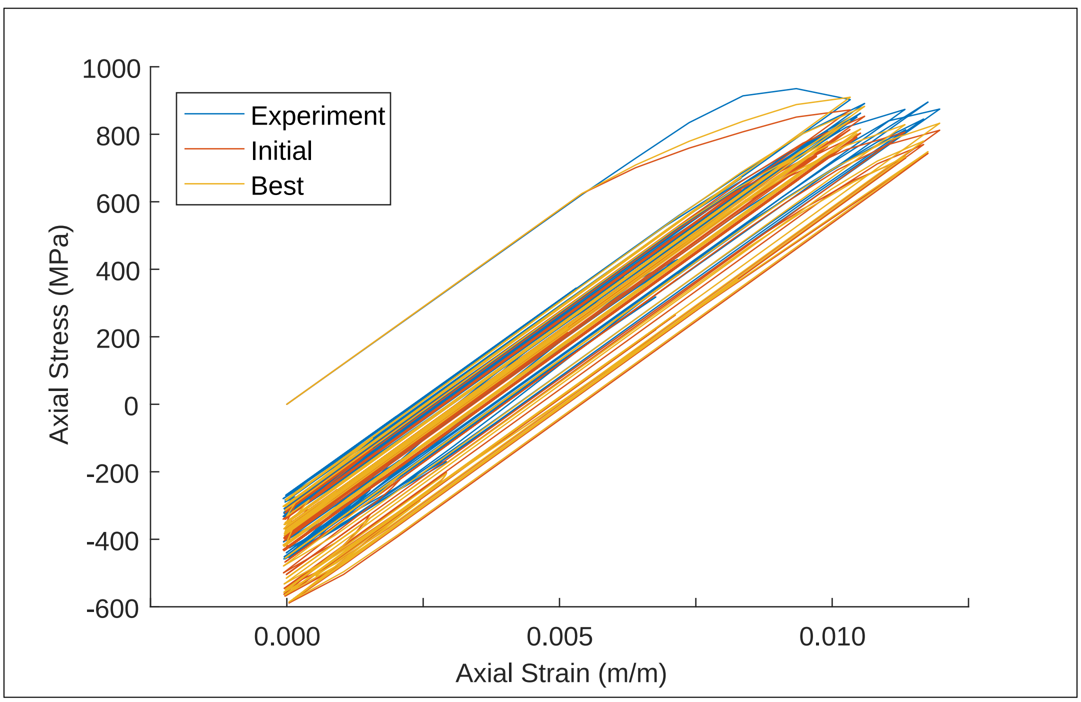

Figure 7.6: Axial stress vs. strain for the second multiaxial test and the corresponding FE results for the initial and best parameters.

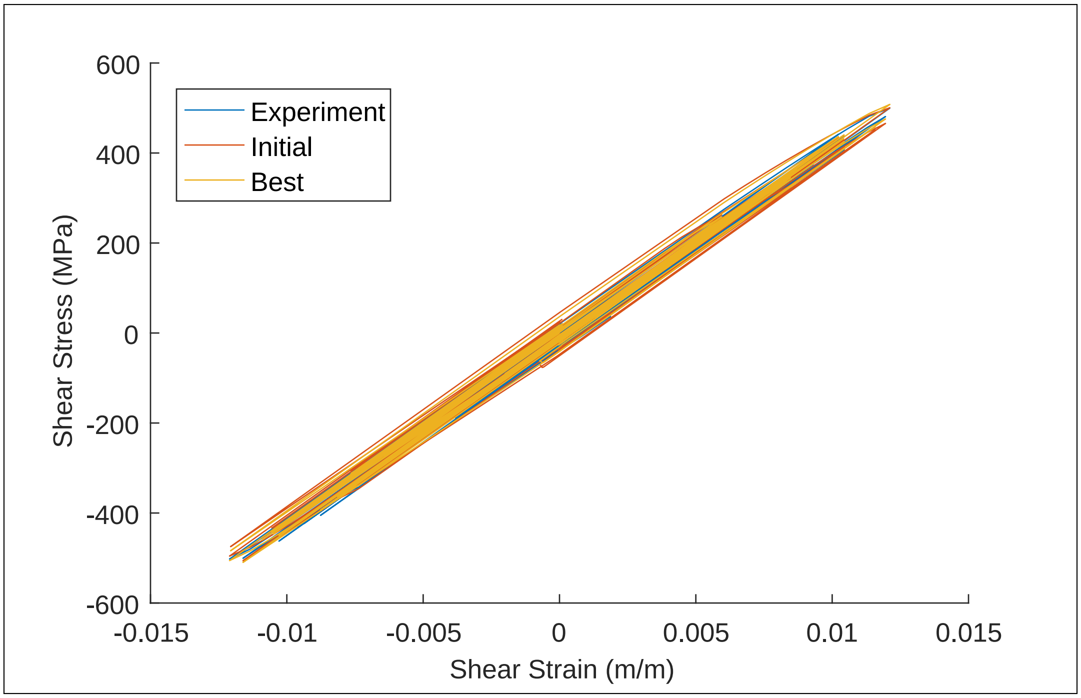

Figure 7.7: Shear stress vs. strain for the first multiaxial test and the corresponding FE results for the initial and best parameters.

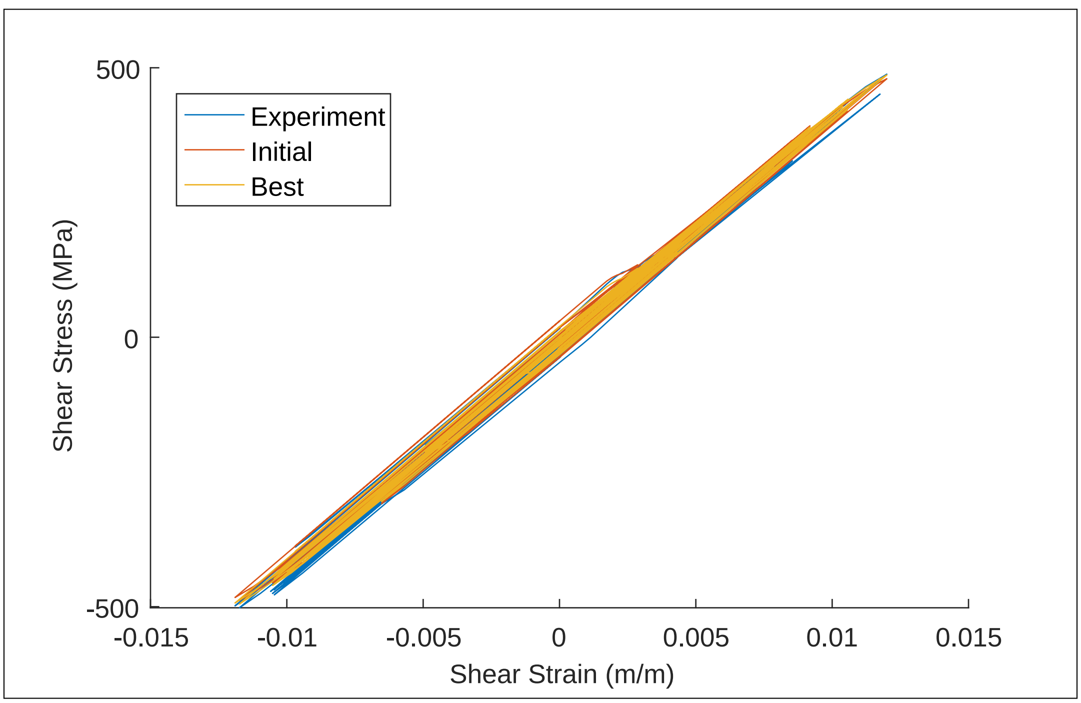

Figure 7.8: Shear stress vs. strain for the second multiaxial test and the corresponding FE results for the initial and best parameters.

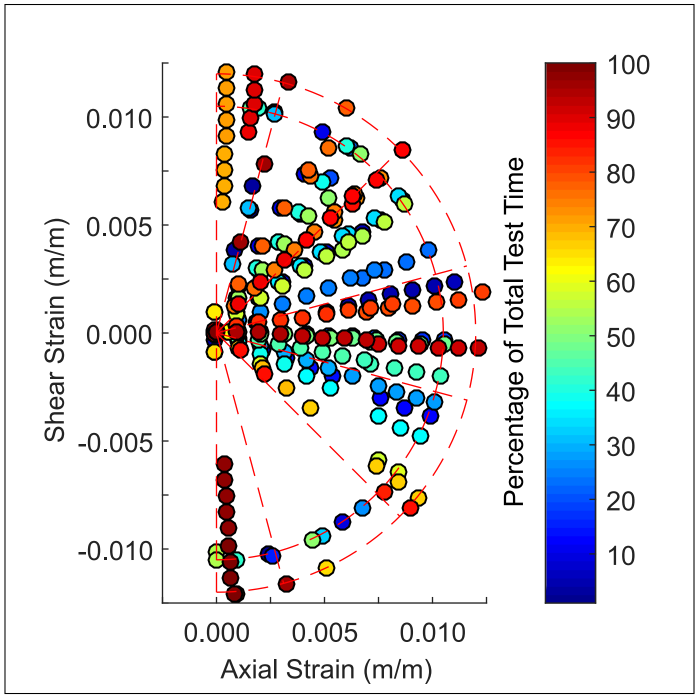

Figure 7.9: Condensed shear strain vs. axial strain for the first multiaxial test with no compressive strain. The color scale indicates increasing time during the test.

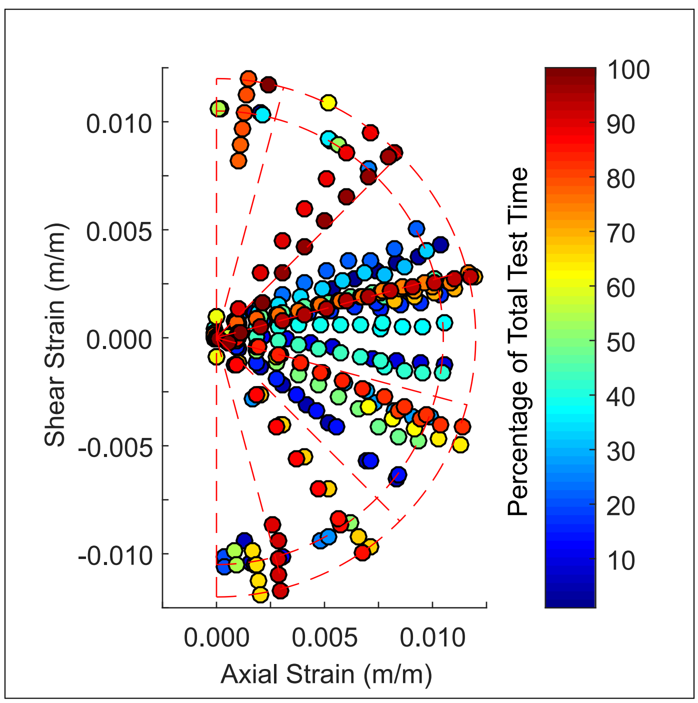

Figure 7.10: Condensed shear strain vs. axial strain for the second multiaxial test with no compressive strain. The color scale indicates increasing time during the test.

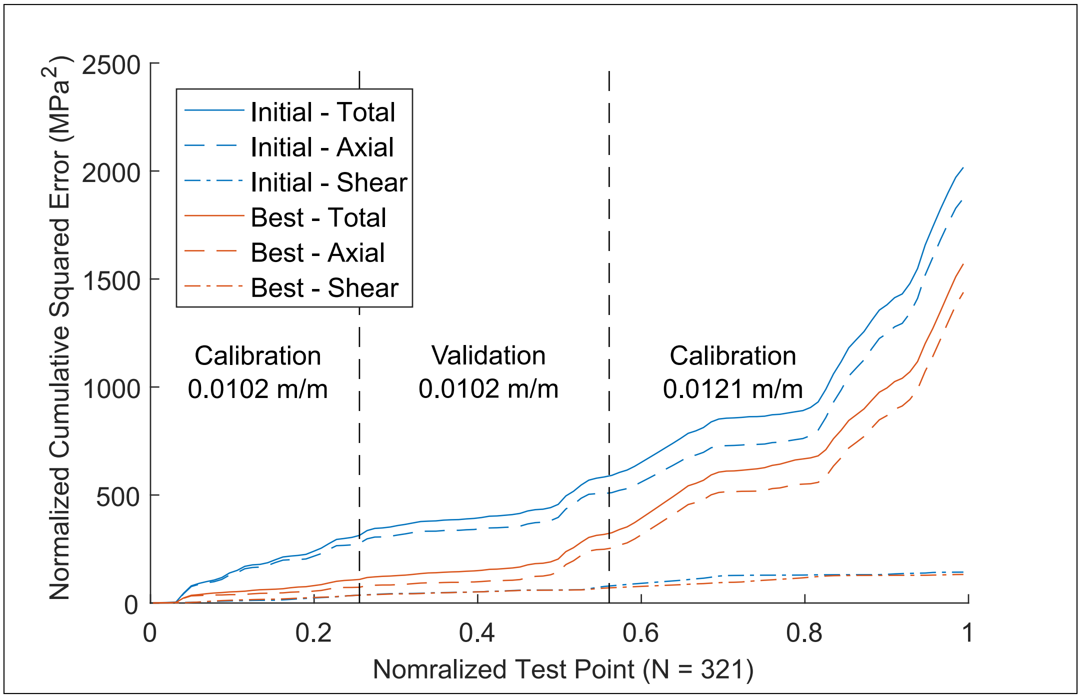

Figure 7.11: Normalized cumulative squared residual error for the first test when using the initial parameters and the best parameters.

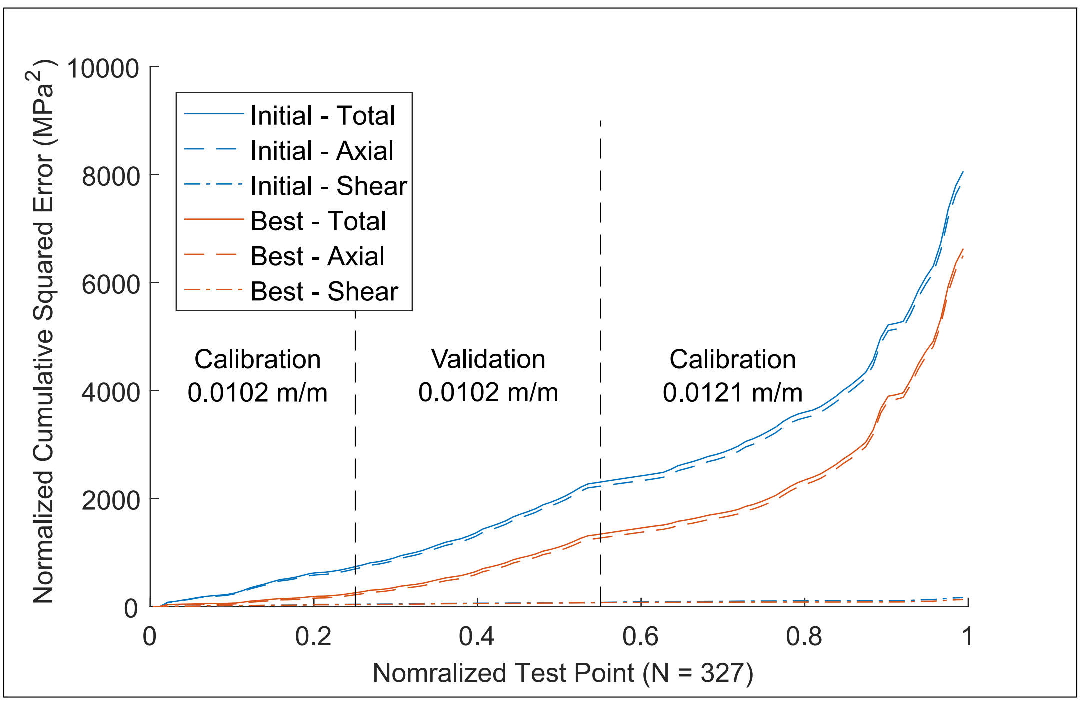

Figure 7.12: Normalized cumulative squared residual error for the second test when using the initial parameters and the best parameters.

7.3 Multiaxial Loading - Fully Reversed

A fully reversed multiaxial test was performed on Ti-6Al-4V using specimen Type II and strain gages to measure both axial and shear strain. The test was controlled using pseudo-strain control with a target total strain rate of 5×10^{-4} m/m/s. The test was allowed to run until the strain gages showed signs of failure, which occurred after four discrete cycles. Modulus checks were performed at the conclusion of each cycle to assess the strain signal integrity. Table 7.4 provides a summary of the load excursions that were completed and includes the stress and strain at the end of each excursion. The errors (defined as the difference between experimental and predicted stress) are given for the initial parameters and the best parameters. Figure 7.13 shows the experimental and FE results for the axial stress and strain. Similarly, Fig. 7.14 shows the shear stress and strain. Figure 7.15 shows the condensed axial strain and shear strain data points. Figure 7.16 compares the normalized cumulative squared residual error for the best parameters and the top initial seed for the fully reversed multiaxial cycles.

The best parameter set outperforms the initial parameters again. However, both sets have larger errors for the axial compressive strain endpoints. This is likely due to the non-symmetric behavior seen in the axial stress-strain curve (Fig. 7.13). The general trend of the constitutive model is correct, but initial errors from the first load excursion cause continual error in subsequent measurements leading to higher normalized residual errors.

Table 7.4: Segment end points, experimental strain, stress, and finite element error for the multiaxial fully reversed test. Errors are shown for the initial parameters and the best parameters.

					Error (MPa) = Exp. Stress - FE Stress			
	Exp. Strain (m/m)		Exp. Stress (MPa)		Initial Parameters		Best Parameters	
End Point	Axial	Shear	Axial	Shear	Axial	Shear	Axial	Shear
1	0	0	0.9	0.0	0.2	0.1	0.2	0.1
2	9.18E-03	-4.44E-03	937.8	-167.3	85.4	2.2	43.9	7.3
3	-9.10E-03	4.49E-03	-993.3	164.6	-119.0	-11.2	-76.4	-16.1
4	0	0	140.2	-42.6	-65.8	-16.8	-24.2	-21.6
5	9.10E-03	-4.29E-03	895.8	-162.0	35.2	6.2	-13.0	11.3
6	-9.17E-03	4.47E-03	-988.9	155.7	-121.7	-15.4	-79.3	-20.5
7	0	0	143.9	-45.6	-76.0	-17.7	-34.4	-22.7
8	7.36E-03	8.46E-03	775.2	310.7	25.3	12.4	-15.0	-0.3
9	-7.16E-03	-8.47E-03	-814.2	-383.2	-118.7	-16.7	-88.6	-7.2
10	0	0	56.7	1.6	-97.0	-8.6	-66.5	1.0
11	7.17E-03	8.47E-03	760.4	313.1	31.8	-2.9	-3.0	-10.8
12	-7.15E-03	-8.48E-03	-816.9	-377.4	-116.5	-19.8	-86.4	-9.6
13	0	0	53.9	3.4	-95.5	-16.6	-65.0	-6.3

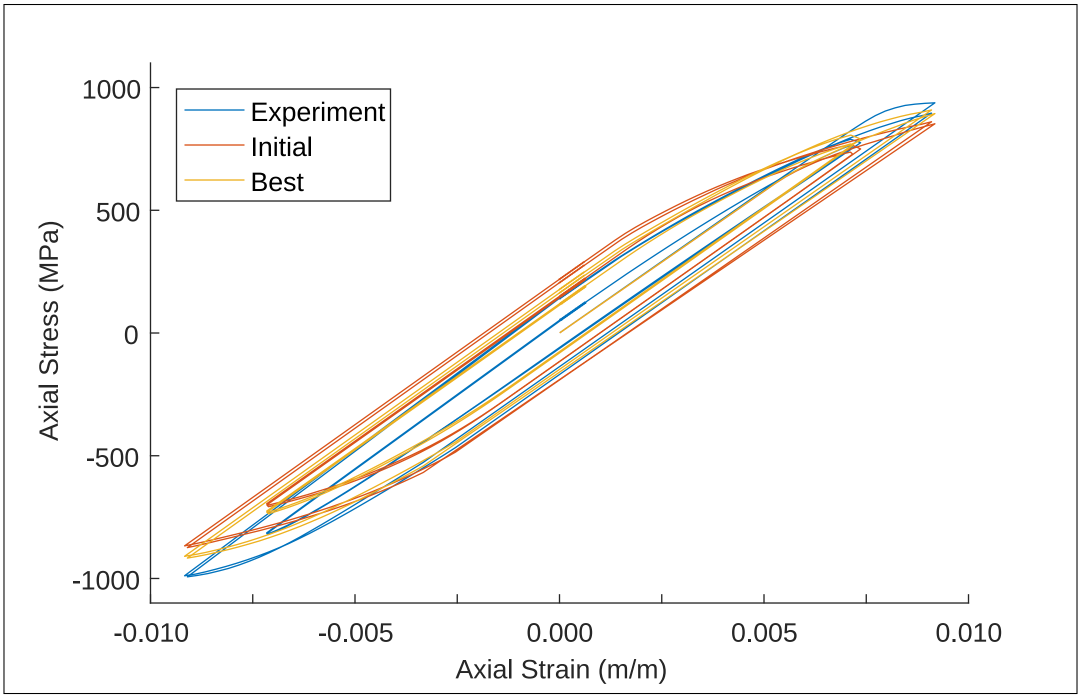

Figure 7.13: Axial stress vs. strain for the fully reversed multiaxial test and the corresponding FE results using the initial and best parameters.

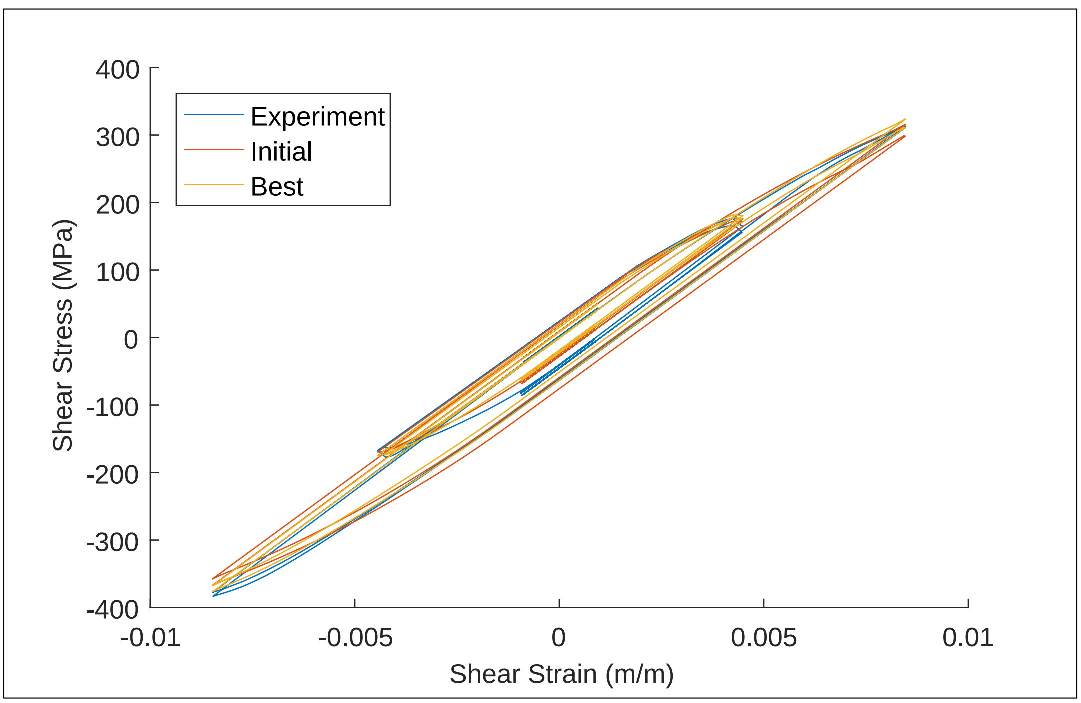

Figure 7.14: Shear stress vs. strain for the fully reversed multiaxial test and the corresponding FE results using the initial and best parameters.

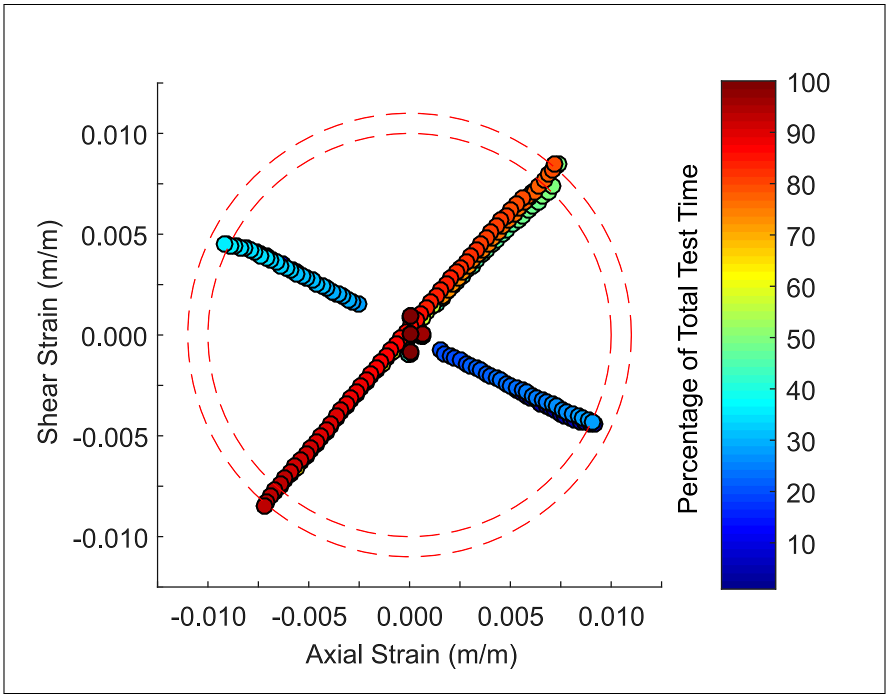

Figure 7.15: Condensed shear strain vs. axial strain for the fully reversed multiaxial test. The color scale indicates increasing time during the test.

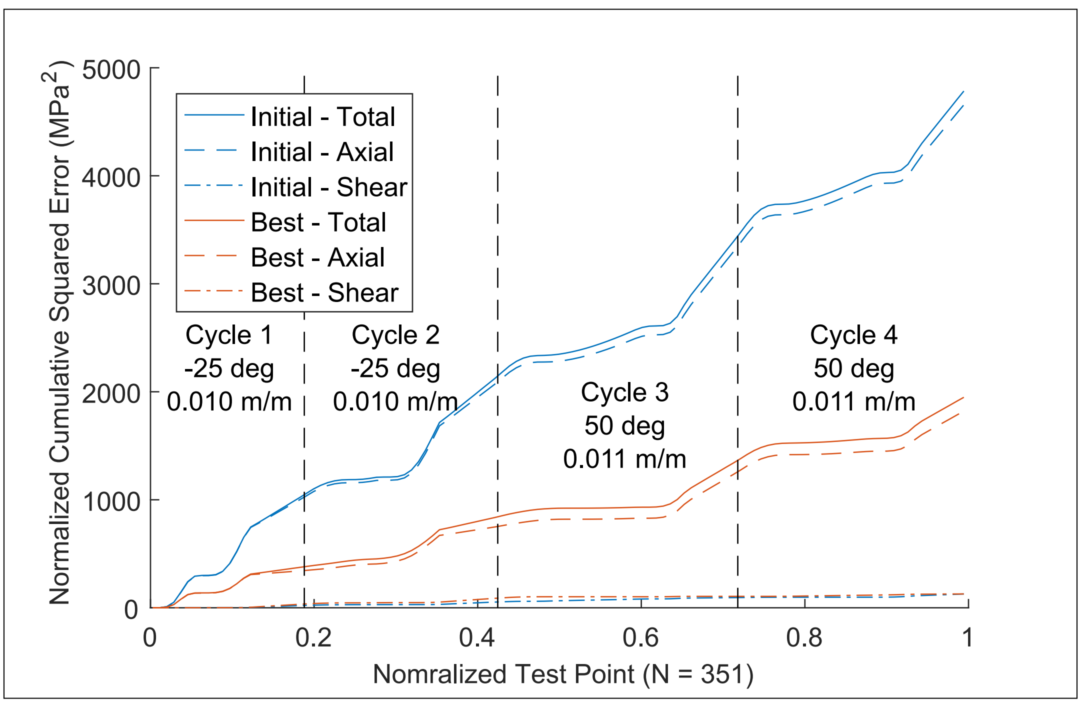

Figure 7.16: Normalized cumulative squared residual error for the fully reversed multiaxial test for the initial and best parameters.

7.4 Torsion

A torsion test has been conducted using specimen Type I which is solid and has a diameter of 9.53 mm in the gage section. While the specimen has a long enough gage section to accommodate the multiaxial extensometer, the extensometer has a rotation limit of 5 degrees. For the specimen diameter, this only allows for strains up to 0.015 m/m. Therefore, strain gages were installed on the specimen and used to measure strain. Modulus checks were performed using both the extensometer and strain gages. Then the extensometer was removed prior to starting the torsion tests to prevent damage to the extensometer.

The rotary actuator is only calibrated for $\pm$ 50 degrees rotation; thus, rotations of $\pm$ 45 degrees were used as the limit for the test. The 45 degree rotation of the actuator only leads to approximately 0.065 m/m shear strain on the surface of the specimen. This is not enough to break the specimen as the shear strain near the center of specimen is negligible due to the radial dependency of shear strain. Therefore, the specimen underwent $\pm$ 45 degree rotation under angular control while holding the axial stroke fixed to prevent axial expansion or contraction.

Table 7.5 shows the progression of cycles, as well as the associated rates and cycle counts. The strain gages lasted for only one cycle. Figure 7.17 shows the shear stress vs. strain curves for the experimental cycles during which the strain gages were still performing well. The figure also shows the FE results using both the initial and best parameters. Both sets of stresses are computed based on the engineering shear stress assumption, $\tau = Tr/J$, where T is torque in N-mm, r is the outer radius in mm, and J is the polar moment of inertia in mm^4.

In the FE solution, the shear stresses within the elements are integrated to obtain the resulting torque for use in the engineering shear stress calculation. Thus, Fig. 7.17 is essentially comparing a normalized torque versus engineering shear strain. This is done because the actual stress within a solid cylinder (or thick-walled tubular specimen) is not uniquely defined once the material is plasticity deformed. Others have developed shear stress formulations for plasticity, but the shear stress quantity is tied to assumptions made in the constitutive relationship. The normalization of torque into engineering stress is convenient for recognizing the approximate stress and also for use in error metrics that combine shear stresses and axial stresses.

Figure 7.18 shows the normalized cumulative squared residual error for the best parameters and the top initial seed. The best parameters led to less residual error than the initial parameters that are only calibrated with axial data. However, both sets of constitutive parameters significantly over-predict the torque upon load reversal.

After failure of the strain gages, shear cycles were continued until the torque required to perform the rotation dropped significantly. When the required torque began to drop, cracks were visible on the surface of the specimen during the rotation. After approximately 70 shear cycles, the rotary actuator was returned to 0 degrees, and the specimen was pulled to failure under axial stroke control so the fracture surfaces within the specimen could be visualized. While data could not be captured for the entire test, the resulting fracture surface is quite intriguing. Figure 7.19 shows different views of the fracture surface under various levels of magnification.

Table 7.5: Definition of test cycles including cycle count and frequency for the torsional test.

Type	Start (deg)	Level 1 (deg)	Level 2 (deg)	Time (sec)	Rate (deg/sec)	Freq	Cycles	Gage Status
ramp	0	45	-	500	0.09	-	-	good
ramp	45	-45	-	500	-0.18	-	-	good
modcheck	-45	-44	-45	-	0.10	0.100	4	good
ramp	-45	0	-	250	0.18	-	-	good
modcheck	0	-1	1	-	-0.20	0.100	4	good
cycles	0	45	-45	-	0.45	0.005	4	bad
cycles	-45	45	-45	-	4.50	0.050	10	bad
cycles	-45	45	-45	-	4.50	0.050	10	bad
cycles		45	-45	-	4.50	0.050	10	bad
cycles		45	-45	-	4.50	0.050	10	bad
cycles		45	-45	-	4.50	0.050	10	bad
cycles	-45	45	-45	-	9.00	0.100	10	bad
ramp	-45	0	-	30	1.50	-	-	bad
pull to failure								bad

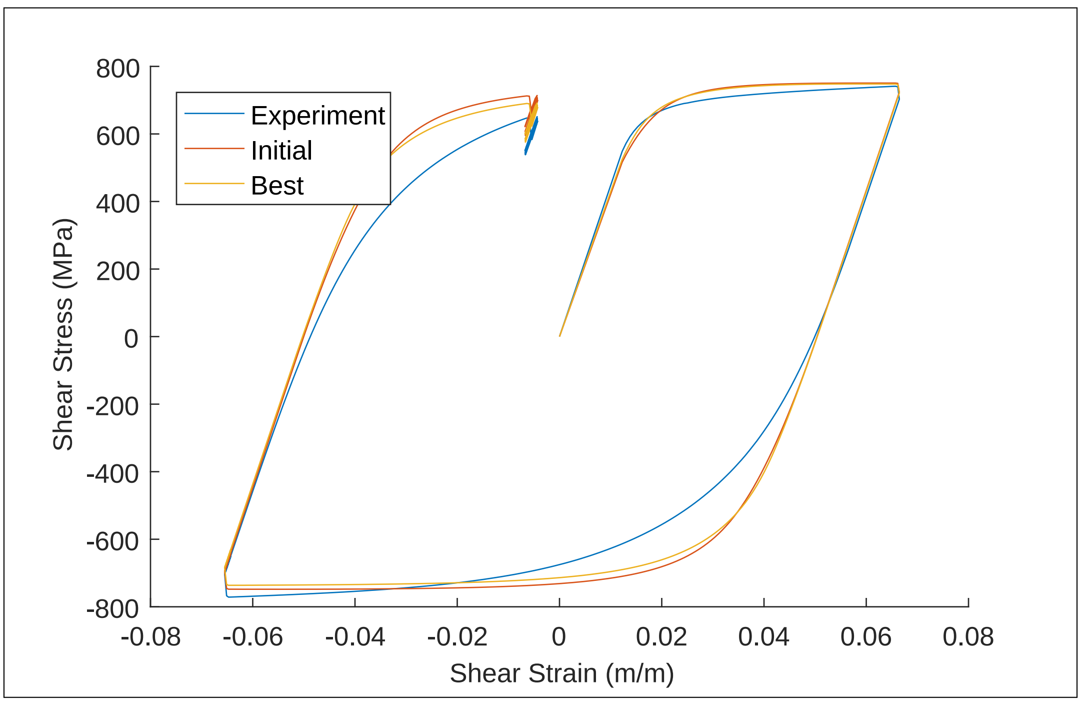

Figure 7.17: Engineering shear stress vs. strain for the torsion test performed on the solid cylindrical specimen and the corresponding FE results using the initial parameters and the best parameters.

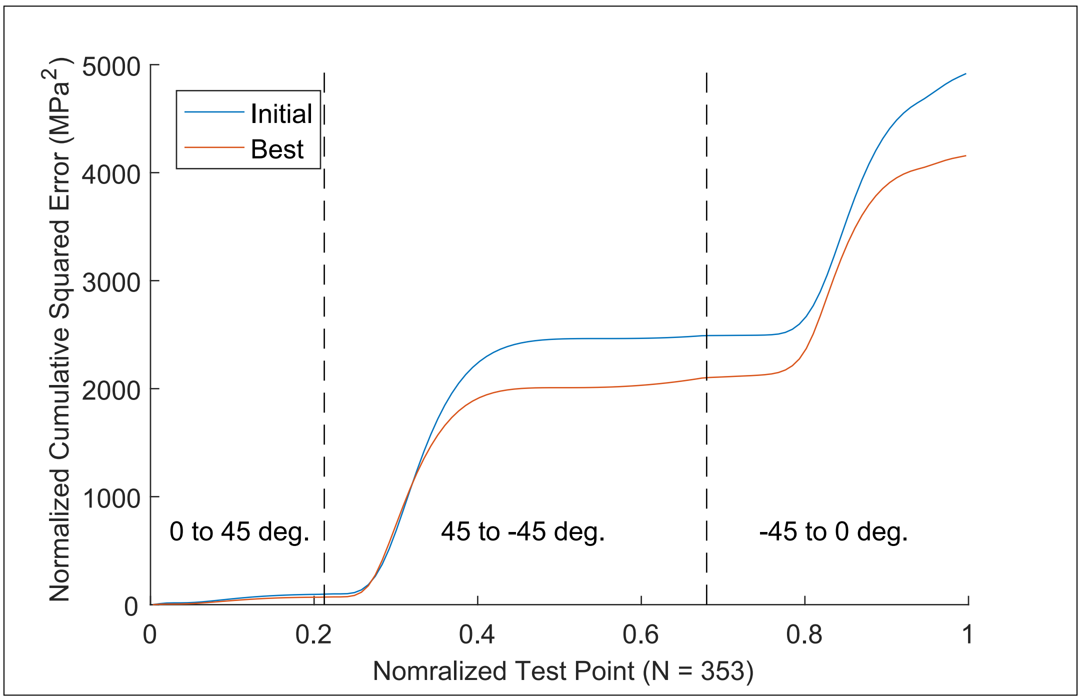

Figure 7.18: Normalized cumulative squared residual error for the torsion test for the best parameters and the top initial seed.

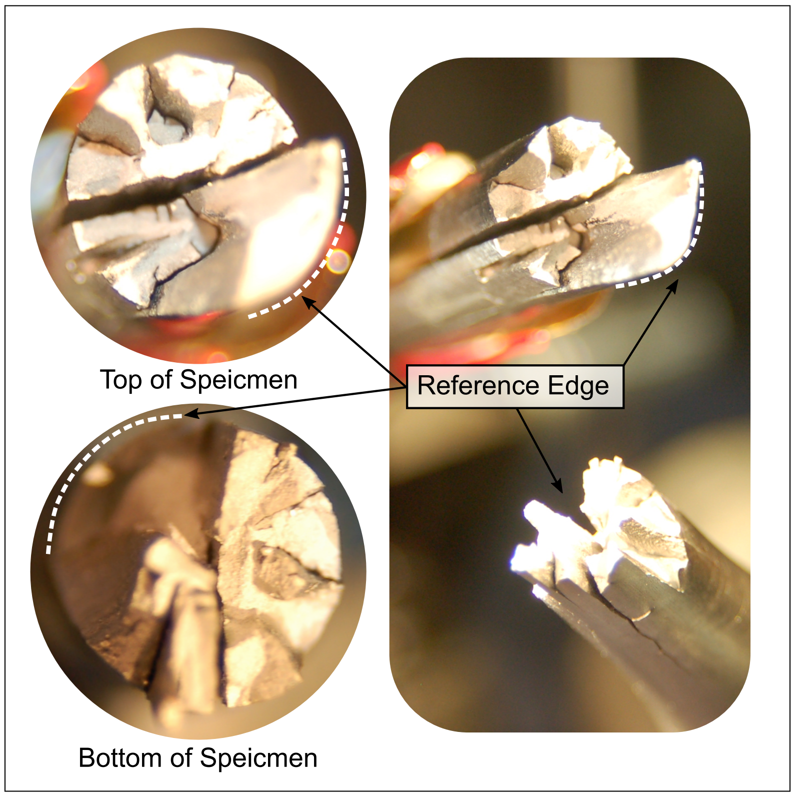

Figure 7.19: Fracture surfaces for the torsion specimen after pulling to failure.

7.5 Multiaxial Loading - Traveling Boxes

The final validation experiment is a complex multiaxial load path that works within the confines of the hardware capacity and the instrumentation limits. Again, a Type I specimen has been used (solid, 9.53 mm gage diameter, 44 mm gage length) to accommodate the axial-torsional extensometer. A large number of the multiaxial experiments have been conducted for proportional loading (traveling along a certain angle in the shear-axial strain space). Additional insight can be gained by varying the type of excursion to determine if the material responds to changes in proportion or loading type. Therefore, a traveling box test has been conducted within the allowable shear-axial strain space. When traveling along a box in this space, one component of strain is changed while the other is held fixed. This is in contrast to the proportional tests in which both components of strain change simultaneously at fixed proportions.

The extensometer has been calibrated for $\pm$ 5 mm displacement (over a 25 mm gage length) and $\pm$ 5 degrees rotation. For the chosen specimen, this limits the axial strain to 0.05 m/m and the shear strain on the surface of the specimen to approximately 0.015 m/m. Therefore, the boxes have been designed to fit within these limits. Figure 7.20 shows the first set of boxes that end at angular positions (when viewed from the origin of the box) of 80, 60, 45, 30, 15, and 0 degrees. The radius of the circle that encompasses every box is 0.014 m/m. Each box has been repeated twice before moving to the next box. For each subsequent box type, the origin of the axial strain is increased by 0.001 m/m, thus arriving at a series of boxes that travel along the axial strain axis. Figure 7.21 shows the complete theoretical history of axial and shear strain for the entire experiment.

After completing the traveling boxes, additional loading excursions shaped like half-circles were conducted. Figure 7.22 and Fig. 7.23 show the shear strain vs. axial strain for the traveling boxes and the subsequent half-circles. Figure 7.24 and 7.25 show the axial and shear stress-strain curves for the experiment and the FE results using the top initial parameter set and the best set of constitutive parameters. Figure 7.26 shows the normalized cumulative squared residual error for both parameter sets. Finally, Fig. 7.27 shows the initial stresses for both axial (top) and shear (bottom) from the experiment and from the predictions using both parameter sets.

The normalized cumulative error for both parameter sets are quite large. The initial stresses shown in Fig. 7.27 reveal that stresses from both FE results deviate from the experiment during the first box. The increase in axial errors occur for the far right vertical segment of the boxes (constant axial strain, while shear strain is decreased from positive to negative). Both parameter sets over-predict the axial softening during the application of shear strain. The traveling boxes prove difficult for the chosen viscoplasticity model. The significant increase in error when compared to the proportional tests highlights the need for varied test conditions throughout the autonomous fitting processes. The box paths can easily be added as an option for the test block design during the autonomous testing. Future autonomous experiments could alternate between proportional excursions and these more complex excursions.

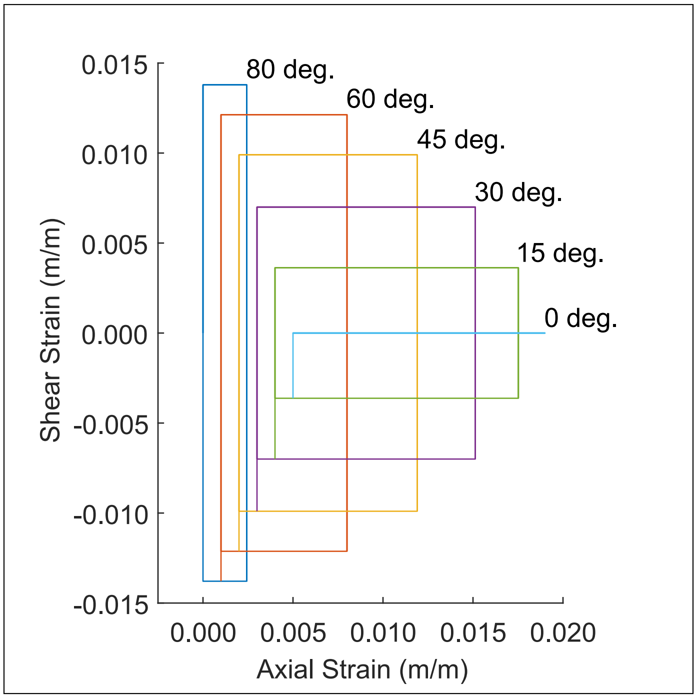

Figure 7.20: Illustration of the first series of boxes at 80, 60, 45, 30, 15, and 0 degrees.

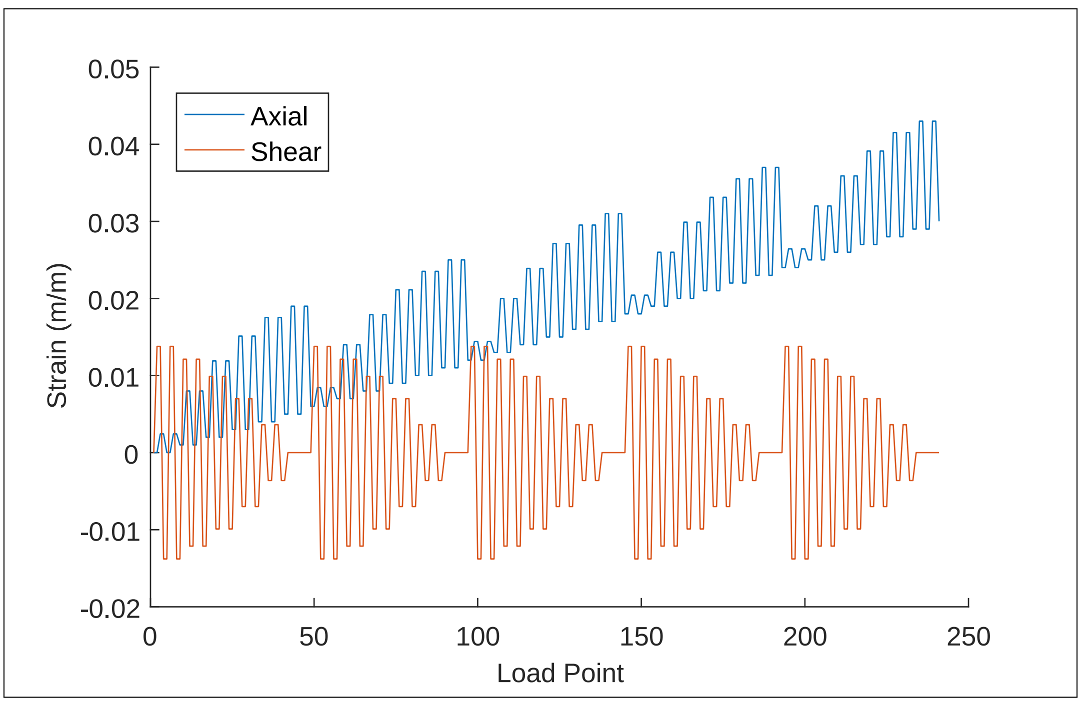

Figure 7.21: Theoretical axial and shear strain for the entire traveling box experiment. Each box is repeated twice and the axial origin of each new box type is increased by 0.001 m/m.

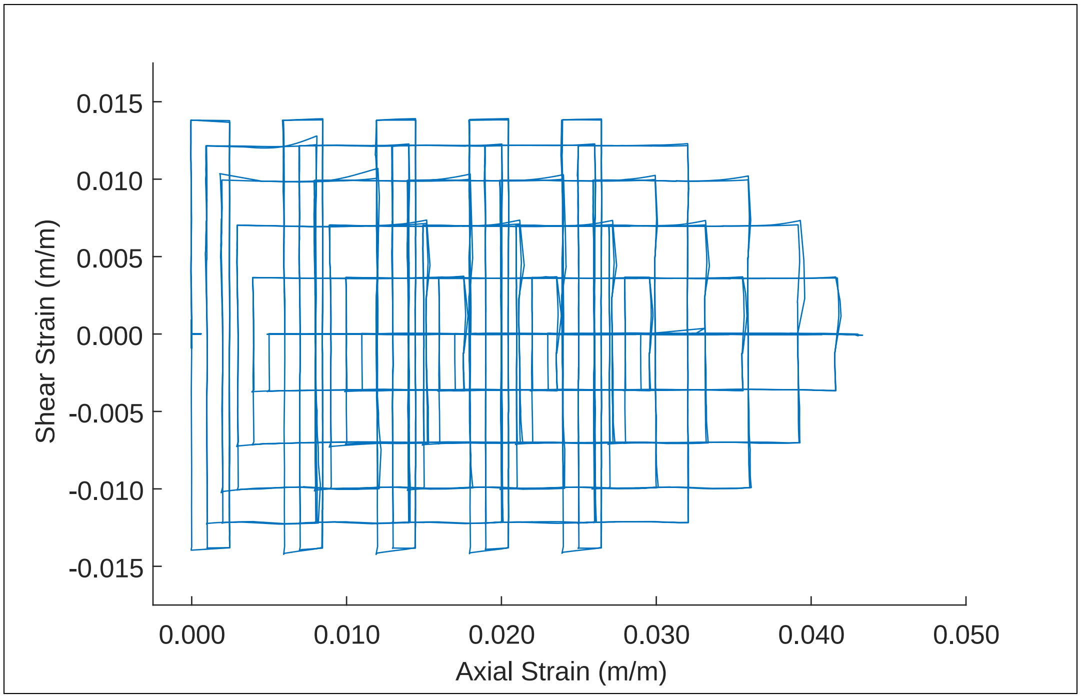

Figure 7.22: Experimental shear vs. axial strain for the traveling box experiment. Each box is repeated twice and the axial origin of subsequent box types is increased by 0.001 m/m.

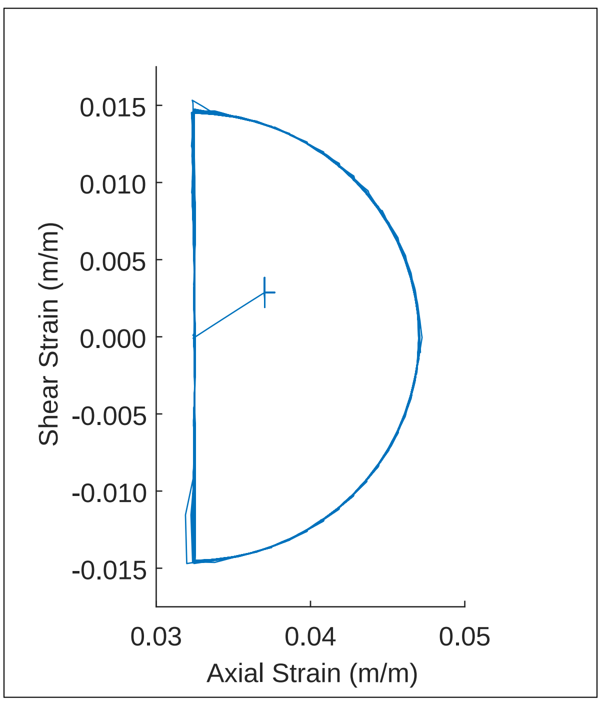

Figure 7.23: Experimental shear vs. axial strain for the half-circles completed after the traveling boxes. The direction of travel along the half-circles was changed periodically.

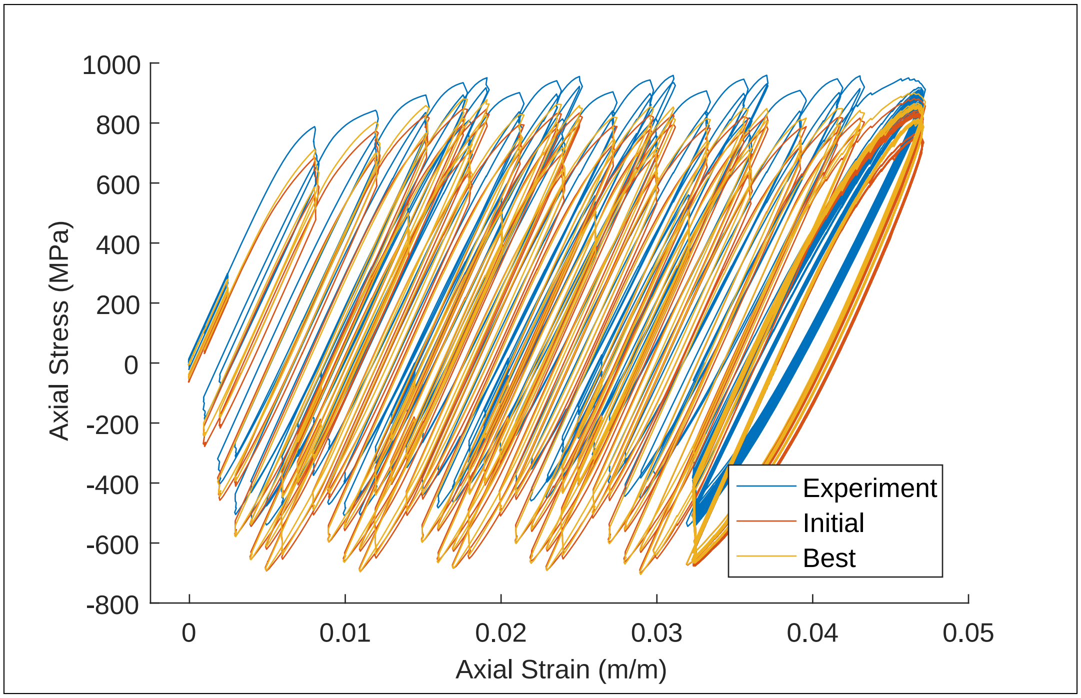

Figure 7.24: Axial stress vs. strain for the traveling box experiment and the corresponding FE analysis using the initial and best parameters.

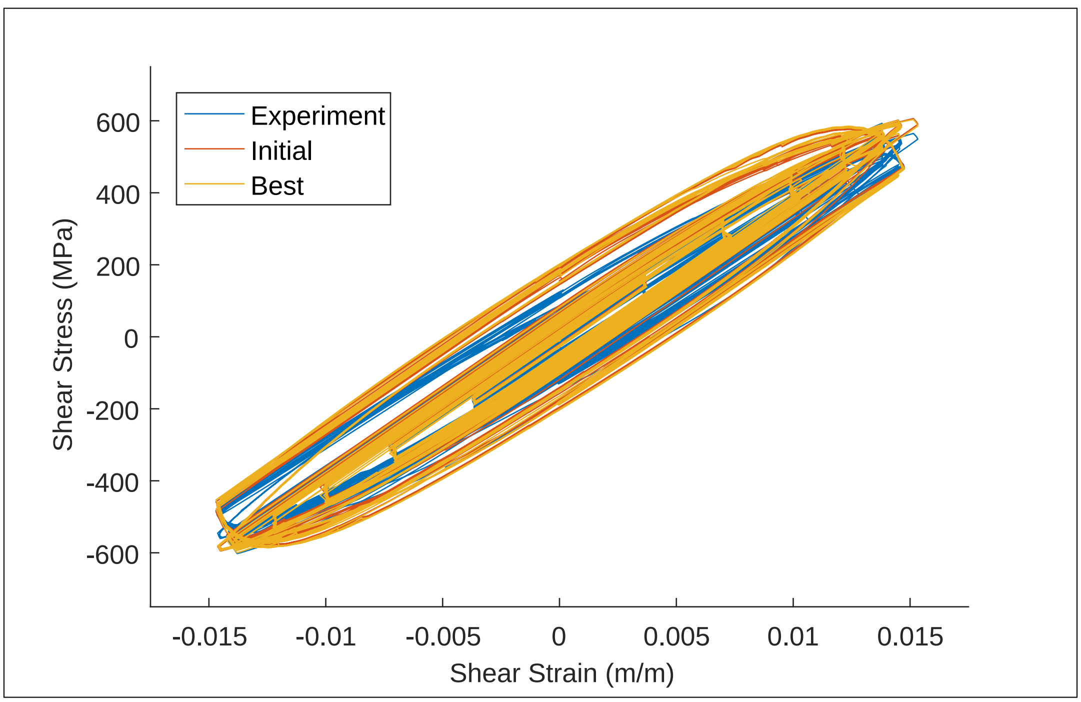

Figure 7.25: Shear stress vs. strain for the traveling box experiment and the corresponding FE analysis using the initial and best parameters.

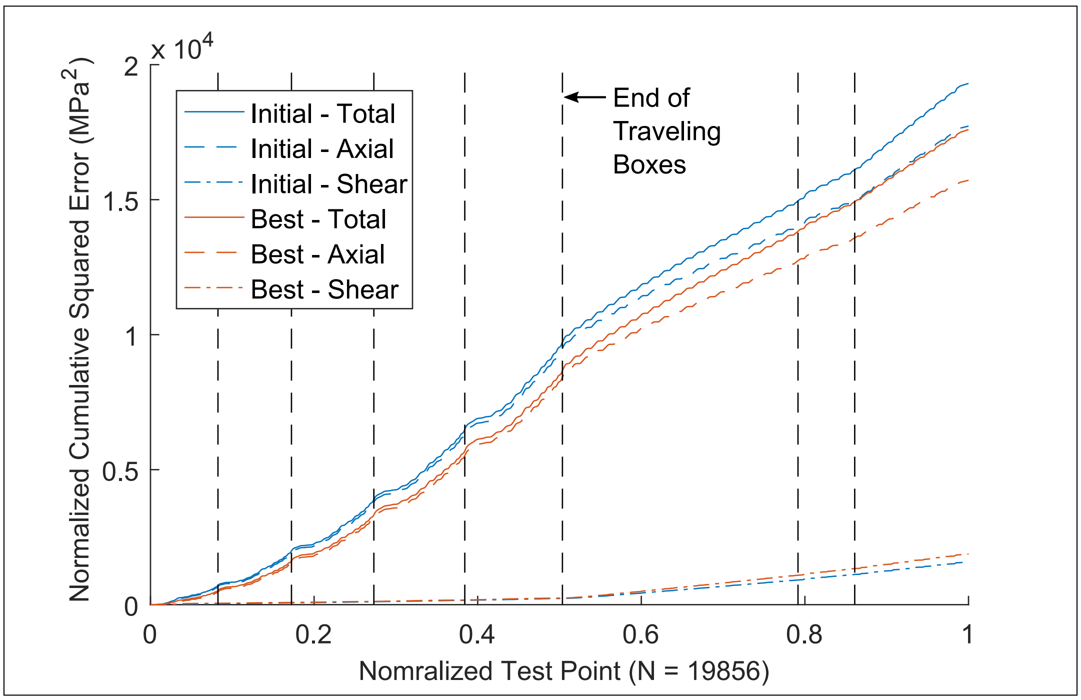

Figure 7.26: Normalized cumulative squared residual error for the FE analysis using the top initial parameters and the best parameters.

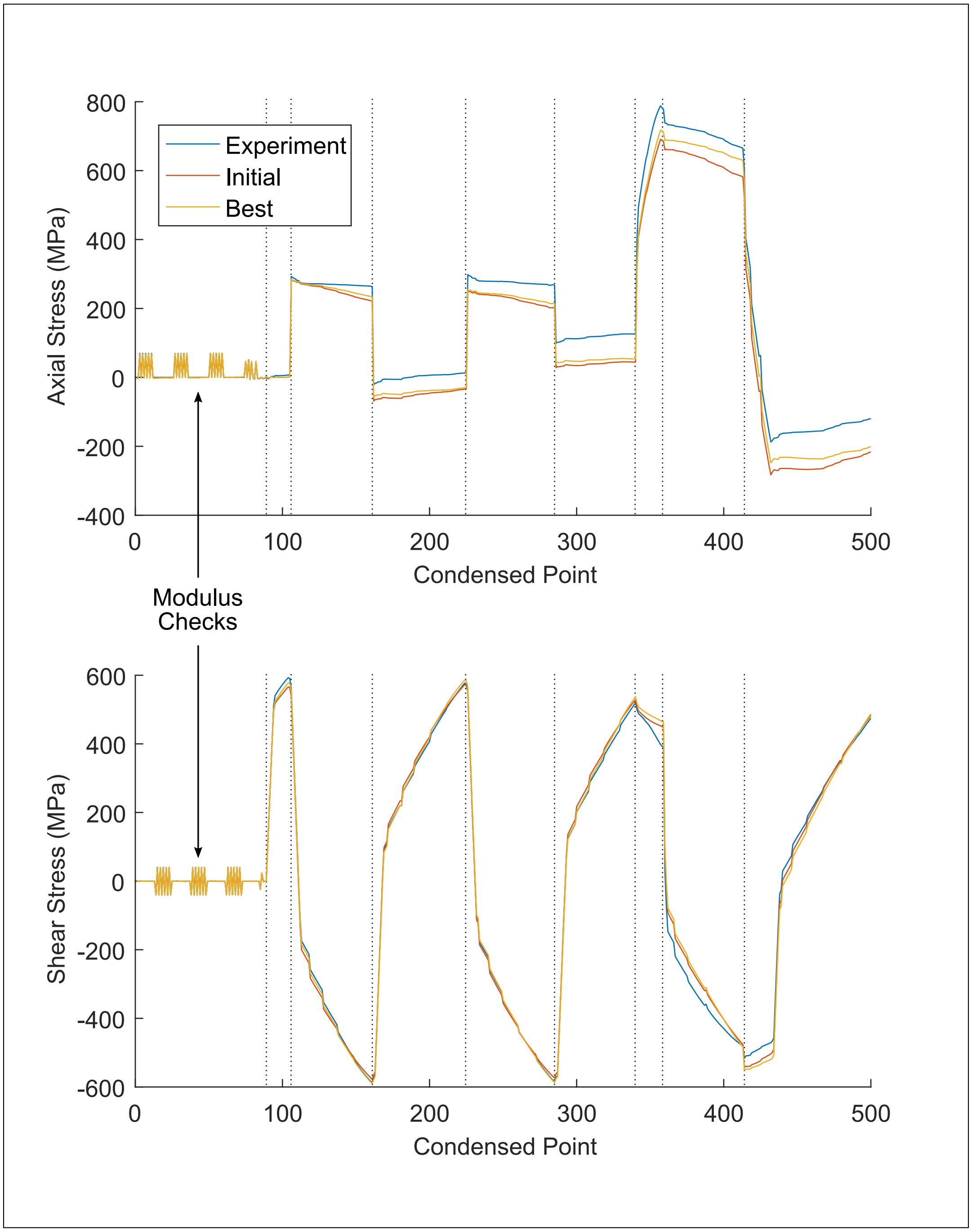

Figure 7.27: Axial stress (top) and shear stress (bottom) for the initial condensed experimental data points, and the corresponding FE results for the top initial parameters and the best parameters.

7.6 Parameter Calibration with all Data

A set of constitutive parameters (labeled as the best or final parameters in the preceding sections) has been generated based on the autonomous integrated multiaxial experiment. Additional influence on the parameters comes from the axial-only supplement test data. Also, the tension test for a rate of 1×10^{-4} m/m/s is used throughout the optimization procedures in conjunction with the ongoing autonomous test results. To further evaluate the response of the selected viscoplasticity model, a new fitting of the hardening parameters has been performed using all the test data for Ti-6Al-4V discussed throughout this work. For reference, Table 7.6 provides a description of the experiments, the number of condensed data points, and the normalized sum of the squares of the residual error for the initial parameter set from axial-only supplemental data, the best parameter set from the autonomous testing, and the final parameters resulting from the all encompassing fitting.

There are a number of challenges to performing a fit over such a large set of experiments. First and foremost, the experimental data needs to be reduced to a reasonable size that is still representative of the interesting portions of the experiments. The reduced size is required to limit the number of times steps performed in each of the finite element simulations. The reduction process is easily handled through the use of filtering and data condensing procedures developed as part of the methodology. Details can be found in Appendix A. Next, an objective function has to be selected to encompass the error from each experiment. This requires either multi-objective optimization or some form of weighted objective functions. For this fitting, a weighted objective function has been selected such that each experiment is given equal weight. This is easily accomplished by normalizing the sum of the squares of the residual error by the number of data points involved in the summation. The objective function equates to the average squared residual error for the experiment.

With the condensed data and the selected weighted objective function, the all-encompassing fitting can be performed using the viscoplasticity model. The particle swarm optimization procedure that was used in the FEMU has been employed for the fitting. The same settings as described in Section 6.4.3 are used for PSO. Five initial seeds are used consisting of the top four initial seeds from the axial-only fitting performed using the supplemental data (Section 6.3) and the best set of parameters from the autonomous tests. The remaining five parameter sets are randomly assigned using Latin hypercube sampling. Table 7.7 summarizes the initial seeds and the parameter bounds which remain the same as in the prior optimizations.

Additional improvement was obtained by performing the fitting using all the Ti-6Al-4V data. Again, Table 7.6 shows a comparison of the normalized sum of the squares of the residual error (SSR/N) for the previously analyzed top initial and best seeds along with the final parameters from the all-encompassing fitting. The different experiment types provide insight into both the accuracies and deficiencies of the constitutive model. The final parameters from the all encompassing fit show improvement over the other parameters in all experiments except the axial-only full reversed cycles and one of the multiaxial no-compression tests. The total sum of the errors for the final set did decrease which indicates improvement in the parameters through the use of all the data. The improvement, and the change in parameter values is relatively small though. The final set of parameters is only slightly different than the Case 81 parameters from the initial fit to supplemental axial-only data (Table 7.7).

Table 7.6: Tests performed on Ti-6Al-4V and their normalized sum of the squares of the residual error using the top initial seed from axial-only data, the best parameters from the autonomous testing, and the final parameters from the all-encompassing fitting.

Test Description	Points	Initial SSR/N	Best SSR/N	Final SSR/N
Tension 1×10^{-2}	96	1,622	1,173	998
Tension 1×10^{-3}	96	1,005	628	443
Tension 1×10^{-4}	96	827	501	302
Axial Fully Reversed	8,271	7,293	9,307	12,698
Multi No Compressive Strain (1)	321	1,878	1,395	938
Multi No Compressive Strain (2)	327	8,236	6,695	2,071
Multi Fully Reversed	351	4,561	1,876	1,684
Torsion Cycles	353	4,579	3,906	4,727
Multi Traveling Boxes	19,856	19,024	17,196	16,637
Multi Autonomous	8,271	9,820	8,990	8,299
Sum	38,038	58,846	51,667	48,796

Table 7.7: Initial seeds that are used for the all-encompassing fit performed for the viscoplasticity model on Ti-6Al-4V. The 'Case' sets come from the initial fit using supplemental axial-only data while the best set comes from the autonomous integrated fitting. Lastly, the final parameters from the all-encompassing fit are shown.

Parameter	q_1	$5/b_1$	q_2	$5/b_2$	A_1/B_1	$5/B_1$	A_2/B_2	$5/B_2$	A_3
Min	0	9.50E-05	-500	1.00E-01	0	9.50E-05	0	9.50E-05	0
Max	750	1.00E-01	0	1.00E+00	750	1.00E-01	750	1.00E-01	2000
Set	q_1	$5/b_1$	q_2	$5/b_2$	A_1/B_1	$5/B_1$	A_2/B_2	$5/B_2$	A_3
Case 99 (Initial)	5.0	2.85E-04	-55.7	1.00E+00	65.2	2.11E-03	281.3	1.40E-02	0.0
Case 63	6.8	1.00E-01	-64.7	1.00E+00	308.8	1.25E-02	34.0	6.91E-03	0.0
Case 38	8.1	1.00E-01	-68.4	1.00E+00	67.2	9.90E-05	291.7	1.37E-02	0.0
Case 81	5.0	9.71E-02	-84.0	7.75E-01	107.2	9.90E-05	218.1	9.17E-03	401.1
Best	0.0	3.01E-02	-72.6	3.95E-01	72.8	4.90E-02	289.8	4.30E-03	150.2
Final	6.0	8.36E-02	-83.1	8.54E-01	111.9	9.50E-05	214.7	7.00E-03	408.4

7.7 Summary

A series of additional multiaxial validation experiments were performed to assess the accuracy of the constitutive parameters identified during the autonomous integrated experiment on Ti-6Al-4V. The top initial parameter set from the supplemental fitting and the best set from the autonomous test have been evaluated for all of the initial axial-only tests, noted as supplemental data, and the additional multiaxial experiments. The best parameter set outperformed the top initial seed (fit using only axial data) in all of the experiments excluding the axial-only fully reversed cycles. The axial-only fully reversed experiment and the traveling box experiment were troublesome for both parameter sets as evident from the high normalized squared errors. These two tests highlight possible deficiencies of the constitutive model itself, not deficiencies of the integrated, autonomous methodology. These two tests had the largest accumulation of plastic strain which highlights the cyclic softening behavior of Ti-6Al-4V that proves difficult for the chosen plasticity model.

Parameter identification has been performed using both the supplemental axial data and the additional multiaxial validation data. Initial seeds have been used from the axial-only fitting and the best parameters from the autonomous test. The final set of parameters identified when using all of the experiments did not change significantly from the best parameters based on the autonomous test. This final set still leads to high errors for the axial fully-reversed cycles and the traveling box experiments. However, there is a slight improvement in the errors for almost all of the other experiments. Analysis of all the validation experiments show the single autonomous integrated experiment that utilized supplemental axial-only test data is significant in that parameters were identified and validated in real-time leading to a fit that is almost as accurate as the all encompassing fit that uses data from ten experiments (compared to five for the autonomous procedure).

CHAPTER VIII

CONCLUSIONS AND EXTENSIONS

The experimental investigation of material behavior continues to serve as a primary means to understand the strength and physical limitations of materials. Additional insight and predictions can be obtained through the use of constitutive material models which seek to explain the behavior observed during experimental testing. Computing resources have grown considerably in recent decades which has accelerated the complexity of constitutive modeling efforts. Modern constitutive models still require parameter fitting, but it has become a difficult, non-unique problem with experimental methodologies available today, even as modern techniques like digital image correlation continue to see tremendous focus and progress.

As constitutive models increase in complexity, their parameters' correlation to experiments is less direct and numerical methods are now used to perform the fitting since the physical meaning of certain model parameters is difficult or impossible to ascertain. Numerical methods are becoming increasingly proficient at identifying optimal constitutive parameters through techniques like the virtual fields method (VFM) and finite element model updating (FEMU). However, these methods are still typically applied post-test, leading to delays in subsequent analysis efforts that rely on the identified constitutive parameters. Furthermore, a serious restriction to the growth of both analytical and experimental capabilities is the lack of integration of such closely related tasks. Currently the fidelity of the material model only becomes known after testing, and a majority of tests used in the calibration are still uniaxial. The work of this thesis bridges the gap between experimentation and constitutive model fitting, to allow the fitting process to dictate the course of the experiment until the constitutive parameters are calibrated and also validated to a desired tolerance.

8.1 Conclusions

The new test methodology and associated software developed in this thesis seamlessly and efficiently integrate experimental testing and analytical modeling for the purpose of fitting and validating non-linear constitutive model parameters in real time. The developed approach is an alternative to the traditional practice of separate experimental and analytical endeavors. Through integration, the new experimental test methodology yields calibrated non-linear material model parameters that are validated over a broad range of multiaxial stress conditions in real time, thereby reducing the time and cost to develop the models for use in finite element simulations of more complicated geometries under realistic loading conditions.

The methodology has initially been demonstrated using simulated experimental responses to remove errors caused by constitutive model deficiencies. Results for the simulated experiments show accurate identification of constitutive parameters using only a single axial-torsional experiment and supplemental axial test data. The methodology has also been verified through an autonomous experiment conducted on Ti-6Al-4V to identify viscoplasticity parameters. Even using an experimental procedure restricted by specimen design and hardware limitations, the new methodology is able to calibrate and validate the selected constitutive parameters over multiaxial states of stress and strain in real time. The autonomous experiment resulted in a set of constitutive parameters that could be utilized immediately upon test completion, thereby seamlessly integrating both the experimental and analytical efforts. The integrated approach leads to a significant reduction in analytical effort required (hours instead of days) because all the analytical work is automated. The integrated approach can also reduce the number of specimens needed for identification of parameters since one specimen is subjected to a vast array of multiaxial conditions.

Lastly, the identified parameters have been evaluated for both the original axial supplemental tests and additional multiaxial experiments. These validation experiments identify some deficiencies of the chosen constitutive model; however, in analyzing both the autonomous test data, and data from separate validation experiments, the parameters identified automatically in the autonomous test outperform those derived from conventional tests in nearly every case.

The new methodology and test software provide a significant step toward the integration of experimentation and constitutive model fitting which are both critically important, but typically disconnected, in many fields of engineering and material science. The new methodology also serves as a platform for the future advancement of integrated experimentation and constitutive modeling. Immediate advancements that can be made are identified in the next section. General applications of the methodology are also discussed, as this integrated approach is not limited to the scope of work presented here as a demonstration.

8.2 Extensions

A specific material and constitutive model have been utilized in this work to demonstrate the integrated testing capability. However, the new methodology and associated software can easily be applied to a range of materials (metals, composites, ceramics, etc.), a variety of constitutive material models (elasticity, plasticity, viscoplasticity, etc.), and an array of testing configurations at multiple length scales (in-situ SEM loading, single-crystal specimens, uniaxial, multiaxial, etc.). Work can be performed in the immediate future to extend the application of the developed methodology to more general test conditions. Some examples are:

- testing at elevated temperatures to incorporate thermal effects into the constitutive models;
- loading at various rates within a single experiment to assess and calibrate time-dependent behavior of materials;
- incorporating combinations of proportional and non-proportional multiaxial loading (like the box test) to improve correlation over a broader range of testing conditions;
- adding new experimental methods like digital image correlation into the autonomous process to not only provide full-field strain or displacement measurements, but to also enable advanced methods such as automated crack growth testing;
- integrating other parameter identification methods like the virtual fields method that work with full-field measurements;
- utilizing the new methods and software to perform investigations for microstructure level properties through optical strain measurement techniques;
- evaluating other advanced materials like ceramics and ceramic matrix composites; and
- providing a platform for the simultaneous calibration and evaluation of multiple constitutive models and their parameters.

The methods and software developed in the present research are suitable as a starting point for each of the capabilities described above, and more. The developed methodology has the flexibility to support a broad scope of material testing and modeling research, and is a step toward changing current conventions for laboratory testing, analytical model development, and model validation.

BIBLIOGRAPHY

[1] A. Phillips and T. Juh-Ling, "The effect of loading path on the yield surface at elevated temperatures," *International Journal of Solids and Structures*, vol. 8, no. 4, pp. 463–474, Apr. 1972. [Online]. Available: http://www.sciencedirect.com/science/article/pii/0020768372900170

[2] A. Phillips, C. S. Liu, and J. W. Justusson, "An experimental investigation of yield surfaces at elevated temperatures," *Acta Mechanica*, vol. 14, no. 2-3, pp. 119–146, 1972. [Online]. Available: http://link.springer.com/article/10.1007/BF01184853

[3] J. R. Ellis, D. N. Robinson, and C. E. Pugh, "Behavior of annealed type 316 stainless steel under monotonic and cyclic biaxial loading at room temperature," *Nuclear Engineering and Design*, vol. 47, no. 1, pp. 115–123, May 1978. [Online]. Available: http://www.sciencedirect.com/science/article/pii/0029549378900092

[4] H. C. Wu and W. C. Yeh, "On the experimental determination of yield surfaces and some results of annealed 304 stainless steel," *International Journal of Plasticity*, vol. 7, no. 8, pp. 803–826, 1991. [Online]. Available: http://www.sciencedirect.com/science/article/pii/074964199190019U

[5] H. Ishikawa, "Subsequent yield surface probed from its current center," *International Journal of Plasticity*, vol. 13, no. 67, pp. 533–549, 1997. [Online]. Available: http://www.sciencedirect.com/science/article/pii/S0749641997000247

[6] C. J. Lissenden, B. A. Lerch, J. R. Ellis, and D. N. Robinson, "Experimental determination of yield and flow surfaces under axial-torsional loading," *ASTM Special Technical Publication*, vol. 1280, pp. 92–112, 1997.

[7] A. S. Khan, A. Pandey, and T. Stoughton, "Evolution of subsequent yield surfaces and elastic constants with finite plastic deformation. Part II: A very high work hardening aluminum alloy (annealed 1100 Al)," *International Journal of Plasticity*, vol. 26, no. 10, pp. 1421–1431, Oct. 2010. [Online]. Available: http://www.sciencedirect.com/science/article/pii/S0749641909000953

[8] A. S. Khan, A. Pandey, and T. Stoughton, "Evolution of subsequent yield surfaces and elastic constants with finite plastic deformation. Part III: Yield surface in tension tension stress space (Al 6061T 6511 and annealed 1100 Al)," *International Journal of Plasticity*, vol. 26, no. 10, pp. 1432–1441, Oct. 2010. [Online]. Available: http://www.sciencedirect.com/science/article/pii/S0749641909000941

[9] S.-J. Sung, L.-W. Liu, H.-K. Hong, and H.-C. Wu, "Evolution of yield surface in the 2d and 3d stress spaces," *International Journal of Solids and Structures*, vol. 48, no. 6, pp. 1054–1069, Mar. 2011. [Online]. Available: http://www.sciencedirect.com/science/article/pii/S0020768310004476

[10] T. C. Chu, W. F. Ranson, and M. A. Sutton, "Applications of digital-image-correlation techniques to experimental mechanics," *Experimental Mechanics*, vol. 25, no. 3, pp. 232–244, 1985. [Online]. Available: http://www.springerlink.com/index/Y002U6538P346776.pdf

[11] M. A. Sutton, S. R. McNeill, J. D. Helm, and Y. J. Chao, "Advances in Two-Dimensional and Three-Dimensional Computer Vision," in *Photomechanics*, ser. Topics in Applied Physics, D. P. K. Rastogi, Ed. Springer Berlin Heidelberg, Jan. 2000, no. 77, pp. 323–372. [Online]. Available: http://link.springer.com/chapter/10.1007/3-540-48800-6_10

[12] M. A. Sutton, "Digital image correlation for shape and deformation measurements," in *Springer Handbook of Experimental Solid Mechanics*. Springer, 2008, pp. 565–600. [Online]. Available: http://link.springer.com/10.1007/978-0-387-30877-7_20

[13] Z. Mroz, "An attempt to describe the behavior of metals under cyclic loads using a more general workhardening model," *Acta Mechanica*, vol. 7, no. 2-3, pp. 199–212, Jun. 1969. [Online]. Available: http://link.springer.com/article/10.1007/BF01176668

[14] M. Doner, H. Chang, and H. Conrad, "Plastic flow and dislocation structure at small strains in OFHC copper deformed in tension, torsion and combined tension-torsion," *Journal of the Mechanics and Physics of Solids*, vol. 22, no. 6, pp. 555–564, Dec. 1974. [Online]. Available: http://www.sciencedirect.com/science/article/pii/0022509674900349

[15] A. Phillips and M. Ricciuti, "Fundamental experiments in plasticity and creep of aluminum - Extension of previous results," *International Journal of Solids and Structures*, vol. 12, no. 3, pp. 159–171, 1976. [Online]. Available: http://www.sciencedirect.com/science/article/pii/0020768376900603

[16] P. J. Bonacuse and S. Kalluri, "Results of Inphase Axial-Torsional Fatigue Experiments on 304 Stainless Steel," Lewis Research Center, Cleveland, Ohio, Tech. Rep. USAAVSCOM-TR-88-C-022, 1989. [Online]. Available: http://oai.dtic.mil/oai/oai?verb=getRecord&metadataPrefix=html&identifier=ADA233434

[17] S. Kalluri and P. J. Bonacuse, "In-Phase and Out-of-Phase Axial-Torsional Fatigue Behavior of Haynes 188 Superalloy at 760 C," *ASTM Special Technical Publication*, vol. 1191, pp. 133–133, 1993.

[18] G. Cailletaud, H. Kaczmarek, and H. Policella, “Some elements on multiaxial behaviour of 316 L stainless steel at room temperature,” *Mechanics of Materials*, vol. 3, no. 4, pp. 333–347, Dec. 1984. [Online]. Available: http://www.sciencedirect.com/science/article/pii/0167663684900334

[19] A. Benallal, P. Le Gallo, and D. Marquis, “An experimental investigation of cyclic hardening of 316 stainless steel and of 2024 aluminium alloy under multiaxial loadings,” *Nuclear Engineering and Design*, vol. 114, no. 3, pp. 345–353, Jun. 1989. [Online]. Available: http://www.sciencedirect.com/science/article/pii/002954938990112X

[20] M. Grediac, F. Pierron, S. Avril, and E. Toussaint, “The virtual fields method for extracting constitutive parameters from full-field measurements: A review,” *Strain*, vol. 42, no. 4, pp. 233–253, Nov. 2006. [Online]. Available: http://onlinelibrary.wiley.com/doi/10.1111/j.1475-1305.2006.tb01504.x/abstract

[21] F. Pierron and M. Grediac, *The Virtual Fields Method*. New York, NY: Springer New York, 2012. [Online]. Available: http://link.springer.com/10.1007/978-1-4614-1824-5

[22] M. H. H. Meuwissen, C. W. J. Oomens, F. P. T. Baaijens, R. Petterson, and J. D. Janssen, “Determination of the elasto-plastic properties of aluminium using a mixed numerical-experimental method,” *Journal of Materials Processing Technology*, vol. 75, no. 13, pp. 204–211, Mar. 1998. [Online]. Available: http://www.sciencedirect.com/science/article/pii/S092401369700366X

[23] S. Belhabib, H. Haddadi, M. Gasprini, and P. Vacher, “Heterogeneous tensile test on elastoplastic metallic sheets: Comparison between FEM simulations and full-field strain measurements,” *International Journal of Mechanical Sciences*, vol. 50, no. 1, pp. 14–21, Jan. 2008. [Online]. Available: http://www.sciencedirect.com/science/article/pii/S0020740307000860

[24] J. L. Dournaux, S. Bouvier, A. Aouafi, and P. Vacher, “Full-field measurement technique and its application to the analysis of materials behaviour under plane strain mode,” *Materials Science and Engineering: A*, vol. 500, no. 12, pp. 47–62, Jan. 2009. [Online]. Available: http://www.sciencedirect.com/science/article/pii/S0921509308010964

[25] L. Robert, V. Velay, N. Decultot, and S. Ramde, “Identification of hardening parameters using finite element models and full-field measurements: some case studies,” *The Journal of Strain Analysis for Engineering Design*, p. 0309324711430022, Nov. 2011. [Online]. Available: http://sdj.sagepub.com/content/early/2011/11/23/0309324711430022

[26] M. Stamborska, F. Simcak, M. Kalina, and M. Schrotter, “Identification of the Stress Fields from the Strain Fields in the Isotropic Materials,” *Procedia Engineering*, vol. 48, pp. 665–672, 2012. [Online]. Available: http://linkinghub.elsevier.com/retrieve/pii/S1877705812046310

[27] H. Haddadi and S. Belhabib, "Improving the characterization of a hardening law using digital image correlation over an enhanced heterogeneous tensile test," *International Journal of Mechanical Sciences*, vol. 62, no. 1, pp. 47–56, Sep. 2012. [Online]. Available: http://www.sciencedirect.com/science/article/pii/S0020740312001221

[28] M. J. D. Powell, "An efficient method for finding the minimum of a function of several variables without calculating derivatives," *The Computer Journal*, vol. 7, no. 2, pp. 155–162, Jan. 1964. [Online]. Available: http://comjnl.oxfordjournals.org/content/7/2/155

[29] D. E. Goldberg and J. H. Holland, "Genetic algorithms and machine learning," *Machine Learning*, vol. 3, no. 2, pp. 95–99, 1988. [Online]. Available: http://www.springerlink.com/index/rw3572714v41q507.pdf

[30] R. C. Eberhart and J. Kennedy, "A new optimizer using particle swarm theory," in *Proceedings of the Sixth International Symposium on Micro Machine and Human Science*, vol. 1. New York, NY, 1995, pp. 39–43. [Online]. Available: http://www.ppgia.pucpr.br/~alceu/mestrado/aula3/PSO_2.pdf

[31] S. Timoshenko, *History of Strength of Materials: With a Brief Account of the History of Theory of Elasticity and Theory of Structures*. New York: Dover Publications, 1983.

[32] K. Osakada, "History of plasticity and metal forming analysis," *Journal of Materials Processing Technology*, vol. 210, no. 11, pp. 1436–1454, Aug. 2010. [Online]. Available: http://linkinghub.elsevier.com/retrieve/pii/S0924013610001111

[33] J. J. Guest, "On the strength of ductile materials under combined stress," *Proceedings of the Physical Society of London*, vol. 17, no. 1, p. 202, 1899. [Online]. Available: http://iopscience.iop.org/1478-7814/17/1/319

[34] W. Lode, "Versuche uber den Einflub der mittleren Hauptspannung auf das Flieben der Metalle Eisen, Kupfer und Nickel," *Zeitschrift fur Physik*, vol. 36, no. 11-12, pp. 913–939, 1926. [Online]. Available: http://link.springer.com/article/10.1007/BF01400222

[35] G. I. Taylor and H. Quinney, "The plastic distortion of metals," *Philosophical Transactions of the Royal Society of London. Series A, Containing Papers of a Mathematical or Physical Character*, pp. 323–362, 1932. [Online]. Available: http://www.jstor.org/stable/91233

[36] M. J. Michno Jr. and W. N. Findley, "An historical perspective of yield surface investigations for metals," *International Journal of Non-Linear Mechanics*, vol. 11, no. 1, pp. 59–82, 1976. [Online]. Available: http://www.sciencedirect.com/science/article/pii/0020746276900391

[37] L. W. Hu, J. Markowitz, and T. A. Bartush, "A triaxial-stress experiment on yield condition in plasticity," *Experimental Mechanics*, vol. 6, no. 1, pp. 58–64, Jan. 1966. [Online]. Available: http://link.springer.com/article/10.1007/BF02327115

[38] K. C. Liu and W. L. Greenstreet, "Experimental studies to examine elastic-plastic behaviors of metal alloys used in nuclear structures," *Constitutive Equations in Viscoplasticity: Computational and Engineering Aspects*, vol. 20, p. 35, 1976.

[39] S. Kalluri and P. J. Bonacuse, “An axial-torsional, thermomechanical fatigue testing technique,” *ASTM Special Technical Publication*, vol. 1280, pp. 184–207, 1997.

[40] J. Abanto-Bueno and J. Lambros, “Investigation of crack growth in functionally graded materials using digital image correlation,” *Engineering Fracture Mechanics*, vol. 69, no. 1416, pp. 1695–1711, Sep. 2002. [Online]. Available: http://www.sciencedirect.com/science/article/pii/S0013794402000589

[41] S. Yoneyama, T. Ogawa, and Y. Kobayashi, “Evaluating mixed-mode stress intensity factors from full-field displacement fields obtained by optical methods,” *Engineering Fracture Mechanics*, vol. 74, no. 9, pp. 1399–1412, Jun. 2007. [Online]. Available: http://linkinghub.elsevier.com/retrieve/pii/S001379440600316X

[42] G. P. Mogadpalli and V. Parameswaran, “Determination of stress intensity factor for cracks in orthotropic composite materials using digital image correlation,” *Strain*, vol. 44, no. 6, pp. 446–452, 2008. [Online]. Available: http://onlinelibrary.wiley.com/doi/10.1111/j.1475-1305.2007.00391.x/full

[43] V. Tarigopula, O. S. Hopperstad, M. Langseth, A. H. Clausen, and F. Hild, “A study of localisation in dual-phase high-strength steels under dynamic loading using digital image correlation and FE analysis,” *International Journal of Solids and Structures*, vol. 45, no. 2, pp. 601–619, Jan. 2008. [Online]. Available: http://www.sciencedirect.com/science/article/pii/S0020768307003411

[44] M. Dunand, A. P. Maertens, M. Luo, and D. Mohr, “Experiments and modeling of anisotropic aluminum extrusions under multi-axial loading Part I: Plasticity,” *International Journal of Plasticity*, vol. 36, pp. 34–49, Sep. 2012. [Online]. Available: http://www.sciencedirect.com/science/article/pii/S0749641912000435

[45] C. C. Roth and D. Mohr, “Effect of strain rate on ductile fracture initiation in advanced high strength steel sheets: Experiments and modeling,” *International Journal of Plasticity*, vol. 56, pp. 19–44, May 2014. [Online]. Available: http://www.sciencedirect.com/science/article/pii/S0749641914000047

[46] G. S. Schajer, B. Winiarski, and P. J. Withers, “Hole-Drilling Residual Stress Measurement with Artifact Correction Using Full-Field DIC,” *Experimental Mechanics*, vol. 53, no. 2, pp. 255–265, Feb. 2013. [Online]. Available: http://link.springer.com/10.1007/s11340-012-9626-0

[47] A. Baldi, “Residual Stress Measurement Using Hole Drilling and Integrated Digital Image Correlation Techniques,” *Experimental Mechanics*, vol. 54, no. 3, pp. 379 – 391, 2014. [Online]. Available: http://journals.ohiolink.edu/ejc/article.cgi?issn=00144851&issue=v54i0003&article=379_rsmuhdaidict

[48] J. S. Lyons, J. Liu, and M. A. Sutton, “High-temperature deformation measurements using digital-image correlation,” *Experimental Mechanics*, vol. 36, no. 1, pp. 64–70, 1996. [Online]. Available: http://link.springer.com/article/10.1007/BF02328699

[49] B. M. B. Grant, H. J. Stone, P. J. Withers, and M. Preuss, "High-temperature strain field measurement using digital image correlation," *The Journal of Strain Analysis for Engineering Design*, vol. 44, no. 4, pp. 263–271, May 2009. [Online]. Available: http://sdj.sagepub.com/lookup/doi/10.1243/03093247JSA478

[50] B. Pan, D. Wu, Z. Wang, and Y. Xia, "High-temperature digital image correlation method for full-field deformation measurement at 1200 C," *Measurement Science and Technology*, vol. 22, no. 1, p. 015701, Jan. 2011. [Online]. Available: http://stacks.iop.org/0957-0233/22/i=1/a=015701?key=crossref.25de3359fafa5d7eba3c78f4a6a9cbda

[51] N. Shamsaei, M. Gladskyi, K. Panasovskyi, S. Shukaev, and A. Fatemi, "Multiaxial fatigue of titanium including step loading and load path alteration and sequence effects," *International Journal of Fatigue*, vol. 32, no. 11, pp. 1862–1874, 2010. [Online]. Available: http://journals.ohiolink.edu/ejc/article.cgi?issn=01421123&issue=v32i0011&article=1862_mfotislpaase

[52] N. Batane, D. Morrison, and J. Moosbrugger, "Cyclic plasticity of polycrystalline nickel under axial-torsional loading," *Materials Science & Engineering A*, vol. 528, no. 1, pp. 467–473, 2010. [Online]. Available: http://journals.ohiolink.edu/ejc/article.cgi?issn=09215093&issue=v528i0001&article=467_cpopnual

[53] M. R. Bees, S. J. Pattison, N. Fox, and M. T. Whittaker, "The non-proportional behaviour of a nickel-based superalloy at room temperature, and characterisation of the additional hardening response by a modified cyclic hardening curve," *International Journal of Fatigue*, vol. 67, pp. 134–141, 2014. [Online]. Available: http://journals.ohiolink.edu/ejc/article.cgi?issn=01421123&issue=v67inone_c&article=134_tnboanbamchc

[54] G. Cailletaud, O. Diard, F. Feyel, S. Forest, and others, "Computational crystal plastiticy: from single crystal to homogenized polycrystals," *Technische Mechanik*, vol. 23, pp. 130–145, 2003. [Online]. Available: http://hal.archives-ouvertes.fr/hal-00142643/

[55] A. Manonukul and F. P. E. Dunne, "High- and low-cycle fatigue crack initiation using polycrystal plasticity," *Proceedings of the Royal Society A: Mathematical, Physical and Engineering Sciences*, vol. 460, no. 2047, pp. 1881–1903, Jul. 2004. [Online]. Available: http://rspa.royalsocietypublishing.org/cgi/doi/10.1098/rspa.2003.1258

[56] J. D. Clayton and D. L. McDowell, "A multiscale multiplicative decomposition for elastoplasticity of polycrystals," *International Journal of Plasticity*, vol. 19, no. 9, pp. 1401–1444, 2003. [Online]. Available: http://www.sciencedirect.com/science/article/pii/S0749641902001092

[57] D. L. McDowell, "Modeling and experiments in plasticity," *International Journal of Solids and Structures*, vol. 37, no. 1, pp. 293–309, 2000. [Online]. Available: http://www.sciencedirect.com/science/article/pii/S0020768399000943

[58] A. Acharya, "A model of crystal plasticity based on the theory of continuously distributed dislocations," *Journal of the Mechanics and Physics of Solids*, vol. 49, no. 4, pp.

761–784, Apr. 2001. [Online]. Available: http://www.sciencedirect.com/science/article/pii/S0022509600000600

[59] Y. S. Choi and T. A. Parthasarathy, "A crystal-plasticity finite element method study on effect of abnormally large grain on mesoscopic plasticity of polycrystal," *Scripta Materialia*, vol. 66, no. 1, pp. 56–59, Jan. 2012. [Online]. Available: http://linkinghub.elsevier.com/retrieve/pii/S1359646211005963

[60] T. J. Turner and S. L. Semiatin, "Modeling large-strain deformation behavior and neighborhood effects during hot working of a coarse-grain nickel-base superalloy," *Modelling and Simulation in Materials Science and Engineering*, vol. 19, no. 6, p. 065010, Sep. 2011. [Online]. Available: http://stacks.iop.org/0965-0393/19/i=6/a=065010?key=crossref.a6e9b4ebb782a7543135955fcb8e1f09

[61] R. A. Brockman, "Analysis of elastic-plastic deformation in TiAl polycrystals," *International Journal of Plasticity*, vol. 19, no. 10, pp. 1749–1772, 2003. [Online]. Available: http://www.sciencedirect.com/science/article/pii/S074964190200102X

[62] R. Hill, *The Mathematical Theory of Plasticity*, ser. Oxford engineering science series. Oxford : New York: Clarendon Press ; Oxford University Press, 1998, no. 11.

[63] J. L. Chaboche, "Time-independent constitutive theories for cyclic plasticity," *International Journal of Plasticity*, vol. 2, no. 2, pp. 149–188, 1986. [Online]. Available: http://www.sciencedirect.com/science/article/pii/0749641986900100

[64] N. Ohno and J. D. Wang, "Kinematic hardening rules with critical state of dynamic recovery, part II: Application to experiments of ratchetting behavior," *International Journal of Plasticity*, vol. 9, no. 3, pp. 391–403, 1993. [Online]. Available: http://www.sciencedirect.com/science/article/pii/074964199390043P

[65] S. Krishna, T. Hassan, I. Ben Naceur, K. Sa, and G. Cailletaud, "Macro versus micro-scale constitutive models in simulating proportional and nonproportional cyclic and ratcheting responses of stainless steel 304," *International Journal of Plasticity*, vol. 25, no. 10, pp. 1910–1949, Oct. 2009. [Online]. Available: http://linkinghub.elsevier.com/retrieve/pii/S0749641908001848

[66] J. Chaboche, "A review of some plasticity and viscoplasticity constitutive theories," *International Journal of Plasticity*, vol. 24, no. 10, pp. 1642–1693, Oct. 2008. [Online]. Available: http://linkinghub.elsevier.com/retrieve/pii/S0749641908000582

[67] Dassault Systemes, "ABAQUS User's Manual, Version 6.13," 2013.

[68] L. Taleb and G. Cailletaud, "An updated version of the multimechanism model for cyclic plasticity," *International Journal of Plasticity*, vol. 26, no. 6, pp. 859–874, 2010. [Online]. Available: http://journals.ohiolink.edu/ejc/article.cgi?issn=07496419&issue=v26i0006&article=859_auvotmmfcp

[69] G. Bolzon, G. Maier, and M. Panico, "Material model calibration by indentation, imprint mapping and inverse analysis," *International Journal of Solids and Structures*, vol. 41, no. 1112, pp. 2957–2975, Jun. 2004. [Online]. Available: http://www.sciencedirect.com/science/article/pii/S0020768304000435

[70] S. M. Rahman, "Finite element analysis and related numerical schemes for ratcheting simulation," Dissertation, North Carolina State University, Raleigh, North Carolina, 2006. [Online]. Available: http://repository.lib.ncsu.edu/ir/handle/1840.16/5967

[71] T. Nakamura and Y. Gu, "Identification of elastic-plastic anisotropic parameters using instrumented indentation and inverse analysis," *Mechanics of Materials*, vol. 39, no. 4, pp. 340–356, Apr. 2007. [Online]. Available: http://www.sciencedirect.com/science/article/pii/S0167663606000718

[72] B. M. Chaparro, S. Thuillier, L. F. Menezes, P. Y. Manach, and J. V. Fernandes, "Material parameters identification: Gradient-based, genetic and hybrid optimization algorithms," *Computational Materials Science*, vol. 44, no. 2, pp. 339–346, Dec. 2008. [Online]. Available: http://www.sciencedirect.com/science/article/pii/S0927025608001766

[73] T. Furukawa and J. G. Michopoulos, "Computational design of multiaxial tests for anisotropic material characterization," *International Journal for Numerical Methods in Engineering*, vol. 74, no. 12, pp. 1872–1895, Jun. 2008. [Online]. Available: http://doi.wiley.com/10.1002/nme.2243

[74] P. L. Phillips, R. A. Brockman, and R. John, "Modelling Strategies for Property Identification Based on Full-Field Surface Displacement Data," *Strain*, vol. 48, no. 2, pp. 143–152, Apr. 2012. [Online]. Available: http://onlinelibrary.wiley.com/doi/10.1111/j.1475-1305.2011.00806.x/abstract

[75] M. Grediac, F. Pierron, and Y. Surrel, "Novel procedure for complete in-plane composite characterization using a single T-shaped specimen," *Experimental Mechanics*, vol. 39, no. 2, pp. 142–149, Jun. 1999. [Online]. Available: http://link.springer.com/article/10.1007/BF02331118

[76] M. Grediac, E. Toussaint, and F. Pierron, "Special virtual fields for the direct determination of material parameters with the virtual fields method. 2-Application to in-plane properties," *International Journal of Solids and Structures*, vol. 39, no. 10, pp. 2707–2730, May 2002. [Online]. Available: http://www.sciencedirect.com/science/article/pii/S0020768302001282

[77] M. Grediac, E. Toussaint, and F. Pierron, "Special virtual fields for the direct determination of material parameters with the virtual fields method. 3-Application to the bending rigidities of anisotropic plates," *International Journal of Solids and Structures*, vol. 40, no. 10, pp. 2401–2419, May 2003. [Online]. Available: http://www.sciencedirect.com/science/article/pii/S0020768303000301

[78] R. Moulart, S. Avril, and F. Pierron, "Identification of the through-thickness rigidities of a thick laminated composite tube," *Composites Part A: Applied Science and Manufacturing*, vol. 37, no. 2, pp. 326–336, Feb. 2006. [Online]. Available: http://www.sciencedirect.com/science/article/pii/S1359835X05002435

[79] R. Moulart, F. Pierron, S. R. Hallett, and M. R. Wisnom, "Full-Field Strain Measurement and Identification of Composites Moduli at High Strain Rate with the Virtual Fields Method," *Experimental Mechanics*, vol. 51, no. 4, pp. 509–536, Nov. 2010. [Online]. Available: http://link.springer.com/article/10.1007/s11340-010-9433-4

[80] M. Grediac and F. Pierron, "Applying the Virtual Fields Method to the identification of elasto-plastic constitutive parameters," *International Journal of Plasticity*, vol. 22, no. 4, pp. 602–627, Apr. 2006. [Online]. Available: http://www.sciencedirect.com/science/article/pii/S0749641905000896

[81] Y. Pannier, S. Avril, R. Rotinat, and F. Pierron, "Identification of Elasto-Plastic Constitutive Parameters from Statically Undetermined Tests Using the Virtual Fields Method," *Experimental Mechanics*, vol. 46, no. 6, pp. 735–755, Nov. 2006. [Online]. Available: http://link.springer.com/article/10.1007/s11340-006-9822-x

[82] F. Pierron, S. Avril, and V. T. Tran, "Extension of the virtual fields method to elasto-plastic material identification with cyclic loads and kinematic hardening," *International Journal of Solids and Structures*, vol. 47, no. 2223, pp. 2993–3010, Nov. 2010. [Online]. Available: http://www.sciencedirect.com/science/article/pii/S002076831000243X

[83] G. Palmieri, M. Sasso, G. Chiappini, and D. Amodio, "Virtual Fields Method on Planar Tension Tests for Hyperelastic Materials Characterisation," *Strain*, vol. 47, pp. 196–209, Dec. 2011. [Online]. Available: http://onlinelibrary.wiley.com/doi/10.1111/j.1475-1305.2010.00759.x/abstract

[84] M. Rossi and F. Pierron, "Identification of plastic constitutive parameters at large deformations from three dimensional displacement fields," *Computational Mechanics*, vol. 49, no. 1, pp. 53–71, Jul. 2011. [Online]. Available: http://link.springer.com/article/10.1007/s00466-011-0627-0

[85] J. H. Kim, A. Serpanti, F. Barlat, F. Pierron, and M. G. Lee, "Characterization of the post-necking strain hardening behavior using the virtual fields method," *International Journal of Solids and Structures*, vol. 50, no. 24, pp. 3829–3842, Nov. 2013. [Online]. Available: http://www.sciencedirect.com/science/article/pii/S0020768313002989

[86] K. Spranghers, I. Vasilakos, D. Lecompte, H. Sol, and J. Vantomme, "Identification of the plastic behavior of aluminum plates under free air explosions using inverse methods and full-field measurements," *International Journal of Solids and Structures*, vol. 51, no. 1, pp. 210–226, Jan. 2014. [Online]. Available: http://www.sciencedirect.com/science/article/pii/S002076831300382X

[87] J.-H. Kim, F. Barlat, F. Pierron, and M.-G. Lee, "Determination of Anisotropic Plastic Constitutive Parameters Using the Virtual Fields Method," *Experimental Mechanics*, vol. 54, no. 7, pp. 1189–1204, May 2014. [Online]. Available: http://link.springer.com/article/10.1007/s11340-014-9879-x

[88] D. Notta-Cuvier, B. Langrand, E. Markiewicz, F. Lauro, and G. Portemont, "Identification of Johnson-Cook's Viscoplastic Model Parameters Using the Virtual Fields Method: Application to Titanium Alloy Ti6al4v," *Strain*, vol. 49, no. 1, pp. 22–45, Feb. 2013. [Online]. Available: http://onlinelibrary.wiley.com/doi/10.1111/str.12010/abstract

[89] D. Notta-Cuvier, B. Langrand, F. Lauro, and E. Markiewicz, "An innovative procedure for characterising a coupled elastoplastic damage model of behaviour using the Virtual Fields Method," *International Journal of Solids and Structures*, vol. 6970, pp. 415–427, Sep. 2015. [Online]. Available: http://www.sciencedirect.com/science/article/pii/S002076831500219X

[90] K. T. Kavanagh and R. W. Clough, "Finite element applications in the characterization of elastic solids," *International Journal of Solids and Structures*, vol. 7, no. 1, pp. 11–23, Jan. 1971. [Online]. Available: http://www.sciencedirect.com/science/article/pii/0020768371900151

[91] D. Lecompte, A. Smits, H. Sol, J. Vantomme, and D. Van Hemelrijck, "Mixed numerical-experimental technique for orthotropic parameter identification using biaxial tensile tests on cruciform specimens," *International Journal of Solids and Structures*, vol. 44, no. 5, pp. 1643–1656, Mar. 2007. [Online]. Available: http://www.sciencedirect.com/science/article/pii/S0020768306002848

[92] M. Teaca, I. Charpentier, M. Martiny, and G. Ferron, "Identification of sheet metal plastic anisotropy using heterogeneous biaxial tensile tests," *International Journal of Mechanical Sciences*, vol. 52, no. 4, pp. 572–580, Apr. 2010. [Online]. Available: http://www.sciencedirect.com/science/article/pii/S0020740309002616

[93] S. Cooreman, D. Lecompte, H. Sol, J. Vantomme, and D. Debruyne, "Identification of Mechanical Material Behavior Through Inverse Modeling and DIC," *Experimental Mechanics*, vol. 48, no. 4, pp. 421–433, Nov. 2007. [Online]. Available: http://link.springer.com/article/10.1007/s11340-007-9094-0

[94] R. Fedele, M. Filippini, and G. Maier, "Constitutive model calibration for railway wheel steel through tension-torsion tests," *Computers & Structures*, vol. 83, no. 1213, pp. 1005–1020, May 2005. [Online]. Available: http://www.sciencedirect.com/science/article/pii/S0045794904004043

[95] S. Avril, F. Pierron, M. A. Sutton, and J. Yan, "Identification of elasto-visco-plastic parameters and characterization of Luders behavior using digital image correlation and the virtual fields method," *Mechanics of Materials*, vol. 40, no. 9, pp. 729–742, Sep. 2008. [Online]. Available: http://www.sciencedirect.com/science/article/pii/S0167663608000422

[96] D. E. Goldberg and K. Deb, “A comparative analysis of selection schemes used in genetic algorithms,” *Foundations of Genetic Algorithms*, vol. 1, pp. 69–93, 1991.

[97] J. L. Foo, V. K. Kalivarapu, and E. H. Winer, “Implementation of digital pheromones for use in particle swarm optimization,” in *Proceedings of the 47th AIAA/ASME/ASCE/AHS/ASC Structures, Structural Dynamics and Materials Conference, Newport, RI*, 2006. [Online]. Available: http://arc.aiaa.org/doi/pdf/10.2514/6.2006-1917

[98] V. Kalivarapu, J.-L. Foo, and E. Winer, “Improving solution characteristics of particle swarm optimization using digital pheromones,” *Structural and Multidisciplinary Optimization*, vol. 37, no. 4, pp. 415–427, Mar. 2008. [Online]. Available: http://link.springer.com/article/10.1007/s00158-008-0240-9

[99] G. Singh, “Effective Simulation and Optimization of a Laser Peening Process,” Ph.D. dissertation, Wright State University, 2009. [Online]. Available: http://web1.cs.wright.edu/cepro/docs/thesis/Effective_Simulation_and_Optimization_of_a_Laser_Peening_Process_SINGH.pdf

[100] “632.68 High-Temperature Axial/Torsional Extensometer,” 2014. [Online]. Available: https://mts.com/ucm/groups/public/documents/library/dev_003705.pdf

[101] MATLAB, *Signal Processing Toolbox User’s Guide*. Natick, Massachusetts: The MathWorks Inc., 2014.

[102] S. J. Orfanidis, *Introduction to Signal Processing*, ser. Prentice Hall Signal Processing Series. Englewood Cliffs, N.J: Prentice Hall, 1996.

[103] J. P. Gallagher, R. H. van Stone, R. E. deLaneuville, P. Gravett, and R. S. Bellows, “Improved High-Cycle Fatigue (HCF) Life Prediction,” *NASA STI/Recon Technical Report N*, vol. 03, Jan. 2001. [Online]. Available: http://adsabs.harvard.edu/abs/2001STIN...0305515G

[104] J. Gallagher, T. Nicholas, A. Gunderson, J. Ruschau, P. Miedlar, A. Hutson, G. Hardy, D. Walls, C. Annis, and R. deLaneuville, “Advanced High Cycle Fatigue (HCF) Life Assurance Methodologies,” University of Dayton Research Institute, Tech. Rep. AFRL-ML-WP-TR-2005-4102, Jul. 2004.

[105] P. J. Armstrong and C. O. Frederick, “A mathematical representation of the multiaxial Bauschinger effect,” Central Electricity Generating Board and Berkeley Nuclear Laboratories, Research & Development Department, Tech. Rep. RD/B/N 731, 1966.

[106] R. d. Borst, M. A. Crisfield, Ohio Library and Information Network, and Wiley Online Library (Online service), Eds., *Nonlinear Finite Element Analysis of Solids and Structures*, 2nd ed. Hoboken, NJ: Wiley, 2012, oCLC: 804860756. [Online]. Available: http://dx.doi.org/10.1002/9781118375938

[107] T. Belytschko, W. K. Liu, B. Moran, and K. Elkhodary, *Nonlinear Finite Elements for Continua and Structures*. John Wiley & Sons, Nov. 2013, google-Books-ID: e_w8AgAAQBAJ.

[108] R. D. Cook and R. D. Cook, Eds., *Concepts and Applications of Finite Element Analysis*, 4th ed. New York, NY: Wiley, 2001.

[109] E. Kirchner and B. Simeon, "A higher-order time integration method for viscoplasticity," *Computer Methods in Applied Mechanics and Engineering*, vol. 175, no. 12, pp. 1–18, Jun. 1999. [Online]. Available: http://www.sciencedirect.com/science/article/pii/S0045782598003697

[110] E. Kirchner, "Modeling single crystals: time integration, tangent operators, sensitivity analysis and shape optimization," *International Journal of Plasticity*, vol. 17, no. 7, pp. 907–942, Jul. 2001. [Online]. Available: http://www.sciencedirect.com/science/article/pii/S0749641900000322

[111] P. L. Phillips and R. A. Brockman, "Finite Element-Based Material Parameter Identification," *UDR-TR-2009-180*, 2009.

[112] M. J. Powell, "The BOBYQA algorithm for bound constrained optimization without derivatives," *Cambridge NA Report NA2009/06, University of Cambridge, Cambridge*, 2009. [Online]. Available: http://citeseerx.ist.psu.edu/viewdoc/download?doi=10.1.1.443.7693&rep=rep1&type=pdf

[113] "Intel Math Kernel Library Developer Reference - Fortran," Intel Corporation, Tech. Rep. Report MKL 2017, Revision 082, 2016.

[114] G. E. Dieter and D. Bacon, *Mechanical Metallurgy*, si metric ed ed., ser. McGraw-Hill series in materials science and engineering. London: McGraw-Hill, 1988.

APPENDIX A

DATA FILTERING

This appendix provides a cursory introduction to the filtering and data condensing methods that are used throughout this work to prepare the experimental data for use with the analytical methods. The parameters of the filters are provided and the filtering routines are described. In addition, a description is provided for the algorithm for condensing experimental stress strain data into noise-free data for use with finite element method updating.

A.1 Infinite Impulse Response (IIR) Filter

A digital Infinite Impulse Response (IIR) filter has been designed to replicate the behavior of the hardware implemented 8th order Butterworth low-pass analog filter used by the University of Dayton Research Institute (UDRI) at the Air Force Research Laboratory (AFRL). The UDRI filter is an 8th order filter implemented using four second order Sallen-Key filters and has a cutoff frequency of 10 Hertz with a drop of -3 dB at the cutoff frequency.

The digital IIR filters have been designed in MATLAB [101] using the *fdatool*. Three 8th-order low-pass Butterworth filters were generated with cutoff frequencies of 5, 10, and 20 percent of the sampling frequency and are designated as 'LP_BUT8_5', 'LP_BUT8_10', and 'LP_BUT8_20'. Table A.1 shows the coefficients and gains for the filters.

The digital filters are implemented as a cascade of second-order sections (SOS) [102, p. 277-284]. The general difference equation for an Mth order filter is

$$y_n = \sum_{i=0}^{M} b_i x_{n-i} - \sum_{i=1}^{M} a_i y_{n-i}. \tag{A.1}$$

The implementation of the difference equation used with the SOS is

$$\begin{aligned} w\left(n\right) &= x\left(n\right) - a_1 w\left(n-1\right) - a_2 w(n-2) \\ y(n) &= b_0 w\left(n\right) + b_1 w\left(n-1\right) + b_2 w\left(n-2\right) \end{aligned} \tag{A.2}$$

where w are the states of the filter. Lastly, because MATLAB reports both the coefficients and the appropriate gain, the value of $y(n)$ is multiplied by the gain for the stage. Waiting until the end to multiply by the gain rather than incorporating the gain in each of the factors is likely to reduce round-off error. The filters are implemented in FORTRAN following the routines sos.c [102, p. 277] and cas.c [102, p. 280] outlined by Orfanidis [102]. Again, the only modification is that multiplication of $y(n)$ by the gain is carried out last.

One drawback of using an IIR filter is the phase distortion and time lag present in the filtered signal. To account for this, all signals that get combined must be filtered, e.g. stress and strain signals, to prevent any time lag misalignments. However, the magnitude of the filtered frequency content is not consistent with the original signal leading to slight changes in the signal. These phase shifts can be prevented through the use of a Finite Impulse Response (FIR) filter as discussed in the next section.

Table A.1: Coefficients for 8th-order IIR low-pass Butterworth filters.

LP_BUT8_5

Stage	b_0	b_1	b_2	a_0	a_1	a_2	gain
1	1	2	1	1	-1.79396184525177E+00	8.86283112007013E-01	2.30803166888105E-02
2	1	2	1	1	-1.62340569764100E+00	7.06949765682682E-01	2.08860170104204E-02
3	1	2	1	1	-1.51329076583890E+00	5.91168074568205E-01	1.94693271823251E-02
4	1	2	1	1	-1.45970625437686E+00	5.34825984961610E-01	1.87799326461858E-02

LP_BUT8_10

Stage	b_0	b_1	b_2	a_0	a_1	a_2	gain
1	1	2	1	1	-1.45157959424784E+00	7.94251053241888E-01	8.56678647485130E-02
2	1	2	1	1	-1.21972536512402E+00	5.07663465174044E-01	7.19845250125051E-02
3	1	2	1	1	-1.08685846136289E+00	3.43430940165366E-01	6.41431197006179E-02
4	1	2	1	1	-1.02635147426106E+00	2.68640190993790E-01	6.05721791831837E-02

LP_BUT8_20

Stage	b_0	b_1	b_2	a_0	a_1	a_2	gain
1	1	2	1	1	-5.21309265637001E-01	6.86992220901831E-01	2.91420738816207E-01
2	1	2	1	1	-4.04372288519085E-01	3.08576213864916E-01	2.26050981336458E-01
3	1	2	1	1	-3.45121039357246E-01	1.16835143825427E-01	1.92928526117045E-01
4	1	2	1	1	-3.19763902271564E-01	3.47777245013790E-02	1.78753455557454E-01

A.2 Finite Impulse Response (FIR) Filter

The second type of digital filter implemented is the Finite Impulse Response (FIR) filter. A FIR filter uses the difference equation, Eq. (A.1), to compute the filtered value but it has no feedback; therefore, the a_i terms all equal zero. The FIR filters have been designed in MATLAB [101] using the *fdatool*. Three 100th-order, low-pass, FIR filters were generated with cutoff frequencies of 5, 10, and 20 percent of the sampling frequency and are designated as 'LP_FIR100_5', 'LP_FIR100_10', and 'LP_FIR100_20'. Tables A.2 through A.4 shows the coefficients for the weights, h_i, of the filters.

The digital filters are implemented using the generalized FIR filter implementation fir.c [102, p. 160] provided by Orfanidis [102]. The implementation of the difference equation is

$$\begin{aligned} y_n &= \sum_{i=0}^{M} h_i w_i \\ w_i &= w_{i+1} \end{aligned} \tag{A.3}$$

where w are the states of the filter.

The benefit of using a FIR filter is the avoidance of phase shifts in the filtered signal. There is a constant time lag of M/2 samples, where M is the order of the filter. There is still a transient response of the filter for the first M samples, however with prior knowledge, the input signal can be started M samples prior to the data of interest so that the transient effect can be removed without significant loss.

Table A.2: Coefficients for LP_FIR100_5 filter.

LP_FIR100_5 Offset i	h_i	h_{i+1}	h_{i+2}	h_{i+3}	h_{i+4}
0	-5.21445825840397E-05	-5.27221493091746E-05	-5.37589113167613E-05	-2.76194422045900E-05	3.22882909714848E-05
5	1.21806945197204E-04	2.22283271638467E-04	3.01009425631104E-04	3.17312660698914E-04	2.34202634633929E-04
10	3.33072783563605E-05	-2.71033129749296E-04	-6.23768764836358E-04	-9.32153807485873E-04	-1.08248967930466E-03
15	-9.69386418389882E-04	-5.31926095484453E-04	2.12659423669110E-04	1.14927486807982E-03	2.06948683497042E-03
20	2.70559850221409E-03	2.79192515719064E-03	2.14250588396318E-03	7.26448545906149E-04	-1.28176088491500E-03
25	-3.49732708239483E-03	-5.37794818755062E-03	-6.33346210433723E-03	-5.87412293257714E-03	-3.76667912815096E-03
30	-1.56866483771410E-04	4.38072944914721E-03	8.89409246194095E-03	1.22134125580561E-02	1.31999241850769E-02
35	1.10387833904289E-02	5.51241585693532E-03	-2.81459043455351E-03	-1.25572128326922E-02	-2.16502624665183E-02
40	-2.76617653706638E-02	-2.82336865541452E-02	-2.15701941379855E-02	-6.87441645875312E-03	1.53637566616146E-02
45	4.33026149647020E-02	7.39382939014201E-02	1.03529741357102E-01	1.28188961978023E-01	1.44529264950467E-01
50	1.50247886125499E-01	1.44529264950467E-01	1.28188961978023E-01	1.03529741357102E-01	7.39382939014201E-02
55	4.33026149647020E-02	1.53637566616146E-02	-6.87441645875312E-03	-2.15701941379855E-02	-2.82336865541452E-02
60	-2.76617653706638E-02	-2.16502624665183E-02	-1.25572128326922E-02	-2.81459043455351E-03	5.51241585693532E-03
65	1.10387833904289E-02	1.31999241850769E-02	1.22134125580561E-02	8.89409246194095E-03	4.38072944914721E-03
70	-1.56866483771410E-04	-3.76667912815096E-03	-5.87412293257714E-03	-6.33346210433723E-03	-5.37794818755062E-03
75	-3.49732708239483E-03	-1.28176088491500E-03	7.26448545906149E-04	2.14250588396318E-03	2.79192515719064E-03
80	2.70559850221409E-03	2.06948683497042E-03	1.14927486807982E-03	2.12659423669110E-04	-5.31926095484453E-04
85	-9.69386418389882E-04	-1.08248967930466E-03	-9.32153807485873E-04	-6.23768764836358E-04	-2.71033129749296E-04
90	3.33072783563605E-05	2.34202634633929E-04	3.17312660698914E-04	3.01009425631104E-04	2.22283271638467E-04
95	1.21806945197204E-04	3.22882909714848E-05	-2.76194422045900E-05	-5.37589113167613E-05	-5.27221493091746E-05
100	-5.21445825840397E-05				

Table A.3: Coefficients for LP_FIR100_10 filter.

LP_FIR100_10 Offset i	h_i	h_{i+1}	h_{i+2}	h_{i+3}	h_{i+4}
0	3.23852814004876E-08	1.95639733047478E-07	3.86190590272571E-07	1.06973546900679E-07	-1.20172752274904E-06
5	-2.92131990731852E-06	-2.37853541066280E-06	3.29864309084602E-06	1.21770356508078E-05	1.42417371958452E-05
10	-2.36413327943482E-06	-3.48659871542758E-05	-5.41037436757278E-05	-2.01057543401049E-05	7.19497364338421E-05
15	1.53630028050493E-04	1.12367101398877E-04	-9.76665447957807E-05	-3.46833912707760E-04	-3.65060969990470E-04
20	2.47857212135220E-05	6.34147687905860E-04	9.03750757972398E-04	3.32399655231792E-04	-9.17052060809359E-04
25	-1.84038617907458E-03	-1.27145338854716E-03	9.16318265240396E-04	3.17233951224653E-03	3.16016888158837E-03
30	-1.06016894292701E-04	-4.64063123969781E-03	-6.32310116132814E-03	-2.30214769364626E-03	5.58032002453143E-03
35	1.08754108766448E-02	7.32793556784751E-03	-4.78049979799814E-03	-1.65658036390823E-02	-1.62664417911679E-02
40	2.38065181447832E-04	2.27129871064821E-02	3.12968745870022E-02	1.19182226217937E-02	-2.82999516588143E-02
45	-5.91857306420825E-02	-4.44039297484823E-02	3.22266744759096E-02	1.49707710674769E-01	2.56588661128772E-01
50	2.99690992245546E-01	2.56588661128772E-01	1.49707710674769E-01	3.22266744759096E-02	-4.44039297484823E-02
55	-5.91857306420825E-02	-2.82999516588143E-02	1.19182226217937E-02	3.12968745870022E-02	2.27129871064821E-02
60	2.38065181447832E-04	-1.62664417911679E-02	-1.65658036390823E-02	-4.78049979799814E-03	7.32793556784751E-03
65	1.08754108766448E-02	5.58032002453143E-03	-2.30214769364626E-03	-6.32310116132814E-03	-4.64063123969781E-03
70	-1.06016894292701E-04	3.16016888158837E-03	3.17233951224653E-03	9.16318265240396E-04	-1.27145338854716E-03
75	-1.84038617907458E-03	-9.17052060809359E-04	3.32399655231792E-04	9.03750757972398E-04	6.34147687905860E-04
80	2.47857212135220E-05	-3.65060969990470E-04	-3.46833912707760E-04	-9.76665447957807E-05	1.12367101398877E-04
85	1.53630028050493E-04	7.19497364338421E-05	-2.01057543401049E-05	-5.41037436757278E-05	-3.48659871542758E-05
90	-2.36413327943482E-06	1.42417371958452E-05	1.21770356508078E-05	3.29864309084602E-06	-2.37853541066280E-06
95	-2.92131990731852E-06	-1.20172752274904E-06	1.06973546900679E-07	3.86190590272571E-07	1.95639733047478E-07
100	3.23852814004876E-08				

Table A.4: Coefficients for LP_FIR100_20 filter.

LP_FIR100_20 Offset i	h_i	h_{i+1}	h_{i+2}	h_{i+3}	h_{i+4}
0	5.36755336095553E-05	7.55573618619739E-06	-8.57055356563023E-05	-5.58435808710261E-05	1.22803649846051E-04
5	1.38861057125727E-04	-1.49950916847842E-04	-2.82916891503013E-04	1.18391647500839E-04	4.69059173682685E-04
10	-1.13132535359300E-06	-6.86367544503273E-04	-2.57413891854891E-04	8.70977474040061E-04	6.76618973125797E-04
15	-9.54109432360451E-04	-1.27105940464918E-03	8.23183401167539E-04	1.99160071523286E-03	-3.76221951821183E-04
20	-2.75076199137326E-03	-4.92094366412334E-04	3.38227707570014E-03	1.82872424467423E-03	-3.67796781542204E-03
25	-3.62135344292491E-03	3.37796406557394E-03	5.74367697012469E-03	-2.22807540650331E-03	-7.96132634531171E-03
30	-2.48334198767612E-06	9.90343082904757E-03	3.45433981184967E-03	-1.10914524372585E-02	-8.15644820162432E-03
35	1.09376790540600E-02	1.39786839165244E-02	-8.77592500360702E-03	-2.06390149156450E-02	3.82218346208093E-03
40	2.77017707612647E-02	4.94705178479335E-03	-3.46308754863658E-02	-1.92942071236900E-02	4.08348212033363E-02
45	4.34903390311595E-02	-4.57513860439112E-02	-9.33746251413399E-02	4.89080259993594E-02	3.13958189070442E-01
50	4.50002601848541E-01	3.13958189070442E-01	4.89080259993594E-02	-9.33746251413399E-02	-4.57513860439112E-02
55	4.34903390311595E-02	4.08348212033363E-02	-1.92942071236900E-02	-3.46308754863658E-02	4.94705178479335E-03
60	2.77017707612647E-02	3.82218346208093E-03	-2.06390149156450E-02	-8.77592500360702E-03	1.39786839165244E-02
65	1.09376790540600E-02	-8.15644820162432E-03	-1.10914524372585E-02	3.45433981184967E-03	9.90343082904757E-03
70	-2.48334198767612E-06	-7.96132634531171E-03	-2.22807540650331E-03	5.74367697012469E-03	3.37796406557394E-03
75	-3.62135344292491E-03	-3.67796781542204E-03	1.82872424467423E-03	3.38227707570014E-03	-4.92094366412334E-04
80	-2.75076199137326E-03	-3.76221951821183E-04	1.99160071523286E-03	8.23183401167539E-04	-1.27105940464918E-03
85	-9.54109432360451E-04	6.76618973125797E-04	8.70977474040061E-04	-2.57413891854891E-04	-6.86367544503273E-04
90	-1.13132535359300E-06	4.69059173682685E-04	1.18391647500839E-04	-2.82916891503013E-04	-1.49950916847842E-04
95	1.38861057125727E-04	1.22803649846051E-04	-5.58435808710261E-05	-8.57055356563023E-05	7.55573618619739E-06
100	5.36755336095553E-05				

A.3 Condensing Stress-Strain Data

In the analysis domain, stress-strain curves are smooth, noise-free representations of the generally noisy signals actually collected during experimentation. Figure A.1 shows data collected at 100 Hz for a cylindrical 4340 steel specimen using an axial/torsional extensometer that has been filtered with a 10 Hz FIR low-pass filter. There may still be slight scatter in the data after filtering and there could even be a slight bend in the elastic portion of the stress-strain curve. In the analysis world, there is no deviation from the straight line defined by the elastic modulus until plasticity is reached; therefore, before the yield surface is even reached, there would be error between the experiment and the analysis. If a series of points were taken in the elastic range of the experimental data, there would be error present when optimizing the plasticity parameters due solely to the elastic range for which the modulus was already determined. Therefore, the experimental data needs to be filtered and massaged into a form more representative of the analytical domain. This reduces the number of data points and also eliminates unnecessary sampling within the elastic domain when fitting plasticity parameters.

A procedure for condensing stress-strain data has been developed with enough flexibility to work for a wide variety of experimental data. Figure A.1 illustrates the important criteria and options of the method. The condensing procedure operates on a single segment of the curve at a time. Individual segments are differentiated by the change in loading direction (loading/unloading). The data can be condensed using uniform suggested increments in strain with or without the addition of linear region condensing. User input required for the algorithm is

- *stress* - matrix of experimental stresses where each row is a different point in time and column 1 and 2 are the axial and shear stresses

- *strain* - matrix of experimental engineering strains where each row is a different point in time and column 1 and 2 are the axial and shear strains
- number of points in the segment to be condensed
- *end tolerance* - strain window over which the start and end of the segment are averaged
- *nonlinear increment* - suggested strain increment for the condensed data
- *averaging window* - strain window centered on the nonlinear increment locations for which data is averaged to compute the condensed points
- *increment tolerance* - additional increment outside the *averaging window* to search for strain point inside of the averaging window. This tolerance is used to compensate for noisy data that may not be monotonic
- option to determine if axial or shear data determines the condensing process
- elastic axial and shear modulus
- *elastic stress tolerance* - stress difference from linear elastic line that designates the onset of non-linear behavior

The beginning of the data is averaged over the strain range given by the *end tolerance*. If the difference between the first strain point and the current strain is no more than *end tolerance*, that strain point is included in the data averaging. The data are then averaged to compute the beginning strain, ε_0, and the beginning stress, σ_0. The same process is repeated for the last strain point to find the end strain, ε_{end}, and stress, σ_{end}. The remaining condensed points can be computed using two different methods. Method one searches for the extent of the linear region defined by the elastic modulus, while method two assumes uniform strain increments over the entire segment. If linear behavior is included, the nonlinear strain initiation point, ε_{NL}, is sought where the value, σ_{diff}, given in the following equation exceeds the *elastic stress tolerance*

$$\sigma_{diff} = \sigma_0 + E\left(\varepsilon_i - \varepsilon_0\right) - \sigma_i. \tag{A.4}$$

If method one is used, the data between ε_{NL} and ε_{end} is condensed at equal intervals given by the *nonlinear increment*. If method two is used, the data between ε_0 and ε_{end} is condensed at equal intervals given by the *nonlinear increment*.

The user specifies the desired *nonlinear increment*, but the actual value used is determined from the number of increments, s, computed as follows

$$\begin{aligned} x &= \frac{(\varepsilon_1 - \varepsilon_2)}{nlinc} - floor\left[\frac{(\varepsilon_1 - \varepsilon_2)}{nlinc}\right] \\ s &= \begin{cases} floor\left[\frac{(\varepsilon_1 - \varepsilon_2)}{nlinc}\right] & if\,(x \leq 0.5) \\ floor\left[\frac{(\varepsilon_1 - \varepsilon_2)}{nlinc}\right] + 1 & if\,(x > 0.5) \end{cases} \end{aligned} \tag{A.5}$$

where $nlinc$ is the user suggested *nonlinear increment*, and ε_1 and ε_2 are the end points dictated by the chosen method. The actual value of $nlinc$ used is then computed as

$$nlinc = \frac{\varepsilon_1 - \varepsilon_2}{s}. \tag{A.6}$$

The strain and corresponding stress within the *averaging window* centered on the condensed strain locations, $\varepsilon_k^{(c)}$, are averaged for both stress and strain. While marching through the points in order, the first strain value within the window defines the starting point. The end point of the window is computed by finding the last point that falls within the window while searching over one half the *averaging window* plus an additional *increment tolerance* specified by the user. This allows for capturing the correct amount of data when the experimental data is not monotonically increasing or decreasing due to noise.

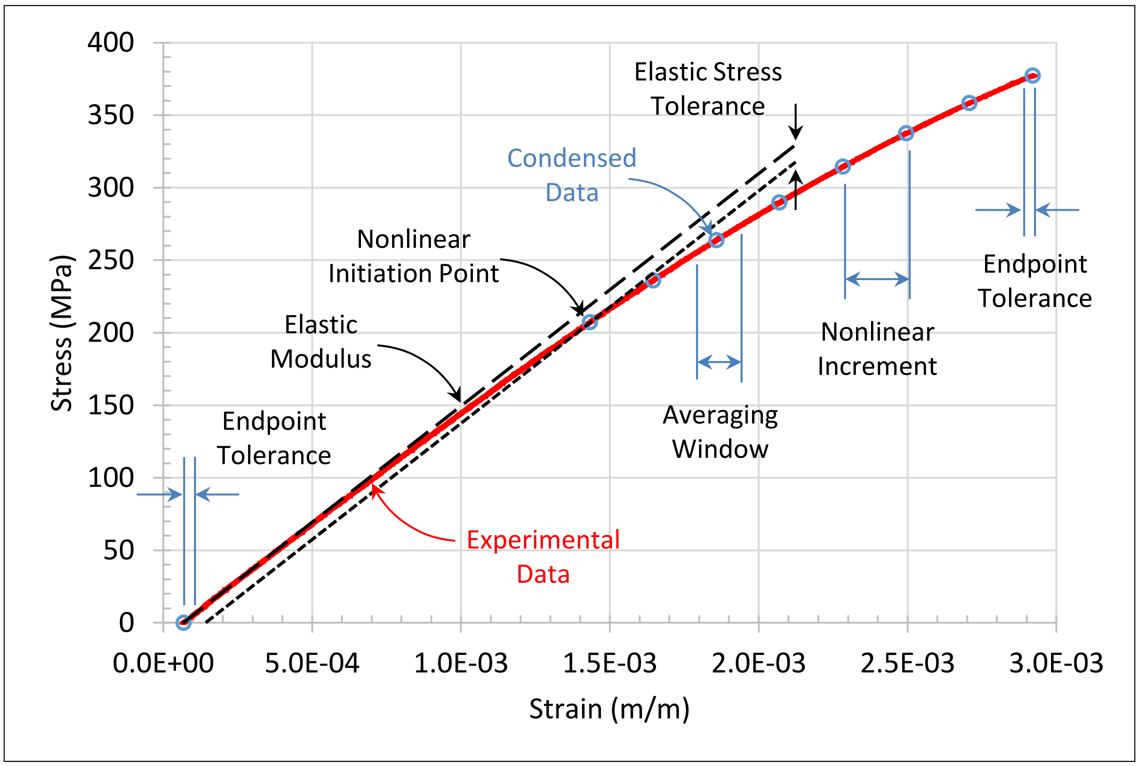

Figure A.1: Experimental data for single segment, condensing criteria, and condensed data points.

APPENDIX B

SPECIMEN DESIGN

This appendix provides information pertaining to the design and analysis of the specimens to be used on the axial-torsional test machine. Details are also provided on the material processing of the Ti-6Al-4V material from which the specimens are machined. Section B.1 summarizes an elastic-plastic buckling analysis that considers the following factors: plasticity, crosshead misalignment, geometric imperfection sensitivity, and torque. Section B.2 provides results from the analysis of strain uniformity in the gage section of the specimens when considering both elastic and plastic loading. Finally, Section B.3 provides details on the material processing of the Ti-6Al-4V.

B.1 Ti-6Al-4V Specimen Buckling Analysis

Two different specimen designs have been considered for Ti-6Al-4V, which are referred to as Type I and Type II. Figure B.1 shows the geometry and provides the measurements for both solid cylindrical specimens. The Type I specimen, which is discussed in Section B.1.1, has a gage length long enough to accommodate the axial-torsional extensometer. The Type II specimen, discussed in Section B.1.2, has a shorter gage length to allow for fully reversed loading. However, the shorter gage length prohibits the use of the extensometer. For all specimen design analyses, a simple isotropic plasticity model shown in Table B.1 has been used.

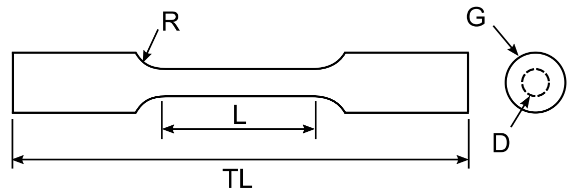

	Type I		Type II	
	mm	in	mm	in
D	9.53	0.375	6.35	0.250
L	44.50	1.752	19.00	0.748
R	50.80	2.000	25.40	1.000
G	12.70	0.500	12.70	0.500
TL	136.00	5.354	136.00	5.354

Figure B.1: Specimen geometry and dimensions for the solid cylindrical specimens.

Table B.1: Basic isotropic plasticity model for Ti-6Al-4V specimen design.

E (MPa)	115,800		
ν	0.31		
True Stress (MPa)	**Plastic Strain**	**True Stress** (MPa)	**Plastic Strain**
904.4	0.0000E+00	993.2	3.2263E-02
920.2	1.5658E-04	1,005.3	3.9759E-02
926.4	1.0702E-03	1,017.8	4.7810E-02
931.1	2.6105E-03	1,030.4	5.6510E-02
942.4	7.4252E-03	1,043.0	6.6026E-02
954.2	1.2724E-02	1,053.8	7.4824E-02
962.5	1.6460E-02	1,062.3	8.1886E-02
970.4	2.0006E-02	1,066.6	8.5820E-02
980.3	2.5313E-02	1,070.0	1.5000E-01

B.1.1 Type I - Extended Gage Length

A buckling analysis of the Type I specimen made of Ti-6Al-4V has been performed to determine the sensitivity to plasticity, geometric imperfections, crosshead misalignment, and the addition of torsional loading. A three-dimensional finite element (FE) model of the specimen has been created with the specimen axis aligned with the FE y-axis. In the FE model, the specimen is assumed to be gripped over a 25.4 mm region on both ends. The gripped regions are excluded and boundary conditions are applied to both the top and bottom surfaces. The bottom surface is completely constrained in the three displacement degrees of freedom (DOF). The nodes on the top surface are coupled to a reference point at the center of the top surface in all possible DOF. The reference point is then constrained in all DOF except axial displacement and rotation about the specimen axis.

A natural frequency analysis was performed using the commercial finite element code Abaqus to extract the first 10 modes. To introduce imperfections, only the bending modes in the x-direction (modes 1, 6, 8) are utilized to encourage buckling. Figure B.2 shows these bending modes. The displacement results from the natural frequency modes are scaled by Abaqus so the largest component of displacement is 1.0. Therefore, to introduce a known maximum geometric imperfection, the corresponding modal displacement components (excluding the y-axis displacement) are multiplied by a random factor and like components are summed. The displacements are scaled such that the largest imperfection magnitude is equal to the specified tolerance. For the sensitivity study, values of 0.0, 0.005, 0.01, 0.10, and 1.00 mm have been used.

An initial buckling analysis was performed using Abaqus's linear elastic buckling solution procedure (*Buckle). The geometric imperfections were included, and a basic isotropic plasticity model for Ti-6Al-4V was used. A procedure similar to the Shanley buckling method was attempted. Incremental axial loading was prescribed using nonlinear geometric effects. After each increment, a *Buckle linear perturbation step was performed to determine the additional load required for the buckling. The procedure predicted large buckling loads well above the corresponding ultimate stresses for the Ti-6Al-4V. The results did not seem reasonable given the magnitude of the geometric imperfections. The analysis indicates that the combined elastic buckling loads and preloads are still above the ultimate loads of the material. However, the buckling problem is likely dominated by plasticity and geometric imperfections. The *Buckle procedure completely disregards plasticity and is not sensitive to geometric imperfections [67]. As such, the Riks method has been used for further analysis to determine the influence of plasticity and imperfections on the buckling solution.

The Riks solution procedure is similar to a static implicit solution; however, the applied loads and non-zero boundary conditions are related to a new set of variables that describe the path length along the scaled load-displacement curve. The solution procedure is thus controlled using the new path length degrees of freedom. This allows for surpassing buckling loads where the stiffness matrix becomes singular and at which point the regular static implicit method based on displacement DOFs fails to converge.

The axial load at the bifurcation points (where the stiffness matrix is singular and the load decreases for increasing displacements) has been determined for a variety of sensitivity parameters. As mentioned earlier, five different geometric imperfection magnitudes are used: 0.0, 0.005, 0.01, 0.10, and 1.00 mm. Additionally, crosshead misalignment is considered by applying axial displacement in the y-axis, along with a displacement in the x-axis. The value of the x-axis displacement is determined based on the desired misalignment angle and the corresponding percent bending strain as computed using ASTM E1012. For all misalignment angles, the y-axis displacement was held constant at 3 mm. The misalignment angles used are 0, 1, 10, and 20 degrees corresponding to 0, 0.25, 2.5, and 5.5 percent bending strains, respectively. Typical crosshead alignment procedures yield around 3 percent bending strain at 500 microstrain, which are within ASTM E1012 specifications. Lastly, an imposed rotation about the specimen axis was considered. Rotations of 0.0, 0.5, and 1.0 radians have been used to establish the compressive buckling load under combined axial and torsional stress trajectories.

Figure B.3 shows the axial force versus displacement for the case of zero imperfections, but with varying degrees of crosshead misalignment. Figure B.4 shows axial force versus displacement for both geometric imperfections and crosshead misalignment. Misalignment alone does not significantly affect the buckling characteristics of the specimen. The addition of both factors contributes to buckling near the yield point in almost all cases (except those with zero imperfections as was shown in Figure B.3). In both figures, the dashed black line represents the specimen with zero imperfections and no misalignment.

For the perfect specimen, the simulation of the misalignment of the crosshead lowers the axial force and at 20 degrees, which is approximately equal to 5 percent bending strain, causes the specimen to buckle asymmetrically in a similar manner to mode 1 from the natural frequency analysis. For a perfectly aligned crosshead, the addition of minor geometric imperfections facilitates the initiation of buckling shortly after the onset of plastic strain. Furthermore, if small geometric imperfections of approximately 0.005 to 0.01 mm are coupled with crosshead misalignment, the buckling of the specimen almost always occurs shortly after the onset of plasticity. Figure B.5 provides an example of the common mode of buckling for this specimen for a geometric imperfection of 0.010 mm, axial only loading, and crosshead misalignment of 10 degrees (2.5 percent bending strain).

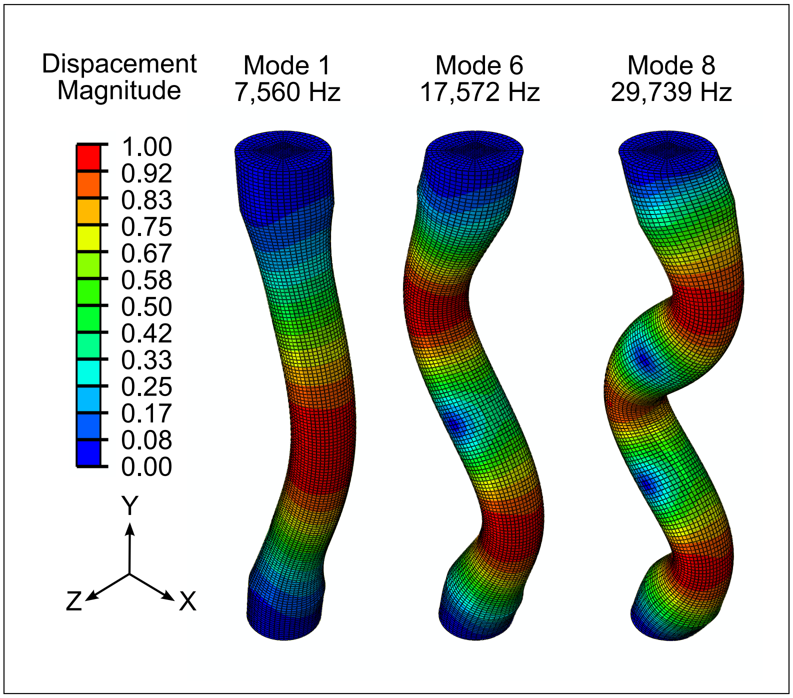

Figure B.2: Specimen Type I bending modes along x-axis.

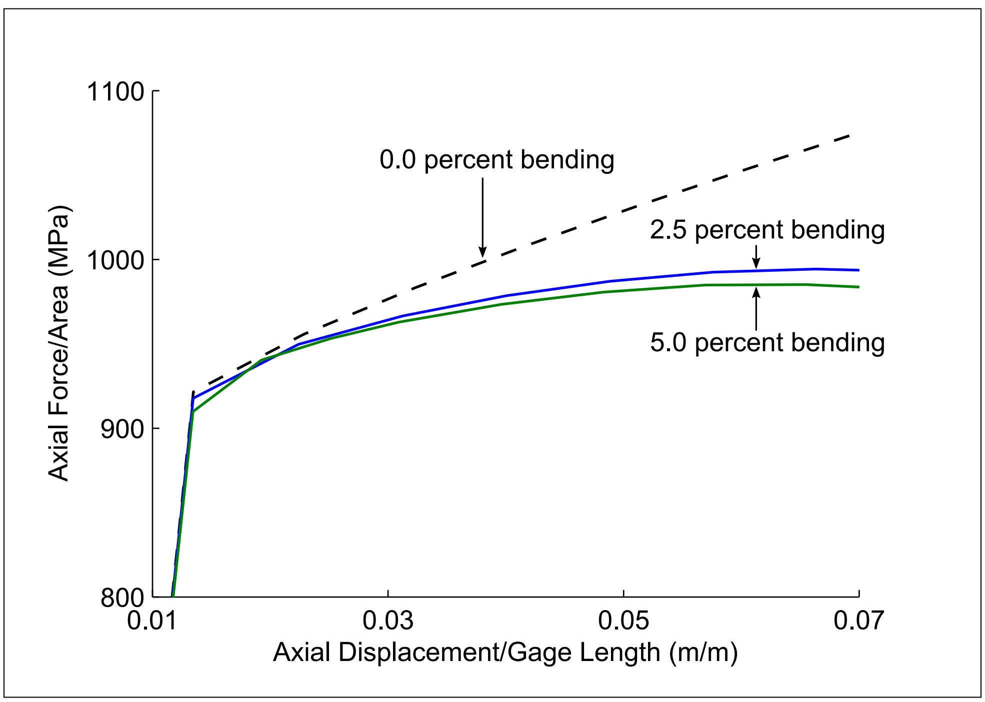

Figure B.3: Specimen Type I axial force/area versus displacement/gage length for zero imperfections, and crosshead misalignment leading to 0, 2.5, and 5.0 percent bending strain.

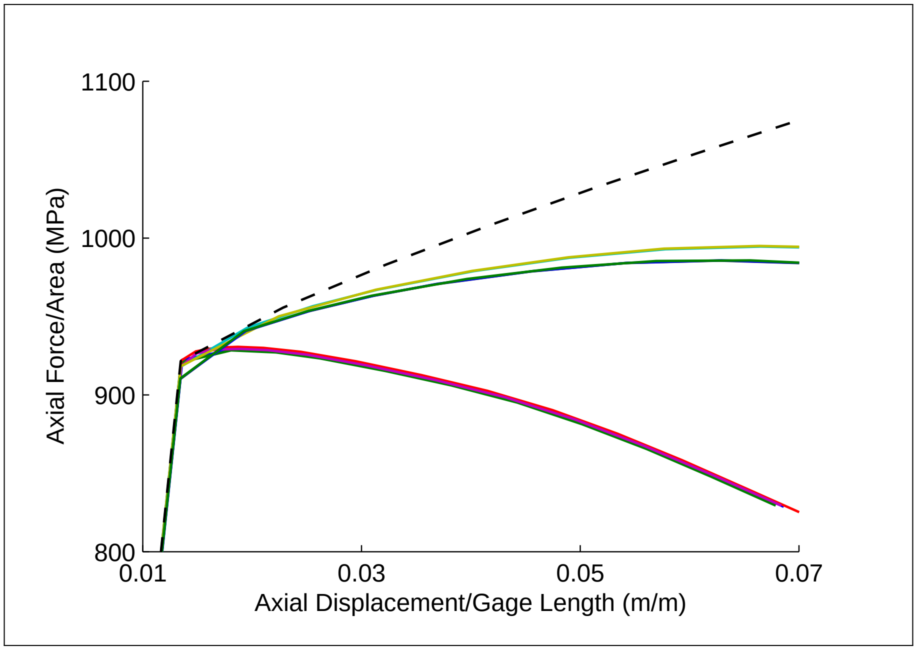

Figure B.4: Specimen Type I axial force/area versus displacement/gage length for 0.01 mm imperfections, and crosshead misalignment leading to 0, 2.5, and 5.0 percent bending strain. The dashed black line corresponds to zero imperfections and zero bending strain.

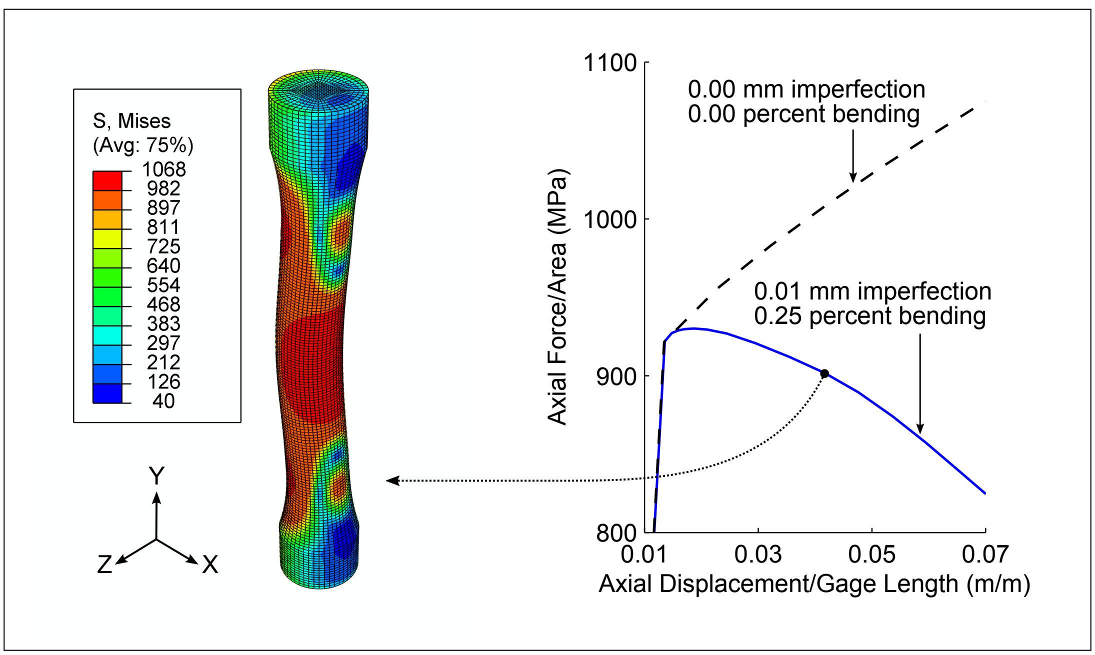

Figure B.5: Specimen Type I stress contours on displaced specimen for 0.01 mm imperfections and 0.25 percent bending strain. Axial force/area versus displacement/gage length is shown on the right.

B.1.2 Type II - Fully Reversed Loading

A buckling analysis has also been performed for Ti-6Al-4V using the Type II specimen. Comparisons between the two specimen designs have been completed for misalignments of 0.0, 2.5, and 5.5 percent bending strain and geometric imperfections of 0.00, 0.01, and 0.10 mm. Figure B.6 shows the results for axial loading only for Type II on the left and Type I on the right. There is significant improvement in the response around the compressive yield strength when the gage length is shortened (as done in Type II). Figure B.6 (left) shows that for the Type II design all of the load-deflection curves are monotonically increasing, unlike those from the Type I design.

Figure B.7 shows results for the same misalignment (0.0, 2.5, and 5.5 percent bending strain) and geometric imperfections (0.0, 0.10, and 0.10 mm) but with added rotation of the specimen. Values of 0.5 radian and 1.0 radians have been used for Type I and Type II specimens, respectively. The larger value of 1.0 radian is used on the smaller diameter specimen (Type II) to introduce approximately the same shear strains on the surface. Rotation levels of 0.5 and 1.0 radian were previously analyzed, and the trends for the perfect geometry case (dashed black line) show similar force/area levels; therefore, the strain levels appear close enough that comparisons should be valid. The Type II specimen also performs significantly better under combined compressive and torsional loading. It does not appear to buckle under combined axial-torsional loading, unlike the Type I specimen which buckles near the onset of plasticity.

B.1.3 Conclusions and Recommendations

If the Type I specimen is used, limits need to be placed on the compressive loads to prevent buckling near the onset of yielding. Possible ways to increase the compressive load limits in the Type I specimen prior to buckling are to 1) increase the diameter of the gage section, or 2) shorten the specimen gage length (as done in the Type II specimen). The force capacity of the test frame used for

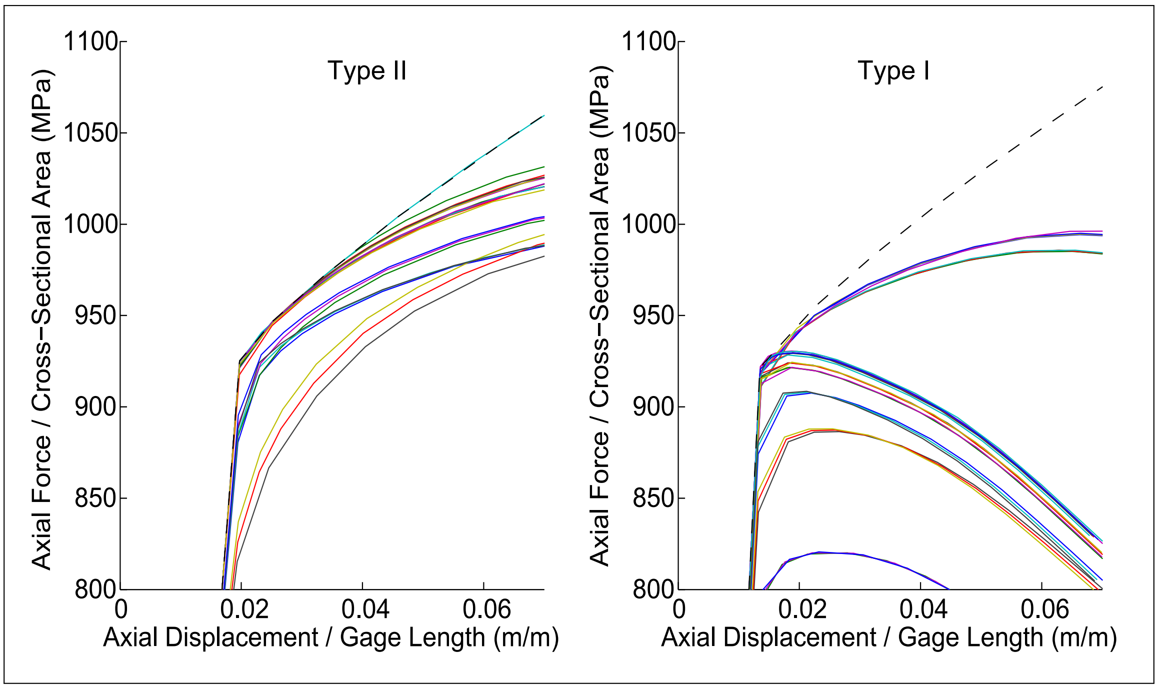

Figure B.6: Axial force divided by cross-section area versus axial displacement divided by gage length for left) Type II specimen and right) Type I specimen. Parameters are 1) axial only loading conditions, 2) crosshead misalignments of 0.0, 2.5, and 5.5 percent bending strain, and 3) geometric imperfections of 0.00, 0.01, and 0.10 mm. Dashed black line in each plot is for the specimen with zero geometric imperfections and misalignment.

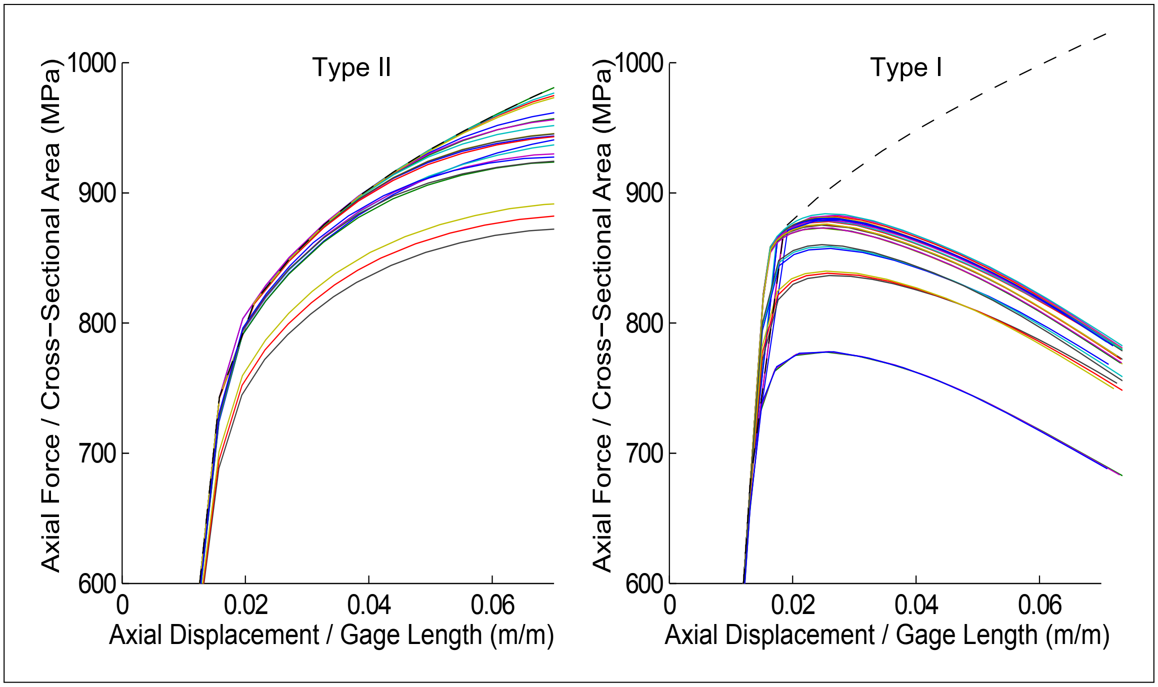

Figure B.7: Axial force divided by cross-section area versus axial displacement divided by gage length for left) Type II specimen and right) Type I specimen. Parameters are 1) 1.0 radians of twist for Type I specimen and 0.5 radians of twist for Type II specimen, 2) crosshead misalignments of 0.0, 2.5, and 5.5 percent bending strain, and 3) geometric imperfections of 0.00, 0.01, and 0.10 mm. The dashed black line in each plot is for the specimen with zero geometric imperfections and misalignment.

axial-torsional testing is only 100 kN. As such, to develop 1,000 MPa of stress typical of titanium, the diameter of specimen could be at most 11.2 mm. Ideally, the same specimen configuration would be used for multiple materials for repeatability and equipment calibration processes. As such, a 1,200 MPa yield stress typical of Ni-based super alloys limits the diameter to 10.3 mm. Currently, the diameter of the Type I specimen is 9.53 mm and could likely be increased to 10 mm to stay in the recommended range of the actuator; however, the positive effects of this increase are probably negligible compared to the detrimental effects of combining geometric imperfections and crosshead misalignment for the given gage length.

Decreasing the gage length eliminates the option of using the high-temperature axial-torsional extensometer, and it requires the use of strain gages. However, the axial-torsional extensometer is currently the only way to obtain strain measurements at AFRL for axial-torsional testing at elevated temperatures, which is of interest for future work. To use the Type I specimen, compressive loads for the Ti-6Al-4V specimen will likely need to be limited to levels near the onset of compressive yielding (-900 MPa). While this may be limiting for certain constitutive model fitting procedures, valuable information can be gained through verification of the extensometer at room temperature prior to use at elevated temperature.

The fully reversed loading specimen, Type II, behaves significantly better (see Figure B.6 and B.7) with regard to buckling than the extended gage length specimen design (Type I). If the Type II specimen is used, it is likely that fully reversed loading can be developed for Ti-6Al-4V which is critical to calibration of material models. Therefore, fully reversed testing should be conducted using the Type II specimen, while the Type I specimen can be utilized, with limits on compressive loads, to characterize the behavior of the extensometer. A total of 12 specimens, 6 of each type, have been manufactured for this work.

B.2 Strain Uniformity and Instrumentation

B.2.1 Strain Uniformity

The uniformity of the strain field in the gage section has been checked for both Ti-6Al-4V specimens discussed in Section B.1. An axisymmetric FE model was created and analyzed with Abaqus Standard for both specimen types. The simple isotropic plasticity model for Ti-6Al-4V given in Table B.1 has been used. Axial and shear strain data has been obtained along the outer surface of the specimen. Load cases consisted of 1) axial-only, 2) shear-only, and 3) combined (proportional axial and shear loading with equal magnitudes). For all load cases, the final strains at the outer surface were approximately 0.05 m/m, and data were collected at 10 discrete strain levels capturing both the elastic and plastic behavior.

Figure B.8 shows a generic specimen and identifies the gage length (GL), the path length (y), and the distance to the strain tolerance (d). For comparison between the two specimens, the path length is normalized by the gage length such that a value of 1 is the end of the gage length. Figure B.9 shows contour plots of strain at the highest strain level for the different load cases on the Type I specimen where ε is axial strain and γ is shear strain. Figure B.10 show similar contour plots for the Type II specimen. Figure B.11 shows the strain vs. normalized path length (y/GL) for the Type II specimen for axial- and shear-only cases, while Figure B.12 shows results for the combined case.

The strain contour plots (Figures B.9 and B.10) show that the axial strain for a path along the outer surface is similar for axial-only and combined loading. However, the shear strain along the path changes significantly from the shear-only case to the combined case. Figure B.12 shows that for strains in the elastic range, the strain is constant through the gage section, but as plasticity occurs, the region of constant strain is decreased in all cases except the shear-only case. Table B.2 and B.3 show the minimum normalized uniform strain distances for the Type I and Type II specimens, respectively. Results are provided for the strain range 0 - 0.05 m/m and strain tolerances from 1 - 5

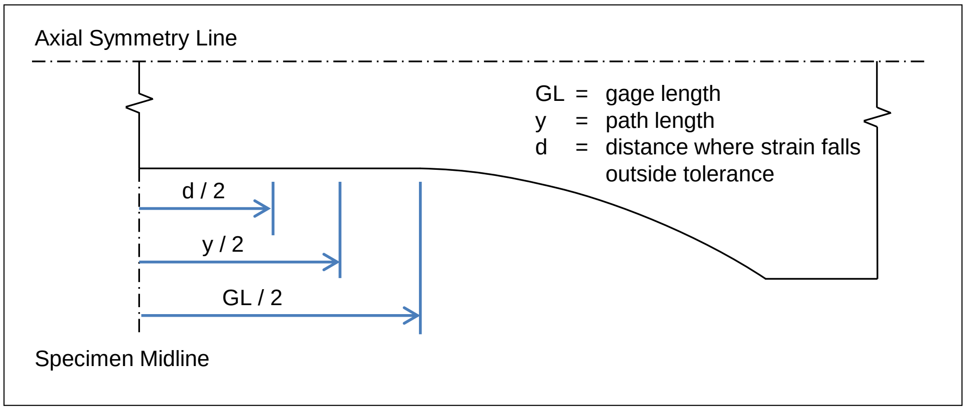

Figure B.8: Specimen geometry with depictions of the half gage length (GL/2) and half path length (y/2).

percent. The distance given in the table is the point at which the magnitude of the strain difference (based on the strain at the middle of the specimen) falls below 100 percent minus the tolerance.

For a tolerance of 1 percent, the usable distance for Type I and Type II is 27.41 mm and 6.08 mm, respectively. The nonuniform strain in Type II would prohibit the use of even a 12 mm gage length extensometer, thus strain gages are required. Furthermore, the grids of the strain gages must be placed within $\pm$ 3 mm of the specimen center to maintain 1 percent uniformity, which limits the ability to apply redundant gages. However, the strain in the Type I specimen is uniform over a sufficient region that the MTS high temperature axial-torsional extensometer with a 25 mm gage length can be used. Additionally, strain gages can be placed between the tips of the extensometer for redundant measurements.

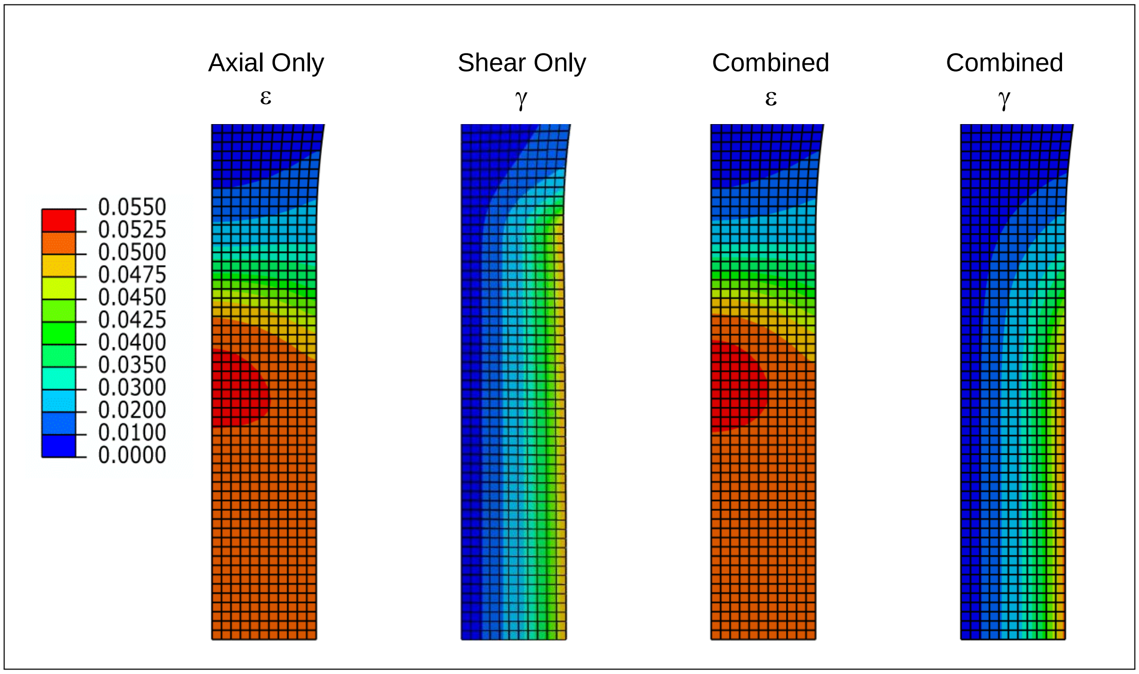

Figure B.9: Type I strain contour plots at the highest strain level for the different load cases where ε is axial strain and γ is shear strain.

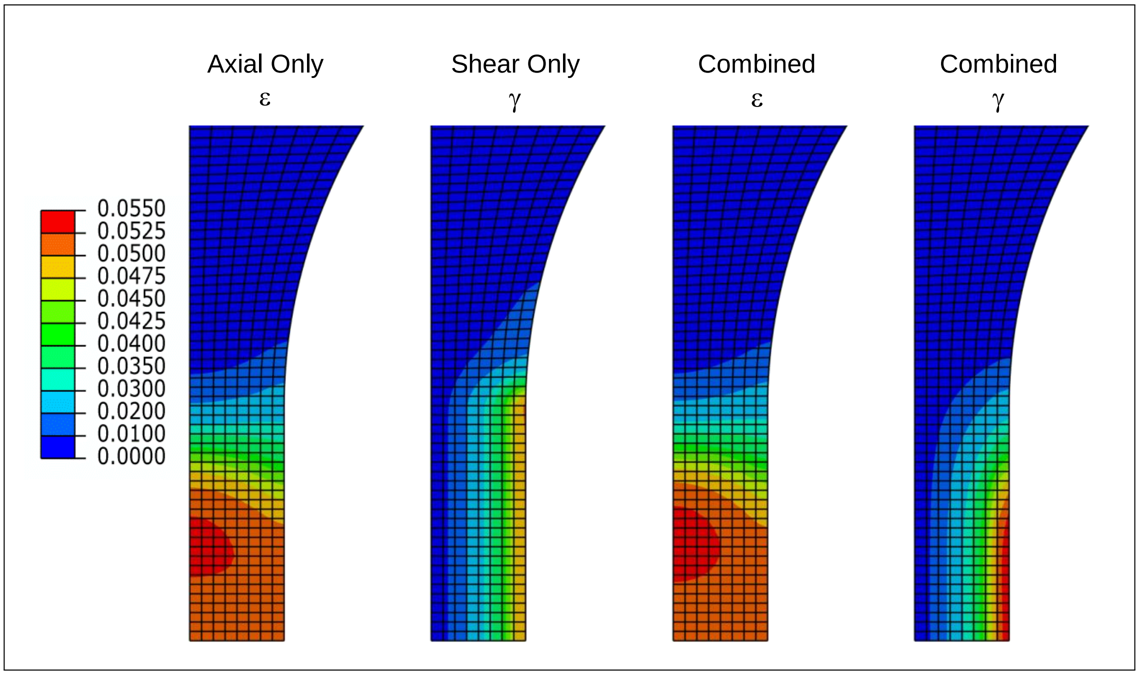

Figure B.10: Type II strain contour plots at the highest strain level for the different load cases where ε is axial strain and γ is shear strain.

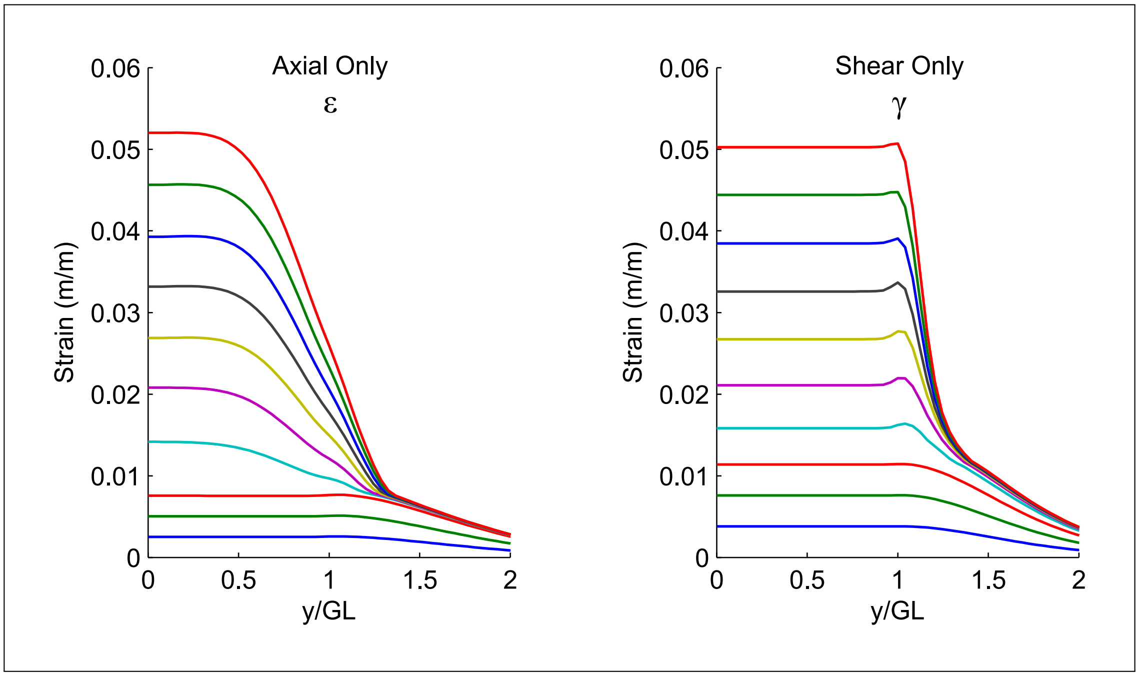

Figure B.11: Type II strain versus normalized path length for left) axial only and right) shear only loading.

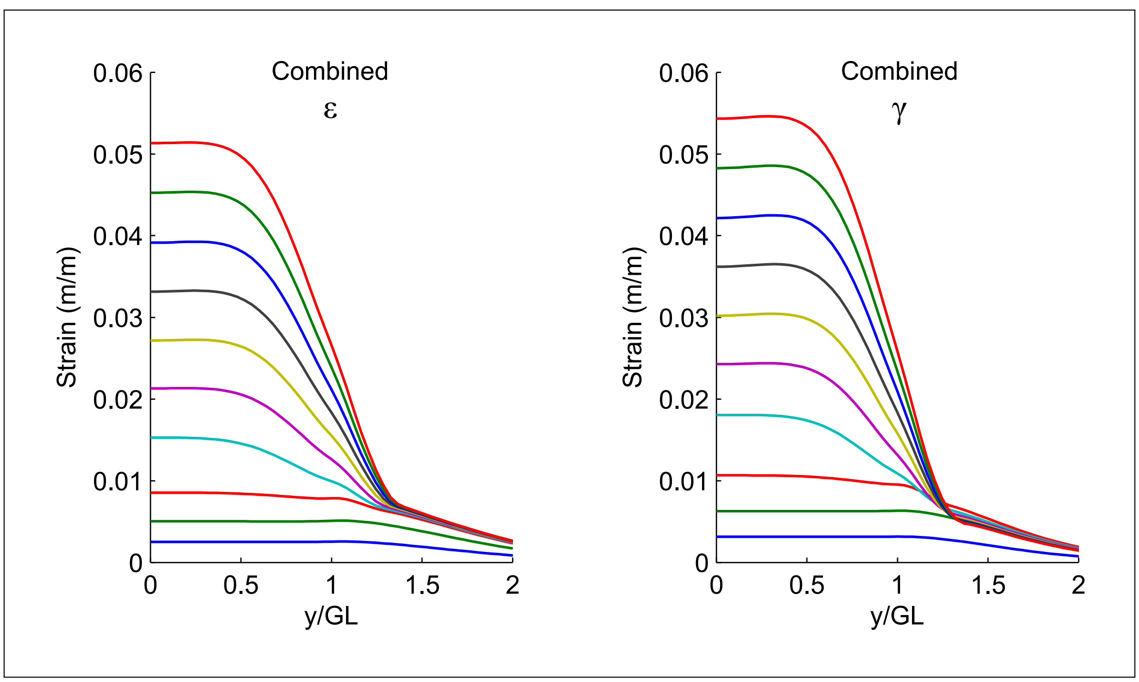

Figure B.12: Type II Strain versus normalized path length for combined loading.

Table B.2: Minimum uniform strain distance for Ti-6Al-4V specimen Type I over the strain range 0 - 0.05 m/m.

Spec:	Type I			GL:	44.50	mm
				Range:	0-0.05	m/m
	d/GL					Usable
Tol.			Combined		Usable	Length
(%)	Axial	Shear	Axial	Shear	Length	(mm)
1	0.62	1.02	0.64	0.66	0.62	27.41
2	0.66	1.05	0.66	0.68	0.66	29.41
3	0.68	1.05	0.68	0.71	0.68	30.41
4	0.71	1.05	0.71	0.73	0.71	31.42
5	0.73	1.05	0.73	0.75	0.73	32.42

Table B.3: Minimum uniform strain distance for Ti-6Al-4V specimen Type II over the strain range 0 - 0.05 m/m.

Spec:	Type II			GL:	19	mm
				Range:	0-0.05	m/m
	d/GL					Usable
Tol.			Combined		Usable	Length
(%)	Axial	Shear	Axial	Shear	Length	(mm)
1	0.32	1.04	0.36	0.40	0.32	6.08
2	0.40	1.04	0.40	0.44	0.40	7.60
3	0.44	1.04	0.44	0.48	0.44	8.36
4	0.48	1.08	0.48	0.52	0.48	9.12
5	0.52	1.08	0.52	0.56	0.52	9.88

B.2.2 Instrumentation

The results from the previous section indicate that strain gages are the only viable option for measuring strains for Type II specimens, due to the short gage length, and the small region over which the strain at the outer surface is uniform. Gage placement is limited to the region of uniform strain which is only 6.0 mm for a 1 percent tolerance, while the width is governed by the circumference of 19.9 mm. A $\pm$ 45 degree pair of gages mounted on the same matrix material (Micro-measurements EA-06-062TV-350) has been chosen to obtain the shear strain, while an axial gage (Micro-measurements CEA-06-062UW-350) has been selected for the axial strain. The grid area for both gages is roughly 1.6 mm tall by 3.0 mm wide which easily fits within the uniform strain field near the middle of the specimen. All selected gages for the Type II specimen have a strain range of $\pm$ 3 percent.

Both the axial-torsional extensometer and strain gages can be used with the Type I specimen. The extensometer has a gage length of 25 mm which allows for placement of strain gages within that region with careful positioning. The length of uniform strain given a 1 percent tolerance is 27.4 mm. Figure B.13 shows the placement of the extensometer and the strain gages. Gaging can include two pairs of $\pm$ 45 degree gages mounted on the same matrix material (Micro-measurements EA-06-125TK-350) and two axial gages (CEA-06-125UW-350) for a total of 6 independent gages. All selected gages for the Type I specimen have a range of $\pm$ 5 percent.

For both specimens, measurements for all strain gages are captured using Wheatstone quarter-bridges so the integrity of each signal can be verified, specifically for the shear strain. Engineering shear strain is found by adding the measurements of the $\pm$ 45 $\deg$ pair of gages, thus if mounted in a half-bridge, the failure of one gage in the pair could be hard to decipher.

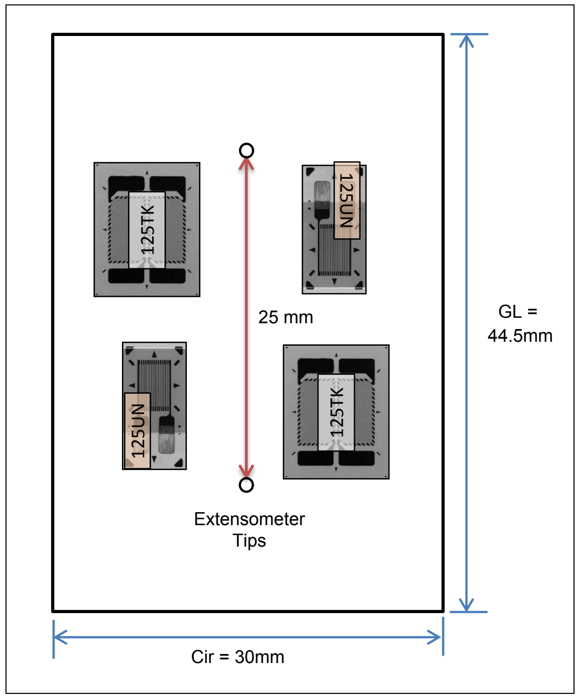

Figure B.13: Extensometer and strain gage layout for the Type I specimen.

B.3 Ti-6Al-4V Material

The Ti-6Al-4V material that is used throughout this work has a specifically designed microstructure developed for the Air Force Research Laboratory's high cycle fatigue and low cycle fatigue programs [103, 104]. The Ti-6Al-4V originated as bar stock with a diameter of 63.5 mm. Prior to the forging process, it was cut into 400 mm long sections. The forging process consisted of a 30 minute preheat at 940°C, coating with a glass lubricant, and forging at 940°C into 400x150x20 mm plates. The plates then underwent solution treatment for 1 hour at 925°C after which they were fan-air cooled. Finally they were stress relieved for 2 hours at 700°C [103].

The resulting microstructure is referred to as either bimodal or solution treated and overaged (STOA). The microstructure consists of a interconnected equiaxed primary-α grains (60 percent by volume) and lamellar colonies of transformed-β (40 percent by volume). The primary-α grains

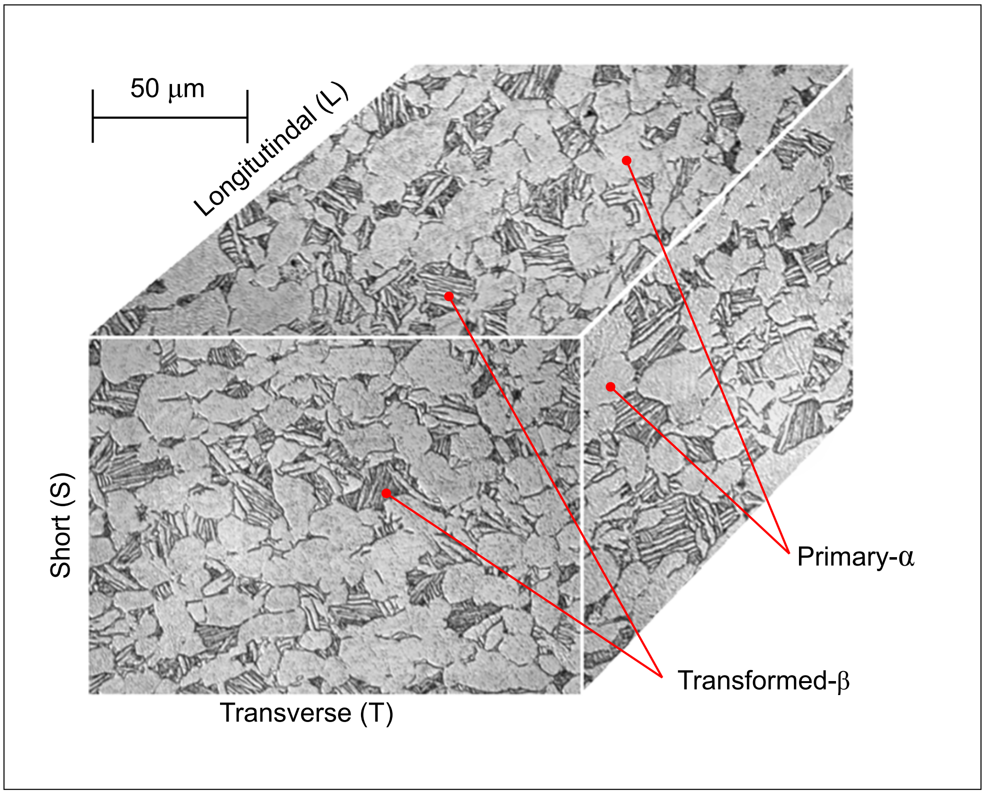

Figure B.14: Optical image of Ti-6Al-4V microstructure illustrating the primary-α grains and lamellar colonies of transformed-β (Image: William J. Porter III, AFRL/RXCM).

have an average grain size of 11.2 μm and are slightly elongated in the longitudinal (L) forging direction. The transformed-β grains have an average α-lath spacing of 1-2 μm. The β-transus temperature was found using differential thermal analysis and was determined to be between 990-1005°C. Figure B.14 shows an optical image of the microstructure in which the primary-α grains and lamellar colonies of transformed-β are clearly visible. Lastly, Figure B.15 shows an electron backscatter image of the Ti-6Al-4V microstructure at two different length scales.

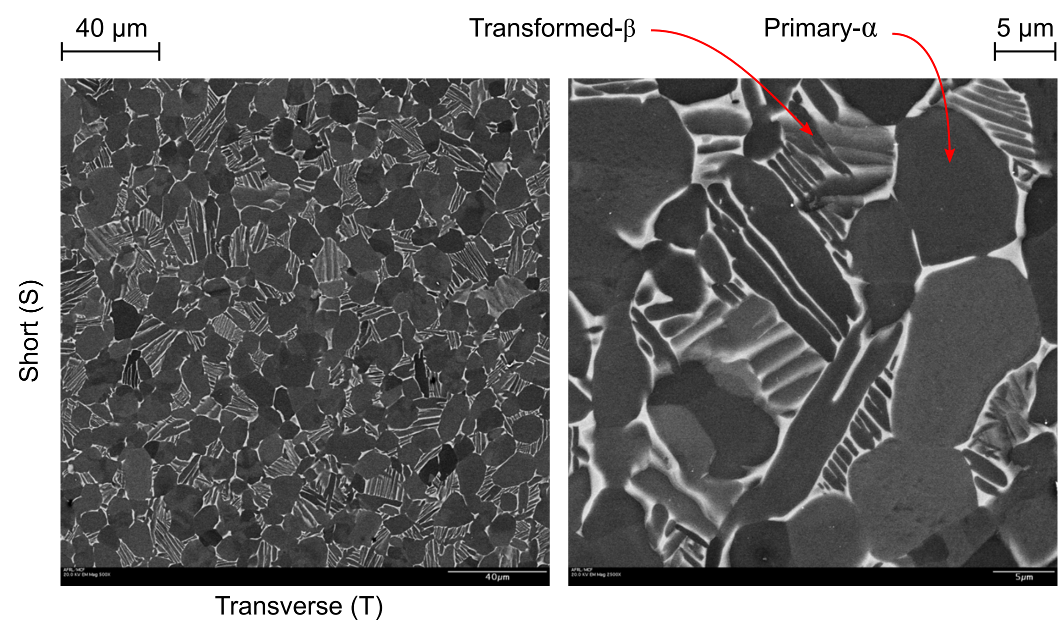

Figure B.15: Electron backscatter image of Ti-6Al-4V microstructure at two different length scales (Image: William J. Porter III, AFRL/RXCM).

APPENDIX C

VISCOPLASTICITY MODEL

This appendix provides an overview of the viscoplasticity model based on the Armstrong-Frederick laws. The equations governing the model are presented, and the overall influence on the material model response for each term is discussed. Alternate constitutive parameters are identified that are more easily related to the stress-strain curves from uniaxial tension tests that are commonly used for model fitting. The alternate parameters are also useful when performing constitutive model fitting because they account for the interdependence of parameters.

C.1 Viscoplasticity Equations

The rate equations for an isotropic viscoplasticity model that uses nonlinear isotropic and kinematic hardening are presented below. The rate form for the backstresses is consistent with the Armstrong-Frederick [105] form in which the linear kinematic hardening terms are proportional to the increment in plastic strain. The relevant rate equations written in indicial notation are

$$\dot{\varepsilon}^p_{kl} = \dot{\gamma}\frac{\partial f}{\partial \sigma_{kl}} = \Omega_\gamma \frac{\partial f}{\partial \sigma_{kl}} \tag{C.1}$$

$$\dot{\gamma} \ = \ \Omega_\gamma(\sigma, \rho, \chi) \ = \ \left\langle \frac{f}{D} \right\rangle^n \tag{C.2}$$

$$\dot{\sigma}_{ij} = \Omega_{\sigma ij}\left(\sigma,\, \rho,\, \chi\right) = D_{ijkl}\left(\dot{\varepsilon}_{kl} - \dot{\varepsilon}^p_{kl}\right) \tag{C.3}$$

$$\dot{\rho}^{(y)} = \Omega^{(y)}_\rho\left(\sigma, \rho, \chi\right) = b^{(y)}\left(Q^{(y)} - \rho^{(y)}\right)\Omega_\gamma \tag{C.4}$$

$$\dot{\chi}^{(w)}_{ij} = \Omega^{(w)}_{\chi ij} = \Omega_\gamma\left(\frac{2}{3}A^{(w)}\frac{\partial f}{\partial \sigma_{ij}} - B^{(w)}{\chi_{ij}}^{(w)}\right). \tag{C.5}$$

The term $\rho^{(y)}$ is the y^{th} isotropic hardening parameter, and $\chi^{(w)}_{ij}$ is the w^{th} set of kinematic hardening parameters (or backstresses). The yield function, f, is$f = q - \sigma_y$ where σ_y is the current radius of the yield surface, $\sigma_y = \rho_0 + \sum\limits_w \rho^{(w)}$, and q is the von Mises stress

$$q = \sqrt{{}^3\!/_2\left(S_{ij} - X_{ij}\right)\left(S_{ij} - X_{ij}\right)}. \tag{C.6}$$

The initial yield surface size is ρ_0 and the terms S_{ij} and X_{ij} are the deviatoric parts of the stresses and backstresses, respectively.

$$S_{ij} = \sigma_{ij} - {}^1\!/_3\sigma_{uu}\delta_{ij} \tag{C.7}$$

$$X_{ij} = \sum_w \left(\chi^{(w)}_{ij} - {}^1\!/_3\chi^{(w)}_{uu}\delta_{ij}\right). \tag{C.8}$$

C.1.1 Slip Rate

The slip rate function, $\dot{\gamma}$, given in Eq. (C.2) corresponds to the increment in equivalent plastic strain for rate-independent models. Insight can be gained by plotting the yield function, f, in terms of the slip rate. Figure C.1 shows a plot with a constant rate coefficient, n = 20, and a series of saturation stresses D = 100, 200, 300, 400. Figure C.2 shows results for a uniaxial tension test with $\dot{\varepsilon} = 1 \times 10^{-6}$ m/m/s, no hardening (i.e. $\dot{\rho} = 0; \dot{\chi} = 0$), ρ_0 = 100 MPa, n = 20, and D = 100, 200, 300, 400. Figure C.3 shows the yield function vs. slip rate for a constant D = 200 MPa,

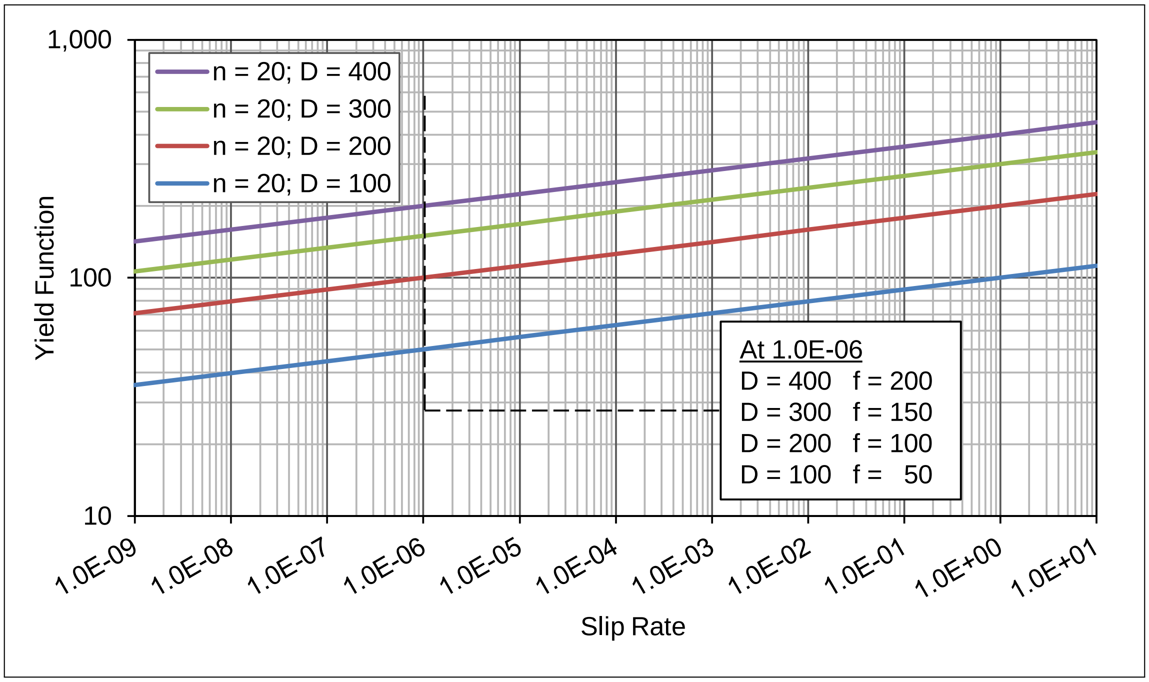

Figure C.1: Yield function versus slip rate for constant rate exponent, n, and varying saturation stresses, D.

with n = 10, 20, 30, 40, and Figure C.4 shows the results for the same conditions for the uniaxial test with $\dot{\varepsilon} = 1 \times 10^{-6}$ m/m/s.

For a given saturation stress, D, and rate exponent, n, the difference between the yield function value at a given slip rate value, $\dot{\gamma}_1$, and the slip rate one decade higher is given as

$$\Delta f = D\dot{\gamma}_1^{1/n}\left(10^{1/n} - 1\right). \tag{C.9}$$

Table C.1 shows the change in yield function for successive decades of the slip rate for D = 200 MPa and n = 20. Figure C.5 shows the uniaxial test results for the same series of rates as shown in Table C.1.

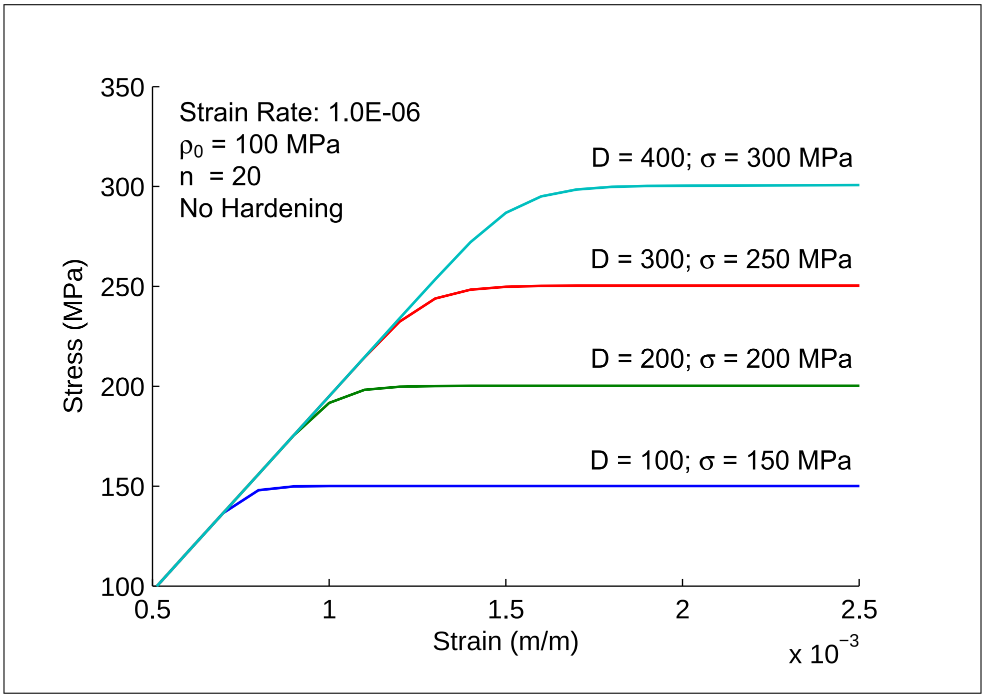

Figure C.2: Series of stress vs. strain curves for uniaxial tension tests at 1×10^{-6} m/m/s for a constant rate exponent, n, and varying saturation stresses, D, with no hardening.

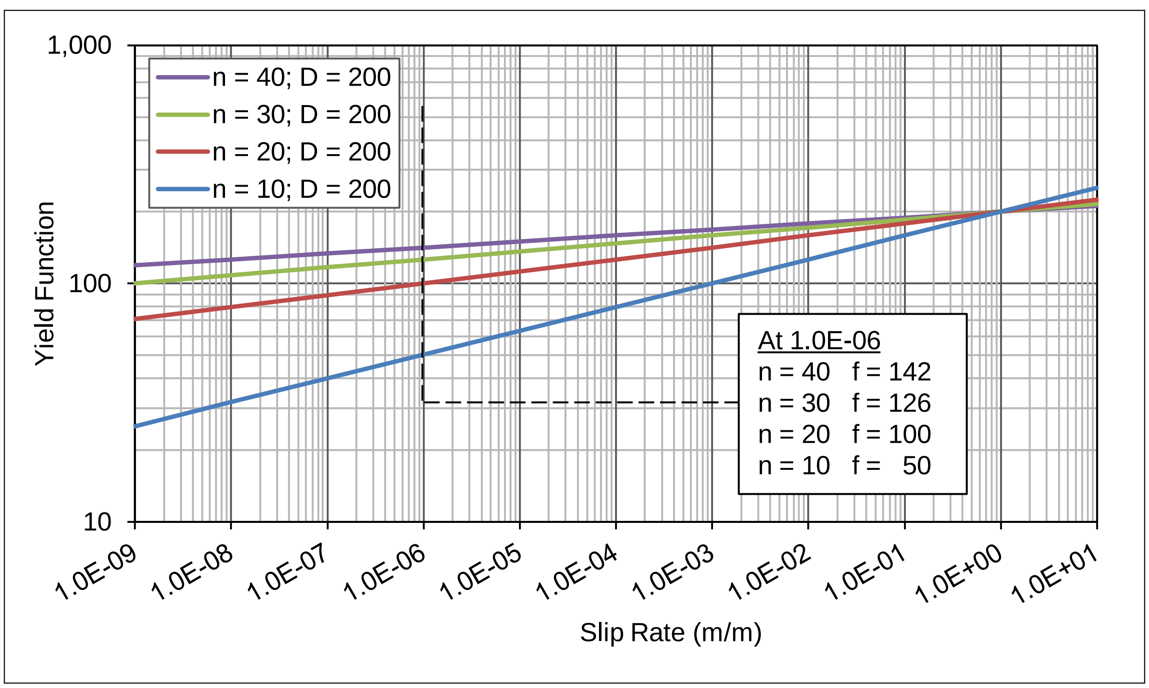

Figure C.3: Yield function versus slip rate for a constant saturation stress, D, and varying rate exponents, n.

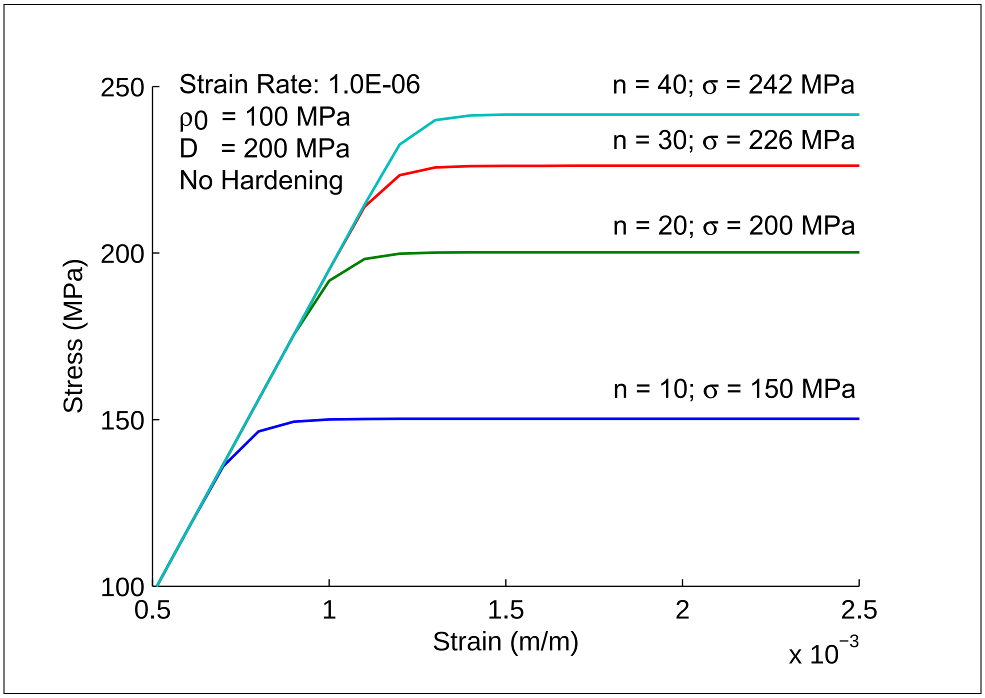

Figure C.4: Series of stress vs. strain curves for uniaxial tension tests at 1×10^{-6} m/m/s for a constant saturation stress, D, with varying rate exponents, n, and no hardening.

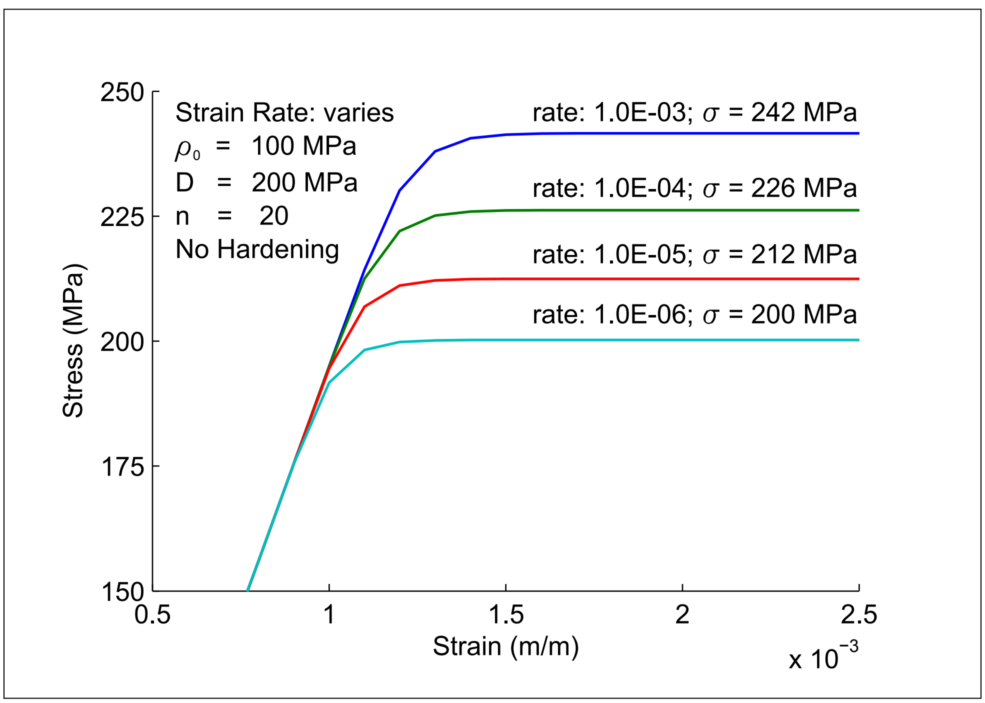

Figure C.5: Series of stress vs. strain curves for uniaxial tension tests at varying strain rates for a constant saturation stress, D, and rate exponents, n, and no hardening.

Table C.1: Influence of decade increase in slip rate.

D = 200 MPa	
n = 20	
$\dot{\gamma}$	Δf
1×10^{-6}	12.2
1×10^{-5}	13.7
1×10^{-4}	15.4
1×10^{-3}	17.3

C.1.2 Kinematic Hardening

The rate of kinematic hardening, $\dot{\chi_{ij}}$, given in Eq. C.5, has a linear term, $A^{(w)}$, with respect to the plastic strain rate and a recovery term, $B^{(w)}$, based on the current value of the backstress and the current slip rate. Figure C.6 shows the uniaxial test case for D = 200, n = 20, A = 10000, B = 0, no isotropic hardening, and strain rates that vary. The difference in stress is solely a function of the slip rate function (see Figure C.5 and Table C.1) as the kinematic hardening is rate-independent.

When the recovery term, B, is added the combination of A and B is easiest to understand when viewed as A/B which is the 'saturation' value, or maximum value of the backstress. Figure C.7 shows the influence of the 'saturation' values for the uniaxial test cases for values of D = 200, n = 20, B = 500, and A/B = 100, 200, 300, for a strain rate of 1×10^{-6}. Controlling where the saturation of the backstress occurs takes some additional thought, as the values of A and B do not provide immediate insight. As pointed out by Chaboche [66], the relationship between stress and equivalent plastic strain for the rate-independent plasticity model under monotonic axial loading is

$$\sigma = k^* + R^*\left(\bar{\varepsilon}^p\right) + \sum_{w=1}^{N} \frac{A^{(w)}}{B^{(w)}} \left(1 - \exp\left(-B^{(w)}\bar{\varepsilon}^p\right)\right) + A^{(LIN)}\bar{\varepsilon}^p \tag{C.10}$$

where

$$k^* = \rho_0 + D\dot{\gamma}^{1/n} \tag{C.11}$$

$$R^* = \sum_{w=1}^{N} Q^{(w)} \left(1 - \exp(-b^{(w)}\bar{\varepsilon}^p\right) \tag{C.12}$$

and where k is the initial yield surface size, and D and n come from the slip rate equation.

Looking at the behavior of the exponential function allows for better understanding of the rapidity coefficients b, and B (as named by Chaboche). The function y is defined as

$$y = 1 - \exp(-\beta x) \tag{C.13}$$

where β is the rapidity coefficient, and x is the independent variable. In the plasticity model, either b or B is the rapidity coefficient and the equivalent plastic strain is the independent variable. If saturation is assumed when $y = y_s$, the value of the independent variable at y_s can be found, which will be referred to as x_s.

$$\begin{aligned} y_s &= 1 - \exp\left(-\beta x_s\right) \\ \exp\left(-\beta x_s\right) &= 1 - y_s \\ -\beta x_s &= \ln\left(1 - y_s\right) \\ x_s &= \frac{-\ln\left(1 - y_s\right)}{\beta} \end{aligned} \tag{C.14}$$

The value of x_s is the equivalent plastic strain for a particular saturation value y_s which is some fraction of either the maximum isotropic hardening, Q, or the maximum kinematic hardening, A/B. It is convenient if a value of $y_s = 0.99326$ is used as the term $-\ln\left(1 - y_s\right) = 5$. Therefore, the point at which the hardening parameters saturate is simply either $5/b$ or $5/B$. A user could much more intuitively pick the equivalent plastic strain value at which the hardening saturates using this relationship than the values of b or B alone. This behavior is shown in Figure C.7 where a dashed vertical line is present at 0.01 total strain (not equivalent plastic strain). For convenience, the single vertical line is used rather than three independent lines for 0.01 equivalent plastic

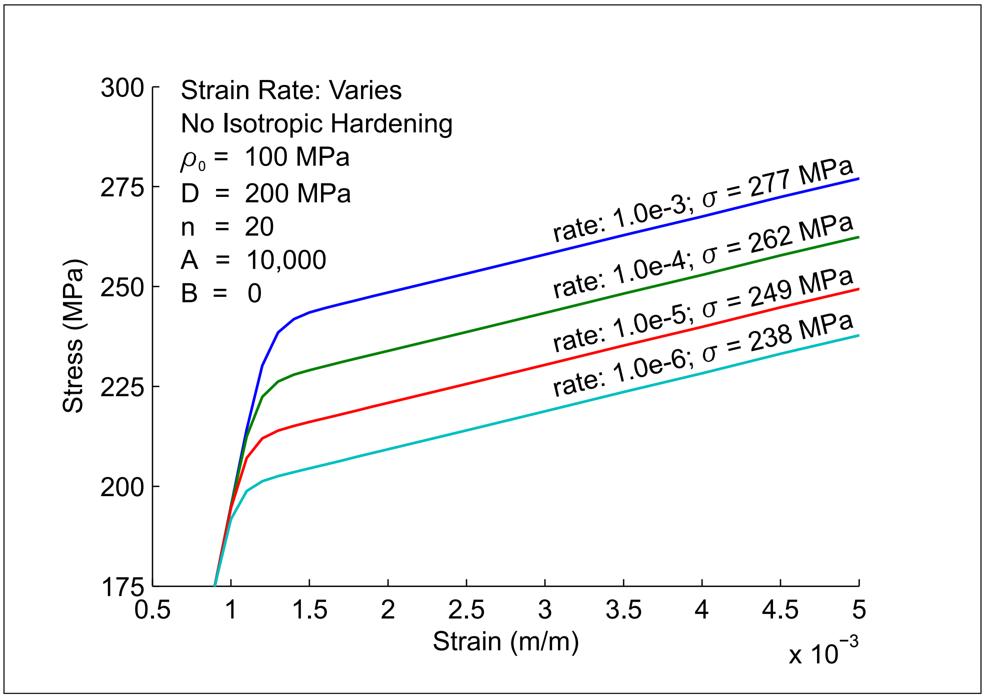

Figure C.6: Series of stress vs. strain curves for uniaxial tension tests at varying strain rates and only linear kinematic hardening illustrating the rate dependence is only influenced by slip rate and not any of the hardening.

strain (which would correspond to total strains of approximately 0.0115, 0.0120, and 0.0126 for A/B = 100, 200, and 300, respectively as the modulus is 195,000).

Figure C.8 shows the influence of the rapidity coefficient, B, for the uniaxial test case for D = 200, n = 20, A/B = 200, 5/B = 0.01, 0.02, 0.03, no isotropic hardening, and a strain rate of 1×10^{-6}. As stated above, it is far more intuitive for this author to think of the kinematic parameters in terms of A/B and 5/B which corresponding to the maximum backstress and the equivalent plastic strain at which the backstress saturates to 0.99326*A/B.

C.1.3 Isotropic Hardening

The rate of change of the isotropic hardening, $\dot{\rho}$, given in Eq. C.4 is directly related to the accumulation of slip. The saturation stress, Q, determines the maximum isotropic hardening available

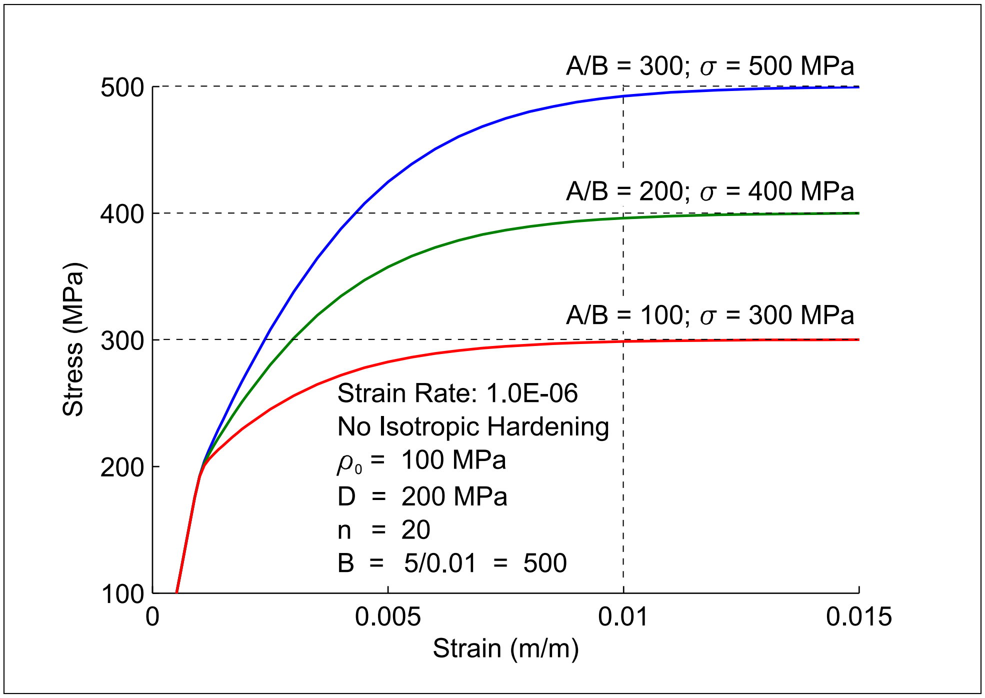

Figure C.7: Series of stress vs. strain curves for uniaxial tension tests for varying levels of non-linear kinematic hardening, A/B, with a constant recovery parameter, B.

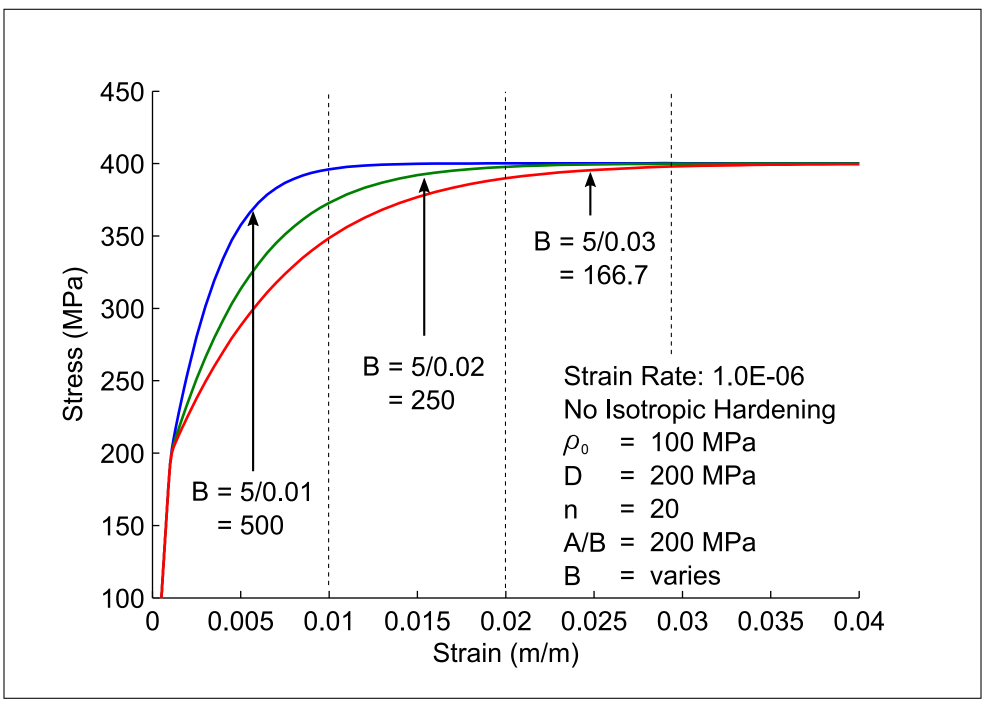

Figure C.8: Series of stress vs. strain curves for uniaxial tension tests for constant non-linear kinematic hardening, A/B, and varying recovery parameters, B.

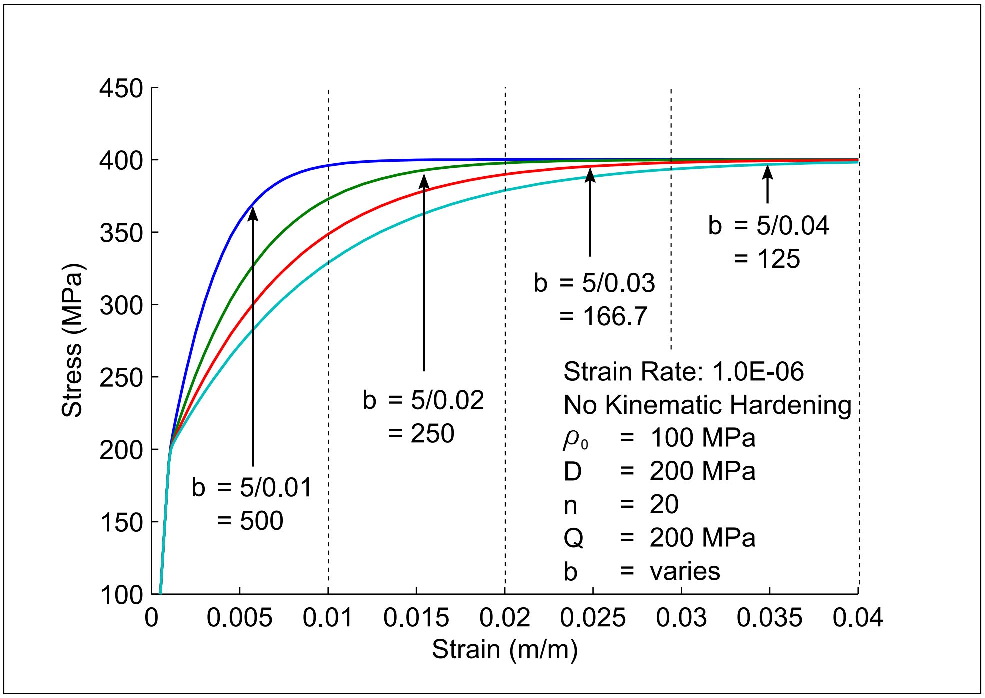

Figure C.9: Series of stress vs. strain curves for uniaxial tension tests for constant isotropic hardening, Q, and varying recovery parameters, b.

and the parameter, b, determines how quickly the isotropic hardening is achieved with increasing plastic strain. Figure C.9 shows the uniaxial results when D = 200, n = 20, Q = 200, the strain rate is 1×10^{-6}, and b = 500, 250, 166.6, 125. As b increases, the isotropic hardening occurs sooner. As pointed out in the discussion on the exponential function in Section C.1.2, it is easier to think about the rapidity coefficient, b, in terms of $b = 5/x_s$ as also shown in Figure C.9. Figure C.10 shows the uniaxial results when D = 200, n = 20, the strain rate is 1×10^{-6}, b = 100 = 5/0.05, and Q = 100, 200, 300.

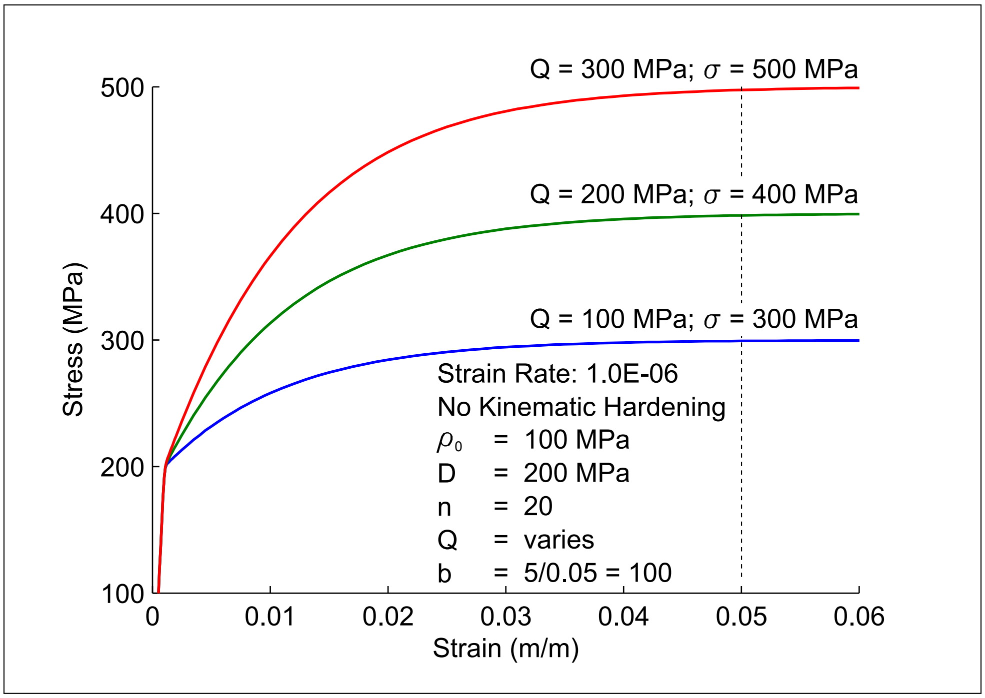

Figure C.10: Series of stress vs. strain curves for uniaxial tension tests for varying levels of isotropic hardening, Q, with a constant recovery parameter, b.

C.1.4 Summary

The behavior of the viscoplasticity model has been explored in terms of the slip rate, isotropic hardening, and kinematic hardening. The slip rate function, Eq. C.2, is the only way the rate behavior of the model is adjusted. Changes to the saturation stress, D, and the rate coefficient, n, affect the rate dependence. Equation C.9 provides a convenient formula for the change expected from increasing the strain rate by a factor of 10. The combination of the initial isotropic yield surface size, ρ_0, and the overstress, $D\dot{\gamma}^{1/n}$, define the point at which significant plastic strain starts to accumulate. This is analogous to the rate-independent yield surface size. After that point, the hardening takes over to define the accumulation of plastic strain. Both the isotropic and kinematic hardening can be thought of in terms of the exponential equation $y = \alpha \left(1 - \exp^{-\beta x}\right)$. As pointed out, the point of saturation is more conveniently thought of in terms of $5/\beta$ which defines to point where $0.99326 * \alpha$

is achieved. The value of y would be the hardening and x would be the accumulated slip (or effective plastic strain). For isotropic hardening, $\alpha = Q$ and $\beta = b$. For kinematic hardening, $\alpha = A/B$ and $\beta = B$. Lastly, Eq. C.10 provides an approximate closed form solution for a monotonic tension test. This can prove useful for more numerically efficient optimizations of parameters based on tension test data.

C.2 Initial Parameter Estimates from Supplemental Data

The parameter identification procedure can be greatly improved through use of supplemental material data to generate initial parameter seeds. The Ti-6Al-4V material, which is the focus of this work, was previously tested under uniaxial loading. Both tension tests and strain-controlled fully reversed cyclic loading were performed. The tension tests were conducted under strain-control at various strain rates which allow for identification of the rate-dependent parameters in the viscoplasticity model. The cyclic loading is ideal for preliminary fitting of the isotropic and kinematic hardening parameters.

Figure C.11 shows three separate strain-controlled tension tests conducted at strain rates of 1×10^{-2}, 1×10^{-3}, and 1×10^{-4} m/m/s. Figure C.12 shows the complete history of the uniaxial cyclic test. The magnitude of strain during the cyclic test was increased after moderate stabilization of the stresses (approximately 20 cycles). Strain loops were performed for 0.005, 0.008, 0.010, 0.0125, 0.0150, 0.0175, 0.020, and 0.0225 m/m. For the initial fitting of parameters, only loops up to 0.015 m/m have been used.

C.2.1 Predefined Parameters

The initial fitting assumed elastic values of E=116,000 MPa and ν=0.31 (G=44,275 MPa). The axial modulus is consistent with the initial excursions during both the tension and cyclic test. During the autonomous procedure, the modulus values are taken from the specimen being tested.

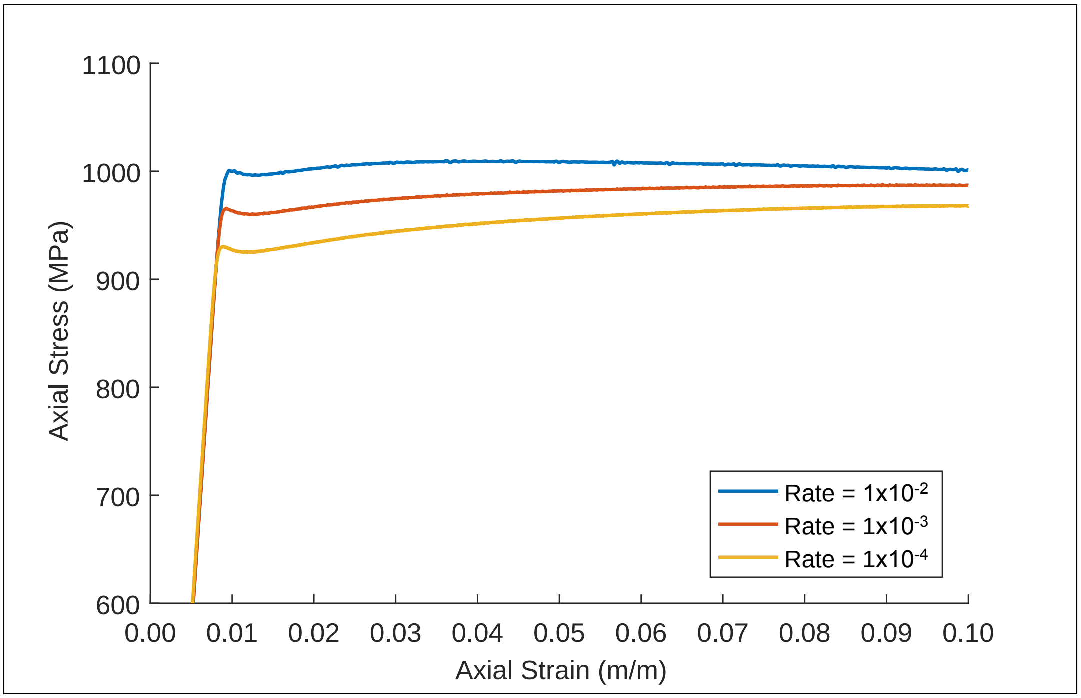

Figure C.11: Strain-controlled tension tests for Ti-6Al-4V at rates of 1×10^{-2}, 1×10^{-3}, and 1×10^{-4} m/m/s.

The rate-dependent parameters, D and n, have been determined based on the tensions tests conducted at three different rates. The 0.2 percent offset stress for each of the rates was determined, as listed in Table C.2. The rate exponent can be identified using linear regression on the 0.2 percent offset stress versus the natural log of the strain rate. From the slope, the parameter n is estimated to be 15.5. The saturation parameter, D, can be identified with the help of the slip rate, $\dot{\gamma}$, given by Eq. (C.2). When positive, the yield function can be solved for in terms of $\dot{\gamma}$, D, and n. The strain rate is approximately equivalent to the slip rate, $\dot{\gamma}$; therefore an equation can be derived for the difference between two slip rates for a constant rate exponent, n. Equation (C.15) provides this relationship.

$$f_1 - f_2 = D\left(\dot{\gamma}_1^{1/n} - \dot{\gamma}_2^{1/n}\right) \tag{C.15}$$

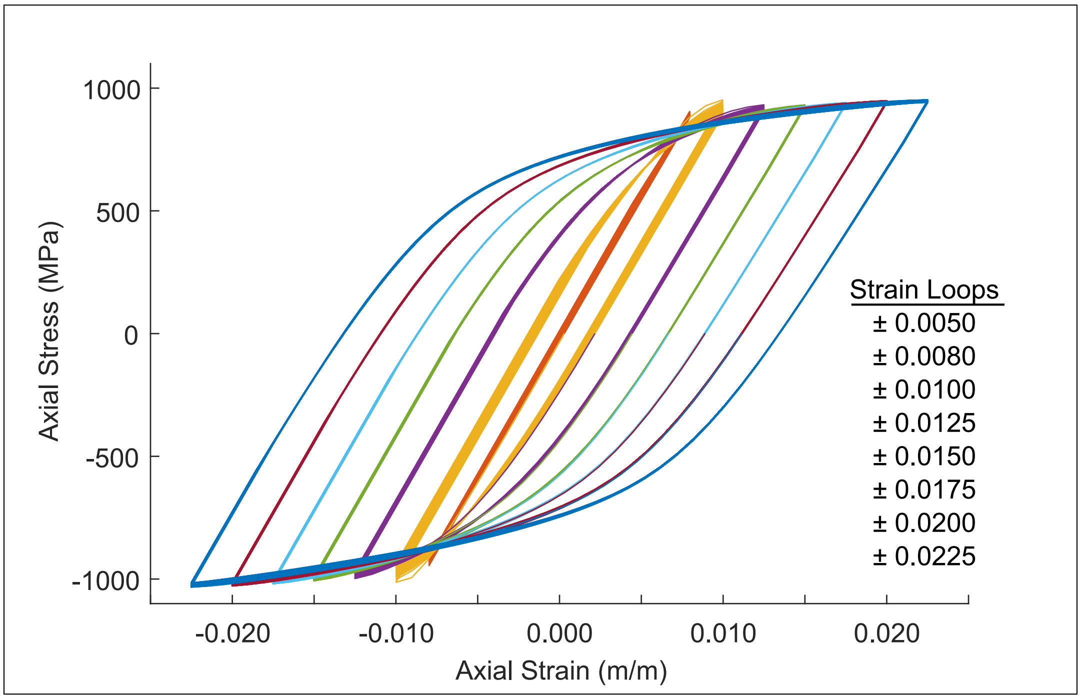

Figure C.12: Experimental results for Ti-6Al-4V strain-controlled (rate of 1×10^{-3} m/m/s), fully-reversed loading with increasing magnitude strain loops. Condensed data is shown at intervals of 1×10^{-3} m/m.

Minimizing the sum of the squares of the residual error between the measured stress differences from Table C.2 and those computed from Eq. (C.15) provides a value of D=371 MPa.

Table C.2: The 0.2% offset stress for Ti-6Al-4V tension tests conducted at various strain rates.

Strain Rate (m/m/s)	0.2% Offset Stress (MPa)	Difference (MPa)
1.00E-02	998.29	
		36.26
1.00E-03	962.03	
		34.91
1.00E-04	927.12	

The last parameter identified prior to the start of the autonomous testing is the initial yield surface size, ρ_0. Using the viscoplasticity model, the uniaxial stress near the onset of plasticity for a tension test is defined as $\rho_0 + D\dot{\gamma}^{1/n}$. By making the onset of plasticity reasonably small, the hardening model can attempt to capture the initial nonlinear behavior visible on the stress-strain curve. Therefore, ρ_0 has been set to 430 MPa, making $\rho_0 + D\dot{\gamma}^{1/n}$= 635 MPa for a rate of 1.0E-04 m/m/s. As seen from Figure C.11, this is still well below the start of the visible nonlinear region.

C.2.2 Initial Parameter Estimates

Supplemental material data is used to determine five sets of initial hardening parameters that can be used to seed the particle swarm optimization used through the autonomous testing finite element method updating (FEMU). Further information on FEMU is provided in Appendix D. Using initial seeds ensures that five of the starting particles (parameter sets) for the optimization are in the area of a local minimum from the supplemental data. If the characteristics of the supplemental data are relatively similar to the behavior during multiaxial testing, the initial five parameter sets should yield favorable objective function values, resulting in close matches to the multiaxial behavior. The alternative is to allow for random generation of the entire particle swarm in the hope that certain particles (parameter sets) are initialized near local minima. If supplemental data are available, the optimization process can be accelerated by starting at favorable locations. This is desirable as it decreases the total time required for the identification and likely yields better results.

Hardening parameter estimates have been computed using FEMU in conjunction with the tension test data and selected loops from the cyclic test. Each FEMU procedure starts with an initial set or sets of parameter estimates, $\xi_i = \{\alpha_1, \ldots, \alpha_N\}$, depending on the optimization method that is used. The outcome from the FEMU procedure is the set of optimization parameters, ξ_{best}, that minimize the objective function within the settings defined. The FEMU procedure has been run 100 times using non-linear least squares regression for the optimization method. Each FEMU process starts from 1 of the 100 sets that have been generated using Latin hypercube sampling to promote uniform design space coverage.

The set of parameters identified during FEMU consist of two pairs of isotropic hardening terms, ($b^{(1)}$, $Q^{(1)}$, $b^{(2)}$, $Q^{(2)}$), and three pairs of kinematic hardening terms ($A^{(1)}$, $B^{(1)}$, $A^{(2)}$, $B^{(2)}$, $A^{(3)}$, $B^{(3)}$). The rapidity term for the last kinematic hardening pair, $B^{(3)}$, is set to zero, thus making $A^{(3)}$ a linear kinematic hardening term. Table C.3 identifies the parameters and the specified lower and upper bounds. The first isotropic pair is restricted to hardening only (positive Q), while the second is restricted to softening only (negative Q). They can both be approximately zero if neither isotropic hardening nor softening is needed to match the experimental data. The parameter values and bounds outlined in Table C.3 are used throughout the FEMU procedures. The alternate hardening parameters introduced in this appendix are used in the computations.

The objective function used during the optimization is given in Eq. (C.16). The objective function, $c^{(m)}$, computes the total normalized sum of the squares of the residual error between the experimental force/torque and the simulation force/torque results generated using the identified hardening

Table C.3: Predefined parameter values, optimization parameters, and minimum and maximum allowable values used for initial fitting based on supplemental data.

Parameter	Value	Min	Max	Units
Elastic				
E	116,000	-	-	MPa
G	44,275	-	-	MPa
ν	0.31	-	-	-
Rate Dependent				
D	371	-	-	MPa
n	15.5	-	-	-
Yield				
ρ_0	430	-	-	MPa
Isotropic Hardening				
Q_1	-	5	750	MPa
$5/b_1$	-	1.00E-04	1.00E-01	-
Q_2	-	-500	0	MPa
$5/b_2$	-	1.00E-01	1.00E+01	-
Kinematic Hardening				
A_1/B_1	-	5	750	MPa
$5/B_1$	-	1.00E-04	1.00E-01	-
A_2/B_2	-	5	750	MPa
$5/B_2$	-	1.00E-04	1.00E-01	-
A_3	-	0	2000	MPa

parameter set. The objective function is computed for each experiment, m, and the final objective function is the total for of all experiments being considered. Consistent with other objective functions used through this work, the force and torque are weighted so the units equate to engineering stress. The weight factors for force and torque are $w_F = 1/A_0^2$ and $w_T = r_{out}^2/J^2$, respectively. The normalizing factor is the number of data points for the test case from which the data comes. This results in the average squared residual error, and allocates equal weight to the errors from the tension test and the cyclic test.

$$c^{(m)} = \frac{1}{N}\sum_{i=1}^{N} w_F\left(F_i^{(exp)} - F_i^{(fe)}\right)^2 + w_T\left(T_i^{(exp)} - T_i^{(fe)}\right)^2 \tag{C.16}$$

A single finite element analysis is composed of multiple time steps during which strains corresponding to the experiment are applied to the finite element mesh. The FE results are compared to the experimental results after each time step. If the stress results differ by a user defined tolerance (600 MPa is used here), the FE solution is stopped prematurely, and an artificially high penalty value of 1.0E+20 is assigned to the objective function. This decreases the amount of analysis time spent on parameter sets that yield undesirable results.

From the 100 different FEMU cases, only 23 resulted in final objective function values that were not set to the artificial penalty value of 1.0E+20. The 67 cases resulting in the penalty value started at poor initial parameter sets that lead to stress errors in excess of 600 MPa. Certain parameter sets from the 23 reasonable outcomes are similar. Therefore; further analysis of these good results has been conducted to narrow the number of sets down to the desired five sets. Table C.4 shows the parameter set and objective function value for the 23 cases.

An initial screening was done to identify parameter sets that had significant isotropic softening prior to 0.10 m/m. Cases 29 and 87 result in sharp softening around 0.015 m/m as seen in Figure C.13 and were eliminated from contention. Also cases 37, 82, 86, and 50 were excluded due to the large jump in the objective function values compared to the other cases. The tension test results for the remaining 17 cases are plotted in Figure C.14 along with the experiment shown as a dashed black line.

Many of the parameter sets are alike and produce similar stress-strain responses for the tensile test. From the 17 cases represented in Figure C.14, five representative parameter sets have been chosen. They are cases 99, 63, 38, 81, and 41 in order from the smallest to the largest objective function. Figure C.15 shows the experimental cyclic test in black and the results for the case 99 parameter set in red. Figure C.16 shows the cumulative distribution of the square residual error between experimental and simulation stress for the cyclic test for the five selected sets. The strain loops progress in order from smallest to largest, and the strain magnitudes are labeled for reference. Case 41 and 81 perform well up to the 0.01 m/m strain loops, but have poor performance for larger strain magnitudes. Case 99 and 38 perform similarly throughout the ranges with Case 63 having slightly higher errors at lower strain magnitude. Case 63 appears it would begin to outperform Case 99 and 38 at strain magnitudes above 0.015 m/m.

Table C.5 lists the five parameter set used to seed the particle swarm optimization procedure during the autonomous, multiaxial experimentation described in Section VI.

Table C.4: Parameter sets and objective function values for initial fit to tension and cyclic test on Ti-6Al-4V.

RANK	ID	Q_1	$5/b_1$	Q_2	$5/b_2$	A_1/B_1	$5/B_1$	A_2/B_2	$5/B_2$	A_3	FIT
MIN		0.0	9.50E-05	-500.0	1.00E-01	0.0	9.50E-05	0.0	9.50E-05	0.0	-
MAX		750.0	1.00E-01	0.0	1.00E+00	750.0	1.00E-01	750.0	1.00E-01	2000.0	-
1	99	5.0	2.85E-04	-55.7	1.00E+00	65.2	2.11E-03	281.3	1.40E-02	0.0	3741
2	63	6.8	1.00E-01	-64.7	1.00E+00	308.8	1.25E-02	34.0	6.91E-03	0.0	3815
3	44	5.0	8.90E-02	-49.1	9.19E-01	169.4	7.96E-03	178.8	1.73E-02	0.0	3858
4	69	5.0	9.03E-02	-46.5	8.59E-01	159.3	1.81E-02	189.7	8.32E-03	0.0	3897
5	29	9.7	1.78E-04	-140.7	1.00E-01	170.2	3.64E-03	227.2	1.39E-02	960.0	3916
6	6	161.0	1.00E-01	-221.5	1.00E-01	20.1	4.62E-02	341.8	1.11E-02	439.5	3978
7	67	5.0	1.00E-01	-44.4	1.00E+00	275.7	1.45E-02	61.6	2.25E-04	0.3	4004
8	74	7.0	1.01E-04	-53.7	8.86E-01	260.0	1.31E-02	72.4	3.31E-04	183.3	4103
9	38	8.1	1.00E-01	-68.4	1.00E+00	67.2	9.90E-05	291.7	1.37E-02	0.0	4174
10	15	24.8	9.56E-02	-88.9	4.26E-01	347.3	1.08E-02	5.0	8.70E-02	182.4	4270
11	87	99.0	6.94E-03	-101.3	1.00E-01	5.1	9.03E-02	304.1	1.37E-02	199.2	4388
12	39	352.8	1.00E-01	-438.3	1.00E-01	77.3	5.92E-02	327.4	7.34E-03	356.7	4555
13	81	5.0	9.71E-02	-84.0	7.75E-01	107.2	9.90E-05	218.1	9.17E-03	401.1	5248
14	41	5.0	3.25E-02	-41.0	4.64E-01	71.2	4.32E-02	272.7	4.68E-03	106.0	5281
15	14	5.0	4.60E-03	-49.5	1.00E+00	61.2	2.26E-03	299.2	1.12E-02	251.1	5626
16	79	160.6	9.87E-02	-230.2	7.46E-01	5.0	8.59E-02	281.5	1.04E-02	45.4	6225
17	20	95.0	8.37E-02	-114.4	3.51E-01	5.0	6.91E-02	340.5	1.33E-02	107.5	6320
18	30	160.4	4.54E-02	-233.4	1.00E-01	306.4	9.54E-03	5.0	3.98E-02	1965.8	6486
19	36	5.0	6.23E-02	-87.5	8.17E-01	5.0	5.44E-02	311.3	9.91E-03	1595.5	7286
20	37	111.5	1.04E-04	-115.0	1.00E+00	5.0	9.68E-02	185.5	4.18E-03	674.6	9614
21	82	139.9	7.66E-02	-158.6	6.41E-01	5.0	4.89E-02	341.4	1.36E-02	185.0	13146
22	86	180.6	8.17E-02	-110.3	5.31E-01	277.8	1.45E-02	5.0	4.39E-02	728.2	16127
23	50	14.9	9.70E-02	-480.3	8.80E-01	504.1	1.38E-03	12.0	9.24E-03	1958.6	52365

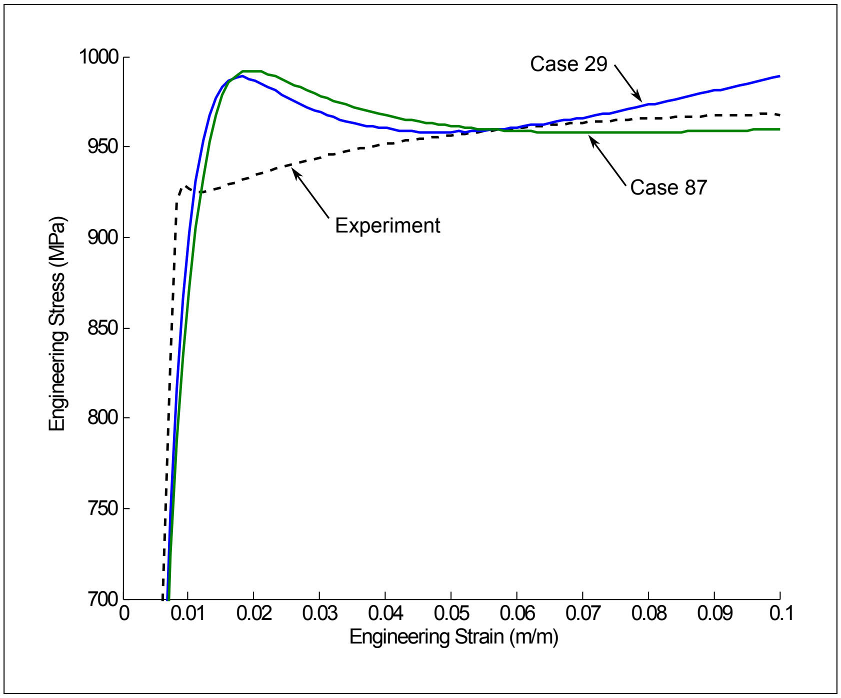

Figure C.13: Experimental stress vs. strain for strain rate of 1×10^{-4} m/m/s and two cases from the initial optimization that produced significant softening around 0.015 m/m.

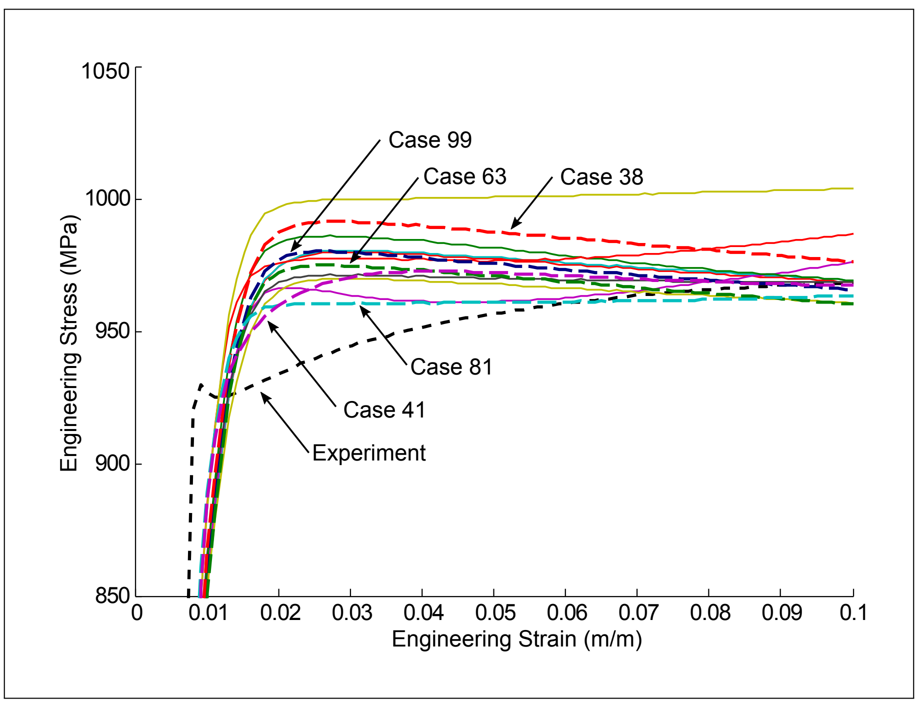

Figure C.14: Experimental stress vs. strain for strain rate of 1×10^{-4} m/m/s and the best fits from the initial optimizations.

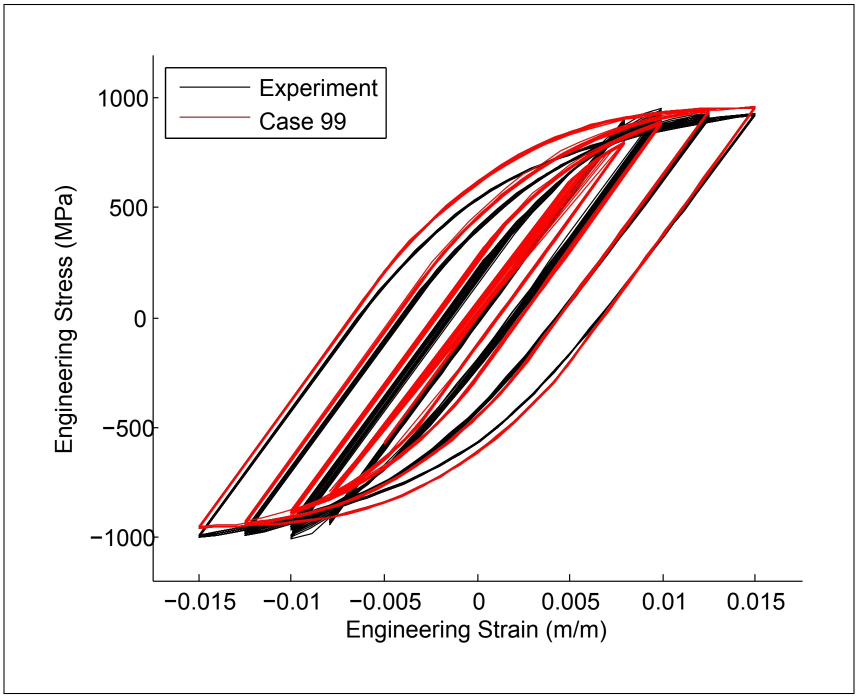

Figure C.15: Experimental stress vs. strain for the Ti-6Al-4V uniaxial cyclic test and the analysis results for the same conditions using the parameter set from case 99.

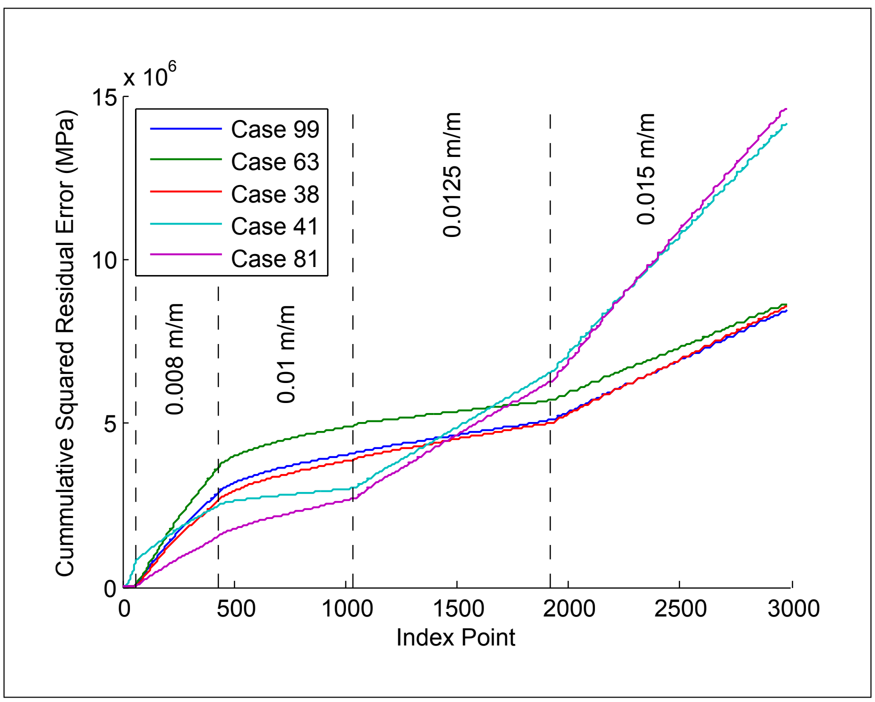

Figure C.16: Cumulative squared residual error between experimental and analytical stress for the cyclic test data for the five selected parameter sets.

Table C.5: Parameter sets and objective function values for the five selected, representative cases. The objective function is computed for the tension test at 1×10^{-4} m/m/s and the cyclic strain-controlled loops of 0.0150 m/m and below.

RANK	ID	Q_1	$5/b_1$	Q_2	$5/b_2$	A_1/B_1	$5/B_1$	A_2/B_2	$5/B_2$	A_3	FIT
MIN		5.0	1.00E-04	-500.0	1.00E-01	5.0	1.00E-04	5.0	1.00E-04	0.0	-
MAX		750.0	1.00E-01	0.0	1.00E+00	750.0	1.00E-01	750.0	1.00E-01	2000.0	-
1	99	5.0	2.85E-04	-55.7	1.00E+00	65.2	2.11E-03	281.3	1.40E-02	0.0	3741
2	63	6.8	1.00E-01	-64.7	1.00E+00	308.8	1.25E-02	34.0	6.91E-03	0.0	3815
9	38	8.1	1.00E-01	-68.4	1.00E+00	67.2	9.90E-05	291.7	1.37E-02	0.0	4174
13	81	5.0	9.71E-02	-84.0	7.75E-01	107.2	9.90E-05	218.1	9.17E-03	401.1	5248
14	41	5.0	3.25E-02	-41.0	4.64E-01	71.2	4.32E-02	272.7	4.68E-03	106.0	5281

APPENDIX D

SOFTWARE FOR FINITE ELEMENT MODEL UPDATING

The use of finite element model updating (FEMU) for parameter identification requires two pieces of software: an optimization program, and a finite element program. As is common in the literature, these two programs are usually separate which leads to time delays when information and data is passed among them. Also, commercial finite element programs are commonly used which adds unnecessary complexity for the relatively simple FE models used, and also adds substantial cost. To provide the most time efficient and cost effective FEMU strategy, the optimization and finite element software have been written as a single piece of software. In addition, the FE software is specialized to the axial-torsional loading of solid or tubular cylindrical specimens to further reduce the overhead present in commercial general purpose FE codes. Section D.1 provides details on the finite element program, while Section D.1.6 provides information on the constitutive model framework implemented in the code. Section D.2 provides details of the optimization program, including the available methods and objective function used.

D.1 Simulator

Most of the FEMU efforts in literature [22, 94, 25] require calls to external finite element (FE) programs like Abaqus. However, there is significant overhead time in calling external programs which require file input and output and additional post-processing. In addition, for widespread use on standalone test machines in a laboratory with no Internet connectivity, each test machine would require a standalone version of the finite element software, as well as a separate software license, or licenses if parallel processing is employed. This can be cost prohibitive in the case of commercial FE software. To overcome this potential financial burden and to minimize computation cost, a specifically formulated axisymmetric finite element code that handles both axial loading and torsion has been written. This code is used to simulate the response of a test specimen subjected to axial-torsional loading. The specifics of the code are presented in the following sections.

D.1.1 Finite Element Equations

Detailed descriptions of the governing equations for non-linear finite element analysis are available in text and literature [106, 107]. A concise overview of the framework used within the developed finite element software is presented below. The general matrix equation for the finite element method based on the principle of virtual work is

$$\delta \boldsymbol{d}^T \left(\int \boldsymbol{B}^T \boldsymbol{\sigma} dV - \int \rho \boldsymbol{N}^T \mathbf{b} dV - \int \boldsymbol{N}^T \boldsymbol{t} dS \right) = 0 \tag{D.1}$$

where $\delta \boldsymbol{d}$ is the virtual displacement vector, $\boldsymbol{B}$ is the strain-displacement matrix, $\boldsymbol{\sigma}$ is the stress vector, $\mathbf{b}$ are the body forces, $\boldsymbol{t}$ are the surface tractions, and $\mathbf{N}$ are the shape functions. Because the variations, $\delta \boldsymbol{d}$, are arbitrary and independent, the terms inside the parentheses have to equal zero. The internal forces are given by the first term

$$\boldsymbol{F}^{int} = \int \boldsymbol{B}^T \boldsymbol{\sigma} dV \tag{D.2}$$

while the external forces are given by the second and third terms

$$\boldsymbol{F}^{ext} = \int \rho \boldsymbol{N}^T \boldsymbol{b} dV + \int \boldsymbol{N}^T \boldsymbol{t} dS. \tag{D.3}$$

The terms within the parentheses in Eq. (D.1) can be written as a residual, $\mathbf{R}$, given as

$$\boldsymbol{R} = \boldsymbol{F}^{int} - \boldsymbol{F}^{ext} = \mathbf{0} \tag{D.4}$$

A displacement solution that makes the residual equal zero is sought through iterations of the Newton Raphson method. If the displacement at iteration ν of the Newton Raphson procedure is $\boldsymbol{d}^{(\nu)}$, then the residual at iteration ν is given as

$$\boldsymbol{R}^{(\nu)} = \boldsymbol{F}^{int}\left(\boldsymbol{d}^{(\nu)}\right) - \boldsymbol{F}^{ext}\left(\boldsymbol{d}^{(\nu)}\right) \tag{D.5}$$

where the force vectors are both functions of $\boldsymbol{d}^{(\nu)}$. If the exact solution that make the residual zero is $\boldsymbol{d}^{*}$, then the Newton Raphson equation can be written as

$$\boldsymbol{R}\left(\boldsymbol{d}^{*}\right) = \boldsymbol{0} = \boldsymbol{R}^{(\nu)} + \left.\frac{\partial \boldsymbol{R}}{\partial \boldsymbol{d}}\right|_{\boldsymbol{d}^{(\nu)}} \cdot \left(\boldsymbol{d}^{*} - \boldsymbol{d}^{(\nu)}\right) + \ldots \tag{D.6}$$

where ... represents higher order terms. The term $\partial\boldsymbol{R}/\partial\boldsymbol{d}$ is commonly indicated by $\boldsymbol{K_T}$. If higher order terms are excluded, then Eq. (D.6) becomes an approximation

$$\boldsymbol{0} \approx \boldsymbol{R}^{(\nu)} + \boldsymbol{K_T} \cdot \left(\boldsymbol{d}^{*} - \boldsymbol{d}^{(\nu)}\right). \tag{D.7}$$

Iterations of the Newton Raphson method are used to determine the displacements at iteration (ν+1)

$$\boldsymbol{0} = \boldsymbol{R}^{(\nu)} + \boldsymbol{K_T} \cdot \left(\boldsymbol{d}^{(\nu+1)} - \boldsymbol{d}^{(\nu)}\right). \tag{D.8}$$

Solving for $\boldsymbol{d}^{(\nu+1)}$ in Eq. (D.8) yields

$$\boldsymbol{d}^{(\nu+1)} = \boldsymbol{d}^{(\nu)} - \boldsymbol{K_T}^{-1}\boldsymbol{R}^{(\nu)}. \tag{D.9}$$

The matrix $\boldsymbol{K_T}$ is the partial derivative of the residual with respect to the displacements, and can be written as

$$\boldsymbol{K_T}\left(\boldsymbol{d}^{(\nu)}\right) = \left.\frac{\partial \boldsymbol{F}^{int}}{\partial \boldsymbol{d}}\right|_{\boldsymbol{d}^{(\nu)}} - \left.\frac{\partial \boldsymbol{F}^{ext}}{\partial \boldsymbol{d}}\right|_{\boldsymbol{d}^{(\nu)}}. \tag{D.10}$$

The first term on the right of Eq. (D.10) is known as the tangent stiffness matrix, while the second term is commonly referred to as the 'load stiffness'. The 'load stiffness' is excluded because deformations are assumed to be small, leaving only the tangent stiffness. Multiple iterations are performed, using Eq. (D.9) until the residual becomes sufficiently close to zero.

When integrating over a solid of revolution (as is necessary for axisymmetric element formulations), the volume integral can be represented as

$$\int f(\ldots)\,dV = \iiint f(\ldots)\,rd\theta drdz = 2\pi \iint f(\ldots)\,rdrdz \tag{D.11}$$

with appropriate limits used for dr and dz. The integrals in both the internal and external force vectors are integrated numerically using Gaussian quadrature

$$2\pi \iint f(\ldots)\,rdrdz = 2\pi \sum_{i=1}^{m}\sum_{j=1}^{n} f(\ldots)\,rw_i w_j J. \tag{D.12}$$

Further discussion on Gaussian quadrature can be found in textbooks [108].

D.1.2 Axisymmetric Representation

The developed finite element software uses an axisymmetric element with twist that allows for the application of torsional loading. The element is a two-dimensional (2D) simplification of a three-dimensional (3D) element and resides in the r-z plane. Figure D.1 shows the 3D element and depicts the stress tensor components. Figure D.2 shows the correlation between a 3D element and the 2D axisymmetric element with twist. The 2D element has degrees of freedom (DOF) for displacement in the r direction, rotation about the z-axis (twist), and displacement in the z direction which aligns with a cylindrical specimen's axis. The displacement DOFs will be referred to as u, v, and w, in the radial, circumferential, and axial directions, respectively.

D.1.3 Shape Functions

Isoparametric elements are utilized because the integration limits are always -1, 1 for each direction regardless of the deviation in shape from square or rectangular elements. Figure D.3 shows the conversion from local element coordinates to isoparametric element coordinates and Eq. (D.13) lists the shape functions. The Gaussian quadrature sampling points used for numerical integration of this element are well defined. For 2x2 Gaussian quadrature, the sampling points are at $\pm 1/\sqrt{3}$

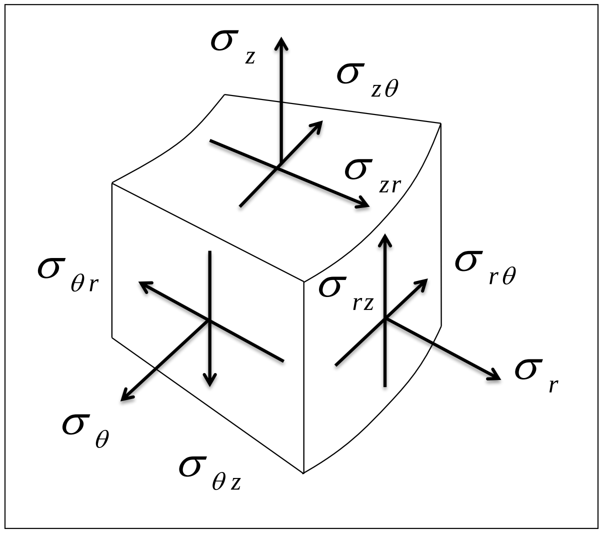

Figure D.1: Three-dimensional axisymmetric finite element with stress component labels.

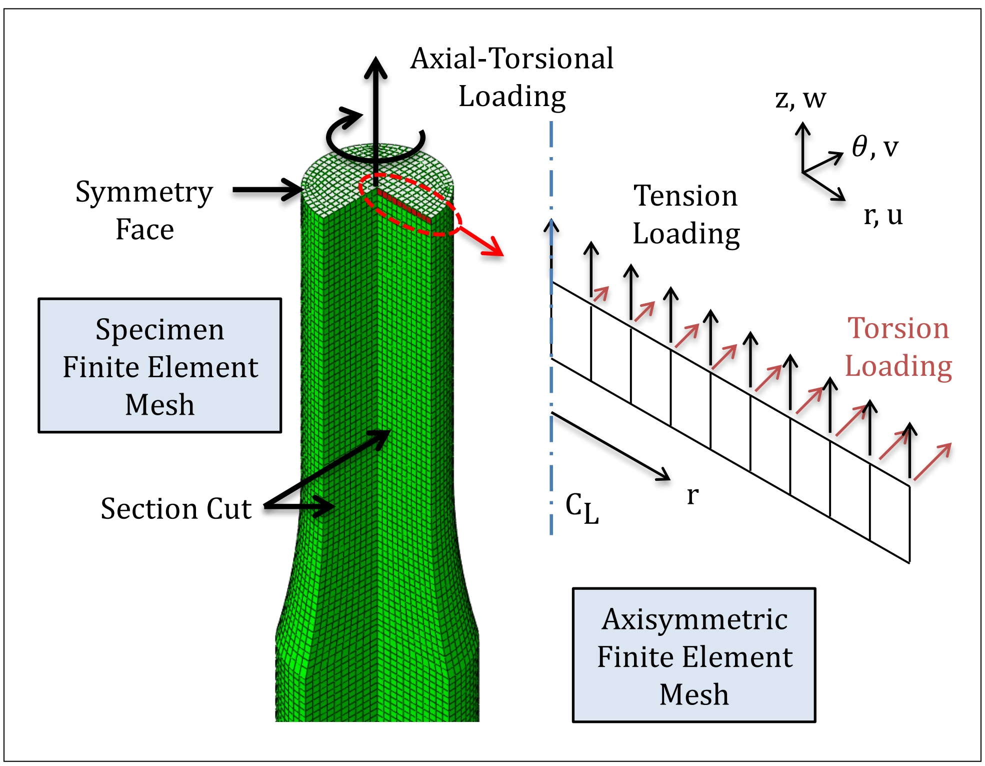

Figure D.2: Finite element mesh for specimen and corresponding axisymmetric gage section mesh.

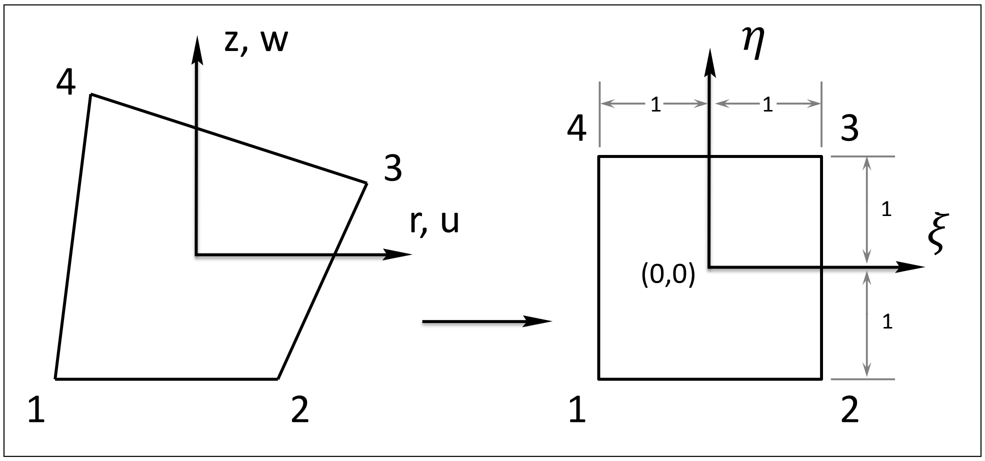

Figure D.3: Isoparametric element coordinates.

with weights of 1.

$$N_1 = \frac{(1-\xi)(1-\eta)}{4} \quad N_2 = \frac{(1+\xi)(1-\eta)}{4} \tag{D.13}$$

$$N_3 = \frac{(1+\xi)(1+\eta)}{4} \quad N_4 = \frac{(1-\xi)(1+\eta)}{4} \tag{D.14}$$

The Jacobian is required to transform the integration limits and derivatives from the original element axes (x,y) to the isoparametric axes (ξ, η). If we assume some function $\phi = \phi(\xi, \eta)$ exists in the isoparametric coordinate system, the partial derivatives with respect to x and y are difficult to derive. An inverse approach is utilized where the partial derivatives are found with respect to ξ, η, which are

$$\begin{array}{c} \dfrac{\partial \phi}{\partial \xi} = \dfrac{\partial \phi}{\partial x}\dfrac{\partial x}{\partial \xi} + \dfrac{\partial \phi}{\partial y}\dfrac{\partial y}{\partial \xi} \\ \dfrac{\partial \phi}{\partial \eta} = \dfrac{\partial \phi}{\partial x}\dfrac{\partial x}{\partial \eta} + \dfrac{\partial \phi}{\partial y}\dfrac{\partial y}{\partial \eta} \end{array}. \tag{D.15}$$

The partial derivatives can be written in matrix form as

$$\left\{ \begin{array}{c} \frac{\partial \phi}{\partial \xi} \\ \frac{\partial \phi}{\partial \eta} \end{array} \right\} = \left[\begin{array}{cc} \frac{\partial x}{\partial \xi} & \frac{\partial y}{\partial \xi} \\ \frac{\partial x}{\partial \eta} & \frac{\partial y}{\partial \eta} \end{array} \right] \left\{ \begin{array}{c} \frac{\partial \phi}{\partial x} \\ \frac{\partial \phi}{\partial y} \end{array} \right\} = [J] \left\{ \begin{array}{c} \frac{\partial \phi}{\partial x} \\ \frac{\partial \phi}{\partial y} \end{array} \right\}, \tag{D.16}$$

where $[J]$ is the Jacobian matrix. Pre-multiplying both sides of Eq. (D.16) by the inverse of the Jacobian yields the partial derivatives with respect to x and y

$$\left\{ \begin{array}{c} \frac{\partial \phi}{\partial x} \\ \frac{\partial \phi}{\partial y} \end{array} \right\} = [J]^{-1} \left\{ \begin{array}{c} \frac{\partial \phi}{\partial \xi} \\ \frac{\partial \phi}{\partial \eta} \end{array} \right\}. \tag{D.17}$$

The value of x and y at any point in the isoparametric element given by the coordinates (ξ, η) can be found using the shape functions

$$x = \sum_{i=1}^{n} N_i (\xi, \eta) \, x_i \qquad y = \sum_{i=1}^{n} N_i (\xi, \eta) \, y_i \tag{D.18}$$

where n is equal to the number of vertices for the element. Because the coordinates of the nodes of the isoparametric element do not vary, the Jacobian is found by determining the partial derivatives of the shape functions.

$$\left\{ \begin{array}{c} \phi_{,\xi} \\ \phi_{,\eta} \end{array} \right\} = \left[\begin{array}{cc} x_{,\xi} & y_{,\xi} \\ x_{,\eta} & y_{,\eta} \end{array} \right] \left\{ \begin{array}{c} \phi_{,x} \\ \phi_{,y} \end{array} \right\} = \left[\begin{array}{cc} \sum (N_i)_{,\xi} x_i & \sum (N_i)_{,\xi} y_i \\ \sum (N_i)_{,\eta} x_i & \sum (N_i)_{,\eta} y_i \end{array} \right] \left\{ \begin{array}{c} \phi_{,x} \\ \phi_{,y} \end{array} \right\} \tag{D.19}$$

D.1.4 Assumptions

The following assumptions are utilized to reduce the numerical cost of the finite element and specialize the element for an axial-torsional experiment on a solid or tubular cylindrical specimen made of isotropic material.

A1. Torsional symmetry: $\partial \left(\, \right) / \partial \theta = 0$; $v \neq 0$

A2. Isotropic material: $\sigma_{ij} = 0$ if $\varepsilon_{ij} = 0$ for $i \neq j$.

Additional assumptions can be used to reduce the problem to one dimension (in r).

A3. Uniform deformation along the axis of symmetry / axis of specimen; uniform stress state with respect to z-direction: $\frac{\partial}{\partial z} \left[u, v, \varepsilon_{ij}, \sigma_{ij} \right] = 0$; $\frac{\partial w}{\partial z} =$ constant.

A4. Planar cross sections remain plane in the test section: $w_{,r} = w_{,\theta} = 0$.

D.1.5 Strain-Displacement

The strain-displacement matrix is computed using the following generalized relationship for solids of revolution. In the equations below, u, w, and v are the displacements in the r, z, and θ direction.

$$\{d\} = \left\{ \begin{array}{cccccc} u_1 & w_1 & v_1 & u_2 & \cdots & v_4 \end{array} \right\}^T \tag{D.20}$$

$$\{u\} = \left\{ \begin{array}{ccc} u & w & v \end{array} \right\}^T = [N]\{d\} \tag{D.21}$$

$$\{\varepsilon\} = [\partial]\{u\} \tag{D.22}$$

$$\left\{ \begin{array}{cccccc} \varepsilon_r & \varepsilon_z & \varepsilon_\theta & \gamma_{zr} & \gamma_{r\theta} & \gamma_{\theta z} \end{array} \right\}^T = [B]\{d\} \tag{D.23}$$

$$[B] = [\partial][N] \tag{D.24}$$

$$[\partial] = \begin{bmatrix} \frac{\partial}{\partial r} & 0 & 0 \\ 0 & \frac{\partial}{\partial z} & 0 \\ \frac{1}{r} & 0 & \frac{1}{r}\frac{\partial}{\partial \theta} \\ \frac{\partial}{\partial z} & \frac{\partial}{\partial r} & 0 \\ \frac{1}{r}\frac{\partial}{\partial \theta} & 0 & \left(\frac{\partial}{\partial r} - \frac{1}{r}\right) \\ 0 & \frac{1}{r}\frac{\partial}{\partial \theta} & \frac{\partial}{\partial z} \end{bmatrix} \tag{D.25}$$

$$[N] = \begin{bmatrix} N_1 & 0 & 0 & N_2 & 0 & 0 & N_3 & 0 & 0 & N_4 & 0 & 0 \\ 0 & N_1 & 0 & 0 & N_2 & 0 & 0 & N_3 & 0 & 0 & N_4 & 0 \\ 0 & 0 & N_1 & 0 & 0 & N_2 & 0 & 0 & N_3 & 0 & 0 & N_4 \end{bmatrix} \tag{D.26}$$

The shape functions, $[N]$, can be used to find the displacements at any point within the element based on the nodal degrees of freedom, $\{d\}$. The strain-displacement matrix is thus $[B] = [\partial][N]$ which when expanded is equal to a 6×12 matrix. Based on the assumption of torsional symmetry

(A1), the operator matrix can be simplified

$$[\partial] = \begin{bmatrix} \frac{\partial}{\partial r} & 0 & 0 \\ 0 & \frac{\partial}{\partial z} & 0 \\ \frac{1}{r} & 0 & 0 \\ \frac{\partial}{\partial z} & \frac{\partial}{\partial r} & 0 \\ 0 & 0 & \left(\frac{\partial}{\partial r} - \frac{1}{r}\right) \\ 0 & 0 & \frac{\partial}{\partial z} \end{bmatrix}. \tag{D.27}$$

We can solve for the partials with respect to the isoparametric coordinates that appear in Eq. (D.27) by using the inverse of the Jacobian.

$$\left\{ \begin{array}{c} \frac{\partial N_i}{\partial r} \\ \frac{\partial N_i}{\partial z} \end{array} \right\} = [J]^{-1} \left\{ \begin{array}{c} \frac{\partial N_i}{\partial \xi} \\ \frac{\partial N_i}{\partial \eta} \end{array} \right\} \tag{D.28}$$

The final set of equations governing the material nonlinear, axisymmetric, finite element method is given by Eqs. (D.1), (D.9), (D.12), (D.26), and (D.27). The particular choice of material model influences the stresses and the tangent stiffness matrix. Information on the material model implementation is provided in the following section.

D.1.6 Material Library

The material point solutions for the element calculations are handled using Fortran subroutines in the form of Abaqus UMATs [67]. This choice provides seamless integration with the Abaqus finite element code. The plasticity framework used for the more complicated constitutive relationships follows the methodology of Kirchner et al. [109, 110].

The strain-driven plasticity model follows the method of strain rate decomposition

$$\dot{\varepsilon}_{kl} = \dot{\varepsilon}^{e}_{kl} + \dot{\varepsilon}^{p}_{kl} \tag{D.29}$$

where the elastic strain rate is the product of the elastic compliance tensor and the stress rate tensor

$$\dot{\varepsilon}^{e}_{kl} = D^{-1}_{ijkl}\,\dot{\sigma}_{ij}. \tag{D.30}$$

Substituting Eq. (D.29) into Eq. (D.30) and solving for the stress rate yields

$$\dot{\sigma}_{ij} = D_{ijkl}\left(\dot{\varepsilon}_{kl} - \dot{\varepsilon}^{p}_{kl}\right) \tag{D.31}$$

By restricting the formulation to small deformations and strains, the reference configuration can be used and thus the total strain increment $\dot{\varepsilon}_{kl}$ is linearly related to the displacements. The total strain rate is computed as

$$\dot{\varepsilon}_{kl} = \frac{\Delta\varepsilon_{kl}}{\Delta t}. \tag{D.32}$$

The implicit integration scheme uses the Newton Raphson method to bring the residuals of the stress tensor, σ, and the vector of state variables in the constitutive model, ξ, to zero. The rate equations are notated as Ω_μ where $\mu = [\sigma, \xi]$ is the set of stress components and all state variables. A common approach is to use the Backward Euler formula to update the stresses and state variables from time t to time $t + \Delta t$

$$\mu^{(t+\Delta\, t)} = \mu^{(t)} + \Delta\, t\Omega_\mu\left(\mu^{(t+\Delta\, t)}, \Delta\,\varepsilon\right). \tag{D.33}$$

The residuals of the stresses and state variables

$$R_\mu = \mu^{(t+\Delta\, t)} - \mu^{(t)} - \Delta\, t\Omega_\mu\left(\mu^{(t+\Delta\, t)}, \Delta\,\varepsilon\right) \tag{D.34}$$

are brought to zero using the Newton Raphson Method to solve for the unknowns $\mu^{(t+\Delta\, t)}$ in an iterative fashion

$$\mu^{(t+\Delta\, t)}_{(v+1)} = \mu^{(t+\Delta\, t)}_{(v)} - \alpha_{(v)} S_{(v)}. \tag{D.35}$$

In Eq. (D.35), $\alpha_{(v)}$ is the step size and $S_{(v)}$ is the search direction for iteration v. The search direction is defined as

$$S_{(v)} = \left[\frac{\partial R_\mu}{\partial \mu}\right]^{-1} R_\mu\left(\mu^{(t+\Delta t)}_{(v)}, \Delta\varepsilon\right) = J^{-1} R_\mu\left(\mu^{(t+\Delta t)}_{(v)}, \Delta\varepsilon\right) \tag{D.36}$$

where J is the Jacobian defined as

$$\mathbf{J} = \begin{bmatrix} \mathbf{J}_{\sigma\sigma} & \mathbf{J}_{\sigma\xi} \\ \mathbf{J}_{\xi\sigma} & \mathbf{J}_{\xi\xi} \end{bmatrix} = \begin{bmatrix} 1 - \Delta t \frac{\partial \mathbf{\Omega}_\sigma}{\partial \sigma} & -\Delta t \frac{\partial \mathbf{\Omega}_\sigma}{\partial \xi} \\ -\Delta t \frac{\partial \mathbf{\Omega}_\xi}{\partial \sigma} & 1 - \Delta t \frac{\partial \mathbf{\Omega}_\xi}{\partial \xi} \end{bmatrix}. \tag{D.37}$$

Following Kirchner's formulation [110], the desired consistent tangent stiffness matrix can be written as

$$\mathbf{D}^{(t+\Delta t)} = \left(\mathbf{J}_{\sigma\sigma} - \mathbf{J}_{\sigma\xi} : \mathbf{J}_{\xi\xi}^{-1} : \mathbf{J}_{\xi\sigma} \right)^{-1} : \mathbf{D}_e. \tag{D.38}$$

Alternatively, the residuals can be derived using a higher-order backward difference formula to increase accuracy at the cost of additional storage requirements. Kirchner and Simeon [109] demonstrated the use of a second-order backward difference formula with variable step sizes. The residual equations for the second-order difference formula are

$$R_\mu = \left(\frac{1 + 2\tau_n}{1 + \tau_n} \right) \mu^{(n+1)} - (1 + \tau_n)\, \mu^{(n)} + \left(\frac{\tau_n^2}{1 + \tau_n} \right) \mu^{(n-1)} - h_n \Omega_\mu \left(\mu^{(t+\Delta\, t)}, \Delta\, \varepsilon \right) \tag{D.39}$$

where $(n+1)$ is the time increment for which the stresses and state variables are being updated. The values of $\mu^{(n)}$ and $\mu^{(n-1)}$ come from previously converged time increments. The time step ratio between successive time steps is $\tau_n = h_n - h_{n-1}$ where $h_n = \Delta t = t_{n+1} - t_n$ and $h_{n-1} = t_n - t_{n-1}$. Kirchner and Simeon [109] give a stability condition which limits the current step size such that $\tau_n < 1 + \sqrt{2}$. The Jacobian matrix consistent with the residuals from Eq. (D.39) and required for computation of the tangent stiffness matrix in Eq. (D.38) is

$$\mathbf{J} = \begin{bmatrix} \mathbf{J}_{\sigma\sigma} & \mathbf{J}_{\sigma\xi} \\ \mathbf{J}_{\xi\sigma} & \mathbf{J}_{\xi\xi} \end{bmatrix} = \begin{bmatrix} \left(\frac{1+2\tau_n}{1+\tau_n} \right) 1 - \Delta t \frac{\partial \mathbf{\Omega}_\sigma}{\partial \sigma} & -\Delta t \frac{\partial \mathbf{\Omega}_\sigma}{\partial \xi} \\ -\Delta t \frac{\partial \mathbf{\Omega}_\xi}{\partial \sigma} & \left(\frac{1+2\tau_n}{1+\tau_n} \right) 1 - \Delta t \frac{\partial \mathbf{\Omega}_\xi}{\partial \xi} \end{bmatrix}. \tag{D.40}$$

To make either the backward Euler or higher-order backward difference formulation specific to a desired constitutive model, three rate functions need to be defined

1. plastic strain rate, $\dot{\varepsilon}^p$;
2. stress rate, $\dot{\sigma} = \mathbf{\Omega}_\sigma$; and

3. state variable rate, $\dot{\xi} = \mathbf{\Omega}_\xi$.

In addition, the partial derivatives of $\mathbf{\Omega}_\sigma$ and $\mathbf{\Omega}_\xi$ must be computed with respect to both σ and ξ. The following two subsections summarize the relevant equations and rate functions for two common isotropic plasticity models.

Isotropic Plasticity with Nonlinear Kinematic Hardening (Armstrong-Frederick)

The rate equations and derivatives for a constitutive model that uses nonlinear isotropic and kinematic hardening are presented below. Additional details on the influence of each constitutive parameter can be found in Appendix C. The model is consistent with Kirchner's model [110] with a simplified yield function. The rate form for the backstresses is consistent with the Armstrong-Frederick [105] form in which the linear kinematic hardening terms are proportional to the increment in plastic strain. The relevant rate equations written in indicial notation are

$$\dot{\varepsilon}^p_{kl} = \dot{\gamma}\frac{\partial f}{\partial \sigma_{kl}} = \Omega_\gamma \frac{\partial f}{\partial \sigma_{kl}} \tag{D.41}$$

$$\dot{\gamma} \;=\; \Omega_\gamma(\sigma,\rho,\chi) \;=\; \left\langle \frac{f}{D} \right\rangle^n \tag{D.42}$$

$$\dot{\sigma}_{ij} = \Omega_{\sigma ij}\left(\sigma,\,\rho,\,\chi\right) = D_{ijkl}\left(\dot{\varepsilon}_{kl} - \dot{\varepsilon}^p_{kl}\right) \tag{D.43}$$

$$\dot{\rho}^{(w)} = \Omega^{(w)}_\rho\left(\sigma,\rho,\chi\right) = b^{(w)}\left(Q^{(w)} - \rho^{(w)}\right)\Omega_\gamma \tag{D.44}$$

$$\dot{\chi}^{(w)}_{ij} = \Omega^{(w)}_{\chi ij} = \Omega_\gamma\left(\frac{2}{3}A^{(w)}\frac{\partial f}{\partial \sigma_{ij}} - B^{(w)}{\chi_{ij}}^{(w)}\right). \tag{D.45}$$

The term $\rho^{(w)}$ is the w^{th} isotropic hardening parameter, and $\chi^{(w)}_{ij}$ is the w^{th} set of kinematic hardening parameters (or backstresses). The yield function, f, is$f = q - \sigma_y$ where σ_y is the current radius of the yield surface, $\sigma_y = \rho_0 + \sum\limits_w \rho^{(w)}$, and q is the von Mises stress

$$q = \sqrt{{}^3\!/_2\left(S_{ij} - X_{ij}\right)\left(S_{ij} - X_{ij}\right)}. \tag{D.46}$$

The initial yield surface size is ρ_0 and the terms S_{ij} and X_{ij} are the deviatoric stresses and back-stresses, respectively.

$$S_{ij} = \sigma_{ij} - {}^1\!/_3\sigma_{uu}\delta_{ij} \tag{D.47}$$

$$X_{ij} = \sum_w \left(\chi_{ij}^{(w)} - {}^1\!/_3\chi_{uu}^{(w)}\delta_{ij}\right). \tag{D.48}$$

The first and second derivatives of the yield function are used frequently. They are

$$\frac{\partial f}{\partial \sigma_{kl}} = \frac{3}{2}\frac{(S_{kl} - X_{kl})}{q} \tag{D.49}$$

$$\frac{\partial f}{\partial \rho^{(w)}} = -1 \tag{D.50}$$

$$\frac{\partial f}{\partial \chi_{kl}^{(w)}} = -\frac{3}{2}\frac{(S_{kl} - X_{kl})}{q} = -\frac{\partial f}{\partial \sigma_{kl}} \tag{D.51}$$

$$\frac{\partial}{\partial \sigma_{rs}}\left(\frac{\partial f}{\partial \sigma_{kl}}\right) = \frac{3}{2q}\left(\delta_{kr}\delta_{ls} - \frac{1}{3}\delta_{rs}\delta_{kl}\right) - \frac{1}{q}\frac{\partial f}{\partial \sigma_{kl}}\frac{\partial f}{\partial \sigma_{rs}} \tag{D.52}$$

$$\frac{\partial}{\partial \chi_{rs}^{(w)}}\left(\frac{\partial f}{\partial \sigma_{kl}}\right) = -\frac{\partial}{\partial \sigma_{rs}}\left(\frac{\partial f}{\partial \sigma_{kl}}\right). \tag{D.53}$$

The required derivatives for $\Omega_{\sigma_{ij}}$ are

$$\frac{\partial \Omega_{\sigma ij}}{\partial \sigma_{rs}} = -D_{ijkl}\left(\Omega_\gamma \frac{\partial}{\partial \sigma_{rs}}\left(\frac{\partial f}{\partial \sigma_{kl}}\right) + \frac{n}{D}\left\langle \frac{f}{D}\right\rangle^{n-1}\frac{\partial f}{\partial \sigma_{rs}}\frac{\partial f}{\partial \sigma_{kl}}\right) \tag{D.54}$$

$$\frac{\partial \Omega_{\sigma ij}}{\partial \rho^{(w)}} = \frac{n}{D}\left\langle \frac{f}{D}\right\rangle^{n-1}\left(D_{ijkl}\frac{\partial f}{\partial \sigma_{kl}}\right) \tag{D.55}$$

$$\frac{\partial \Omega_{\sigma ij}}{\partial \chi_{rs}^{(z)}} = -\frac{\partial \Omega_{\sigma ij}}{\partial \sigma_{rs}}. \tag{D.56}$$

The required derivatives for $\Omega_{\rho^{(w)}}$ are

$$\frac{\partial \Omega_\rho^{(w)}}{\partial \sigma_{rs}} = b^{(w)}\left(Q^{(w)} - \rho^{(w)}\right)\frac{n}{D}\left\langle \frac{f}{D}\right\rangle^{n-1}\frac{\partial f}{\partial \sigma_{rs}} \tag{D.57}$$

$$\frac{\partial \Omega_\rho^{(w)}}{\partial \rho^{(y)}} = -b^{(w)}\left(Q^{(w)} - \rho^{(w)}\right)\frac{n}{D}\left\langle \frac{f}{D}\right\rangle^{n-1} - \Omega_\gamma b^{(w)}\delta_{wy} \tag{D.58}$$

$$\frac{\partial \Omega_\rho^{(w)}}{\partial \chi_{rs}^{(z)}} = -\frac{\partial \Omega_\rho^{(w)}}{\partial \sigma_{rs}}. \tag{D.59}$$

Lastly, the required derivatives for $\Omega_{\chi_{ij}^{(w)}}$ are

$$\frac{\partial \Omega_{\chi ij}^{(w)}}{\partial \sigma_{rs}} = \frac{2}{3} A^{(w)} \Omega_{\gamma} \frac{\partial}{\partial \sigma_{rs}} \frac{\partial f}{\partial \sigma_{ij}} + \frac{n}{D} \left\langle \frac{f}{D} \right\rangle^{n-1} \frac{\partial f}{\partial \sigma_{rs}} \left(\frac{2}{3} A^{(w)} \frac{\partial f}{\partial \sigma_{ij}} - B^{(w)} {\chi_{ij}}^{(w)} \right) \tag{D.60}$$

$$\frac{\partial \Omega_{\chi ij}^{(w)}}{\partial \rho^{(y)}} = -\frac{n}{D} \left\langle \frac{f}{D} \right\rangle^{n-1} \left(\frac{2}{3} A^{(w)} \frac{\partial f}{\partial \sigma_{ij}} - B^{(w)} {\chi_{ij}}^{(w)} \right) \tag{D.61}$$

$$\frac{\partial \Omega_{\chi ij}^{(w)}}{\partial \chi_{rs}^{(z)}} = -\frac{\partial \Omega_{\chi ij}^{(w)}}{\partial \sigma_{rs}} - B^{(w)} \Omega_{\gamma} \delta_{ir} \delta_{js} \delta_{wz}. \tag{D.62}$$

See Appendix C for a thorough description of the influence each parameter in the viscoplasticity model has on the overall response of the material. The appendix also provides useful relationships between parameters that proves beneficial when providing initial estimates and bounds for the fitting process, and for relating the expected behavior to simple experimental relationships.

Isotropic Plasticity with Nonlinear Kinematic Hardening (Ziegler)

Another set of rate equations and derivatives are presented below for a constitutive model that uses nonlinear isotropic and kinematic hardening where the kinematic rate is modeled after Ziegler's model. The linear kinematic terms are proportional to the shifted stress normalized by the current yield surface radius. Many of the equations are identical to those from the Armstrong-Frederick model; therefore, only those equations that are different are presented below. The rate form of the backstress is

$$\dot{\chi}_{ij}^{(w)} = \Omega_{\chi ij}^{(w)} = \Omega_{\gamma} \left(A^{(w)} \frac{1}{\sigma_y} \left(\sigma_{ij} - \chi_{ij} \right) - B^{(w)} {\chi_{ij}}^{(w)} \right), \tag{D.63}$$

and the required derivatives for $\Omega_{\chi_{ij}^{(w)}}$ are

$$\frac{\partial \Omega_{\chi ij}^{(w)}}{\partial \sigma_{rs}} = \Omega_\gamma A^{(w)} \frac{1}{\sigma_y} \delta_{ir}\delta_{js} + \frac{n}{D}\left\langle \frac{f}{D} \right\rangle^{n-1} \frac{\partial f}{\partial \sigma_{rs}} \left(A^{(w)} \frac{1}{\sigma_y} (\sigma_{ij} - \chi_{ij}) - B^{(w)} {\chi_{ij}}^{(w)} \right) \tag{D.64}$$

$$\begin{aligned} \frac{\partial \Omega_{\chi ij}^{(w)}}{\partial \rho^{(y)}} = & -\frac{n}{D}\left\langle \frac{f}{D} \right\rangle^{n-1} \left(A^{(w)} \frac{1}{\sigma_y} (\sigma_{ij} - \chi_{ij}) - B^{(w)} {\chi_{ij}}^{(w)} \right) \\ & - \Omega_\gamma \left(A^{(w)} \frac{1}{\sigma_y^2} (\sigma_{ij} - \chi_{ij}) \right) \end{aligned} \tag{D.65}$$

$$\frac{\partial \Omega_{\chi ij}^{(w)}}{\partial \chi_{rs}^{(z)}} = -\frac{\partial \Omega_{\chi ij}^{(w)}}{\partial \sigma_{rs}} - \Omega_\gamma B^{(w)} \delta_{ir}\delta_{js}\delta_{wz}. \tag{D.66}$$

D.2 Optimizer

An important part of the methodology developed is the optimization software as this directly influences the time required to perform the parameter identification. When using finite element method updating (FEMU) each function evaluation in the optimization requires a numerical solution. While many attempts have been made to simplify and expedite the numerical solution, having fewer function evaluations is highly desirable. The optimization software is an expanded version of code written by Phillips and Brockman [111]. Details regarding the optimization scheme and the integration with the axial-torsional finite element software are provided in the following sections.

D.2.1 Optimization Methods

Multiple optimization methods have been incorporated to provide strategies that seek both local and global minima. Two local, derivative free, minimization methods written by Powell are available. The first is Powell's method [28] which is an unconstrained conjugate gradient method. The second is Powell's Branched Optimization BY Quadratic Approximation (BOBYQA) [112] method, which is a constrained method that seeks the minimum through quadratic approximation. The constitutive parameters have physical bounds; therefore, when using Powell's method a penalty function is imposed to bound the parameters. The BOBYQA is a constrained method and does not need this additional enforcement. These two methods are already present in the software written by Phillips and Brockman [111].

Two evolutionary algorithm methods have been added to the optimization software. The first is a simple genetic algorithm (GA) with concepts taken from Goldberg's text [29]. The constitutive model parameters are the design variables for the optimization method. Each variable is stored using a desired number of chromosomes, or bits. If a variable has N chromosomes, there are 2^N possible values the variable can have. To constrain the variables, lower and upper bounds are provided and the increments in values are computed as $inc = \frac{upper-lower}{N-1}$. The floating point value, v, is computed from the integer value of the chromosomes, i, as $v = lower + inc * i$. A single parent contains chromosomes from all of the design variables in the optimization procedure. An initial sample of parents is generated using either a stochastic sampling or a Latin hypercube sampling.

The GA consists of the following processes: selection, crossover, and mutation. Selection is the process by which parents from the current generation are chosen to generate children for the next generation. Tournament selection has been utilized with the number of participants determined by the user's input options. In tournament selection, a desired number of parents are randomly chosen and the parent with the best fitness wins and is selected for crossover. This is repeated until all the mating pairs are defined. Crossover then occurs using multi-point crossover to form a single child from the two parents. In multi-point crossover, a random number is compared to the crossover tolerance and if the value exceeds the tolerance, the child obtains the chromosome from parent two; otherwise, the child receives parent one's chromosome. This is repeated for all the chromosomes from all the variables. Lastly, mutation occurs to perturb the chromosomes and introduce additional diversity in the population. Both jump and creep mutations are utilized and have separate tolerance levels that control their occurrence. Each variable has the potential for both jump and creep mutations. If a jump mutation occurs, the value of a randomly selected chromosome is changed. If creep mutations occurs, the value of the variable is shifted either up or down by one increment. The GA continues for a prescribed number of generations.

The second evolutionary algorithm implemented, which seeks to mimic the search patterns of animals, is particle swarm optimization (PSO). The method tracks the positions of particles (equivalent to GA parents) and their velocity through the design space over successive iterations. The velocity is affected by three factors: inertia, cognitive, and social. The basic formula to update the velocity for the i^{th} design variable from iteration k to iteration $k+1$ is

$$v_i{}^{(k+1)} = w_i v_i{}^{(k)} + c_{i1} r_{i1} \left(pbest_i - s_i{}^{(k)} \right) + c_{i2} r_{i2} \left(gbest_i - s_i{}^{(k)} \right) \tag{D.67}$$

where the inertia, cognitive, and social factors are w_i, c_{i1}, and c_{i2} respectively. The particle's position at iteration k is $s_i{}^{(k)}$. The particle's best fitness location thus far is given as $pbest_i$ and the best global fitness position is $gbest_i$. Both r_{i1} and r_{i2} are random numbers between zero and one that are multiplied by the factors. An optional pheromone term

$$c_{i3} r_{i3} \left(tbest_i - s_i{}^{(k)} \right) \tag{D.68}$$

can be added to Eq. (D.67) to attract particles to a local best, $tbest_i$, where c_{i3} is the pheromone factor and r_{i3} is again a random number between zero and one. The pheromone term is only added to Eq. (D.67) if the particle falls within a radius of influence defined by the user. The current implementation limits the number of pheromone scents, and also the number of particles that can be attracted to a single pheromone. Every iteration, the fitness of the particle is evaluated and then the position is updated for the next iteration using the equation $s_i{}^{(k+1)} = s_i{}^{(k)} + v_i{}^{(k+1)} * 1$. The PSO is also continued for a specified number of iterations.

One of the major benefits of both the GA and PSO is that fitness evaluations can be done independently for all the parents or particles. Unlike both of Powell's methods that require successive fitness evaluations, the GA and PSO easily lend themselves to parallelization. All portions of the finite element code outlined in Section D.1 have been carefully structured to allow for parallelization through the use of OpenMP (www.openmp.org). Therefore, the optimization procedure can call a desired number of finite element jobs at the same time. The speedup obtained is almost linear as the computation expense of the optimization methods is minimal in comparison to the expense of the implicit finite element solution with material nonlinearity.

The final optimization method available is nonlinear least-squares regression. The Intel Math Kernel Library (MKL) [113] procedure *dtrnlspbc* is used to perform nonlinear least-squares regression. It attempts to minimize Eq. (D.69) within the design space given by Eq. (D.70).

$$\min_{x \in R^n} \|F(v)\|_2^2 = \min_{x \in R^n} \|y - f(v)\|_2^2, y \in R^m, v \in R^n, f : R^n \to R^m, m \geq n \tag{D.69}$$

$$l_i \leq v_i \leq u_i, i = \{1, ..., n\}, l \in R^n, u \in R^n \tag{D.70}$$

Equation (D.69) is specialized to allow for the use of the objective function given in Eq. (D.71). The vector y represents the axial or shear stress at all the desired time points, while the vector f contains the corresponding results from the finite element simulation. If multiple experiments are used in the objective function, each data point $y - f(v)$ is normalized by $\sqrt{N}$ where N is the number of data points for the appropriate experiment.

D.2.2 Objective Function

When using FEMU, each objective function evaluation requires a separate call to the finite element program with a different set of material parameters. The optimization seeks to minimize the objective function given by

$$c^{(m)} = \frac{1}{N} \sum_{i=1}^{N} w_F \left(F_i^{(exp)} - F_i^{(fe)} \right)^2 + w_T \left(T_i^{(exp)} - T_i^{(fe)} \right)^2 \tag{D.71}$$

where N is the number of load steps (experimental data points) used in the FE solution, and i denotes the individual load step. The first and second terms of the objective function are related to the force, F, and torque, T, respectively. The superscript 'exp' denotes experimental results while 'fe' denotes finite element results. Each term has a weight factor that can reconcile the difference in magnitude between the force and torque. For this work, $w_F = A^{-2}$ where A is the initial cross-section area, and $w_T = r^2 J^{-2}$ where r is the outer radius of the specimen and J is the polar moment of inertia. With the chosen weight factors, the objective function has units of stress squared. The experimental values come directly from the load cell, while the FE values are obtained through integration of element stresses. The objective function is computed for each set of experimental data, m, and the final objective function is the sum of all terms, $c^{(m)}$.

For experimental results, the calculation of stresses under axial only loading is uniform even under plastic deformation. However, the stresses under torsional loading are not as well defined unless using a thin-walled tubular specimen. For solid and non-thin-walled tubular specimens, the gradient in the shear stress versus radial position is dependent on the assumed material model. Also when plastic deformation occurs the stresses are no longer a linear function of radial position. Certain more complicated stress equations rooted in specific hardening assumptions have previously been derived by others [114]. However, to make matters worse, when both axial and torsional loading are combined under plastic deformation, the axial stress is no longer uniform. Therefore, in reducing the experimental data the axial force and torque are used to eliminate any assumptions based on an assumed material model yet to be ascertained.